DIGITAL ACCESS TO SCHOLARSHIP AT HARVARD
DASH.HARVARD.EDU

HARVARD LIBRARY
Office for Scholarly Communication

Theoretical study of exciton transport in natural and synthetic light-harvesting systems

Citation

Valleau, Stephanie. 2016. Theoretical study of exciton transport in natural and synthetic light-harvesting systems. Doctoral dissertation, Harvard University, Graduate School of Arts & Sciences.

Permanent link
http://nrs.harvard.edu/urn-3:HUL.InstRepos:33493387

Terms of Use
This article was downloaded from Harvard University's DASH repository, and is made available under the terms and conditions applicable to Other Posted Material, as set forth at http://nrs.harvard.edu/urn-3:HUL.InstRepos:dash.current.terms-of-use#LAA

Share Your Story
The Harvard community has made this article openly available.
Please share how this access benefits you. Submit a story .

Accessibility

Theoretical study of exciton transport in natural and synthetic light-harvesting systems

A dissertation presented

by

Stéphanie Valleau

to

The Committee in Chemical Physics

in partial fulfillment of the requirements

for the degree of

Doctor of Philosophy

in the subject of

Chemical Physics

Harvard University

Cambridge, Massachusetts

April 2016

© 2016 - Stéphanie Valleau
All rights reserved.

Dissertation advisor
Prof. Alán Aspuru-Guzik

Author
Stéphanie Valleau

Theoretical study of exciton transport in natural and synthetic light-harvesting systems

Abstract

In the first part of this dissertation, we investigate on the presence of quantum effects in the exciton dynamics of the Fenna-Matthews-Olson photosynthetic complex of green sulfur bacteria using an atomistic Quantum Mechanics / Molecular Mechanics (QM/MM) model combined with open quantum systems methods. Subsequently, we explore the theoretical connection between the atomistic QM/MM approach and the open quantum system methods and propose the correct theoretical expressions to maintain consistency when using both approaches contemporarily. In particular we show that when using the correct prefactor to extract the spectral density - the strength of coupling between excitation and other degrees of freedom - the atomistic results are in good agreement with experimental predictions. We then describe a first atomistic study of the full light-harvesting complex of green sulfur bacteria. The various units are treated atomistically and the full system's exciton dynamics is obtained using a Markovian open quantum system master equation. To conclude the first part, we describe a Machine Learning algorithm which we developed and implemented to learn time-dependent density functional theory energies by using trained neural networks and supplying these with coulomb matrices extracted from molecular dynamics simulations. This approach provides a much more rapid solution to obtaining a QM/MM Hamiltonian and subsequently extracting dynamics. It is particularly useful when multiple identical molecules are found in similar environments as one can train the network on a single molecule and predict all others. We applied this method to the Fenna-Matthews-Olson complex.

In the second part of this dissertation we focus on model systems and synthetic aggregates. In particular, we investigate the exciton dynamics in thin-film J-aggregates using a Markovian stochastic Schrödinger equation approach. We derive expressions to obtain diffusion constants from the dynamics and compare a series of different thin-film J-aggregates. The parameters of the model are obtained atomistically. From this model we obtain information on the parameters which lead to optimal exciton diffusion. This can guide the design of new exciton transfer materials.

Dissertation advisor	Author
Prof. Alán Aspuru-Guzik	Stéphanie Valleau

We finish by discussing a classical electromagnetic study of exciton dynamics in a dipole array model for the natural Chlorosome antenna complex of green sulfur bacteria Chlorobaculum tepidum. The main advantage of this model is the possibility of treating a large number of degrees of freedom.

Contents

Introduction **1**

1 Introduction to excitonic systems **3**

2 Theoretical methods for exciton transport **10**
- 2.1 Excitons: Frenkel, charge-transfer and Wannier-Mott excitons 10
- 2.2 Exciton transport models: Förster theory 12
- 2.3 Open-quantum system methods for exciton dynamics 12
  - 2.3.1 Coupled two-level excitonic systems 13
  - 2.3.2 Markovian methods for exciton dynamics 17
  - 2.3.3 Non-markovian methods for exciton dynamics: Hierarchy equation of motion 20

I Excitonic energy transport in natural light-harvesting complexes **23**

3 Atomistic study of the long-lived quantum coherences in the Fenna-Matthews-Olson complex **25**
- 3.1 Introduction 25
- 3.2 Methods 27
  - 3.2.1 Molecular dynamics simulations 27
  - 3.2.2 Exciton dynamics 30
  - 3.2.3 Quantum Jump Correction to MD Method (QJC-MD) 31
- 3.3 Results and discussion 32
  - 3.3.1 Site energy distributions 32
  - 3.3.2 Dephasing rates 34
  - 3.3.3 Simulated Spectra 34
  - 3.3.4 Population dynamics and long-lived quantum coherence 35
  - 3.3.5 Comparison between MD, QJC-MD, HEOM, and HSR methods 37
  - 3.3.6 Correlation functions and spectral density 40
- 3.4 Conclusion 42

4 On the alternatives for bath correlators and spectral densities from mixed quantum-classical simulations **45**
- 4.1 Introduction 45
- 4.2 The quantum correlation function and the spectral density 48
  - 4.2.1 Fourier transform of the time correlation function and symmetries of the correlator 49
  - 4.2.2 The spectral density 50
  - 4.2.3 General semiclassical a posteriori approximations 50
- 4.3 Energy gap correlation function for a simple model 53

4.3.1 Quantum correlation function and energy gap correlation function for a single molecule . . . 53
4.3.2 Quantum correlation function and energy gap correlation function for harmonic surfaces . . . 55
4.4 Classical and semiclassical limits of the correlators and spectral densities for harmonic surfaces . . . 58
4.4.1 Classical equations of motion . . . 58
4.4.2 Energy gap correlator . . . 59
4.4.3 Classical and semiclassical correlation functions . . . 59
4.4.4 Classical and semiclassical spectral densities . . . 60
4.5 Models for system-bath coupling: higher order correlators . . . 61
4.6 Application to the FMO complex . . . 63
4.6.1 TDCD and spectral density from mixed QM/MM with a posteriori semiclassical corrections . . . 64
4.6.2 Analysis of prefactors in terms of temperature dependence of the spectral density . . . 66
4.6.3 Comparison to experimental spectral density . . . 66
4.6.4 Higher-order correlation function . . . 70
4.7 Conclusions . . . 72

5 Atomistic study of energy funneling in the light-harvesting complex of green sulfur bacteria 74
5.1 Introduction . . . 74
5.1.1 Molecular aggregate model . . . 75
5.1.2 Exciton transfer model . . . 78
5.2 Excitation energy funneling . . . 82
5.2.1 Exciton population dynamics . . . 83
5.2.2 Cooperativity of the excitonic states . . . 87
5.2.3 Temperature dependence of the energy funneling . . . 88
5.2.4 Population kinetics . . . 89
5.3 Conclusion . . . 90

6 Machine learning exciton dynamics 93
6.1 Introduction . . . 93
6.2 Methods and computational details . . . 94
6.2.1 Ground state QM/MM simulations . . . 94
6.2.2 Machine Learning: neural networks training . . . 96
6.2.3 Exciton dynamics and spectral densities . . . 98
6.3 Results and discussion . . . 99
6.3.1 Excited state energy prediction using neural networks . . . 99
6.3.2 Spectral densities and exciton dynamics with neural networks . . . 103
6.4 Conclusion . . . 107

II Synthetic and model molecular aggregate systems for exciton transport 109

7 Exciton transport in thin-film cyanine dye J-aggregates 111
7.1 Introduction . . . 111
7.2 The model . . . 114
7.2.1 Hamiltonian and single exciton dynamics . . . 114
7.2.2 Static and dynamic noise . . . 117
7.2.3 Diffusion model . . . 119

- 7.3 Computational details 121
  - 7.3.1 Monomer properties 121
  - 7.3.2 Monte Carlo wave function propagation 121
- 7.4 Results and discussion 123
  - 7.4.1 Model parameters 123
  - 7.4.2 Quantum exciton dynamics 128
  - 7.4.3 Diffusion coefficient and diffusion length 131
- 7.5 Conclusions 135

8 Electromagnetic study of the chlorosome antenna complex of Chlorobium tepidum 138

- 8.1 Introduction 138
- 8.2 Results and discussion 141
  - 8.2.1 Antenna spectra and resonances 141
  - 8.2.2 Induced fields 144
  - 8.2.3 Energy flux 149
- 8.3 Conclusions 151
- 8.4 Methods 153
  - 8.4.1 Physical model of the chlorosome structure 153
  - 8.4.2 Polarizability model 154
  - 8.4.3 Optical properties 156

Conclusions and future work 159

Bibliography 182

Citation to previously published work

Chapters 3-8 have, apart from minor modifications, appeared as the following publications:

> "Atomistic study of the long-lived quantum coherences in the Fenna-Matthews-Olson complex" Sangwoo Shim, Patrick Rebentrost, Stéphanie Valleau and Alán Aspuru-Guzik, Biophysical Journal: 102, 649 (2012)
>
> "On the alternatives for bath correlators and spectral densities from mixed quantum-classical simulations" Stéphanie Valleau, Alex Eisfeld and Alán Aspuru-Guzik, Journal of Chemical Physics: 137, 224103 (2012)
>
> "Atomistic study of energy funneling in the light-harvesting complex of green sulfur bacteria" Joonsuk Huh, Semion K. Saikin, Jennifer C. Brookes, Stéphanie Valleau, Takatoshi Fujita, and Alán Aspuru-Guzik. Journal of the American Chemical Society: 136, 2048 (2014)
>
> "Machine learning exciton dynamics" Florian Häse, Stéphanie Valleau, Edward Pyzer-Knapp, and Alán Aspuru-Guzik. Chemical Science, in press, doi: 10.1039/C5SC04786B (2016)
>
> "Exciton transport in thin-film cyanine dye J-aggregates" Stéphanie Valleau, Semion K. Saikin, Man-Hong Yung and Alán Aspuru Guzik, Journal of Chemical Physics: 137, 034109 (2012)
>
> "Electromagnetic study of the chlorosome antenna complex of Chlorobium tepidum" Stéphanie Valleau, Semion K. Saikin, Davood Ansari-Oghol-Beig, Masoud Rostami, Hossein Mosallaei, and Alán Aspuru-Guzik. ACS Nano: 8, 3884 (2014)

Other publications which were carried out during the time of this dissertation but are not explicitly included as independent chapters are listed below:

> "First principles semiclassical calculations of vibrational eigenfunctions", Michele Ceotto, Stéphanie Valleau, Gian Franco Tantardini and Alán Aspuru-Guzik, Journal of Chemical Physics: 134, 234103 (2011)
>
> "Photonics meets excitonics: natural and artificial molecular aggregates", Semion Saikin, Alex Eisfeld, Stéphanie Valleau and Alán Aspuru-Guzik, Nanophotonics: 2, 21 (2013)
>
> "Deep nuclear resonant tunneling thermal rate constant calculations", Salvatore Mandrà, Stéphanie Valleau and Michele Ceotto, International Journal of Quantum Chemistry: 113,1722 (2013)
>
> "Parametric hierarchical matrix approach for the wideband optical response of large-scale molecular aggregates", Davood Ansari-Oghol-Beig, M. Rostami, E. Chernobrovkina, S. K. Saikin, Stéphanie Valleau, H. Mosallaei, and Alán Aspuru-Guzik. Journal of Applied Physics: 114, 164315 (2013)
>
> "Influence of force fields and quantum chemistry approach on spectral densities of BChl a in solution and in FMO proteins", Suryanarayanan Chandrasekaran, Mortaza Aghtar, Stéphanie Valleau, Alán Aspuru-Guzik, and Ulrich Kleinekathöfer. Journal of Physical Chemistry B: 119, 9995 (2015)

Acknowledgments

After these years spent at Harvard I feel I understand why the PhD is so different from a Bachelor's or Master's degrees. It is a an adventure, from the start until the end and one never knows what the path will be and where it will lead. That is the beautiful and contemporarily challenging aspect of doing research at the edge.

I would like to start by thanking my advisor, Prof. Alán Aspuru-Guzik. Alán, thank you for teaching me how to navigate through my PhD during these years and for your incredible optimism and enthusiasm. Your mentoring and feedback have helped me arrive to where I am today. Thank you for being my advisor and friend.

I thank Prof. Heller for the many useful scientific discussions. I feel lucky to have had the opportunity to get his feedback and advice on science and life as a scientist throughout my PhD. I would like to thank Prof. Cohen as well for being a member of my committee and providing me with another view of the problems I was tackling as well as many interesting questions and suggestions. I also thank Prof. Shakhnovich for providing me with feedback on a project I began at the end of my PhD. I thank my former advisor Prof. Michele Ceotto for his support and feedback from Italy.

The Aspuru-Guzik group has evolved a lot in the last five years and it was wonderful to meet everyone who became part of the group or left. I would like to thank a few people in particular.

I thank Dr. Semion K. Saikin, for mentoring me scientifically at the start of my PhD. I was happy to collaborate with him on various interesting projects related to exciton transport in molecular aggregates. I thank Dr. Alex Eisfeld who taught me to love J-aggregates, Dresden and open quantum systems models. I thank Dr. Dmitrij Rappoport for his help on multiple scientific questions, in particular on the computation of excited states. I would like to thank visiting student Florian Haese who is beginning his own scientific adventure. It was great to mentor him and work with him. I also thank Dr. Davood Ansari-Oghol-Beig and Masoud Rostami for our collaboration on the electromagnetic study of exciton dynamics in the chlorosome. I thank my colleagues in the first "excitonics" offices with whom I had interesting discussions on exciton dynamics. In particular I thank David Gelbwaser, Christoph Kreisbeck and Doran Bennett.

I thank Dr. Jarrod McClean, J*, above all for his friendship, but also for the many interesting scientific discussions. Our multiple tea/coffee/lunch/tgif breaks helped during the ups and downs of the PhD adventure. I thank Gian Giacomo Guerreschi, Borja Peropadre and the QI office for their friendship, the many discussions, pool games and games of Catan. I thank Dr. Joel Yuen-Zhou for his friendship and for introducing me to the Aspuru-Guzik group, Harvard and the mexican community in Boston. I thank all other members of the group and collaborators who are not explicitly mentioned for our scientific exchanges.

Outside the world of science I truly thank my family, dispersed around the world, in Italy, Canada and Switzerland, for all their love and support. It would not have been possible for me to finish without them and without Skype. My parents have always been encouraging me to pursue my dreams and now the dream of obtaining a PhD has become a reality. I treasure the memories of our summer hikes in the Italian alps and the rewarding dinners in the *crotto* afterwards. I thank them both from the bottom of my heart.

I am really happy to thank my little sister, Annick, for her continuous support and love. Our overseas discussion brought joy in my life every day and visiting her and Iacopo in Switzerland was always a great experience filled with laughter, swimming, sushi, bbq, wonderful chocolate and fondue.

I thank my elder sister Carine and my niece Jessica for their love and for their many visits to Cambridge. Our multiple snow-fights made the 8 hour greyhound trip to Montreal in December worth the ride.

I also thank my wonderful aunt Cathy who came to visit often, took me to New-York and helped me move-in the first year. She reminded me that as much as I love science there are many other things worth doing in life.

I thank my friends of the kebab crew, our kebab lunches were great to catch up and have some good laughs over tasty tandoori and curries.

I thank my special and dear friend Reem Hannun for her great friendship and affection. I will really miss our hugs, tea breaks, discussions outside Widener, spinning classes, PS1 sections, movie nights, party nights and simply our gossip conversations.

I thank the great salsa dancers and singers Viviana, Alexi, Joel and Araceli for their friendship. We shared many crazy party nights, karaoke until the early morning, pot-lucks, drinks and tea breaks.

Last but not least, I thank my life companion, Salvatore, who sustains me everyday and has been traveling with me since the start of this journey.

To my family, all around the world

There are only two ways to live your life.
One is as though nothing is a miracle.
The other is as though everything is a miracle.

— Albert Einstein

Introduction

Page intentionally left blank.

Chapter 1

Introduction to excitonic systems

According to the U.S. Energy Information Administration Annual Energy Outlook 2014 report, "Solar energy is the fastest-growing source of renewable generation, increasing by 7.5%/year from 2012 to 2040". This type of growth prognostic is possible, amongst other things, due to the huge scientific effort dedicated to improving the efficiency of solar cell materials. In the time during which I have worked on my PhD, the number of papers published per year which mention the words solar cell have almost tripled (Fig. 1.1).

Inspiration for new pathways to capture sunlight has come from a variety of sources. Amongst these, natural photosynthetic systems have received a large amount of attention [1–8]. These systems have evolved for millions of years to optimize their organisms for survival and energy production using sunlight. The idea of creating nature inspired materials, which can be tuned to increase the exciton transport is fascinating. Such materials could be auto-generated in bacterial organisms at the cost of sunlight, water and a few nutrients.

As a young theoretical chemist, entering this field was both challenging and exciting. Using quantum mechanics, classical mechanics and a combination of these to make predictions and understand the physics of exciton transport provided me with a new vision and invaluable skills for the study of the development of optimal light-capturing materials.

This thesis is divided in two main parts. In the first, I investigated exciton transport in natural light-harvesting complexes. In the latter, I investigated model systems and synthetic aggregates in the context of finding optimal exciton transport materials. A description of each of these parts is provided below.

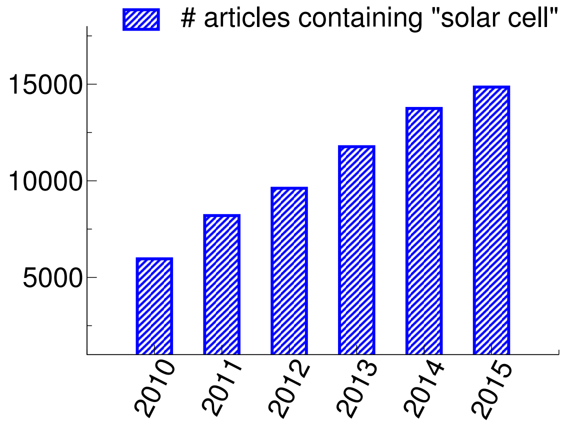

Figure 1.1: Graph showing number of scientific articles containing the words “solar cell”. Data taken from the web of knowledge database by refining number of articles per year.

Part I: Excitonic energy transport in natural light-harvesting complexes, from understanding to design

Here I will briefly introduce the systems which are studied theoretically: photosynthetic bacteria. In the second section I will discuss the theoretical work which was carried out to elucidate the exciton dynamics in these natural systems.

Photosynthetic bacteria and green sulfur bacteria

Theoretical predictions and analyses rely on the knowledge of molecular structures. Sometimes models can be employed to make educated guesses on unknown or partially known structures. Nonetheless most information can be extracted from a chemical or biological system when a structure is available.

The first crystal structure for a pigment-protein photosynthetic complex was obtained by Roger Fenna, Brian Matthews and John Olson in 1974-75 [9, 10]. This complex is a water soluble bacteriochlorophyll protein which is found in green sulfur bacteria. It now takes the name FMO complex from the scientists who resolved its structure. FMO is found in all of the Chlorobi phyla and recently it has also been found in Candidatus Chloracidobacterium Thermophilum of the Acidobacteria phyla [11]. In these organisms, the FMO complex forms a homo-trimer where each monomer (see Fig. 1.2) consists of 7/8 bacteriochlorophyll-a (BChl-a) pigment molecules enclosed in a protein scaffolding. The BChl pigment molecules are held within the protein scaffold through coordination bonds of amino acid polar groups (e.g. NH_2) to the Mg atom of the porphyrin ring and through hydrogen bonds. The complex is thought to act as an excitonic wire, funneling the excitation to the so-called "reaction center".

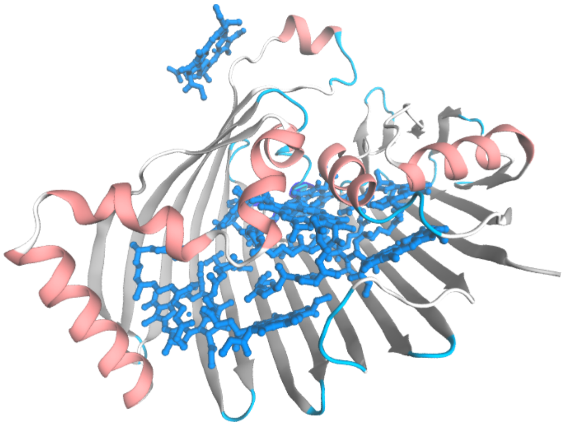

Figure 1.2: FMO complex crystal structure for *Chlorobaculum-tepidum*: monomer protein scaffold, (PDB code: 3ENI), the monomer contains 366 amino acids. The BChl-a molecules are colored in blue and the surrounding protein is colored based on the structure (alpha-helix / pink, beta sheet / grey, loop / cyan,).

Green sulfur bacteria have existed since the Proterozoic era and survive through anoxygenic photosynthesis: they use sulfide and other reduced sulfur compounds or hydrogen as photosynthetic electron donors [1]. The light-harvesting complex apparatus (LHC) in green sulfur bacteria is composed of bacteriochlorophyll (BChl) pigment molecules. These monomers aggregate in several interconnected functional units, as shown in Fig.1.3. The main element of LHC is the chlorosome - an ellipsoidal shaped body of size ranging from tens to hundreds of nanometers [12]. The chlorosome is densely packed with BChl c pigments. Two other functional units - the baseplate [13] and the Fenna-Matthews-Olson (FMO) trimer complex [14] are composed of BChl a pigments held together by a protein scaffold. Energy in the form of molecular excitations (*i.e.* exciton) is collected by the chlorosome and funneled through these antenna units to the reaction center where charge carriers are then generated.

After the FMO complex crystal structure was resolved, the first crystal structure for a membrane-protein complex was obtained for purple photosynthetic bacteria in 1984 by Hartmut Michel, Johann Deisenhofer and Robert Huber [15]. This important work earned them the 1988 Nobel prize. Finally, in the nineties, a series of crystal structures were resolved for membrane protein light-harvesting complexes: LHCII [16] of green plants, LH2 of Rhodopseudomonas acidophila [17], the core of

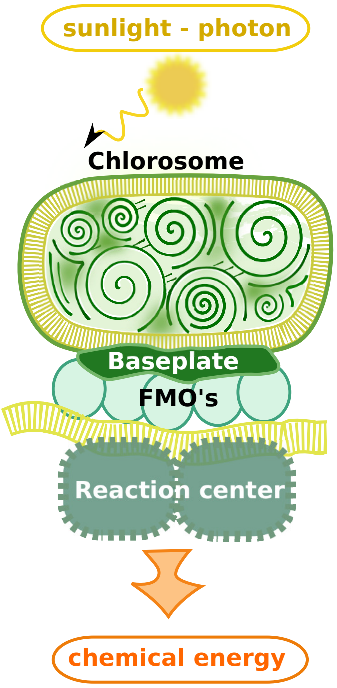
sunlight - photon
Chlorosome
Baseplate
FMO's
Reaction center
chemical energy

Figure 1.3: Sketch of the light-harvesting complex elements of the photosynthetic apparatus of green sulfur bacteria. Sunlight is absorbed by the chlorosome and transferred in the form of an exciton through the baseplate and Fenna-Matthews-Olson (FMO) complexes to the reaction center where charge separation occurs.

Photosystem I of cyanobacteria [18]. These experimental discoveries opened up the road to the possibility of exploring exciton dynamics in these systems with theoretical chemistry.

Theoretical study of exciton transport in green sulfur bacteria

Given that FMO was the first light-harvesting complex for which a structure was available, it is one of the most extensively studied [19–25]. Researchers showed a renewed interest in the FMO complex in recent years when 2D-spectroscopy experiments suggested the presence of quantum coherent effects [26] in the exciton dynamics. Following these experiments, much theoretical work was carried out [27–38] with the main goal of understanding whether quantum effects were present and if so, how they contributed to the exciton transport. Most theoretical studies relied on the existence of an X-ray crystal structure of the FMO complex of either *Chlorobaculum tepidum* or *Prosthecochloris Aestuarii*.

The initial theoretical work on FMO [28, 31, 39, 40] was carried out using model Hamiltonians. These Hamiltonians were based on specific studies where energies of the BChls and couplings had been extracted using ab-initio methods [22]. The exciton dynamics was then carried out using a series of open-quantum system master equation or stochastic Schrödinger approaches were the excitation density evolved under the influence of coupling to a bath of harmonic oscillators. These approaches will be described in Chapter 2. While this is a good first approach to the problem, an atomistic study where time-dependent QM/MM trajectories are obtained can provide much more information. We performed one of the first of these studies, contemporarily with the group of prof. Kleinekhatöfer [33]. This work in described in Chapter 3. In this work I will also describe a method for correcting the ground state QM/MM method by introducing a term which accounts for zero point fluctuations which are missing in the classical MD.

The connection between ground state QM/MM and the quantities introduced in the open-quantum system models is often unclear. In the open-quantum system approach the atomistic degrees of freedom are grouped into three parts, a system part, a system-bath part and a bath, which can each be treated with various levels of approximations. The interaction of the system, in our case, the excitonic degrees of freedom, with the bath, everything else, is described by a quantity defined as the spectral density. The spectral density, for each frequency, provides the strength of coupling of the system to the bath. One problem that arises in this context is how to extract this theoretical quantity from an atomistic ground state QM/MM simulation. I investigated this theoretically using a model system in Chapter 4 and found that specific prefactors had to be used in order to be consistent with both the QM/MM and open-quantum system approaches. The resulting spectral densities for FMO were in good agreement with the corresponding experimental results.

Following the interest in the FMO complex, the community became interested in the full LHC system of green-sulfur bacteria. In Chapter 5 for the first time, we investigated the exciton dynamics in the combined system consisting of the chlorosome, baseplate and FMO complexes atomistically.

In Chapter 6, we describe our approach to predict TDDFT energies by using machine learning with neural networks. Using neural networks provides a huge speed up. Indeed, once the networks are trained we can extract excited state energies at the cost of molecular dynamics simulations. This method is particularly useful when one needs to compute multiple excited state energies of the same molecules, e.g. for QM/MM simulations. We applied it to the FMO complex and were able to determine the average energy of each site based on networks trained on a single BChl molecule.

Part II: Synthetic and model molecular aggregates systems for exciton transport

In this second part of the thesis I will discuss my work on the exciton dynamics of synthetic molecular aggregates and aggregates inspired by natural systems. In Chapter 7, I will describe a study of exciton diffusion for various thin-film J-aggregate systems. Subsequently I will introduce a model structure for the chlorosome antenna complex found in green-sulfur bacteria and discuss a classical electrodynamic study of the system.

J-aggregates

Discovered over 80 years ago independently by Scheibe and Jelley [41, 42], J-aggregates are typically formed by organic fluorescent dye molecules and can be identified spectroscopically by the narrowing and batochromic shift (J-band) of the lowest electronic excitation relative to the monomer band [43, 44]. These structures are characterized by the unique properties associated with their J-band: a large absorption cross-section, short radiative lifetimes, a small Stokes shift of the fluorescence line and efficient energy transfer within the aggregate [44]. These aggregates can be synthesized layer by layer and are characterized by a red batochromic line narrowed absorption spectra and strong intermolecular couplings. I investigate and extract the parameters which are mainly responsible for enhanced diffusion in these J-aggregates.

Respect to natural aggregates these systems present the advantage of control over the synthesis process. This in turn allows for many applications. For instance, the applications of J-aggregates range from their use as "reporter molecules" in mitochondrial membrane potentials in living cells [45] to photosensitizing silver halides in photography [46]. Moreover, J-aggregates are employed in dye-sensitized organic solar cells which provide several advantages over inorganic solar cells [47, 48]. Recently, cyanine dye J-aggregates have been combined with optical cavities [49–51] or coupled to quantum dots [52] to form hybrid systems.

Nature-inspired antenna systems

In the last Chapter 8, I will present a classical electrodynamics study of a model system: an aggregate of dipoles based on the structure of the chlorosome antenna complex of green-sulfur bacteria. This represents an effort to extract excitonic information from a system with a huge number of degrees of freedom by using a classical theory. It is a nice example of the fact that often a more complicated theory will not necessarily provide more information and that simpler and numerically faster models can provide robust initial answers. This work also introduces the idea of generating nanoantennas based on the natural antenna complexes.

Chapter 2

Theoretical methods for exciton transport

In general, to obtain the dynamics of a system quantum mechanically, we need to solve the time-dependent Schrödinger equation for that system. This quickly becomes impossible to carry out exactly, indeed only for the two body problem there exists and exact solution. For this reason, many clever approximations have been made and theories developed to enable one to extract the dynamics in certain regimes or for specific parts of systems without having to solve for the full problem.

2.1 Excitons: Frenkel, charge-transfer and Wannier-Mott excitons

In the field of excitonics, one is often interested in understanding how an *exciton*, either localized on a single molecule or delocalized over several units, propagates in a system of interacting molecules. There are three main categories of excitons. With the term *Frenkel exciton*, named after Yakov Frenkel, we refer to a quantum mechanical state which consists of a bound excited electron / hole pair localized at the same molecule [53, 54] (radius of about $10\,\text{Å}$ and binding energy $\sim 1\,\text{eV}$). Frenkel excitons are found in non-covalently bound systems such as molecular crystals, j-aggregates or photosynthetic complexes. Note that the excitation in the aggregate is not necessarily confined to a single monomer but can be coherently delocalized over many molecules.

When the excited electron and hole are very distant (radius of about $100\,\text{Å}$, binding energy $\sim 10\,\text{meV}$), ie separated by a distance much larger than the intermolecular spacing, we refer to the excitation as a *Wannier-Mott* exciton [55]. These excitons are found when there are strong binding forces (e.g. covalent) between the molecules, for instance they are typical in inorganic semiconduc-

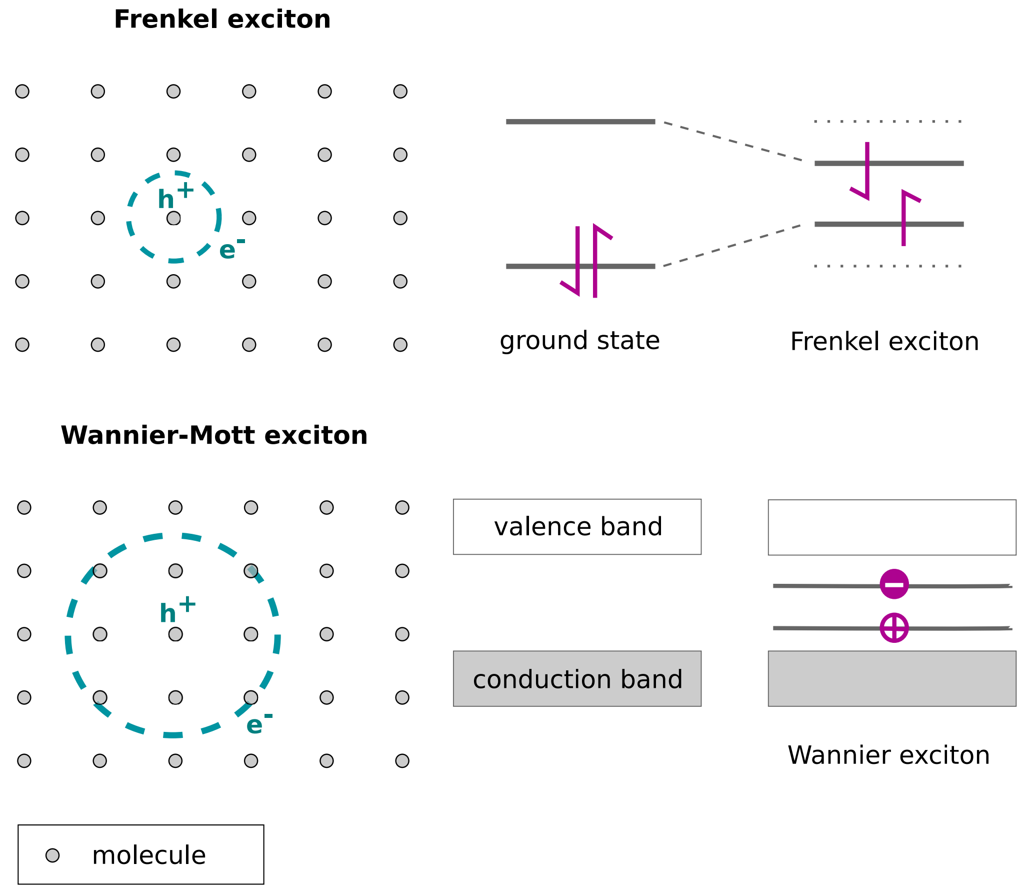
Frenkel exciton
h+
e-
ground state
Frenkel exciton
Wannier-Mott exciton
h+
e-
valence band
conduction band
Wannier exciton
molecule

Figure 2.1: Sketch of the two limiting cases of an exciton. In the top panel a Frenkel exciton with the electron-hole pair localized on a molecule. To the right the molecular states of the system in the ground state are shown and then those of a singlet Frenkel exciton are shown. Similarly in the bottom panel we see the picture of a Wannier-Mott exciton where the electron-hole pair is delocalized with a bohr radius covering several molecules. The diagram of bands and exciton states is shown on the right.

tors.

In the intermediate situation where the excited electron and the hole are not localized on the same molecule but are close enough that the wavefunctions of the involved molecules still overlap, we refer to the excitation as a *charge transfer* exciton.

A sketch of the two limiting cases of the Frenkel and Wannier-Mott excitons is shown in Fig. 2.1. In this thesis we will be dealing with Frenkel type excitons.

2.2 Exciton transport models: Förster theory

The initial theoretical models for exciton transport in molecular aggregates were based on an incoherent rate approach. This work was carried out by T. Förster and D. L. Dexter [56, 57]. An incoherent type of energy transfer (weak intermolecular coupling) can occur when the interaction with the environment is much stronger than the resonant excitation transfer and the excitation is localized on a single molecule, as in the case of Frenkel excitons. In these cases Förster theory predicts the rate constants for transport of excitation from one donor molecule to an acceptor molecule as the overlap of the donor emission spectrum and the absorption spectrum [53, 58],

$$k_{\text{acc-don}} = \text{const} \cdot \frac{\left[\mathbf{u}_{\text{acc}} \cdot \mathbf{u}_{\text{don}} - 3\left(\mathbf{u}_{\text{acc}} \cdot \mathbf{r}_{\text{acc-don}}\right)\left(\mathbf{u}_{\text{don}} \cdot \mathbf{r}_{\text{acc-don}}\right)\right]^2}{n^4 R^6_{\text{acc-don}}} \times \int_0^\infty \alpha_{\text{acc}}(\omega) \cdot I_{\text{don}}(\omega)\, \frac{\mathrm{d}\omega}{\omega^4}. \tag{2.1}$$

Here $\mathbf{u}_{\text{acc}}$ and $\mathbf{u}_{\text{don}}$ are the unit vectors which are directed along the transition dipoles of the acceptor and donor molecule respectively. $R_{\text{acc}-\text{don}}$ is the distance in between the center of the two molecules (acceptor and donor), n is the index of refraction of the solvent, and $\mathbf{r}_{\text{acc}-\text{don}}$ is the unit vector directed from the center of the acceptor to the donor. Finally, $\alpha_{\text{acc}}(\omega)$ is the acceptor absorption coefficient and $I_{\text{don}}(\omega)$ is the donor emission spectrum. Förster theory thus assumes that the donor in its electronic excited state may transfer energy to an acceptor through a non radiative dipole-dipole coupling. The rate is very sensitive to changes in distance given the dependence on $R^6_{\text{acc-don}}$ at the denominator. Further it depends on a good overlap of the acceptor absorption and donor emission spectra.

The real situation is often much more complex, one cannot describe transport through this incoherent hoping model, transport may neither be entirely coherent or incoherent and thus different models are needed to describe the exciton dynamics. Nonetheless, Förster theory or FRET (Fluorescence Resonant Energy Transfer) has had an enormous success in predicting rates of transfer for many systems and situations [59–62].

2.3 Open-quantum system methods for exciton dynamics

To obtain the exciton dynamics in photosynthetic complexes or molecular aggregates, one needs to deal with a large number of degrees of freedom. Often it is possible to focus on a subset of these degrees of freedom (system, S) and study the dynamics of this part while it interacts with the rest of the degrees of freedom (bath, B). This is the formalism of methods for open-quantum systems. One example is the dynamics of Frenkel excitons (system) interacting with all other degrees of freedom (bath), e.g. the chromophores, protein scaffold, solvent.

The total Hamiltonian can be expressed generically as

$$\hat{H} = \hat{H}_S + \hat{H}_B + \hat{H}_{SB}, \tag{2.2}$$

where $\hat{H}_S$ is the system Hamiltonian, $\hat{H}_B$ is the bath Hamiltonian and $\hat{H}_{SB}$ is the system-bath Hamiltonian, which captures the interaction amongst the two quantum systems. The Liouville equation for the total density matrix, $\hat{\rho}$ is

$$\frac{\partial \hat{\rho}(t)}{\partial t} = -\frac{i}{\hbar}\left[\hat{H}, \hat{\rho}(t)\right] \tag{2.3}$$

For such an open-quantum system, given that environment and system are assumed to be distinguishable, the Hilbert space of the two coupled quantum systems is given by the tensor product $\mathcal{H}_S \otimes \mathcal{H}_B$. Therefore, given an observable $\hat{O} = \hat{O}_S \otimes \hat{I}_B$ of the entire system, $\left\langle \hat{O}(t) \right\rangle = \mathrm{tr}_S\left(\hat{O}_S \rho_S(t)\right)$. This shows that all the information we require can be extracted from the reduced density operator $\hat{\rho}_S(t) = \mathrm{tr}_B \hat{\rho}(t)$. The equation of motion of $\hat{\rho}_S$ will be derived in the next subsection. From now on, we will orient the discussion with a specific emphasis on excitonic molecular aggregate systems. For a general discussion and derivation of open-quantum system methods the reader can refer e.g. to Ref. [63].

2.3.1 Coupled two-level excitonic systems

In all the molecular aggregate systems considered in this thesis, we restrict the description to that of a single ground state, S_0, and the first excited state S_1 for each molecule. It is straightforward to include more states (triplet states, higher singlet states), but for the sake of simplicity and related computational cost, the description will be given for a set of N coupled two level molecules. Following the description of Ref. [53], in this case, the system Hamiltonian represents the electronic degrees of freedom and can be expressed as

$$\hat{H}_S \equiv \hat{H}^{el} = \sum_{m=1}^{N} \sum_{\alpha=g,e} \epsilon_{m\alpha} \left|\psi_{m\alpha}\right\rangle \left\langle\psi_{m\alpha}\right| + \sum_{mn} V_{mn} \left|\psi_{me}\psi_{ng}\right\rangle \left\langle\psi_{ne}\psi_{mg}\right| . \tag{2.4}$$

Here, only two electronic quantum numbers, $\alpha = g$ or e, ground and excited state, are possible for each molecule, m, given the two-level system assumption. The wavefunctions $\psi_{m\alpha}$ are the adiabatic electronic eigenstates of the molecular Hamiltonian of the $m-$th molecule, $\hat{H}^{el}_m \psi_{m\alpha} = \epsilon_{m\alpha}\psi_{m\alpha}$. For now, we imagine that the nuclear degrees of freedom are fixed. This assumption will be relaxed further on by introducing coupling to the environment and allowing for interaction between system and bath.

The couplings V_{mn} between molecules m and n include four terms. The first set accounts for interactions between charges at two different molecules $V_{mn}(\alpha\alpha, \alpha\alpha) \equiv \langle \psi_{m\alpha}\psi_{n\alpha}|V_{mn}|\psi_{n\alpha}\psi_{m\alpha}\rangle$ (here we have introduced a short hand notation for the couplings) and $V_{mn}(\alpha\beta, \beta\alpha)$, where α, β indicate each of the two possible quantum numbers. The second terms account for interactions between transitions at the $m - \mathrm{th}$ molecule with charges at the $n - \mathrm{th}$ molecule, $V_{mn}(\alpha\beta, \beta\beta)$, $V_{mn}(\beta\beta, \beta\alpha)$. The third set includes interactions between the $S_0 \rightarrow S_1$ transition at one molecule and the $S_1 \rightarrow S_0$ transition at another molecule, $V_{mn}(\alpha\beta, \alpha\beta)$, and finally the fourth corresponds to simultaneous excitation and de-excitation of two different molecules, $V_{mn}(\alpha\alpha, \beta\beta)$. The first two types of couplings are usually much smaller than the last two and can be neglected so long as the electrostatic interaction energy between all charge carriers is well balanced. This statement is nicely justified in Ref. [53]. Thus one is left with resonant $V_{mn}(\alpha\beta, \alpha\beta)$ and off-resonant $V_{mn}(\alpha\alpha, \beta\beta)$ interaction terms. The off-resonant interaction term, i.e the fourth set, can be neglected according to the Heitler-London approximation. This corresponds to keeping only terms which conserve the number of excitations. The reason for which those terms can be neglected is that the energy difference between singly and doubly excited states is typically much larger (by one to two orders of magnitude) respect to the energy difference between singlet excitations. Thus the mixing between states with a different number of excitation quanta will be quite small [64]. The system Hamiltonian we will consider then only includes the third type of matrix elements which give rise to the resonant contributions

$$V_{mn} = V_{mn}(\alpha, \beta, \alpha, \beta) = \int dr_m dr_n \rho_{meg}(r_m; R) J_{mn}^{(el-el)} \rho^*_{neg}(r_n, R), \tag{2.5}$$

with the transition density $\rho_{meg}(r_m; R) = \psi^*_{me}(r_m; R)\psi_{mg}(r_m; R)$ and $J^{(el-el)}_{mn}$ the intermolecular coulombic electron-electron interaction. Often, the intermolecular distance is large compared to the degree of local wavefunction overlap between ground and excited state. In this case, one can use the dipole-dipole coupling approximation and

$$J^{(el-el)}_{mn} \approx \frac{\hat{\mu}_m \hat{\mu}_n}{|\mathbf{R}_{mn}|^3} - 3\frac{(\mathbf{R}_{mn} \cdot \hat{\mu}_m)(\mathbf{R}_{mn} \cdot \hat{\mu}_n)}{|\mathbf{R}^5_{mn}|}, \tag{2.6}$$

with $\mathbf{R}_{mn} = \mathbf{R_m} - \mathbf{R}_n$ the intermolecular distance and $\hat{\mu}_m$ is the electronic dipole operator.

Now, one needs to define the bath Hamiltonian $\hat{H}_B$ and the system-bath Hamiltonian $\hat{H}_{SB}$. The bath term includes all nuclear degrees of freedom and all electronic degrees of freedom not explicitly included in the system. For instance, in the case of pigments in a protein scaffold all the electrons of the protein are treated as part of the environment. In general, the nuclear degrees of freedom are not fixed, and the electron-electron interaction terms will be modulated by nuclear motion. The usual approximation that is made is that the environment (bath) can be modeled as an infinite set of harmonic oscillators. Thus

$$\hat{H}_B = \sum_{k,m} \left(\hbar\omega_k \hat{a}^\dagger_k \hat{a}_k\right)_m, \tag{2.7}$$

where $\hat{a}_k$ and $\hat{a}^\dagger_k$ are the creation and annihilation operators for mode k and a different set of environment modes is allowed for each molecule m.

Finally, the system will interact with the bath through the system-bath Hamiltonian. The most general form is that of a tensor product between system and bath operator. In this case, given the form of the system and bath hamiltonians we can write

$$\hat{H}_{SB} = \sum_m \left(\sum_k \hbar\omega_k \lambda_k \left(\hat{a}_k + \hat{a}^\dagger_k\right)\right)_m |m\rangle\langle m|, \tag{2.8}$$

where we have introduced the basis $|n\rangle$ of singly excited states, $|n\rangle = |\psi_{ne}\rangle \sum_{m\neq n} |\psi_{ng}\rangle$. Here λ_{km} is the coupling constant of the exciton on molecule m with bath mode k. In this basis and with these new definitions of system-bath and bath Hamiltonian, the system Hamiltonian can be written in the tight-binding form

$$\hat{H}_S = \sum_{m=1}^{N} \tilde{\epsilon}_m |m\rangle\langle m| + \sum_{n<m} V_{mn} \left(|m\rangle\langle n| + |n\rangle\langle m|\right), \tag{2.9}$$

where $\tilde{\epsilon}_m = \epsilon_{me} - \epsilon_{mg}$, and the electronic ground state energy of the aggregate $E_0 = \sum_m \epsilon_{mg}$ has been rescaled to zero for simplicity.

Once the system, bath and system-bath interaction have been specified, we can proceed to write an the equation of motion for the density matrix of the system, i.e. the excitonic degrees of freedom. We start with the Liouville-von Neumann equation for the total density matrix and trace over the bath degrees of freedom to obtain

$$\begin{aligned} \frac{\partial}{\partial t}\hat{\rho}_S(t) &= -\frac{i}{\hbar}\mathrm{tr}_B\left\{\left[\hat{H}_S + \hat{H}_B + \hat{H}_{SB}, \hat{\rho}(t)\right]\right\} && (2.10)\\ &= -\frac{i}{\hbar}\left[\hat{H}_S, \hat{\rho}_S(t)\right] - \frac{i}{\hbar}\mathrm{tr}_B\left\{\left[\hat{H}_{SB}, \hat{\rho}(t)\right]\right\}. && (2.11) \end{aligned}$$

Here, going from the first to the second line, the term proportional to the commutator of $\hat{H}_B$ with the full density matrix vanishes due to the fact that $\hat{H}_B$ only acts in the bath space and thus by using the cyclic invariance of the trace, the commutator goes to zero.

At this point in the derivation, it is convenient to switch to the interaction picture. Using the notation $\tilde{O}$ to indicate the operator $\hat{O}$ in the interaction picture (with $\hat{H}_S + \hat{H}_B$ the zeroth-order Hamiltonian), we can rewrite Eq. 2.11 as

$$\frac{\partial}{\partial t}\tilde{\rho}_S(t) = -\frac{i}{\hbar}\mathrm{tr}_B\left\{[\tilde{H}_{SB}(t), \tilde{\rho}(t)]\right\} \tag{2.12}$$

with

$$\tilde{\rho}(t) = \hat{U}_0^\dagger(t, t_0)\hat{\rho}(t_0)\hat{U}_0(t, t_0) \tag{2.13}$$

and

$$\hat{U}_0(t, t_0) = \exp\left(-\frac{i}{\hbar}\int_{t_0}^{t} \hat{H}_S(s) + \hat{H}_B(s)\,\mathrm{d}s\right). \tag{2.14}$$

Now, using $\tilde{\rho}(t) = \tilde{\rho}(t_0) - \frac{i}{\hbar}\int_{t_0}^{t} \mathrm{d}s\left[\tilde{H}_{SB}(s), \tilde{\rho}(s)\right]$ and inserting it into Eq. 2.12, we obtain

$$\frac{\partial}{\partial t}\tilde{\rho}_S(t) = \frac{i}{\hbar}\mathrm{tr}_B\left\{[\tilde{H}_{SB}(t), \tilde{\rho}(t_0)]\right\} - \frac{1}{\hbar^2}\int_{t_0}^{t}\mathrm{d}s\,\mathrm{tr}_B\left[\tilde{H}_{SB}(t), [\tilde{H}_{SB}(s), \tilde{\rho}(s)]\right]. \tag{2.15}$$

Assuming that $\mathrm{tr}_B\left[\tilde{H}_{SB}(t), \tilde{\rho}(t_0)\right] = 0$, i.e that the initial state is such that the interaction does not generate any (first-order) dynamics in the bath, we can write

$$\frac{\partial}{\partial t}\tilde{\rho}_S(t) = -\frac{1}{\hbar^2}\int_{t_0}^{t} \mathrm{d}s\,\mathrm{tr}_B\left[\tilde{H}_{SB}(t), \left[\tilde{H}_{SB}(s), \tilde{\rho}(s)\right]\right]. \tag{2.16}$$

To obtain a closed expression for the evolution of the system density matrix in time, further approximations need to be made. In fact, the equation we have obtained still depends on the full density matrix $\tilde{\rho}$. A first approximation which is made is the Born approximation. This consists in assuming weak system-bath coupling, i.e. the system only weakly influences the reservoir and one can say that at a given time t, $\tilde{\rho}(t) \approx \tilde{\rho}_S(t) \otimes \tilde{\rho}_B(t)$. This removes the explicit dependence on the full density matrix. Then, one assumes that the bath is in thermal equilibrium and thus not time-dependent $\tilde{\rho}_B(t) = \hat{\rho}_B$. Still more work needs to be done to get a closed expression. One of the most common approximations is the Markov approximation and it will be discussed in the next section.

2.3.2 Markovian methods for exciton dynamics

Redfield equation

Let us consider the expression previously obtained for the reduced density matrix and include the Born approximation and the assumption that the bath is at thermal equilibrium. We obtain

$$\frac{\partial}{\partial t}\tilde{\rho}_S(t) = -\frac{1}{\hbar^2}\int_{t_0}^{t} \mathrm{d}s\,\mathrm{tr}_B\left[\tilde{H}_{SB}(t), \left[\tilde{H}_{SB}(s), \tilde{\rho}_S(s) \otimes \hat{\rho}_B\right]\right]. \tag{2.17}$$

Equation 2.17 is non-markovian in the sense that the future evolution of $\tilde{\rho}_S$ depends on the density matrix at all previous times through the integration of $\tilde{\rho}_S(s)$ in $\mathrm{d}s$. The first Markov approximation consists in replacing $\tilde{\rho}_S(s)$ with $\tilde{\rho}_S(t)$ to obtain a master equation in the Born-Markov approximation

$$\frac{\partial}{\partial t}\tilde{\rho}_S(t) = -\frac{1}{\hbar^2}\int_{t_0}^{t} \mathrm{d}s\,\mathrm{tr}_B\left[\tilde{H}_{SB}(t), \left[\tilde{H}_{SB}(s), \tilde{\rho}_S(t) \otimes \hat{\rho}_B\right]\right]. \tag{2.18}$$

An extensive and interesting discussion of the implications of this approximation can be found in Ref. [65] and is left to the interest of the reader as it is beyond the scope of the current description. It is sufficient to know that the Markov approximation relies on the presence of two different time scales, a fast time scale for the bath and a much slower time scale for the dynamics of the system. Equation 2.18 is known as *Redfield's* equation [66]. This equation is still not fully markovian as the time evolution of the system density matrix depends on a specific choice for the initial preparation at time $t = t_0$ [63].

One can now make the second Markov approximation, i.e one replaces s with $t - s$ in the integral and take the limit of t going to infinity in the upper integration limit:

$$\frac{\partial}{\partial t}\tilde{\rho}_S(t) = -\frac{1}{\hbar^2}\int_{t_0}^{\infty} \mathrm{d}s \, \mathrm{tr}_B \left[\tilde{H}_{SB}(t), \left[\tilde{H}_{SB}(t-s), \tilde{\rho}_S(t) \otimes \hat{\rho}_B\right]\right]. \tag{2.19}$$

This approximation is valid so long as the state of the system varies over a time scale which is large compared to that over which the bath correlation functions decay. We need to simplify this expression further to obtain a closed equation.

Starting from Eq. 2.8 for $\hat{H}_{SB}$, we define $\hat{A}_m = |m\rangle\langle m|$ and $\hat{B}_m = \left(\sum_k \hbar\omega_k\lambda_k \left(\hat{a}_k + \hat{a}_k^\dagger\right)\right)_m$. We now switch to the energy basis, i.e the eigenbasis $|N\rangle$ of the system hamiltonian $\hat{H}_S\,|N\rangle = E_N\,|N\rangle$ to introduce $\hat{A}_m(\omega) = \sum_{E_N - E_M = \hbar\omega} c_m^*(M)c_m(N)\,|M\rangle\langle N|$. Using these definitions, after some algebra and the use of the rotating wave approximation, we obtain the following equation in the interaction picture:

$$\frac{\partial}{\partial t}\tilde{\rho}_S(t) = -\frac{i}{\hbar}\left[\hat{H}_{LS}, \tilde{\rho}_S(t)\right] + \sum_{\omega}\sum_{mn}\gamma_{mn}(\omega)\left(\hat{A}_n(\omega)\tilde{\rho}_S\hat{A}_m^\dagger(\omega) - \frac{1}{2}\left\{\hat{A}_m^\dagger(\omega)\hat{A}_n(\omega), \tilde{\rho}_S\right\}\right) \tag{2.20}$$

where

$$\hat{H}_{LS} = \sum_{\omega}\sum_{mn} S_{mn}(\omega)\hat{A}_m^\dagger(\omega)\hat{A}_n(\omega) \tag{2.21}$$

is the Lamb-shift Hamiltonian and it introduces a renormalization of the energy levels. Here, to define $S_{mn}(\omega)$ we introduce the two point bath correlation function

$$C_{mn}(t) = \mathrm{tr}_B\left\{\hat{B}_m(t)\hat{B}_n(0)\hat{\rho}_B\right\} \equiv S_{mn}(t) + \frac{i}{2}\chi_{mn}(t) \tag{2.22}$$

with

$$S_{mn}(t) = \frac{1}{2}\mathrm{tr}_B\left\{\hat{B}_m(t)\hat{B}_n(0)\hat{\rho}_B\right\} \tag{2.23}$$

and

$$\chi_{mn}(t) = -i\mathrm{tr}_\mathrm{B}\left\{\hat{B}_m(t)\hat{B}_n(0)\hat{\rho}_B\right\}, \tag{2.24}$$

the symmetrized and antisymmetrized correlation functions. Now $S_{mn}(\omega)$ is simply the Fourier transform of $S_{mn}(t)$, and the rates $\gamma_{mn}(\omega)$ are defined as a function of $C_{mn}(t)$

$$\gamma_{mn}(\omega) = \int_{-\infty}^{\infty} dt e^{i\omega t} C_{mn}(t). \tag{2.25}$$

Equation 2.20 can be recast into the Lindblad form if one so desires. In the Schrödinger picture the master equation is

$$\begin{aligned} \frac{\partial}{\partial t}\hat{\rho}_S(t) &= -\frac{i}{\hbar}\left[\hat{H}_S + \hat{H}_{LS}, \hat{\rho}_S(t)\right] + \\ & \sum_{\omega}\sum_{mn}\gamma_{mn}(\omega)\left(\hat{A}_n(\omega)\hat{\rho}_S\hat{A}^{\dagger}_m(\omega) - \frac{1}{2}\left\{\hat{A}^{\dagger}_m(\omega)\hat{A}_n(\omega), \hat{\rho}_S\right\}\right). \end{aligned} \tag{2.26}$$

We see we have a first term which corresponds to free evolution under the system Hamiltonian and the lamb-shift (which is usually neglected). Then, the second term is the dissipative term which introduces the interaction with the environment explicitly. The operators $\hat{A}_n$ induce jumps in the dynamics by projecting from a state to another. The jumps occur with rates γ_{mn} which depend on the oscillations in the environment degrees of freedom. Thus, there will be a dephasing contribution, when $m = n$ which does not lead to jumps between states and a relaxation contribution which comes from the other terms which induce jumps.

The main limitations of this expression come from the Markov approximation and the weak system-bath coupling approximation, in the next section we will be looking at a method which is non Markovian.

Secondly, one needs to deal with the density matrix and clearly, as the number of pigment molecules increases, storing the operators becomes problematic. Due to this, various stochastic Schrödinger equation approaches based on the use of monte-carlo evolution have been developed [67]. With these methods one can reduce the dimensionality of the problem from N^2 to N. I will discuss this in the context of a pure dephasing model for J-aggregates in Chapter 7. In the next section we will describe a Markovian model which only includes dephasing.

Haken-Strobl-Reineker model

The Haken-Strobl-Reineker model is a markovian model in which the environment is described by classical stochastic variables [68, 69]. This is a pure-dephasing model. One assumes that thermal fluctuations of the environment couple to the chromophores by the electron-phonon Hamiltonian:

$$\hat{H}_{\mathrm{SB}}(t) = \sum_m q_m(t)|m\rangle\langle m|, \tag{2.27}$$

where the $q_m(t)$ describe stochastic bath fluctuations. Here, one can consider only the fluctuations which are diagonal in the electronic degrees of freedom as they are typically larger than fluctuations of the inter-molecular couplings [22]. The random variables $q_m(t)$ are taken to be unbiased Gaussian fluctuations, with $\langle q_m(t)\rangle = 0$ and a two-point correlation function:

$$\langle q_m(t)q_n(0)\rangle = \delta_{mn}\delta(t)\gamma_m, \tag{2.28}$$

where γ_m is the site-dependent dephasing rate. With these assumptions, one obtains the Haken-Strobl-Reineker equation for the density operator in the Schrödinger picture as [68, 69]:

$$\frac{\partial \hat{\rho}_S}{\partial t}(t) = -\frac{i}{\hbar}[\hat{H}_{\mathrm{S}}, \hat{\rho}_S(t)] + L_\phi(\hat{\rho}_S(t)), \tag{2.29}$$

where the pure-dephasing Lindblad operator is given by:

$$L_\phi(\hat{\rho}_S(t)) = \sum_m \gamma_m[\hat{A}_m\hat{\rho}_S(t)\hat{A}_m^\dagger - \frac{1}{2}\hat{A}_m\hat{A}_m^\dagger\hat{\rho}_S(t) - \frac{1}{2}\hat{\rho}_S(t)\hat{A}_m\hat{A}_m^\dagger], \tag{2.30}$$

with the system operators $\hat{A}_m = |m\rangle\langle m|$ and pure dephasing rates γ_m. This Lindblad equation leads to exponential decay of all coherences in the density operator and to an equal distribution of populations in the infinite time limit. Notice that Eq. 2.29 is simply the pure dephasing part of the Redfield master equation (Eq. 2.26). The Haken-Strobl model will be employed in Chapters 3 and 7 to describe the exciton dynamics.

2.3.3 Non-markovian methods for exciton dynamics: Hierarchy equation of motion

As an example of a non-markovian method, I will briefly describe the Hierarchy Equation of Motion approach [29, 70]. This approach is used in Chapter 3 to describe the single exciton dynamics in the Fenna-Matthews-Olson complex.

We start from the total quantum Hamiltonian, partitioned in its system and bath components as described earlier, with the same definitions for each Hamiltonian: see Eq. 2.9, Eq. 2.8 and Eq. 2.7. We consider the specific case of seven coupled pigment molecules as the system part, thus $N = 7$. As seen before, in the interaction picture, we can write the evolution of the system density matrix by tracing over the bath degrees of freedom and assuming factorized initial conditions as

$$\tilde{\rho}_S(t) = \tilde{U}_S(t)\,\tilde{\rho}_S(0), \tag{2.31}$$

where the tilde indicates operators in the interaction picture and

$$\tilde{U}_S(t) = \left\langle \mathcal{T}_{\leftarrow} \exp\left(-\frac{i}{\hbar} \int_0^t dt_1 \tilde{\mathcal{L}}^{SB}(t_1) \right) \right\rangle_B \tag{2.32}$$

where $\tilde{\mathcal{L}}^{SB}(t)$ is the system-bath Liouvillian. Carrying out the cumulant expansion and using Wick's theorem for the Gaussian fluctuations we can obtain the following equation of motion of the system density operator in the Schrödinger picture

$$\hat{\rho}_S(t) = -\frac{i}{\hbar}\mathcal{L}^S \hat{\rho}_S(t) + \sum_{m=1}^{7} \hat{\Phi}_m \hat{\sigma}^{\boldsymbol{\delta}_m}(t), \tag{2.33}$$

where $\boldsymbol{\delta}_m = (\delta_{1m}, \delta_{2m}, ..., \delta_{mm}, .., \delta_{7m}) = (0, 0, ..., 1, ..., 0)$, $\hat{\Phi}_m = i\hat{V}_m^{\times} = i\,|m\rangle\,\langle m|^{\times}$ and the auxiliary operators $\hat{\sigma}(t)$ in the interaction picture are defined as

$$\begin{aligned}\tilde{\sigma}^{(n_1,n_2,...,n_7)}(t) = {} & \mathcal{T}_{\leftarrow} \prod_{m=1}^{7} \left[\int_0^t dt_1 e^{-\gamma_m(t-t_1)} \tilde{\Theta}_j(t_1) \right]^{n_m} \times \\ & \exp\left[\int_0^t dt_1 \tilde{W}_m(t_1) \right] \tilde{\rho}_S(0).\end{aligned} \tag{2.34}$$

Here, $\hat{\Theta}_j = i\left(\frac{2\lambda_j}{\beta\hbar^2}\hat{V}_j^{\times} - i\frac{\lambda_j}{\hbar}\gamma_j \hat{V}_j^{\circ} \right)$. The subscripts are defined so that $\hat{V}^{\times}\hat{O} = [\hat{V}, \hat{O}]$ acts as a commutator and $\hat{V}^{\circ}\hat{O} = \left\{\hat{V}, \hat{O}\right\}$ operates as an anticommutator, with $\hat{V}_m = |m\rangle\langle m|$. The other term $\tilde{W}$ is defined as following, $\tilde{W}_m(t) = \int_0^t ds \tilde{\Phi}_m(t) e^{-\gamma_m(t-s)} \tilde{\Theta}_m(s)$. The constant λ_j is the reorganization energy for the $j-th$ molecule which is obtained from the Drude-Lorentz spectral density employed in this model to describe the interaction of the system with the bath of harmonic oscillators. It is now possible to incorporate more than one peak in the spectral density, however, the original derivation was carried out for the single peaked spectral density.

The $\hat{\sigma}$ auxiliary operators evolve in time in the Schrödinger picture as

$$\begin{aligned}\frac{\partial}{\partial t}\hat{\sigma}^{(n_1,n_2,\ldots,n_7)}(t) &= -\frac{i}{\hbar}\mathcal{L}^S\hat{\sigma}^{(n_1,n_2,\ldots,n_7)}(t)-\sum_m n_m\gamma_m\hat{\sigma}^{(n_1,n_2,\ldots,n_7)}(t) \\ &+ \sum_m \hat{\Phi}_m\hat{\sigma}^{(n_1,\ldots,n_m+1,..,n_7)}(t)+\sum_m n_m\hat{\Theta}_m\hat{\sigma}^{(n_1,\ldots,n_m-1,\ldots,n_7)}.\end{aligned} \quad (2.35)$$

This hierarchy results in an infinite set of coupled equations, but generally one can truncate it after a finite number of auxiliary operators and reach convergence.

The HEOM equations are not time local and therefore the phonon modes of the bath for each site are influenced by the electronic states of the chromophore at that site. Hence, the dynamics also explicitly includes site-dependent reorganization processes of the bath. This method is used in Chapter 3 to compute the exciton dynamics and compare to the Redfield master equation approach.

Part I

Excitonic energy transport in natural light-harvesting complexes

Page intentionally left blank.

Chapter 3

Atomistic study of the long-lived quantum coherences in the Fenna-Matthews-Olson complex[i]

3.1 Introduction

Recent experiments suggest the existence of long-lived quantum coherence during the electronic energy transfer process in photosynthetic light-harvesting complexes under physiological conditions [26, 71, 72]. This has stimulated many researchers to seek for the physical origin of such a phenomenon. The role and implication of quantum coherence during the energy transfer have been explored in terms of the theory of open quantum systems [6,28–31,73–80], and also in the context of quantum information and entanglement [32,81,82]. However, the characteristics of the protein environment, and especially its thermal vibrations or phonons, have not been fully investigated from the molecular viewpoint. A more detailed description of the bath in atomic detail is desirable; to investigate the structure-function relationship of the protein complex and to go beyond the assumptions used in popular models of photosynthetic systems.

Protein complexes constitute one of the most essential components in every biological organism. They remain one of the major targets of biophysical research due to their tremendously diverse and, in some cases, still unidentified structure-function relationship. Many biological units have been optimized through evolution and the presence of certain amino acids rather than others is fundamental for functionality [83–85]. In photosynthesis, one of the most well-characterized pigment-protein complexes is the Fenna-Matthews-Olson (FMO) complex which is a light-harvesting complex found in green sulphur bacteria. It functions as an intermediate conductor for exciton transport located between the antenna complex where light is initially absorbed and the reaction center. Since the resolution of its crystal structure over 30 years ago [14], the FMO trimer, composed of 3 units each comprising 8 bacteriochlorophylls has been extensively studied both experimentally [21, 86, 87] and theoretically [22, 88]. For instance regarding the structure-function relationship, it has been shown [89] that amino acid residues cause considerable shifts in the site energies of bacteriochlorophyll a (BChl) molecules of the FMO complex and in turn causes changes to the energy transfer properties.

---

[i] Sangwoo Shim, Patrick Rebentrost, **Stéphanie Valleau** and Alán Aspuru-Guzik, Atomistic study of the long-lived coherences in the Fenna-Matthews-Olson complex, *Biophysical Journal*, 102, 649 (2012)

Have photosynthetic systems adopted interesting quantum effects to improve their efficiency in the course of evolution, as suggested by the experiments? In this chapter, we provide a first step to answer this question by characterizing the protein environment of the FMO photosynthetic system to identify the microscopic origin of the long-lived quantum coherence. We investigate the quantum energy transfer of a molecular excitation (exciton) by incorporating an all-atom molecular dynamics (MD) simulation. The molecular energies are computed with time-dependent density functional theory (TDDFT) along the MD trajectory. The evolution of the excitonic density matrix is obtained as a statistical ensemble of unitary evolutions by a time-dependent Schrödinger equation. Thus, this work is in contrast to many studies based on quantum master equations in that it includes atomistic detail of the protein environment into the dynamical description of the exciton. We also introduce a novel approach to add quantum corrections to the dynamics. Furthermore, a quantitative comparison to the hierarchical equation of motion and the Haken-Strobl-Reineker method is presented. As the main result, the time evolution of coherences and populations shows characteristic beatings on the time scale of the experiments. Surprisingly, we observe that the cross-correlation of site energies does not play a significant role in the energy transfer dynamics.

The chapter is structured as follows: In the first part we present the methods employed and in the second part the results followed by conclusions. In particular, the partitioning of the system and bath Hamiltonian in classical and quantum degrees of freedom and details of the MD simulations and calculation of site energies are discussed in Section 3.2.1. The exciton dynamics of the system under the bath fluctuations is then presented in Section 3.2.2. In Section 3.2.3 we introduce a quantum correction to the previous exciton dynamics. Using the discussed methods we evaluated site energies and their distribution at 77 K and 300 K in Section 3.3.1 and we also computed the linear absorption spectrum of the FMO complex in Section 3.3.3. The site basis dephasing rates are discussed in

Section 3.3.2. From the exciton dynamics of the system we obtained populations and coherences and compared to the QJC-MD approach in Section 3.3.4. We then compare the MD and quantum corrected MD methods to the hierarchical equation of motion (HEOM) and Haken-Strobl-Reineker (HSR) methods in Section 3.3.5. In Section 3.3.6 we determined the spectral density for each site from the energy time bath-correlator and studied the effect of auto and cross-correlations on the exciton dynamics by introducing a comparison to first-order autoregressive processes. We conclude in Section 3.4 by summarizing our results.

3.2 Methods

3.2.1 Molecular dynamics simulations

A computer simulation of the quantum evolution of the entire FMO complex is certainly unfeasible with the currently available computational resources. However, we are only interested in the electronic energy transfer dynamics among BChl molecules embedded in the protein support. This suggests a decomposition of the total system Hamiltonian operator into three parts: the relevant system, the bath of vibrational modes, and the system-bath interaction Hamiltonians. The system Hamiltonian operates on the excitonic system alone which is defined by a set of two-level systems. Each two-level system represents the ground and first excited electronic state of a BChl molecule. In addition, the quantum mechanical state of the exciton is assumed to be restricted to the single-exciton manifold because the exciton density is low. On the other hand, factors affecting the system site energies have intractably large degrees of freedom, so it is reasonable to treat all those degrees of freedom as the bath of an open quantum system.

More formally, to describe the system-bath interplay by including atomistic detail of the bath, we start from the total Hamiltonian operator and decompose it in a general way such that no assumptions on the functional form of the system-bath Hamiltonian are necessary [53]:

$$\begin{aligned} H_{total} &= \sum_m \int d\boldsymbol{R}\, \epsilon_m(\boldsymbol{R}) |m\rangle\langle m| \otimes |\boldsymbol{R}\rangle\langle\boldsymbol{R}| \\ &+ \sum_{m,n} \int d\boldsymbol{R}\ \{J_{mn}(\boldsymbol{R}) |m\rangle\langle n| \otimes |\boldsymbol{R}\rangle\langle\boldsymbol{R}| + c.c.\} \\ &+ |\mathbf{1}\rangle\langle\mathbf{1}| \otimes \hat{T}_{\boldsymbol{R}} + \sum_m \int d\boldsymbol{R}\, V_m(\boldsymbol{R}) |m\rangle\langle m| \otimes |\boldsymbol{R}\rangle\langle\boldsymbol{R}|. \end{aligned} \tag{3.1}$$

Here, $\boldsymbol{R}$ corresponds to the nuclear coordinates of the FMO complex including both BChl molecules, protein, and enclosing water molecules. The set of states $|m\rangle \otimes |\boldsymbol{R}\rangle$ denote the presences of the exciton at site m given that the FMO complex is in the configuration $\boldsymbol{R}$, $\epsilon_m(\boldsymbol{R})$ represents the site energy of the m-th site and $J_{mn}(\boldsymbol{R})$ is the coupling constant between the m-th and n-th sites. Note that the site energies and coupling terms can be modulated by $\boldsymbol{R}$. $|\mathbf{1}\rangle\langle\mathbf{1}|$ is the identity operator in the excitonic subspace, $\hat{T}_{\boldsymbol{R}}$ is the kinetic operator for the nuclear coordinates of the FMO complex, and $V_m(\boldsymbol{R})$ is the potential energy surface for the complex when the exciton at site m under Born-Oppenheimer approximation. Given multiple Born-Oppenheimer surfaces, one would need to carry out a coupled nonadiabatic propagation. However, as a first approximation, we assume that the change of Born-Oppenheimer surfaces does not affect the bath dynamics significantly. This approximation becomes better at small reorganization energies. Indeed, BChl molecules have significantly smaller reorganization energies than other chromophores [90]. With this assumption, we can ignore the dependence on the excitonic state in the V term, thus the system-bath Hamiltonian only contains the one-way influence from the bath to the system. We also adopted Condon approximation so that the J terms do not depend on $\boldsymbol{R}$:

$$
\begin{aligned}
H_S &= \sum_m \int d\boldsymbol{R}\, \bar{\epsilon}_m |m\rangle\langle m| \otimes |\boldsymbol{R}\rangle\langle\boldsymbol{R}| + \sum_{m,n} \int d\boldsymbol{R}\ \{J_{mn}(\boldsymbol{R})|m\rangle\langle n| \otimes |\boldsymbol{R}\rangle\langle\boldsymbol{R}| + c.c.\}\,, \\
&\approx \sum_m \int d\boldsymbol{R}\, \bar{\epsilon}_m |m\rangle\langle m| \otimes |\boldsymbol{R}\rangle\langle\boldsymbol{R}| + \sum_{m,n} \int d\boldsymbol{R}\ \{\bar{J}_{mn}|m\rangle\langle n| \otimes |\boldsymbol{R}\rangle\langle\boldsymbol{R}| + c.c.\}\,, \\
H_B &= |\mathbf{1}\rangle\langle\mathbf{1}| \otimes \hat{T}_{\boldsymbol{R}} + \sum_m \int d\boldsymbol{R}\, V_m(\boldsymbol{R})|m\rangle\langle m| \otimes |\boldsymbol{R}\rangle\langle\boldsymbol{R}|, \\
&\approx |\mathbf{1}\rangle\langle\mathbf{1}| \otimes \hat{T}_{\boldsymbol{R}} + \int d\boldsymbol{R}\, V_{ground}(\boldsymbol{R})|\mathbf{1}\rangle\langle\mathbf{1}| \otimes |\boldsymbol{R}\rangle\langle\boldsymbol{R}|, \\
H_{SB} &= \sum_m \int d\boldsymbol{R}\ \{\epsilon_m(\boldsymbol{R}) - \bar{\epsilon}_m\}\, |m\rangle\langle m| \otimes |\boldsymbol{R}\rangle\langle\boldsymbol{R}|, \qquad (3.2) \\
H_{total} &= H_S + H_B + H_{SB}. \qquad (3.3)
\end{aligned}
$$

Based on this decomposition of the total Hamiltonian, we set up a model of the FMO complex with the AMBER 99 force field [91, 92] and approximate the dynamics of the protein complex bath by classical mechanics. The initial configuration of the MD simulation was taken from the x-ray crystal structure of the FMO complex of *Prosthecochloris aestuarii* (PDB ID: 3EOJ.). Shake constraints were used for all bonds containing hydrogen and the cutoff distance for the long range interaction was chosen to be 12 Å. After a 2 ns long equilibration run, the production run was obtained for a total time of 40 ps with a 2 fs timestep. For the calculation of the optical gap, snapshots were taken every 4 fs. Two separate simulations at 77 K and 300 K were carried out with an isothermal-isobaric (NPT) ensemble to investigate the temperature dependence of the bath environment. Then, parameters for the system and the system-bath Hamiltonian were calculated using quantum chemistry methods along the trajectory obtained from the MD simulations.

We chose not to include the newly resolved eighth BChl molecule [89] in our simulations because up to now, the large majority of the scientific community has focused on the seven site system which is therefore a better benchmark to compare our calculations to previous work. It is important to note however that this eighth site may have an important role on the dynamics. In particular, as suggested in [40, 93] this eighth site is considered to be the primary entering point for the exciton in the FMO complex and its position dictates a preferential exciton transport pathway rather than two independent ones. Also when starting with an exciton on this eighth site, the oscillations in the coherences are largely suppressed.

The time-dependent site energy ϵ_m was evaluated as the excitation energy of the Q_y transition of the corresponding BChl molecule. We employed the time-dependent density functional theory (TDDFT) with BLYP functional within the Tamm-Dancoff approximation (TDA) using the Q-Chem quantum chemistry package [94]. The basis set was chosen to be 3-21G after considering a trade-off between accuracy and computational cost. The Q_y transition was identified as the excitation with the highest oscillator strength among the first 10 singlet excited states. Then, the transition dipole of the selected state was verified to be parallel to the y molecular axis. Every atom which did not belong to the TDDFT target molecule was incorporated as a classical point charge to generate the external electric field for the QM/MM calculation. Given that the separation between BChl molecules and the protein matrix is quite clear, employing this simple QM/MM method with classical external charges to calculate the site energies is a good approximation. The external charges were taken from the partial charges of the AMBER force field [91, 92]. The coupling terms, J_{mn}, can also be obtained from quantum chemical approaches like transition density cube or fragment-excitation difference methods [95, 96]. However, in this case we employed the MEAD values of the couplings of the Hamiltonian presented in the literature [22] and considered them to be constant in time. $\bar{\epsilon}_m$ was straightforwardly chosen as the time averaged site energy for the m-th site.

3.2.2 Exciton dynamics

In this section, we describe the method for the dynamics of the excitonic reduced density matrix within our molecular dynamic simulation framework. It is based on a simplified version of the quantum-classical hybrid method (Ehrenfest) described in [53]. The additional assumption on Hamiltonian (3.2) is that the bath coordinate $\boldsymbol{R}$ is a classical variable, denoted by a superscript "cl". As discussed above, the time-dependence of these variables arises from the Newtonian MD simulations. The additional force on the nuclei due to the electron-phonon coupling [53] is neglected. Hence, the Schrödinger equation for the excitonic system is given by:

$$i\hbar\frac{\partial}{\partial t}|\psi(t)\rangle \approx \Big\{H_S + H_{SB}(\boldsymbol{R}^{cl}(t))\Big\}\,|\psi(t)\rangle. \tag{3.4}$$

The system-environment coupling leads to an effective time-dependent Hamiltonian $H_{eff}(t) = H_S + H_{SB}(\boldsymbol{R}^{cl}(t))$. This equation suggests a way to propagate the reduced density matrix as an average of unitary evolutions given by Eq. (3.4). First, short MD trajectories (in our case 1 ps long) are uniformly sampled from the full MD trajectory (40 ps). Then, for each short MD trajectory, the excitonic system can be propagated under unitary evolution with a simple time-discretized exponential integrator. The density matrix is the classical average of these unitary evolutions:

$$\rho_S(t) = \frac{1}{M}\sum_{i=1}^{M}|\psi_i(t)\rangle\langle\psi_i(t)|, \tag{3.5}$$

where M is the number of sample short trajectories. Each trajectory is subject to different time-dependent fluctuations from the bath, which manifests itself as decoherence when averaged to the statistical ensemble. Compared to many methods based on the stochastic unraveling of the master equation, e.g. [97, 98], our formalism directly utilizes the fluctuations generated by the MD simulation. Therefore, the detailed interaction between system and bath is captured. The temperature of the bath is set by the thermostat of the MD simulation, thus no further explicit temperature dependence is required in the overall dynamics. The dynamics obtained by this numerical integration of the Schrödinger equation will also be compared to the HEOM approach.

3.2.3 Quantum Jump Correction to MD Method (QJC-MD)

The MD/TDDFT simulation above leads to crucial insights into the exciton dynamics. However, it does not capture quantum properties of the vibrational environment such as zero-point fluctuations. At zero temperature all the atoms in the MD simulation are completely frozen. Moreover, similarly to an infinite-temperature model, at long times of the quantum dynamical simulation the exciton is evenly distributed among all molecules, as we will see below. In order to obtain a more realistic description, we modify the stochastic simulation by introducing quantum jumps derived from the zero-point (zp) fluctuations of the modes in the vibrational environment. We refer to this corrected version of the MD propagation as QJC-MD.

Introducing harmonic bath modes explicitly we reformulate the system-bath Hamiltonian as:

$$H_{SB} = \sum_m |m\rangle\langle m| \sum_\xi g_\xi^m R_\xi. \tag{3.6}$$

Here, each g_ξ^m represents the coupling strength of a site m to a particular mode ξ and R_ξ is the dimensionless position operator for that mode. We now formulate our correction by separating the bath operators into two parts, $R_\xi = R_\xi^{zp} + R_\xi^{MD}$, the first part is due to zero-point fluctuations and the second comes from our MD simulations. As above, the MD part is replaced by the classical time-dependent variables, $R_\xi^{MD} \to R_\xi^{cl}(t)$. The zero-point operator is expressed by creation and annihilation operators, $R_\xi^{zp} = b_\xi^{zp} + \left(b_\xi^{zp}\right)^\dagger$, which satisfy the usual commutation relations $\left[b_\xi^{zp}, \left(b_{\xi\prime}^{zp}\right)^\dagger\right] = \delta_{\xi\xi\prime}$. By construction, for the zp-fluctuations one has $\left\langle \left(b_\xi^{zp}\right)^\dagger b_\xi^{zp} \right\rangle = 0$.

The zp-fluctuations can only induce excitonic transitions from higher to lower exciton states in the instantaneous eigenbasis of the Hamiltonian, thus leading to relaxation of the excitonic system. The evolution of the populations P_M of the instantaneous eigenstates $|M\rangle(t)$ due to the zero-point correction is expressed by a Pauli master equation as:

$$\left(\dot{P}_M\right)_{zpc} = -\sum_N \gamma(\omega_{MN}) P_M + \sum_N \gamma(\omega_{NM}) P_N, \tag{3.7}$$

and for the coherences as:

$$\left(\dot{C}_{MN}\right)_{zpc} = -\frac{1}{2}\gamma(|\omega_{MN}|) C_{MN}. \tag{3.8}$$

The associated rate can be derived from a secular Markovian Redfield theory [63] to be $\gamma(\omega_{MN}) = 2\pi J\left(\omega_{MN}\right) \sum_m |c_m\left(M\right)|^2 |c_m\left(N\right)|^2$, where the spectral density $J\left(\omega\right)$ is only non-zero for positive transition frequencies $\omega_{MN} = E_M - E_N$ and taken to be as in [28]. The coefficients $c_m(M)$ translate from site to energy basis. The time evolution given by Equations (3.7) and (3.8) is included in the dynamics simulation by introducing quantum jumps as in the Monte-Carlo wavefunction (MCWF) method [97]. We thus arrive at a hybrid classically averaged $H(t)$ simulation with additional quantum transitions induced by the vacuum fluctuations of the vibrational modes.

3.3 Results and discussion

3.3.1 Site energy distributions

Using the coupled QM/MD simulations, site energies were obtained for each BChl molecule. These energies and their fluctuations are reported in Figure 3.1. We note that the magnitude of the fluctuations are of the order of hundreds of cm^{-1}. Although the order of the site energies does not perfectly match previously reported results [22, 99], the overall trend does not deviate much, especially considering that our result is purely based on *ab initio* calculations without fitting to the experimental result. The Q_y transition energies calculated by TDDFT are known to be systematically blue-shifted with respect to the experiment [100]. However, the scale of the fluctuations remains reasonable. Therefore, the comparison in Fig. 3.1 was made after shifting the overall mean energy to zero for each method.

The excitation energy using TDDFT does not always converge when the configuration of the molecule deviates significantly from its ground state structure. The number of points which failed to converge was on average less than 4% for configurations at 300 K, and less than 2% at 77 K. We interpolated the original time series to obtain smaller time steps and recover the missing points. Interpolation could lead to severe distortion of the marginal distribution when the number of available points is too small. However, in our case, the distributions virtually remained the same with and without interpolation.

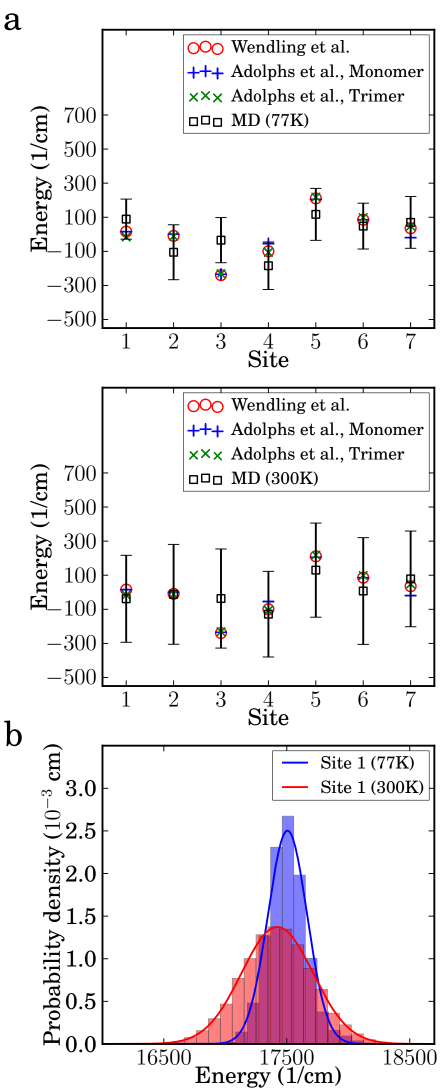

Figure 3.1: Panel **a**) Comparison of the calculated site energies for each BChl molecule to the previous works by Wendling et al. and Adolphs et al. [22, 99]. Our calculation, labeled as MD, was obtained using QM/MM calculations with the TDDFT/TDA method at 77 K and 300 K. Vertical bars represent the standard deviation for each site. Panel **b**) Marginal distribution of site 1 energy at 77 K and 300 K. Histograms represent the original data, and solid lines correspond to the estimated Gaussian distribution.

3.3.2 Dephasing rates

In the Markovian approximation and assuming an exponentially decaying autocorrelation function, the dephasing rate γ_ϕ is proportional to the variance of the site energy σ_ϵ^2 [63]:

$$\gamma_\phi = \frac{2}{\hbar}\sigma_\epsilon^2 \tau, \tag{3.9}$$

where τ is a time decay parameter which we estimated through a comparison to first order autoregressive processes, as described in Section 3.3.6. The dependence on the variance is clearly justified: states associated with large site energy fluctuations tend to undergo faster dephasing. Figure 3.2, panel a), presents the approximate site basis dephasing rates for each site with $\tau \approx 5\,\text{fs}$. The averaged value of the slopes is $0.485\,\text{cm}^{-1}\ \text{K}^{-1}$, which is in good agreement with the experimentally measured value of $0.52\,\text{cm}^{-1}\ \text{K}^{-1}$ obtained from a closely related species *Chlorobium tepidum* in the exciton basis [72]. From this plot we note the presence of a positive correlation between temperature and dephasing rate. This correlation is plausible: as temperature increases so does the energy disorder, hence the coherences should decay faster. In fact, in the Markovian approximation, dephasing rates increase linearly with temperature [63, 101]. Calculations at other temperatures are underway to verify this and to obtain more information on the precise temperature dependence of the dephasing rates.

3.3.3 Simulated Spectra

The absorption, linear dichroism (LD), and circular dichroism (CD) spectra can be obtained from the Fourier transform of the corresponding response functions. The spectra can be evaluated for the seven BChl molecules using the following expressions [102, 103]:

$$\begin{aligned}
I_{Abs}(\omega) &\propto \text{Re}\int_0^\infty dt\, e^{i\omega t} \sum_{m,n=1}^{7} \langle \vec{d}_m \cdot \vec{d}_n \rangle \{\langle U_{mn}(t,0)\rangle - \langle U^*_{mn}(t,0)\rangle\}, \qquad (3.10)\\
I_{LD}(\omega) &\propto \text{Re}\int_0^\infty dt\, e^{i\omega t} \sum_{m,n=1}^{7} \langle 3(\vec{d}_m \cdot \hat{r})(\vec{d}_n \cdot \hat{r}) - \vec{d}_m \cdot \vec{d}_n \rangle \{\langle U_{mn}(t,0)\rangle - \langle U^*_{mn}(t,0)\rangle\},\\
I_{CD}(\omega) &\propto \text{Re}\int_0^\infty dt\, e^{i\omega t} \sum_{m,n=1}^{7} \langle \bar{\epsilon}_m (\vec{R}_m - \vec{R}_n) \cdot (\vec{d}_m \times \vec{d}_n) \rangle \{\langle U_{mn}(t,0)\rangle - \langle U^*_{mn}(t,0)\rangle\},
\end{aligned}$$

where m and n are indices for the BChl molecules in the complex, $\vec{d}_m$ is the transition dipole moment of the m-th site, $U_{mn}(t,0)$ is the (m,n) element of the propagator in the site basis, $\hat{r}$ is the unit vector in the direction of the rotational symmetry axis, $\vec{R}_m$ is the coordinate vector of the site m, and $\langle\cdots\rangle$ indicates an ensemble average. The ensemble average was evaluated by sampling and averaging over 4000 trajectories. We applied a low-pass filter to smooth out the noise originated from truncating the integration and due to the finite number of trajectories. Figure 3.2 panel b) and c) show direct comparison of the calculated and experimental spectra at 77 K and 300 K. As discussed in Section 3.3.1, TDDFT tends to systematically overestimate the excitation energy of the Q_y transition [104] yet the fluctuation widths of the site energies are reasonable. In fact, the width and overall shape of the calculated spectrum is in good agreement with the experimental spectrum at each temperature. Calculated LD and CD spectra also reproduce well the experimental measurements, considering that no calibration to experiments was carried out. Since both LD and CD spectra are sensitive to the molecular structure it appears that our microscopic model correctly captures these details.

3.3.4 Population dynamics and long-lived quantum coherence

The MD method is based on minimal assumptions and directly evaluates the dynamics of the reduced density matrix from the total density matrix as described in Section 3.2. The reduced density matrix was obtained after averaging over 4000 trajectories. Figure 3.3 shows the population and coherence dynamics of each of the seven sites according to the dephasing induced by the nuclear motion of the FMO complex. In particular, the populations and the absolute value of the pairwise coherences, as defined in [82] ($2\cdot|\rho_{12}(t)|$ and $2\cdot|\rho_{56}(t)|$) are plotted at both 77 K and 300 K starting with an initial state in site 1 (first three panels) and then in site 6 (last three panels). Until very recently [40,93] site 1 and 6 have been thought as the entry point of an exciton in the FMO complex, therefore most of the previous literature chose the initial reduced density matrix to be either pure states $|1\rangle\langle 1|$ or $|6\rangle\langle 6|$ [28, 79, 105]. However, our method could be applied to any mixed initial state without modification. We note that coherent beatings last for about 400 fs at 77 K and 200 fs at 300 K. These timescales are in agreement with those reported for FMO [28, 72] and with what was found in Section 3.3.2. Although quite accurate in the short time limit, the MD method populations do not reach thermal equilibrium at long times. This was verified by propagating the dynamics to twice the time shown in Figure 3.3. This final classical equal distribution is similar to the HSR model result.

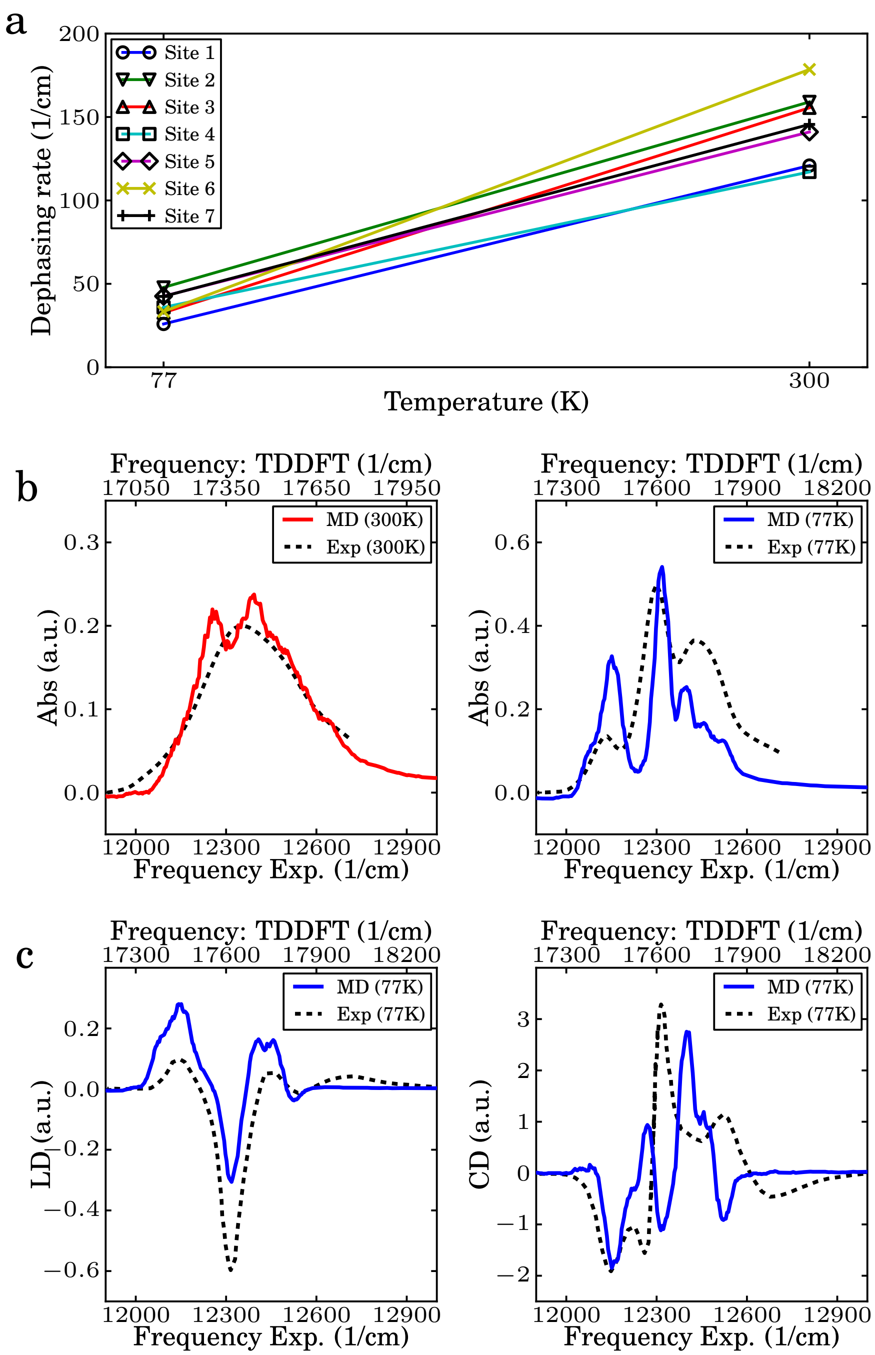

Figure 3.2: Panel **a**) shows the calculated dephasing rate for each site at 77 K and 300 K. Panel **b**) shows the simulated linear absorption spectra of the FMO complex at 77K and 300K. They were shifted to be compared to the experimental spectra as obtained by Engel through personal communication. Panel **c**) shows the simulated linear dichroism (LD) and circular dichroism (CD) spectra at 77 K. Experimental spectra were obtained from Wendling et al. [99] Although TDDFT-calculated spectra shows systematically overestimated site energies, the width and overall shape of the spectra is in good agreement.

The three central panels of Figure 3.3 show the same populations and coherences obtained from the QJC-MD method. As discussed in Section 3.2, this method includes a zero point correction through relaxation transitions and predicts a more realistic thermal distribution at 77 K. At 300 K the quantum correction is less important in the dynamics because the Hamiltonian fluctuations dominate over the zero temperature quantum fluctuations.

3.3.5 Comparison between MD, QJC-MD, HEOM, and HSR methods

Figure 3.4 shows a direct comparison of the population dynamics of site 1 calculated using the HEOM method discussed by Ishizaki and Fleming [28, 70], our MD and quantum corrected methods at 77 K and 300 K, and the HSR model [68, 69] with dephasing rates obtained from Eq. (3.9). We observe that the short-time dynamics and dephasing characteristics are surprisingly similar, considering that the methods originate from very different assumptions. Atomistic detail can allow for differentiation of the system-environment coupling for different chromophores. For example, at both temperatures (right panels), the MD populations of site 6 undergo faster decoherence than the corresponding HEOM results. We attribute this to the difference in energy gap fluctuations of site energy between site 1 and 6 obtained from the MD simulation as can be seen in 3.1. On one hand, in the HEOM method, site energy fluctuations are considered to be identical across all sites, on the other, in our method the fluctuations of each site are obtained from the MD simulation in which each site is associated with a different chromophore-protein coupling. Nevertheless, the fact that we obtain qualitatively similar results to the HEOM approach (at least when starting in $\rho(0) = |1\rangle\langle 1|$) without considering non equilibrium reorganization processes suggests that such processes might not be dominant in the FMO. The quantum correction results (QJC-MD), for every temperature and initial state, are in between the HEOM and MD results. This is due to the induced relaxation from zero-point fluctuations of the bath environment, which are not included in the MD method but included in the QJC-MD and HEOM methods.

The HSR results take into account the site-dependence of the dephasing rates based on Eq. (3.9). Due to the Markovian assumption, this model shows slightly less coherence than the HEOM method and similarly to the MD method it converges to an equal classical mixture of all sites in the long time limit.

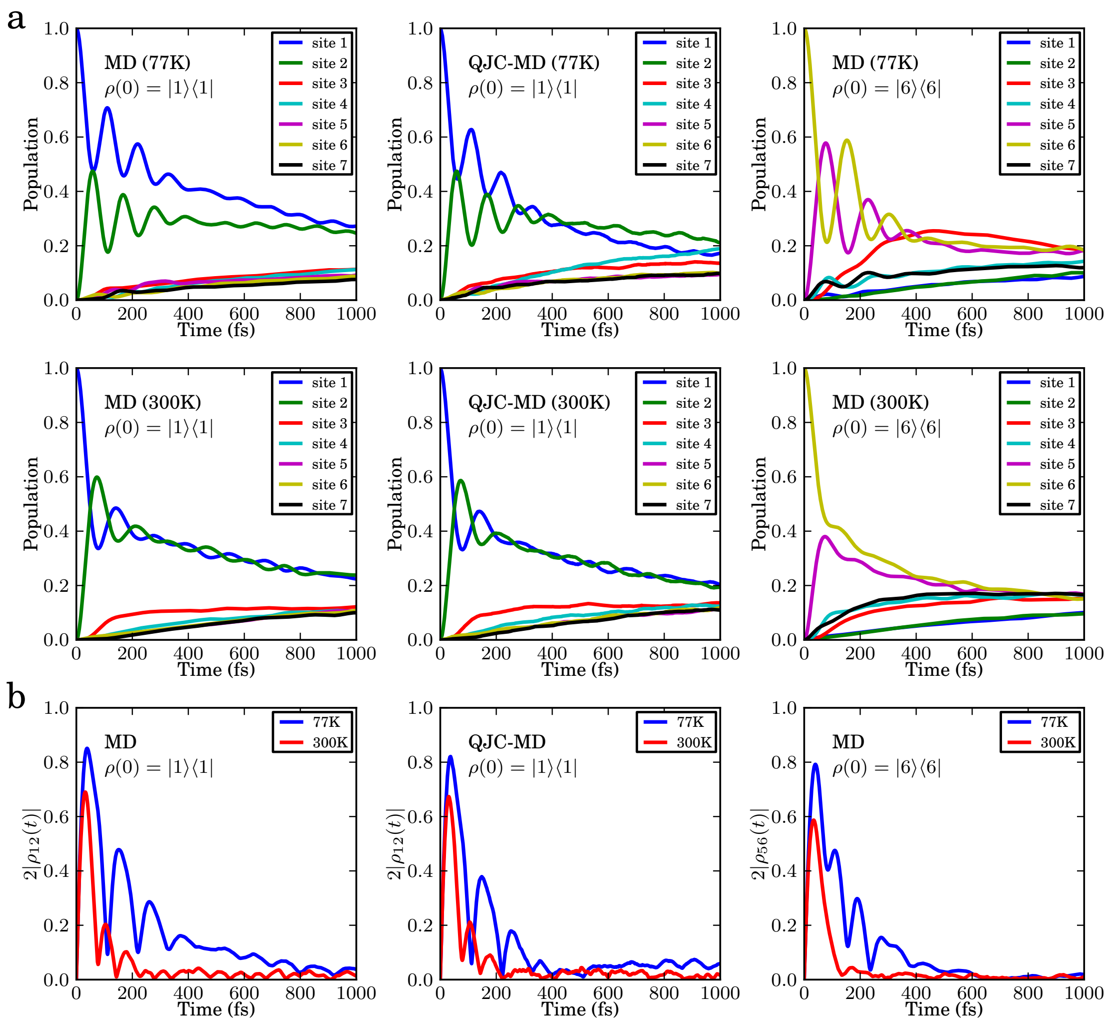

Figure 3.3: Panel **a**) Time evolution of the exciton population of each chromophore in the FMO complex at 77 K and 300 K. Panel **b**) Change of the pairwise coherence, or concurrence in time. Initial pure states, $\rho_S(0) = |1\rangle\langle 1|$ for the top and center panels were propagated using the two formulations developed in this chapter, MD and QJC-MD, to utilize the atomistic model of the protein complex bath from the MD/TDDFT calculation. For the last column of plots, the initial state was set to $|6\rangle\langle 6|$ and propagated using the MD method.

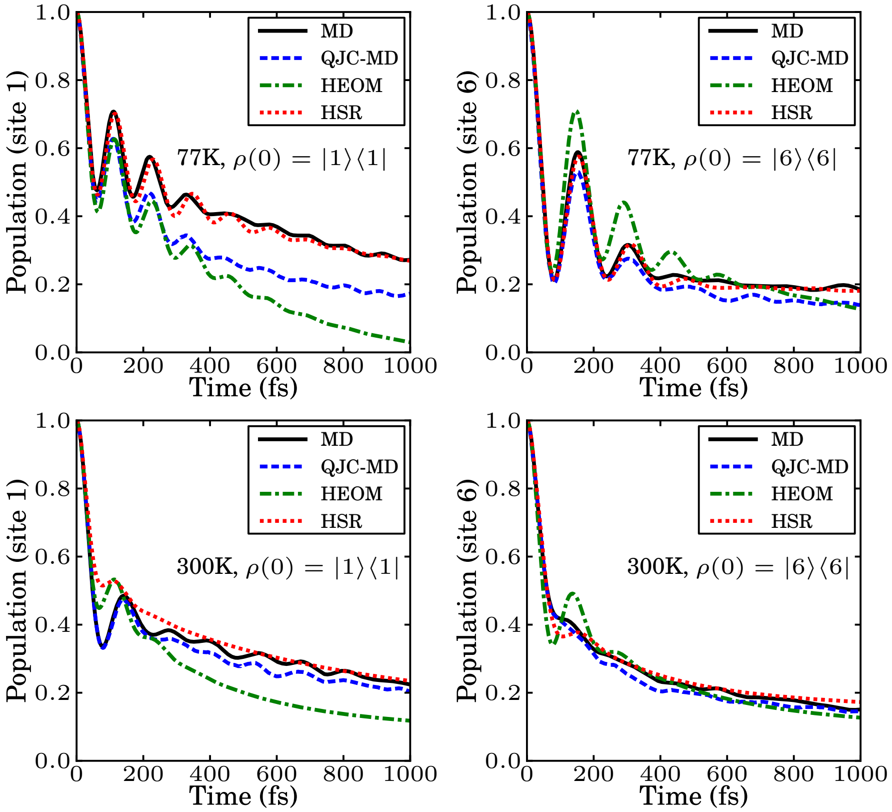

Figure 3.4: Comparison of the population dynamics obtained by using the MD method, the corrected MD, the hierarchy equation of motion approach and the Haken-Strobl-Reineker model at 77 K and 300 K. Panels on the right correspond to the initial state in site 1 and those on the left to an initial state in site 6. All methods show similar short-time dynamics and dephasing, while the long time dynamics is different and the different increases as relaxation is incorporated in the various methods.

3.3.6 Correlation functions and spectral density

The bath autocorrelation function and its spectral density contain information on interactions between the excitonic system and the bath. The bath correlation function is defined as $C(t) = \langle \delta\epsilon(t)\delta\epsilon(0)\rangle$ with $\delta\epsilon = \epsilon(t) - \bar{\epsilon}$. For the MD simulation, $C(t)$ is shown in Fig. 3.5, panel a) for the two temperatures.

To study the effect of the decay rate of the autocorrelation function on the population dynamics, we modeled site energies using first-order autoregressive (AR(1)) processes [106]. The marginal distribution of each process was tuned to have the same mean and variance as for the MD simulation. The autocorrelation function of the AR(1) process is an exponentially decaying function:

$$C(t) \propto \exp(-t/\tau). \tag{3.11}$$

We generated three AR(1) processes with different time constants τ and propagated the reduced density matrix using the Hamiltonian corresponding to each process. As can be seen in Fig. 3.5, panel a), the autocorrelation function of the AR(1) process with $\tau \approx 5\,\mathrm{fs}$ has a similar initial decay rate to that of the MD simulation at both temperatures. Therefore, as shown in the last three horizontal panels, its spectral density is in good agreement with the MD simulation result in the low frequency region, i.e up to $600\,\mathrm{cm}^{-1}$. Modes in this region are known to be the most important in the dynamics and in determining the the decoherence rate. Also, as panels b) and c) show, that same AR(1) process with $\tau \approx 5\,\mathrm{fs}$ exhibits similar population beatings and concurrences to those of the MD simulation. The relation of this 5fs time scale to others reported in [28, 107] is presently unclear. We suspect that the discrepancy between the two results should decrease when one propagates the MD in the excited state. Work in this direction is in progress in our group.

The spectral density can be evaluated as the reweighted cosine transform of the corresponding bath autocorrelation function $C(t)$ [103, 104],

$$J(\omega) = \frac{2}{\pi\hbar}\tanh(\beta\hbar\omega/2)\int_0^\infty C(t)\cos(\omega t)\,dt. \tag{3.12}$$

With the present data the spectral density exhibits characteristic phonon modes from the dynamics of the FMO complex, see Fig. 3.5d) first panel. However, high-frequency modes tend to be overpopulated due to the limitation of using classical mechanics. Most of these modes are the local modes

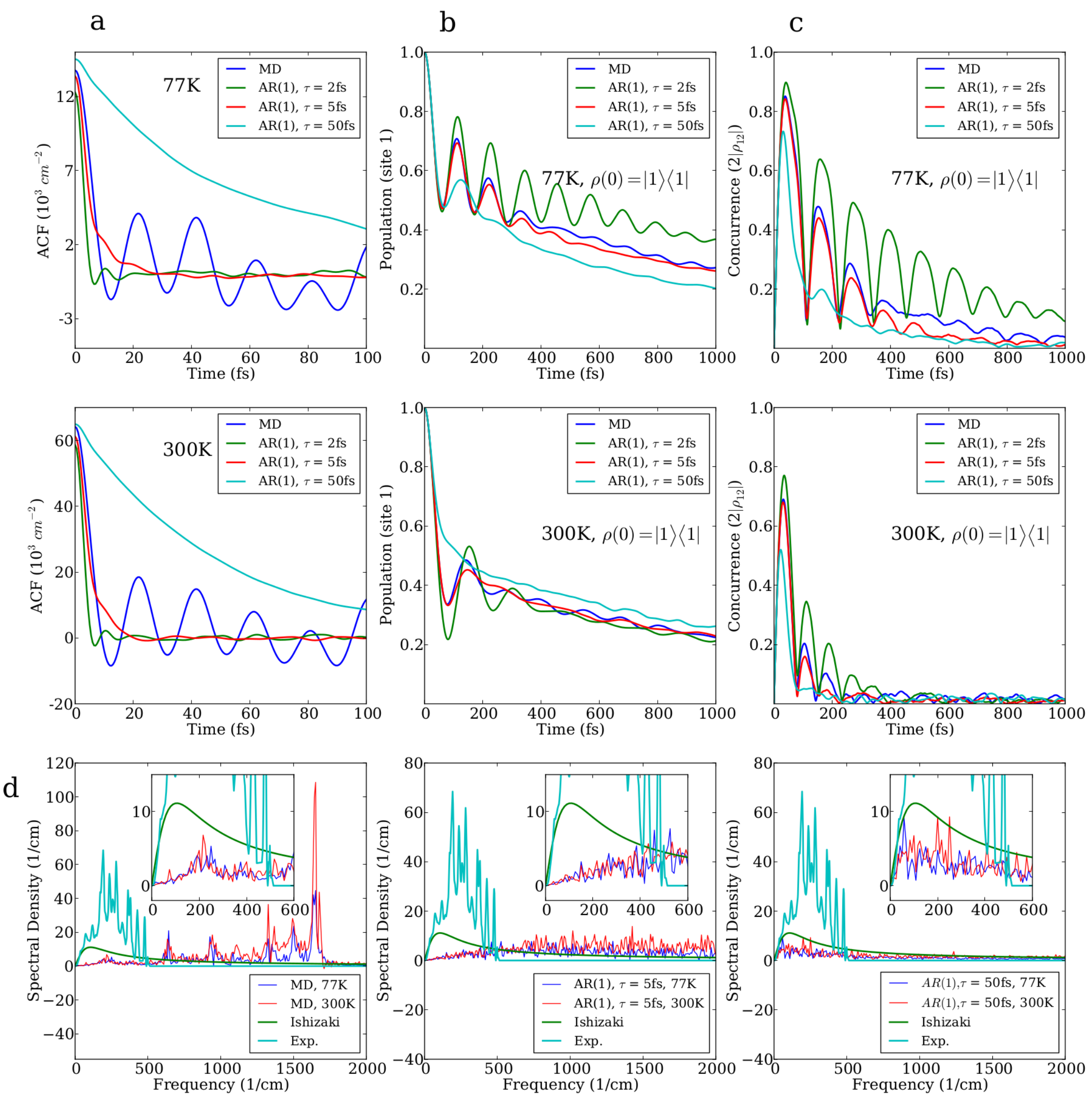

Figure 3.5: Panel **a**) Site 1 autocorrelation functions using MD and AR(1) processes generated with time constant equal to 2 fs, 5 fs, and 50 fs at 77 K and 300 K. Panel **b**) Site 1 population dynamics of MD and AR(1) processes with the different time constants at 77 K and 300 K. Panel **c**) The change of pairwise coherence between site 1 and 2 of MD and AR(1) processes with the different time constants at 77 K and 300 K. Panel **d**) Spectral density of site 1 of the FMO complex from the MD simulation at 77 K and 300 K. They clearly show the characteristic vibrational modes of the FMO complex. High-frequency modes are overpopulated due to the ultraviolet catastrophe observed in classical mechanics. The Ohmic spectral density used by Ishizaki and Fleming in [28] was presented for comparison. The spectral densities of site 1 from AR(1) processes are also presented.

of the pigments, which can be seen from the pigment-only calculation in [92]. There are efforts to incorporate quantum effects into the classical MD simulation in the context of vibrational coherence [108–110]. We are investigating the possibilities of incorporating corrections based on a similar approach. Moreover, we also obtain a discrepancy of the spectral density in the low frequency region. On one hand, the origin could lie in the harmonic approximation of the bath modes leading to the $\tanh$ prefactor in Eq. (3.12) or in the force field used in this work. On the other, the form of the standard spectral density is from [21] which measures fluorescence line-narrowing on a much longer timescale, around ns, than considered in our simulations (around ps). Assuming correctness of our result, this implies that for the simulation of fast exciton dynamics in photosynthetic light-harvesting complexes a different spectral density than the widely used one has to be employed.

Site energy cross-correlations between chromophores due to the protein environment have been postulated to contribute to the long-lived coherence in photosynthetic systems [71]. Many studies have explored this issue, e.g. recently [22, 31, 33, 79, 111, 112]. We tested this argument by decorrelating the site energies. For each unitary evolution, the site energies of different molecules at the same time were taken from different parts of the MD trajectory. In this way, we could significantly reduce potential cross correlation between sites while maintaining the autocorrelation function of each site. As can be seen in Fig. 3.6, no noticeable difference between the original and shuffled dynamics is observed.

3.4 Conclusion

The theoretical and computational studies presented in this chapter show that the long-lived quantum coherence in the energy transfer process of the FMO complex of *Prosthecochloris aestuarii* can be simulated with the atomistic model of the protein-chromophore complex. Unlike traditional master equation approaches, we propagate in a quantum/classical framework both the system and the environment state to establish the connection between the atomistic details of the protein complex and the exciton transfer dynamics. Our method combines MD simulations and QM/MM with TDDFT/TDA to produce the time evolution of the excitonic reduced density matrix as an ensemble average of unitary trajectories.

The conventional assumption of unstructured and uncorrelated site energy fluctuations is not necessary for our method. No *ad hoc* parameters were introduced in our formalism. The tempera-

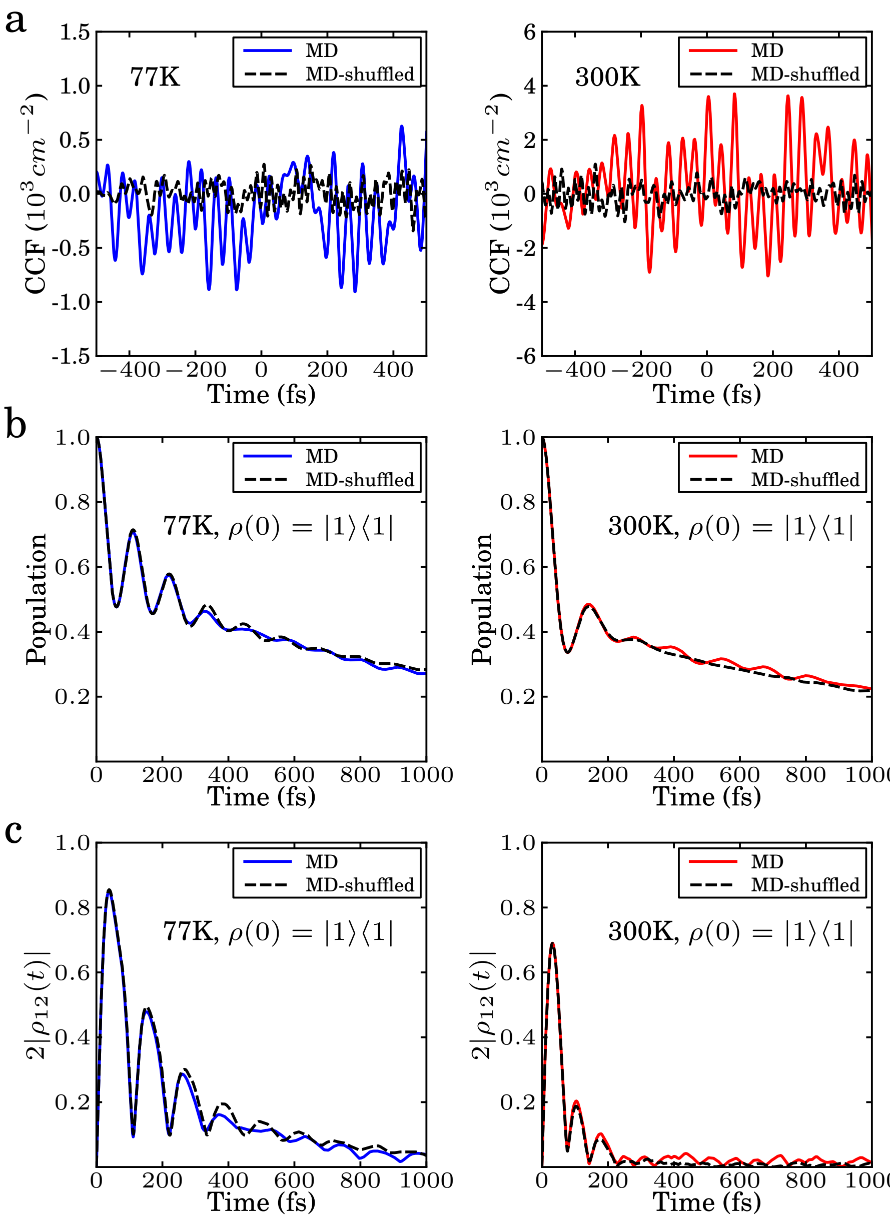

Figure 3.6: Panel **a**) Cross-correlation function of the original MD trajectory and a randomly shuffled trajectory between sites 1 and 2 at 77 K and 300 K. Panel **b**) Site 1 population dynamics of the original dynamics and the shuffled dynamics at 77 K and 300 K. Panel **c**) The pairwise coherence between sites 1 and 2. Original and shuffled dynamics are virtually identical at both temperatures.

ture and decoherence time were extracted from the site energy fluctuation by the MD simulation of the protein complex. The simulated dynamics clearly shows the characteristic quantum wave-like population change and the long-lived quantum coherence during the energy transfer process in the biological environment. On this note it is worth mentioning that one has to be careful in the choice of force-field and in the method used to calculated site energies. In fact as presented in Olbrich et al. [113] a completely different energy transfer dynamics was obtained by using the semiempirical ZINDO-S/CIS to determine site energies.

Moreover, we determined the correlations of the site energy fluctuations for each site and between sites through the direct simulation of the protein complex. The spectral density shows the influence of the characteristic vibrational frequencies of the FMO complex. This spectral density can be used as an input for quantum master equations or other many-body approaches to study the effect of the structured bath. The calculated linear absorption spectrum we obtained is comparable to the experimental result, which supports the validity of our method. The characteristic beating of exciton population and pairwise quantum coherence exhibit excellent agreement with the results obtained by the HEOM method. It is also worth noting the remarkable agreement of the dephasing timescales of the MD simulations, the HEOM approach, and experiment.

Recently, characterization of the bath in the LH2 [103, 104] and FMO [33] photosynthetic complexes were reported using MD simulation and quantum chemistry at room temperature. Those studies mostly focused on energy and spatial correlations across the sites, the linear absorption spectrum, and spectral density. The detailed study in [33] also suggests that spatial correlations are not relevant in the FMO dynamics.

This work opens the road to understanding whether biological systems employed quantum mechanics to enhance their functionality during evolution. We are planning to investigate the effects of various factors on the photosynthetic energy transfer process. These include: mutation of the protein residues, different chromophore molecules, and temperature dependence. Further research in this direction could elucidate on the design principle of the biological photosynthesis process by nature, and could be beneficial for the discovery of more efficient photovoltaic materials and in biomimetics research.

Chapter 4

On the alternatives for bath correlators and spectral densities from mixed quantum-classical simulations[i]

4.1 Introduction

In the study of the dynamics of large systems such as photosynthetic complexes, reduced models, which provide information on a small set of system degrees of freedom at the price of tracing out the rest of the bath degrees of freedom, have become very popular. Amongst these methods, which are open quantum systems approaches, one can find various Quantum Master Equations [29, 34, 35, 40, 70, 73, 74, 79, 82, 114–124] and Stochastic Schrödinger Equations [125, 126], which often rely on describing the system-bath interaction through a two-time bath correlation function or a bath spectral density. Therefore, it is of considerable interest to obtain these quantities. While a full quantum mechanical treatment of such large systems is out of reach, one viable approach is to use a mixed quantum-classical approach for the nuclear-electronic degrees of freedom. However, there is no unique way of obtaining a bath correlation function or a bath spectral density when resorting to quasiclassical theories. In this work, we provide criteria that can be helpful to choose an appropriate strategy for this task.

As a case study, we consider the Fenna-Matthews-Olson (FMO) light-harvesting pigment protein complex found in green sulfur bacteria. For this system, recent efforts have been undertaken to extract the bath spectral densities from mixed quantum-classical calculations [25, 33, 127]. The FMO complex has a trimeric structure, where each monomer contains, within the protein scaffolding, eight bacteriochlorophyll (BChl) molecules, which can transport electronic excitation energy. Up to recently, it was thought that only seven of the BChl's actually were present and most of the previous studies have focused on that case. Shim's results [25] which we employ in this work, are indeed based on the case of one monomer with seven BChl molecules. Experimentally, it has been possible to extract a spectral density for the BChl with the lowest transition energy [21, 22]. However, one can expect that each BChl has a different spectral density, due to its specific protein environment.

---

[i] **Stéphanie Valleau**, Alex Eisfeld and Alán Aspuru-Guzik, On the alternatives for bath correlators and spectral densities from mixed quantum-classical simulations, *Journal of Chemical Physics*, 137, 224103 (2012)

One theoretical approach to obtain the spectral densities from a microscopic description is a mixed quantum mechanics/classical mechanics (QM/MM) model [128]. In this approach, the nuclear degrees of freedom are treated classically and the relevant system quantities are calculated quantum mechanically. Then, from the microscopic description, spectral densities and correlation functions can be extracted and employed in the reduced models.

A specific QM/MM approach, which has become popular in recent years in the context of photosynthetic complexes [25, 103, 104, 127] and has been employed for FMO [25, 33], consists in propagating the nuclei in the ground electronic state of the FMO complex, thus the change in the classical forces due to excitation of the BChls is ignored. The bath correlation function and spectral densities are then extracted from the energy gap trajectories, i.e. the electronic transition energies which depend on the time dependent nuclear configuration. This transition energy is calculated using quantum chemistry, for example TDDFT [25] or semi-empirical approaches [33]. One thus obtains a time dependent energy gap two-time correlation function. Usually, a spectral density (SD) is derived from the time correlation function, to characterize the frequency dependent coupling of the electronic transitions to the environmental degrees of freedom. In the previous investigations on the FMO complex [25, 33, 127], the spectral densities differ by orders of magnitude respect to each other and also with respect to the SD extracted from experiment [21, 22].

In this work we revisit the data of Shim [25]. We shed light on the connection between the mixed QM/MM gap correlation function and the open quantum system bath correlation function using a simple model. The mixed QM/MM gap correlation function is real. However, in general, the full quantum correlation function will have an imaginary part. We employ different semiclassical *a posteriori* corrections to recover this part and compare the resulting spectral densities. Much work has been carried out on these *a posteriori* semiclassical corrections [108, 110, 129–132], but the question of which approximation is best remains open. Towards answering this question, we show that a simple model of shifted harmonic Born-Oppenheimer surfaces leads to two of the semiclassical *a posteriori* corrections, each obtained with a different phase space probability distribution. We thus establish the link to a microscopic picture. This model of shifted harmonic potential surfaces is of particular interest, since the spectral density used in the open quantum system approaches emerges from such a description.

Finally, we will investigate whether the results of the QM/MM fulfill the requirements needed to employ the extracted spectral density in open quantum system methods. These methods rely on the validity of assumptions such as linear coupling of the system to the bath and a bath of harmonic oscillators. We attempt to investigate whether these assumptions are valid in our case by evaluating higher order correlators of the energy gap time traces. In addition, we compare the spectral densities obtained at different temperatures. In most open quantum system approaches, when the harmonic bath approximation is employed, the spectral density is temperature independent. Thus, one can use this invariance as a criteria for choosing which of the applied *a posteriori* corrections is most reasonable to be employed in these methods. In particular, our findings suggest that the best *a posteriori* semiclassical approximation for FMO is the Harmonic [133, 134] correction rather than the Standard [135–137] one, which has so far been employed in the context of the simulation of exciton dynamics in photosynthetic complexes [25, 33, 103, 127]. Together, these aspects provide a clearer microscopic picture of the complex approximations involved in combining ground state QM/MM and open quantum system approaches.

The chapter is structured as follows: we begin by introducing the general quantum two-time correlation function in Section 4.2. We introduce its time symmetries and its Fourier transform and subsequently we define the spectral density. A brief summary of the general *a posteriori* semiclassical approximations to the quantum Fourier transform of the correlator from the classical Fourier transform is given in Section 4.2.3. In Section 4.3, we introduce the concept of an energy gap correlation function for two-level systems as models for molecules coupled to a bath and show how this leads to a quantum bath correlation function and spectral density which are consistent with the open quantum system approach. In Section 4.4, we show that one can introduce a microscopic model which leads to some of the same prefactors described in the general case in Section 4.2.3. Finally, we investigate the conditions of linear system-bath coupling and harmonic bath in Section 4.5. In particular, we evaluate high-order multi-time correlation functions for the bath. These considerations are applied to our specific QM/MM calculations for FMO in Section 7.4. We conclude in Section 4.7 by summarizing our findings.

4.2 The quantum correlation function and the spectral density

In this section, we introduce the definition of the quantum two-time bath correlation function. The generic Hamiltonian of a system coupled to a bath, in the absence of external fields, can be expressed as

$$\hat{H} = \hat{H}_{\mathrm{S}}\left(\mathbf{q},\mathbf{p}\right) + \hat{H}_{\mathrm{B}}\left(\mathbf{Q},\mathbf{P}\right) + \hat{H}_{\mathrm{SB}}\left(\mathbf{q},\mathbf{p},\mathbf{Q},\mathbf{P}\right), \tag{4.1}$$

where $\hat{H}_{\mathrm{S}}$ is the system Hamiltonian, $\hat{H}_{\mathrm{B}}$ is the bath Hamiltonian, $\hat{H}_{\mathrm{SB}}$ is the system-bath Hamiltonian. In addition, $(\mathbf{q},\mathbf{p}) = (q_j, p_j)$ and $(\mathbf{Q},\mathbf{P}) = (Q_k, P_k)$, indicate the generalized multidimensional conjugated coordinates for the system and the bath respectively. The indexes $j = 1, ..., f$ and $k = 1, ..., F$ run over the system (f) and bath (F) degrees of freedom respectively. The system-bath Hamiltonian can be written as a function of the system, $\hat{A}$, and bath, $\hat{B}$, operators:

$$\hat{H}_{\mathrm{SB}}\left(\mathbf{q},\mathbf{p},\mathbf{Q},\mathbf{P}\right) = \sum_{m} \hat{A}_m\left(\mathbf{q},\mathbf{p}\right) \otimes \hat{B}_m\left(\mathbf{Q},\mathbf{P}\right). \tag{4.2}$$

The influence of the bath on the system can be described by time-correlation functions. We will mostly focus on the two-time bath correlation function

$$C_{nm}(t-t') = \mathrm{tr}_{\mathrm{B}}\{\hat{B}_n(t,\mathbf{Q},\mathbf{P})\hat{B}_m(t',\mathbf{Q},\mathbf{P})\hat{\rho}_{\mathrm{B}}\}. \tag{4.3}$$

Here, $\hat{B}_m(t,\mathbf{Q},\mathbf{P}) = e^{i\hat{H}_{\mathrm{B}}t/\hbar}\hat{B}_m(\mathbf{Q},\mathbf{P})e^{-i\hat{H}_{\mathrm{B}}t/\hbar}$, and

$$\hat{\rho}_{\mathrm{B}} = \frac{e^{-\beta\hat{H}_{\mathrm{B}}}}{\mathrm{tr}_{\mathrm{B}}\{e^{-\beta\hat{H}_{\mathrm{B}}}\}}, \tag{4.4}$$

where $\beta = 1/\left(k_{\mathrm{B}}T\right)$ and T is the temperature. In the following, we will be interested only in the $n = m$ correlators, which we will indicate as $C(\tau)$ with $\tau = t - t'$, dropping the subscript notation for simplicity. In section 4.5, we will briefly discuss higher order correlators.

The correlator defined above is in general complex and one can show, see e.g. [135, 138], that it has the following symmetries with respect to time,

$$C(-t) = C^{*}(t) = C(t - i\beta\hbar). \tag{4.5}$$

4.2.1 Fourier transform of the time correlation function and symmetries of the correlator

We define $G(\omega)$, the Fourier transform of the time correlation function

$$G(\omega) \equiv \mathcal{F}[C(t)](\omega) = \int_{-\infty}^{\infty} e^{i\omega t} C(t) dt. \tag{4.6}$$

The function $G(\omega)$ is in general, temperature-dependent, real and positive. In this work, we will refer to it as the Temperature-Dependent Coupling Density (TDCD).

It will be convenient to split $G(\omega)$ into a symmetric and antisymmetric component which originate respectively from the real and imaginary parts of $C(t)$,

$$\begin{aligned} G(\omega) &= G_{\rm sym}(\omega) + G_{\rm asym}(\omega), && (4.7) \\ G_{\rm sym/asym}(\omega) &= \frac{1}{2}\left(G\left(\omega\right) \pm G\left(-\omega\right)\right). && (4.8) \end{aligned}$$

In this definition, we have followed the convention of Ref. [108]. Note that in the literature there exist other definitions, e.g. the corresponding equations in Ref. [53], differ by a factor of 2 from the ones used here[ii]. The detailed-balance condition, which follows directly from the second time symmetry in Eq. 4.5, implies that the overall TDCD is related to its asymmetric[iii] part by

$$\begin{aligned} G(\omega) &= \frac{2}{1-e^{-\beta\hbar\omega}} G_{\rm asym}(\omega) && (4.9) \\ &= \left(1 + \coth\left(\frac{\beta\hbar\omega}{2}\right)\right) G_{\rm asym}(\omega). && (4.10) \end{aligned}$$

It will be convenient to abbreviate $G_{\rm asym}(\omega)$ by defining

$$J(\omega) \equiv G_{\rm asym}(\omega).$$

Using Eq. 4.9 and the definition of $G(\omega)$, Eq. 4.6, one can express the correlation function as a function of $J(\omega)$,

$$C(t) = \frac{1}{2\pi} \int_{-\infty}^{\infty} d\omega \, e^{-i\omega t} \Big(\coth(\beta\hbar\omega/2) + 1 \Big) \, J(\omega). \tag{4.11}$$

[ii] This means that when comparing to these definitions we need to multiply $G_{\rm asym}(\omega)$ by two.

[iii] Alternatively, one can employ the symmetric part to obtain, $G(\omega) = 2/(1 + exp(-\beta\hbar\omega)G_{\rm sym}(\omega)$, $G(\omega) = \left(1 - \coth\left(\beta\hbar\omega/2\right)\right) G_{sym}(\omega)$.

4.2.2 The spectral density

Another quantity which is often of interest is the so-called “spectral density”. The spectral density describes the frequency dependent coupling of the system to the bath. There are different definitions of spectral density in the literature (for example $J(\omega)$ is sometimes referred to as the spectral density). We follow the convention of defining the spectral density as a positive frequency function

$$j(\omega) = \Theta(\omega)\, J(\omega)/\pi. \tag{4.12}$$

Here $\Theta(\omega)$ is the Heavyside function, which is one for positive arguments and zero for negative ones. The scaling by π has been introduced for later convenience. Note that

$$J(\omega) = \pi \cdot \big(j\,(\omega) - j\,(-\omega)\big). \tag{4.13}$$

4.2.3 General semiclassical a posteriori approximations

For systems of more than a few degrees of freedom, and in general, it is difficult to calculate the exact correlation function, and therefore its Fourier transform, by using a fully quantum mechanical treatment. However, using classical mechanics one can obtain its classical counterpart with much less effort. Therefore, it is common to attempt to construct the quantum spectral density from the classical one.

We define the fully-classical correlation function as the classical $\hbar \to 0$ limit of Eq. 4.3,

$$C^{\mathrm{cl}}(t) = \int d\mathbf{Q}d\mathbf{P}\, B(t, \mathbf{Q}, \mathbf{P})\; B(0, \mathbf{Q}, \mathbf{P})\; \mathcal{W}(\mathbf{Q}, \mathbf{P})\,. \tag{4.14}$$

Here $\mathcal{W}\left(\mathbf{Q}, \mathbf{P}\right)$ is the classical bath phase-space density, defined as

$$\mathcal{W}\left(\mathbf{Q}, \mathbf{P}\right) = \frac{e^{-\beta H_{\mathrm{B}}(\mathbf{Q}, \mathbf{P})}}{\int d\mathbf{Q}d\mathbf{P} e^{-\beta H_{\mathrm{B}}(\mathbf{Q}, \mathbf{P})}} \tag{4.15}$$

and the quantum bath operators $\hat{B}$ in Eq. 4.3 have been substituted by classical functions of the phase space variables $B\left(t, \mathbf{Q}, \mathbf{P}\right)$.

The classical TDCD is defined as

$$G^{\mathrm{cl}}(\omega) = \mathcal{F}[C^{\mathrm{cl}}(t)](\omega) = \int_{-\infty}^{\infty} e^{i\omega t} C^{\mathrm{cl}}(t) dt. \tag{4.16}$$

Note that $C^{\mathrm{cl}}(t)$ is a real and symmetric function in contrast to its quantum counterpart. This is also the case in the mixed QM/MM simulations employed for FMO [25,33]. The QM/MM correlation function obtained is real and no information about the important imaginary part of the quantum correlator is available *a priori* .

It is now desirable to be able re-construct, at least partially, the exact quantum spectral density from the classical one, through a simple description. Ideally, such a correction should be applied *a posteriori* and should not require extensive additional computation. Much work has been carried out in this direction, see e.g. [108, 110, 129–132]. As described in Ref. [108], one can define various semiclassical approximations to the full quantum mechanical $G(\omega)$ starting from its classical counterpart $G^{\mathrm{cl}}(\omega)$. We report each of these approximations in Table 4.1, second column.

These corrections all originate from expansions in $\hbar$ and use of the symmetry properties of the two-time correlation function and its Fourier transform. Note that if one expands the quantum correlator $C(t)$ in powers of $\hbar$, the first term is real and symmetric and corresponds to $C^{\mathrm{cl}}(t)$. The assumption that $C(t) = C^{\mathrm{cl}}(t)$, which leads to the standard approximation, is in general not correct. In fact, since both of the correlation functions are obtained after thermal averaging, we see that they must differ at least by their respective partition functions.

At low frequencies, $\omega\beta\hbar \equiv \omega_{\mathsf{b}} < 1$ (i.e. $\hbar\omega < k_B T$) all approximations give nearly identical results and give the same value for $\omega_{\mathsf{b}} = 0$.

The various approximations for $J(\omega)$, and thus for the spectral density, can straightforwardly be derived from those of $G(\omega)$ by using Eq. 4.9. The resulting expressions are reported in column three of Table 4.1 and the prefactors follow the same trend as those for $G(\omega)$ as a function of frequency.

Now, given all the functional forms described above, the question is how to choose the most appropriate one. For the FMO complex, it is unclear at first sight which one would be the best. In Section 4.4, we will investigate a model to elucidate the origin of these prefactors. This will help to discriminate between these corrections. In Section 7.4, we will apply all of the corrections listed in Table 4.1 to our energy gap traces and discuss the differences between each approach.

Table 4.1: Column two: Various expressions for obtaining a semiclassical temperature-dependent coupling density TDCD $G(\omega)$ from the classical $G^{\mathrm{cl}}(\omega)$ as discussed in, e.g. [108]. Column three: Expressions for obtaining the semiclassical asymmetric TDCD $J(\omega)$ from the classical $G^{\mathrm{cl}}(\omega)$. These follow from the expressions in column two and from detailed balance (Eq. 4.9).

Method	*Expression for* $G(\omega)$	*Expression for* $J(\omega) = G_{\mathrm{asym}}(\omega)$
Standard [135–137]	$G^{\mathrm{std}}(\omega) = \frac{2}{1+e^{-\beta\hbar\omega}} G^{\mathrm{cl}}(\omega)$	$J^{\mathrm{std}}(\omega) = \tanh(\frac{\beta\hbar\omega}{2}) G^{\mathrm{cl}}(\omega)$
Harmonic [133–135]	$G^{\mathrm{harm}}(\omega) = \frac{\beta\hbar\omega}{1-e^{-\beta\hbar\omega}} G^{\mathrm{cl}}(\omega)$	$J^{\mathrm{harm}}(\omega) = \frac{\beta\hbar\omega}{2} G^{\mathrm{cl}}(\omega)$
Schofield [139]	$G^{\mathrm{scho}}(\omega) = e^{\beta\hbar\omega/2} G^{\mathrm{cl}}(\omega)$	$J^{\mathrm{scho}}(\omega) = \sinh(\frac{\beta\hbar\omega}{2}) G^{\mathrm{cl}}(\omega)$
Egelstaff [140]	$G^{\mathrm{egel}}(\omega) = e^{\beta\hbar\omega/2} \int_{-\infty}^{\infty} e^{i\omega t} C^{\mathrm{cl}}\left(\sqrt{t^2+(\beta\hbar/2)^2}\right) dt$	$J^{\mathrm{egel}}(\omega) = \sinh(\frac{\beta\hbar\omega}{2}) \mathcal{F}\left[G^{\mathrm{cl}}(\sqrt{t^2+(\beta\hbar/2)^2})\right](\omega)$
Schofield-Harmonic [108]	$G^{\mathrm{s-h}}(\omega) = e^{\beta\hbar\omega/4} \sqrt{\frac{\beta\hbar\omega}{1-e^{-\beta\hbar\omega}}} G^{\mathrm{cl}}(\omega)$	$J^{\mathrm{s-h}}(\omega) = \sqrt{\frac{\beta\hbar\omega}{2} \sinh(\frac{\beta\hbar\omega}{2})} G^{\mathrm{cl}}(\omega)$

4.3 Energy gap correlation function for a simple model

In the mixed QM/MM calculations for photosynthetic systems [25, 33, 103], the nuclear trajectories are propagated in the electronic ground state using MD with short time steps. For a set of longer times steps within these trajectories, the electronic transition energies of the BChl molecules are computed using an electronic structure calculation method. Because it is computationally costly to calculate the electronic states for the full set of seven/eight coupled BChls simultaneously [33], the system was divided into seven/eight subsystems for which the electronic states were calculated separately. Thus, in these calculations no excited state interactions are included explicitly[iv]. The Hamiltonian of the coupled BChls is then written as $H = \sum_{n=1}^{N} H_n + \sum_{n<m} V_{nm}$ where H_n denotes the Hamiltonian of BChl n and $V_{nm}$is the Coloumb (transition dipole-dipole) interaction between them. To establish a connection to the open quantum system approach, each BChl is treated as an electronic two level system. These two-level systems and the electronic interaction between them are taken to be the system part. The coupling to internal nuclear degrees of freedom and the surrounding protein will then lead to fluctuations of these quantities in time (for more details see e.g. [103]). From the time dependence of the transition energy between electronic ground and excited state for each BChl, a classical ground-excited state energy-gap correlation function can be obtained. In turn, spectral densities can be extracted from the energy-gap correlation functions.

The gap correlation function, as obtained from the MD simulations, is a quantity which up to the previous section, has not been connected to the open quantum system approach described in Sec. 4.2. In this Section, we will explore a simple model with Born-Oppenheimer (BO) surfaces which can clarify the connection.

4.3.1 Quantum correlation function and energy gap correlation function for a single molecule

Lets us begin by considering a single molecule (BChl) treated in the Born-Oppenheimer approximation. The molecule is modeled as a two-level system with an electronic adiabatic ground $|g\rangle$ and excited $|e\rangle$ state. We can think of the BO-surfaces as having the dependence of the environment (protein and other BChls) already included, ignoring however the resonant dipole-dipole interaction. The approximation of two levels is reasonable in the limit where the next excited state is very far in energy space from the first. Usually, non-adiabatic couplings can be also neglected, as chosen in our calculations.

[iv] Approximations such as the transition density cube [96] can be employed to obtain couplings between the local excited states. More sophisticated models that include polarization effects [141, 142] can also be employed for this purpose.

Given this model, we investigate how the general correlation function, Eq. 4.3, is related to the energy gap correlation function.

We write the full Hamiltonian formally as

$$\hat{H} = \hat{H}_{\mathrm{g}}(\mathbf{Q},\mathbf{P})\,|g\rangle\langle g| + \hat{H}_{\mathrm{e}}(\mathbf{Q},\mathbf{P})\,|e\rangle\langle e|\,, \tag{4.17}$$

where $\hat{H}_{\mathrm{g}}(\mathbf{Q})$ and $\hat{H}_{\mathrm{e}}(\mathbf{Q})$ are the nuclear Hamiltonians for the ground and excited state in the BO approximation. In mass scaled coordinates $\left(Q_j = \sqrt{m_j}q_j\,;\, P_j = p_j/\sqrt{m_j}\right)$, the Hamiltonians can be expressed as $\hat{H}_{\mathrm{g}}(\mathbf{Q},\mathbf{P}) = \sum_{j=1}^{F} P_j/2 + V_{\mathrm{g}}(\mathbf{Q})$ and $\hat{H}_{\mathrm{e}}(\mathbf{Q},\mathbf{P}) = \hat{H}_{\mathrm{g}}(\mathbf{Q},\mathbf{P}) + \hat{\Delta}_{\mathrm{eg}}(\mathbf{Q})$, where $V_{\mathrm{g}}(\mathbf{Q})$ denotes the grounds state potential energy surface. For later purpose, we have expressed the excited state nuclear Hamiltonian with respect to the ground state potential by introducing the energy gap operator,

$$\begin{aligned} \hat{\Delta}_{\mathrm{eg}}(\mathbf{Q}) &= \hat{H}_{\mathrm{e}}(\mathbf{Q},\mathbf{P}) - \hat{H}_{\mathrm{g}}(\mathbf{Q},\mathbf{P}) \\ &= \hbar\omega_{\mathrm{eg}} + \lambda_0 + V_{\mathrm{e}}(\mathbf{Q}) - V_{\mathrm{g}}(\mathbf{Q}). \end{aligned} \tag{4.18}$$

This operator quantifies the energy difference between the excited state and the ground state surface. A coordinate independent constant energy difference $\hbar\omega_{eg} + \lambda_0$ has been explicitly written down, so that the remaining part $V_{\mathrm{e}}(\mathbf{Q}) - V_{\mathrm{g}}(\mathbf{Q})$ does not contain any coordinate independent contributions. This division and the meaning of $\hbar\omega_{eg}$ and λ_0 will become clear in Section 4.3.2.

The total Hamiltonian can be rewritten as

$$\hat{H} = \hat{H}_{\mathrm{g}} \cdot \hat{\mathbb{I}} + (\hbar\omega_{\mathrm{eg}} + \lambda_0)\,|e\rangle\langle e| + \hat{\Delta}\,|e\rangle\langle e|\,, \tag{4.19}$$

where we have defined the *reduced* gap operator $\hat{\Delta} \equiv \hat{\Delta}_{\mathrm{eg}} - \hbar\omega_{\mathrm{eg}} - \lambda_0$.

To establish a connection to the open quantum system model, as presented in Sec. 4.2, we choose

$$\hat{H}_{\mathrm{B}} = \hat{H}_{\mathrm{g}}(\mathbf{Q},\mathbf{P}) \tag{4.20}$$

$$\hat{H}_{\mathrm{SB}} = \hat{\Delta}(\mathbf{Q})\,|e\rangle\langle e| \tag{4.21}$$

$$\hat{H}_{\mathrm{S}} = (\hbar\omega_{\mathrm{eg}} + \lambda_0)\,|e\rangle\langle e|\,, \tag{4.22}$$

where we have set the energy of the electronic ground state $|g\rangle$ to zero. From the form of $\hat{H}_{\mathrm{SB}}$ we identify the system operator $\hat{A}_{\mathrm{e}} = |e\rangle\langle e|$ and the bath operator $\hat{B} = \hat{\Delta}_{\mathrm{eg}}(\mathbf{Q})$. We can now define the usual bath correlation function as

$$C(t) = \mathrm{tr}_{\mathrm{B}}\left\{\hat{\Delta}(t)\hat{\Delta}(0)\hat{\rho}_{\mathrm{B}}\right\}, \tag{4.23}$$

where we have dropped the dependence on bath coordinates in the notation for simplicity. $\hat{\Delta}$ can be thought of as a “gap” operator, that is, as a measure of the energy difference between the ground and excited state at a given nuclear configuration. From now on we will indicate reduced gap correlation functions as

$$\alpha(t) \equiv \mathrm{tr}_{\mathrm{B}}\left\{\hat{\Delta}(t)\hat{\Delta}(0)\hat{\rho}_{\mathrm{B}}\right\}, \tag{4.24}$$

to distinguish them from the general bath correlation function $C(t)$. Eq. 4.24 corresponds to the full quantum gap correlation function that one would obtain, e.g., from a quantum simulation on the FMO complex, considering only two electronic levels per molecule and after including the protein environment.

4.3.2 Quantum correlation function and energy gap correlation function for harmonic surfaces

While the approach outlined in the previous section is applicable to arbitrary potential surfaces, in most of the open quantum system approaches used to describe the FMO complex, the bath is taken as an (infinite) set of harmonic oscillators for the environment of each BChl. Each oscillator coordinate is then assumed to be linearly coupled to the electronic excitation of the BChls, i.e. $\hat{H}_{\mathrm{SB}} = |e\rangle\langle e| \otimes \sum_j \tilde{\kappa}_j Q_j$ where $\tilde{\kappa}_j$ is a coupling constant.

To establish the connection between the reduced gap operator and this system-bath interaction,

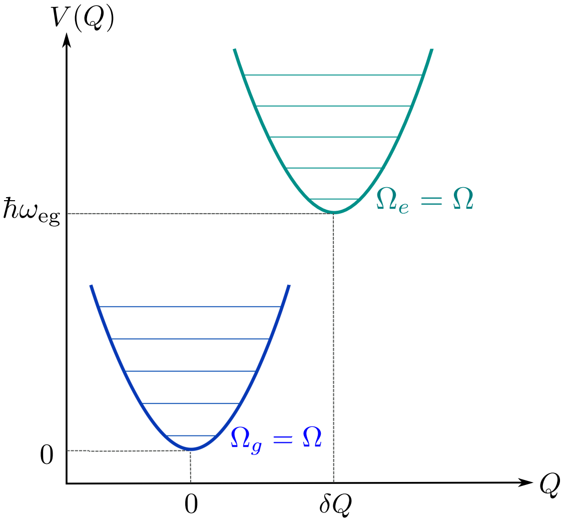

Figure 4.1: Shifted identical harmonic Born-Oppenheimer surfaces, Ω is the frequency of each harmonic potential and δQ is the coordinate shift between the minima of the ground and excited state potentials. This model is the one employed in Sec. 4.3.2 to derive classical and semiclassical expressions for the Fourier transform of the bath correlation function $G(\omega)$ and for the spectral density.

we now consider identical shifted harmonic potential surfaces, as sketched in Fig. 4.1. The nuclear Hamiltonians defined in the general case in the previous Section 4.3.1 become, $\hat{H}_{\mathrm{g}}(\mathbf{Q},\mathbf{P}) = \frac{1}{2}\sum_{j=1}^{F}(P_j^2 + \Omega_j^2 Q_j^2)$ and $\hat{H}_{\mathrm{e}}(\mathbf{Q},\mathbf{P}) = \hbar\omega_{\mathrm{eg}} + \frac{1}{2}\sum_j (P_j^2 + \Omega_j^2(Q_j - \delta Q_j)^2)$ where Ω_j is the frequency of the j-th oscillator. This model for a finite small number of vibrational modes of the chromophores, has been successfully employed to describe the optical properties of molecular aggregates [143–146]. These Hamiltonians can be rewritten as function of $a_j^\dagger$ and a_j, the ground state bosonic creation and annihilation operators which are related to the conjugated coordinates by $Q_j = \sqrt{\hbar/\left(2\Omega_j\right)}(a_j^\dagger + a_j)$ and $P_j = i\sqrt{\hbar\Omega_j/2}(a_j^\dagger - a_j)$. One obtains

$$\begin{aligned} \hat{H}_{\mathrm{g}} &= \sum_j \hbar\Omega_j a_j^\dagger a_j \\ \hat{H}_{\mathrm{e}} &= \hat{H}_{\mathrm{g}} + \hbar\omega_{\mathrm{eg}} + \lambda_0 - \sum_j \kappa_j (a_j^\dagger + a_j). \end{aligned} \tag{4.25}$$

Here, the constant shift λ_0, previously introduced in Eq. 4.18, corresponds to the frequently employed reorganization energy $\lambda_0 \equiv \lambda_R = \sum_j \frac{1}{2}\Omega_j^2 \delta Q^2 = \sum_j \hbar\Omega_j X_j$. We have also introduced the so-called Huang-Rhys factor [147]: $X_j = \frac{\Omega_j}{2\hbar}\delta Q_j^2$and a (frequency dependent) coupling constant $\kappa_j = \hbar\Omega_j\sqrt{X_j}$. Note that the total Hamiltonian is now in the standard form of an open quantum

Table 4.2: Expressions of the system bath quantities for the case of two Born-Oppenheimer harmonic surfaces as sketched in Fig. 4.1.

Quantity	*Expression*
System Hamiltonian	$\hat{H}_\mathrm{S} = (\hbar\omega_\mathrm{eg} + \lambda_R)\,\lvert e\rangle\langle e\rvert$
System-bath Hamiltonian	$\hat{H}_\mathrm{SB} = \lvert e\rangle\langle e\rvert\,\hat{\Delta}(\mathbf{Q})$
Bath Hamiltonian	$\hat{H}_\mathrm{B} = \hat{H}_\mathrm{g} = \sum_j \hbar\Omega_j a_j^\dagger a_j$
Energy gap operator	$\hat{\Delta}_\mathrm{eg}(\mathbf{Q}) = \hbar\omega_\mathrm{eg} + \lambda_\mathrm{R} - \sum_j \sqrt{2\hbar\Omega_j^3 X_j} Q_j$
Reduced energy gap operator	$\hat{\Delta}(\mathbf{Q}) = \hat{\Delta}_\mathrm{eg}(\mathbf{Q}) - (\hbar\omega_\mathrm{eg} + \lambda_\mathrm{R})$
Reorganization energy	$\lambda_0 = \lambda_\mathrm{R} = \sum_j \frac{1}{2}\Omega_j^2 \delta Q_j^2$
Coupling constant	$\kappa_j = \hbar\Omega_j\sqrt{X_j}$
Huang-Rhys factor	$X_j = \Omega_j \delta Q_j^2/\left(2\hbar\right)$
Unitless constant	$\zeta_j = \hbar\Omega_j/\left(k_B T\right)$

system model, as in Eq. 4.1, with the relevant quantities given in Table 4.2. In particular the reduced energy gap operator is given by

$$\hat{\Delta} = -\sum_j \kappa_j (a_j^\dagger + a_j). \tag{4.26}$$

From this expression of the energy gap operator one obtains the quantum two-time bath correlation function (see e.g. [53])

$$\alpha(t) = \int_0^\infty j(\omega)\left[\coth\left(\frac{\hbar\omega\beta}{2}\right)\cos\left(\omega t\right) - i\sin\left(\omega t\right)\right] d\omega \tag{4.27}$$

with the temperature independent spectral density

$$j(\omega) = \sum_{j=1}^{F} \kappa_j^2\,\delta(\omega - \Omega_j). \tag{4.28}$$

Note that from the definition Eq. 4.13 we have $J(\omega) = \pi\left(j(\omega) - j(-\omega)\right) = \pi\sum_{j=1}^{F}\kappa_j^2\left[\delta(\omega - \Omega_j) - \delta(\omega + \Omega_j)\right]$, which is also temperature independent.

To establish a connection to the classical correlator, which is real and symmetric, we note that $j(\omega)$ can be obtained from the real part of $\alpha(t)$ via

$$j(\omega) = \frac{2}{\pi}\tanh\!\left(\frac{\hbar\omega\beta}{2}\right)\int_0^\infty \mathrm{Re}\{\alpha(t)\}\cos\left(\omega t\right) dt. \tag{4.29}$$

When using this expression to obtain the spectral density from QM/MM simulations one often assumes that $C^\mathrm{cl}(t) \approx \mathrm{Re}\{\alpha(t)\}$, following the Standard approximation. Then, after a Fourier transform and use of symmetry relations for $G(\omega)$ one finds the following expression,

$$j(\omega) \;=\; \frac{1}{\pi}\tanh\!\left(\frac{\hbar\omega\beta}{2}\right)G^{\mathrm{cl}}(\omega). \tag{4.30}$$

This is the expression (up to the constant prefactor $1/\hbar$) used in Refs. [25, 103], to obtain spectral densities.

4.4 Classical and semiclassical limits of the correlators and spectral densities for harmonic surfaces

As outlined in the previous section, the harmonic model allows for a simple analytic solution in the quantum mechanical case. Now we will show that the system also has a solution in the classical case. In particular, in this section, we will introduce a model to construct exact relations between the classical gap-correlation and the quantum one. To this end, we will consider classical dynamics in the ground state BO potentials within an initial value representation of the initial state which is consistent with the mixed QM/MM approach. For each initial value, we calculate a trajectory and the corresponding reduced classical energy gap between the two surfaces, i.e. $\Delta(\mathbf{Q}(t), \mathbf{P}(t))$. We then average over many trajectories.

4.4.1 Classical equations of motion

The classical equation of motion of the j-th harmonic bath coordinate is $\ddot{Q}_j + \Omega_j^2 Q_j = 0$. Solving this differential equation with the initial condition $(Q_{j0}, P_{j0}) = (Q_j(t=0), P_j(t=0))$ yields the time dependent coordinate trajectories

$$\begin{aligned} Q_j(t) &= Q_j(t; Q_{j0}, P_{j0}) \\ &= Q_{j0}\cos(\Omega_j t) + \frac{P_{j0}}{\Omega_j}\sin(\Omega_j t). \end{aligned} \tag{4.31}$$

For each trajectory, the energy gap is then given by

$$\begin{aligned}\Delta(t) &= \Delta(t; Q_{j0}, P_{j0}) \\ &= -\sum_j (\Omega_j^2 \delta Q_j)\, Q_j(t; Q_{j0}, P_{j0})\end{aligned} \tag{4.32}$$

where the parametric dependence of Q_j and Δ on the initial conditions (Q_{j0}, P_{j0}) has been explicitly indicated.

4.4.2 Energy gap correlator

The evaluation of the reduced gap correlation function, Eq. 4.24, in the classical limit, results in the following expression

$$\begin{aligned}\alpha(t) &= \sum_{jk} \int d\mathbf{P}_0 d\mathbf{Q}_0 \mathcal{W}(\mathbf{Q}_0, \mathbf{P}_0) \times \\ &\quad \Delta(t; Q_{j0}, P_{j0}) \Delta(0; Q_{k0}, P_{k0})\end{aligned} \tag{4.33}$$

where $\mathcal{W}(\mathbf{Q}_0, \mathbf{P}_0)$ is the initial distribution and $d\mathbf{P}_0 d\mathbf{Q}_0$ denotes the set of all coordinates, i.e. $d\mathbf{Q_0} = dQ_{10} \cdots dQ_{M0}$. For harmonic potential surfaces, Eq 4.14, is time-evolved following Eq. (4.32). In this Section, we will investigate two different choices for the initial distribution, namely a Boltzmann distribution, as in Ref. 4.16, and a Wigner distribution which resembles the quantum thermal state. We will refer to the two cases as the classical limit and the semi-classical limit, respectively.

4.4.3 Classical and semiclassical correlation functions

Classical limit

To obtain the classical limit of the correlator, we choose the Boltzmann distribution for the initial coordinates which corresponds to a purely classical thermal state. The distribution is defined as follows

$$\mathcal{W}^{\mathrm{boltz}}(\mathbf{Q}_0, \mathbf{P}_0) = \prod_j \mathcal{W}_j^{\mathrm{boltz}}(Q_{j0}, P_{j0}), \tag{4.34}$$

with $\mathcal{W}_j^{\mathrm{boltz}}(Q_{j0},P_{j0}) = \frac{\beta\Omega_j}{2\pi}e^{-\frac{\beta}{2}(P_{j0}^2+\Omega_j^2Q_{j0}^2)}$, and it is normalized to one, i.e.,$\int dP_{j0}dQ_{j0}\mathcal{W}_j^{\mathrm{boltz}}(Q_{j0},P_{j0}) = 1$. Note that $(\Omega_j^2\delta Q_j)^2 = 2\hbar X_j\Omega_j^3$. Using Eq. 4.33 and the Boltzmann distribution for initial positions and momenta, we obtain,

$$\alpha_{\mathrm{boltz}}(t) = \sum_j (\hbar\Omega_j)^2 X_j \cos(\Omega_j t)\, \left(\frac{2}{\zeta_j}\right). \tag{4.35}$$

Here we have introduced the abbreviation $\zeta_j \equiv \hbar\Omega_j/\,(k_B T)$.

Semiclassical limit

In order to obtain the semiclassical limit, we take the quantum Wigner distribution for the initial coordinates and use it in Eq. 4.33. The Wigner distribution is given by

$$\mathcal{W}^{\mathrm{wig}}(\mathbf{Q}_0,\mathbf{P}_0) = \prod_j \mathcal{W}_j^{\mathrm{wig}}(Q_{j0},P_{j0}), \tag{4.36}$$

where we have used the compact notation

$$\mathcal{W}_j^{\mathrm{wig}}(Q_{j0},P_{j0}) \equiv 2\tanh\!\left(\frac{\zeta_j}{2}\right) e^{-\tanh(\zeta_j/2)\left(\frac{\Omega_j}{\hbar}Q_{j0}^2+\frac{1}{\hbar\Omega_j}P_{j0}^2\right)}.$$

The normalization of the Wigner distribution is chosen such that $\int \frac{dP_{j0}dQ_{j0}}{2\pi\hbar}\mathcal{W}_j^{\mathrm{wig}}(Q_{j0},P_{j0}) = 1$. The resulting expression of the energy gap correlation function is

$$\alpha_{\mathrm{wig}}(t) = \sum_j (\hbar\Omega_j)^2 X_j \cos(\Omega_j t)\coth\!\left(\frac{\zeta_j}{2}\right). \tag{4.37}$$

4.4.4 Classical and semiclassical spectral densities

After a Fourier transform of the classical correlators in Eq. 4.35 and 4.37 we obtain, for the Boltzmann distribution

$$G_{\mathrm{boltz}}(\omega) = \pi\sum_j \left(\frac{2k_{\mathrm{B}}T}{\hbar\omega}\right)\kappa_j^2\left(\delta\left(\omega-\Omega_j\right)+\delta\left(\omega+\Omega_j\right)\right), \tag{4.38}$$

and for the Wigner distribution

$$G_{\mathrm{wig}}(\omega) = \pi \sum_j \coth\left(\frac{\hbar\omega}{2k_{\mathrm{B}}T}\right) \kappa_j^2 \left(\delta\left(\omega - \Omega_j\right) + \delta\left(\omega + \Omega_j\right)\right). \tag{4.39}$$

Here $\kappa_j = \hbar\Omega_j\sqrt{X_j}$ as in Tab. 4.2. Now, using Eq. 4.28 for the spectral density $j(\omega)$ in the quantum case, and using $J(\omega) = \pi(j(\omega) - j(-\omega))$ we can write

$$G_{\mathrm{boltz}}(\omega) = \frac{2k_{\mathrm{B}}T}{\hbar\omega} J(\omega) \tag{4.40}$$

$$G_{\mathrm{wig}}(\omega) = \coth\left(\frac{\hbar\omega}{2k_{\mathrm{B}}T}\right) J(\omega). \tag{4.41}$$

By inverting these equations the exact quantum $J(\omega)$ can be expressed in terms of the classical $G_{\mathrm{boltz}}(\omega) = \int_{-\infty}^{\infty} e^{i\omega t}\alpha_{\mathrm{boltz}}(t)dt$ or the semiclassical $G_{\mathrm{wig}}(\omega) = \int_{-\infty}^{\infty} e^{i\omega t}\alpha_{\mathrm{wig}}(t)dt$

$$J_{\mathrm{boltz}}(\omega) = \frac{\hbar\omega}{2k_B T} G_{\mathrm{boltz}}(\omega) \tag{4.42}$$

$$J_{\mathrm{wig}}(\omega) = \tanh\left(\frac{\hbar\omega}{2k_B T}\right) G_{\mathrm{wig}}(\omega). \tag{4.43}$$

We see that in our harmonic model the semiclassical Wigner distribution yields the same prefactor as for the Standard approximation described in Section 4.2.3 while the Boltzmann distribution gives the same prefactor as the Harmonic approximation, also described in Section 4.2.3.

4.5 Models for system-bath coupling: higher order correlators

As discussed in the introduction, there has been a lot of interest in modeling the exciton dynamics of the FMO complex using open quantum system approaches. These usually require as input a bath two-time correlation function or (equivalently) a spectral density and they rely on the assumption of linear coupling to the bath and on a bath described by harmonic oscillators.[v]

In the previous Section 4.3.2, we have discussed that this model corresponds to shifted adiabatic BO surfaces of identical curvature. We have shown that in this case, the energy gap two-time correlation function for a classical ground-state propagation is directly proportional to the quantum one and we have extracted the appropriate (frequency dependent) proportionality constant. For other shapes of the potential surfaces involved, one will in general obtain different proportionality constants, although the delta-peaks of the spectral densities can be located at the same energies (the positions are determined by the shape of the ground state potential).

---

[v] Note that there are two common approximations for which the information on the system bath coupling is entirely described by the two-time bath correlation function, namely linear response theory and second order perturbation theory in system bath coupling.

It is not clear, *a priori,* if the approximation of shifted harmonic surfaces (or equivalently linear coupling to a harmonic bath) is a good one for the system under consideration. To gain some insight on this question, from an analysis of QM/MM trajectories, one possibility is to consider higher order correlators. If the approximation of linearly coupled harmonic oscillators is inadequate, one expects that higher order correlators will have a significant relative weight.

We proceed to discuss some properties of correlations of the bath gap operator, Eq. 4.18. The energy gap operators can be described by a function of the bath coordinates and expanded in terms of these as

$$\hat{\Delta} = \sum_i \xi_i^{(0)} + \sum_i \xi_i^{(1)} Q_i + \sum_{ij} \xi_{ij}^{(2)} Q_i Q_j + \dots . \tag{4.44}$$

When only terms up to first order in Q are significant, as in the case of the Harmonic surfaces in the linear system bath coupling limit, Tab. 4.2, we can write the two-time correlation function as

$$\alpha(t,0) = \left\langle \hat{\Delta}(t)\hat{\Delta}(0) \right\rangle = \sum_{ij} \xi_i^{(1)} \xi_j^{(1)} \left\langle Q(t) Q_j(0) \right\rangle. \tag{4.45}$$

Here, we have excluded the zeroth-order term which corresponds, e.g., to a reorganization energy, and is usually renormalized into the system Hamiltonian. The angular brackets $\langle ... \rangle = \mathrm{tr_B}\left\{ ..., \hat{\rho}_\mathrm{B} \right\}$ indicate thermal averaging over the bath degrees of freedom. Similarly, the three-time correlation function becomes

$$\begin{aligned} \alpha(t',t,0) &= \left\langle \hat{\Delta}(t')\hat{\Delta}(t)\hat{\Delta}(0) \right\rangle \\ &= \sum_{ijk} \xi_i^{(1)} \xi_j^{(1)} \xi_k^{(1)} \left\langle Q_i(t') Q_j(t) Q_k(0) \right\rangle . \end{aligned} \tag{4.46}$$

In the case of a harmonic bath, the three-time correlation function will vanish, and in general any odd permutation of the harmonic bath coordinates will vanish.

However, if one considers the case where one retains the second order term in Eq. 4.44, the two-time correlator will become:

$$\alpha(t,0) \quad = \quad \sum_{ijkl} \Xi_{ij}\Xi_{kl} \left\langle \mathbf{Q}_{ij}(t)\mathbf{Q}_{kl}(0) \right\rangle, \tag{4.47}$$

where we have defined Ξ_{ij} and $\mathbf{Q}_{ij}(t)$ as

$$\Xi_{ij} = \begin{cases} 0 & ;\ i = j = 0 \\ \xi_i^{(1)} & ;\ j = 0 \ \wedge \ i \neq 0 \\ \xi_j^{(1)} & ;\ i = 0 \ \wedge \ j \neq 0 \\ \xi_{ij}^{(2)} & ;\ i, j \neq 0 \end{cases}$$

$$\mathbf{Q}_{ij}(t) = \begin{cases} 0 & ;\ i = j = 0 \\ Q_i(t) & ;\ j = 0 \ \wedge \ i \neq 0 \\ Q_j(t) & ;\ i = 0 \ \wedge \ j \neq 0 \\ Q_i(t) \cdot Q_j(t) & ;\ i, j \neq 0 \end{cases}.$$

Analogously the three-time correlator becomes

$$\alpha(t', t, 0) = \sum_{ijklmn} \Xi_{ij}\Xi_{kl}\Xi_{mn} \left\langle \mathbf{Q}_{ij}(t')\mathbf{Q}_{kl}(t)\mathbf{Q}_{mn}(0) \right\rangle. \tag{4.48}$$

If the bath is harmonic, it is straightforward to show that all terms with an odd number of coordinate operators in the averages will vanish. Yet, we see that in general, unless the coupling to the bath coordinates is linear and the bath consists of Harmonic oscillators, the three-point correlator will not vanish. It may therefore be necessary to go beyond the simple description using only the two-time correlator.

4.6 Application to the FMO complex

In this section, we apply the approximations discussed in Section 4.2.3, to the energy gap trajectories obtained from the mixed QM/MM simulations for the FMO complex of *Prosthecochloris aestuarii* as carried out recently by us in Ref. [25]. The nuclear trajectories were obtained by classical MD using the AMBER 99 force field. An isothermal-isobaric (NPT) ensemble was employed in the MD simulations. For the calculation of the energy gap, snapshots of the nuclear coordinates were taken at every 4 fs. For each ground state configuration, the gap was obtained by computing the energy corresponding to the Q_y transition of the BChl's using time-dependent time-dependent density functional theory with BLYP functional within the Tamm-Dancoff approximation.

The calculations were carried out at 77 and 300K and both temperature were treated on the same footing. We do not expect there to be additional sampling problems for the low temperatures because, up to current knowledge, FMO does not undergo any major conformational changes in this temperature range. More details on the computation can be found in Ref. [25].

The calculation of the SD from the time dependent gap energy is based on the model described in Section 4.3. The actual MD simulation might deviate from this model e.g. because the thermostat could influence the dynamical evolution and thus the correlation function. We plan to investigate this aspect in future work. For now we will assume that the thermostat doesn't influence the dynamics and that the models introduced in Section 4.3 provide a reasonable description of a two level molecule treated in the QM/MM approach.

4.6.1 TDCD and spectral density from mixed QM/MM with a posteriori semiclassical corrections

Using the energy gap trajectories obtained in Ref. [25], we evaluated the different semiclassical approximations as reported in Tab. 4.1. We denote the time-points at which the energy gap is calculated by t_i and the corresponding energy gap by X_i where $i = 0, \dots, N-1$ runs over the N the time-points. As in Ref. [25] we evaluated the correlator by using a discrete representation, which implements the k-th element of the two-time correlator as

$$C_k = \frac{1}{(N-k)} \sum_{i=1}^{N-k} \left(X_i - \bar{X}\right)\left(X_{i+k} - \bar{X}\right) \tag{4.49}$$

where $\bar{X}$ is the mean. Here, one assumes that the $N-k$ values X_i give a faithful initial distribution which reproduces the Boltzmann distribution. To minimize spurious effects in the Fourier transform, we multiplied the time trace by a Gaussian of variance $\sigma^2_{\text{gaussian}} = 0.09 \cdot t^2_{\text{max}} = 2.304 \cdot 10^5\,\text{fs}^2$ with $t_{\text{max}} = 1600\,\text{fs}$, the length of the correlation function (as reported in [25]). The Gaussian

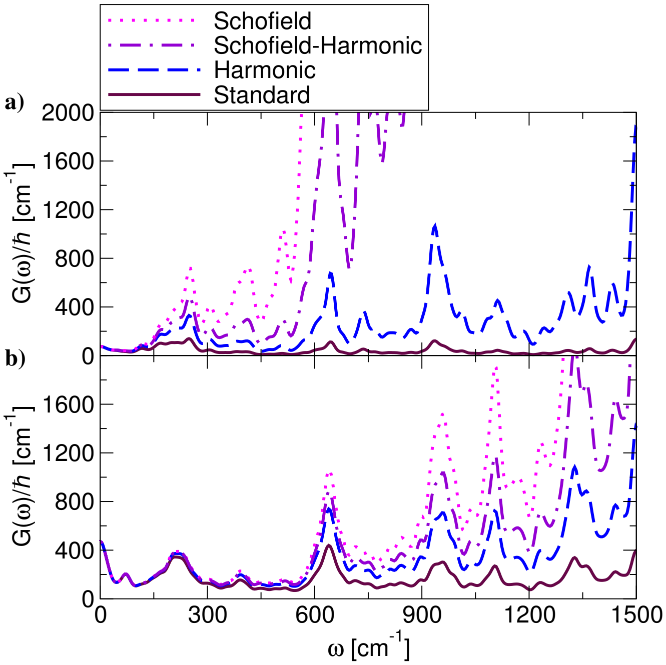

Figure 4.2: Positive frequency part of the temperature-dependent coupling densities $G(\omega)$ obtained, as described in the Section 4.6.1 with each of the Standard, Harmonic, Schofield and Schofield-Harmonic corrections as (see Tab. 4.1, column two). In panel **a**) results are at 77 K and in panel **b**) 300 K.

is normalized to have unitary area in frequency domain[vi] following our definition of the Fourier transform in Eq. 4.6, so that in frequency domain this corresponds to a convolution with a Gaussian with a FWHM of 26 cm^{-1}. Next, we computed the different semiclassical quantities of Table 4.1 using our initial time trace.

In Figure 4.2, we show the temperature-dependent coupling densities TDCDs (as defined in Eq. 4.6), for site 1 of the FMO complex (site 1 at 77 K and 300 K) evaluated using the different approximations listed in Table 4.1 column two. We notice how, as expected, there are little differences between the approximations at low frequencies. Only at higher frequencies the TDCD differs significantly for each approach. The Egelstaff approximation incorrectly predicts a negative spectral density for low frequencies in this case and was therefore not shown in the plots.

From the general definition of each semiclassical correction, it isn't clear which one is most accurate. To better reason on which one to choose, we will look at the temperature dependence of the spectral density. Further, we will compare to experimental results and finally we will evaluate the three point correlator (Sec.4.6.4).

[vi] The variance in frequency domain is $\sigma_\omega^2 = 4.3403 \cdot 10^{-6} \frac{1}{\mathrm{fs}^2} = 122.33\,\mathrm{cm}^{-1}$. This give a FWHM of 26 cm^{-1}.

4.6.2 Analysis of prefactors in terms of temperature dependence of the spectral density

From our discussion in Section 7.1, we recall that many open quantum system approaches rely on the assumption of linear coupling to a bath of harmonic oscillators. This leads to a temperature-independent spectral density $j(\omega)$, as discussed in Section 4.3.2. Inspection of Fig. 4.2 shows that for all but the Harmonic approximation the TDCD (from which one obtains $J(\omega)$ which is directly proportional to the spectral density $j(\omega)$) obtained from the QM/MM is not similar at different temperatures. This is more apparent at higher frequencies. To gain further insight into this temperature dependence, in Fig. 4.3, we compare the asymmetric TDCD ($J(\omega) = \pi j(\omega)\, ;\, \omega > 0$) obtained using the Standard (panel a) and the Harmonic (panel b) approximations for site 1 of the FMO complex. One clearly sees that for the Standard correction there is a huge difference between the 77 K and the 300 K results. However, in the case of the Harmonic correction the spectral densities obtained at the two temperatures nicely lie on top of each other, as one would require for a temperature-independent spectral density. This result suggests that the Harmonic correction is the appropriate one to employ to obtain spectral densities to be used in open quantum system models which assume linear coupling to a bosonic bath.

Note, that the good agreement at both temperatures for the Harmonic correction might be purely accidental or due to the fact that the MD is not fully converged. We would need to run much longer QM/MM trajectories to improve the statistics and check the convergence of the distributions. This lack of statistics could also explain the fact that for the SD averaged over all chromophores (panels c) and d)), the agreement between both temperatures is slightly better than for the individual sites.

Finally we would like to remark that a temperature dependence of the reorganization energy has been observed in the context of electron transfer (ET) donor-acceptor energy gap spectral densities [148, 149].

4.6.3 Comparison to experimental spectral density

In Fig. 4.4 panel a) and b) we compare the asymmetric TDCD for site 3 (Standard and Harmonic correction), with the asymmetric TDCD obtained from fluorescence line narrowing (FLN) experiments [21]. We focus on the low frequency part (up to ~500 cm^{-1}), which is relevant for energy transfer in the FMO complex. The FLN results are obtained from the lowest excitonic peak of the

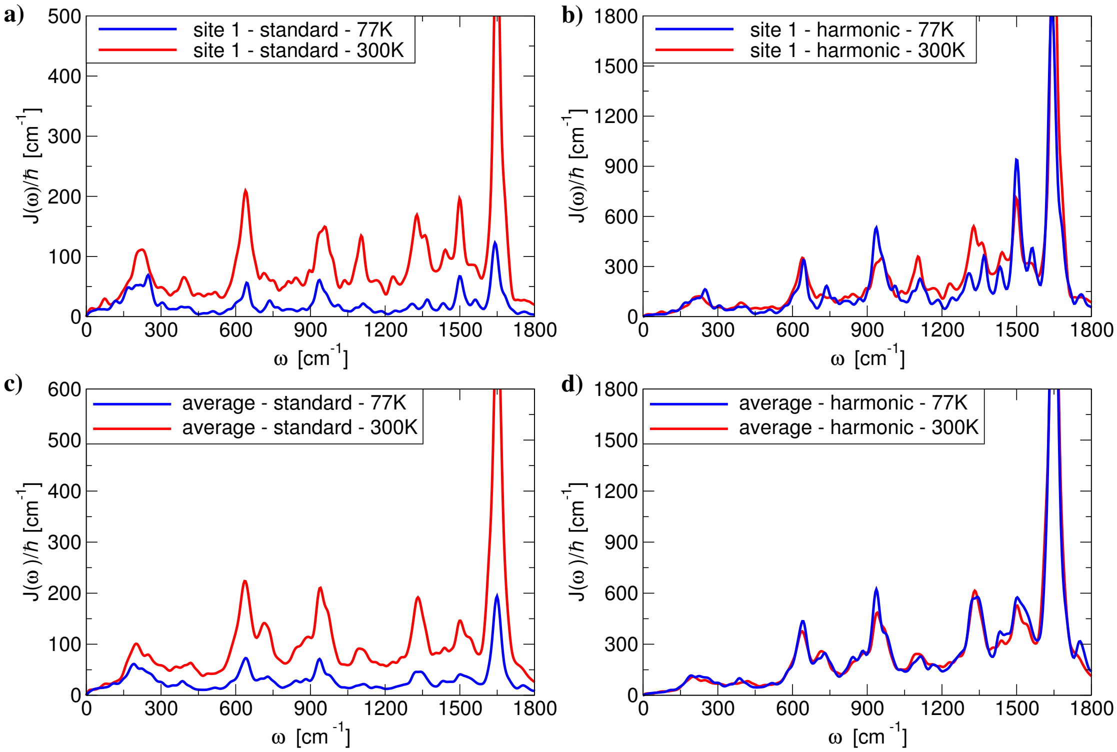

Figure 4.3: Panel **a**) comparison of the asymmetric component of temperature-dependent coupling density $J(\omega) \equiv G_{\mathrm{asym}}(\omega)$; for site 1 of the Fenna-Matthews-Olson complex, obtained with the Standard approximation (Tab. 4.1, first line, third column) at 77 K and at 300 K. Panel **b**) comparison of $J(\omega)$ obtained for site 1 with the Harmonic approximation (Tab. 4.1, second line, third column) at 77 K and at 300 K. We see clearly that the Harmonic prefactor gives a roughly temperature independent $J(\omega)$, while large differences are seen using the Standard prefactor. Panels **c**) and **d**) report the average spectral densities.

FMO absorption spectrum which is believed to be generated almost entirely by BChl 3. Therefore, we compare the experiment to the theoretical spectral density obtained from the QM/MM for BChl 3.

The experimental spectral density shown in Fig. 4.4 is based on the dotted curve $\tilde{j}^{\exp}(\omega)$ of Fig. 2 of Ref. [22], which is in good agreement with the one-phonon vibrational profile (OPVP) of Ref. [21], because of the small total Huang-Rhys factor. Note that the extraction of the OPVP uses the same model of shifted harmonic potential surfaces as we did in Section 4.3.2. Thus it corresponds to a SD which is suitable as input in the open system approaches. In this harmonic model the profile $\tilde{j}^{\exp}(\omega)$ is related to our definition of the spectral density by $j^{\exp}(\omega) = (\hbar\omega)^2\, \tilde{j}^{\exp}(\omega)$. The positive frequency part of the asymmetric TDCD, $J(\omega)$ is obtained from the spectral density, as defined in Eq. 4.13, by $J^{\exp}(\omega) = \pi\, j^{\exp}(\omega)$.

From panel e) and f) of Fig. 4.4, we see that the magnitude and overall lineshape of both the Standard and the Harmonic correction are in good agreement with the FLN data, in contrast with previous results[vii] [25].

A closer inspection of the curves in panels c) and d) of Fig. 4.4 shows that the width of the peaks obtained from the QM/MM simulation is much broader than that obtained from the FLN data. As described in Section 4.6.1, this broadening is due to the finite length of the numerical correlator, and to the convolution with a gaussian function in frequency domain, which results in a broadening of FWHM $26\,\mathrm{cm}^{-1}$. Also, the position of the peaks do not perfectly coincide. There might be various reasons for this discrepancy: The trajectories might be too short, the quantum chemical calculations of the transition gap are not accurate enough, or the thermostat leads to some spurious effects. One has also to keep in mind that there are uncertainties in the experimental data as well. The experimental data (in particular at higher frequencies) probably do not represent the actual spectral density of BChl 3 (excitonic effects might play a relevant role, and it was difficult to extract the lineshape from the representation of Refs. [22] and [21]).

Nevertheless, this good agreement in magnitude and overall lineshape makes us confident, that the QM/MM procedure can indeed be useful to extract spectral densities.

Finally, it seems that the Harmonic correction describes the FLN data slightly better in terms of amplitude, respect to the Standard correction.

[vii] The standard asymmetric component $J(\omega) = G_{\mathrm{asym}}(\omega)$ shown in Fig. 4.4 panel a), corresponds to the spectral density in Ref. [25] if one multiplies the Shim result by $\pi \cdot \tanh(\omega\beta\hbar/2)/\tanh(\nu\beta\hbar/2)$ to obtain $J(\omega)$ (here $\nu = \omega/(2\pi)$). We would like to point out that a different convention was employed in [25].

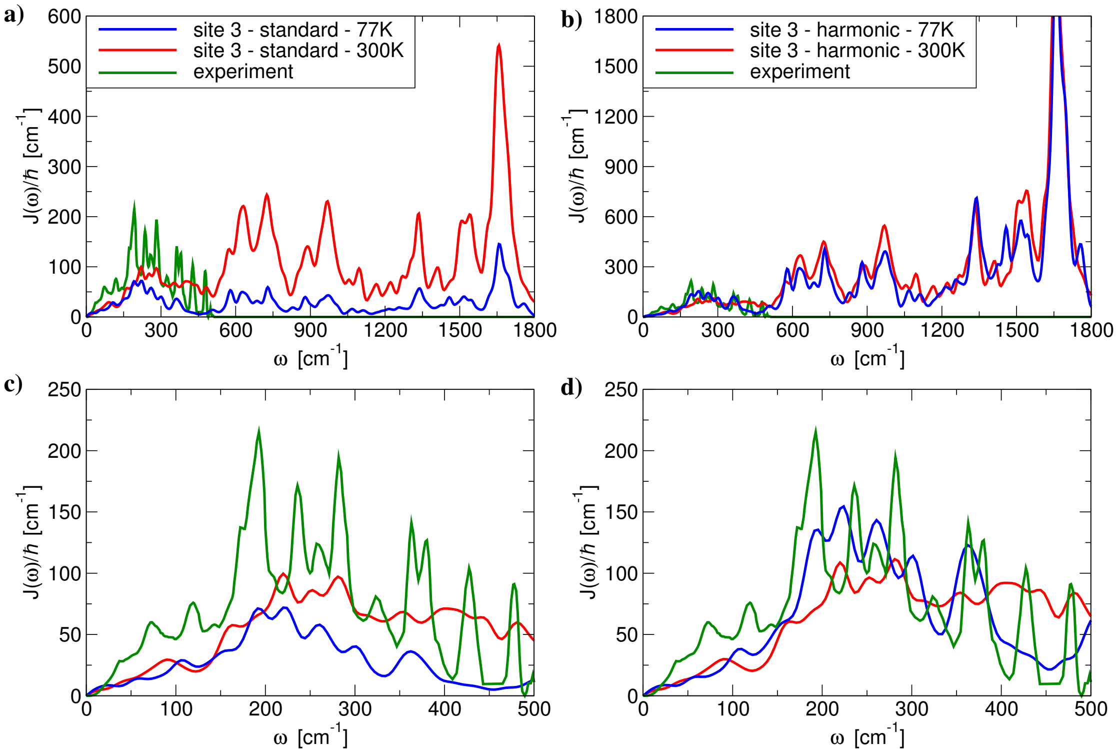

Figure 4.4: Panel **a**) shows $J(\omega)$ for site 3 of the FMO complex calculated with the Standard approximation at 77 K and 300 K and the green curve corresponds to the experimental spectral density rescaled by π to obtain $J(\omega)$ as defined in Eq. 4.13 [21, 22](More details on the experimental spectral density are given in the text). Panel **b**) shows $J(\omega)$ for site 3 calculated with the Harmonic approximation at 77 K and 300 K and again the green curve corresponds to the experimental spectral density [21, 22]. The agreement with the experimental (green) spectral density is slightly better for the Harmonic approximation than for the Standard approximation. Panels **c**) and **d**) correspond to the same quantities as those of panels a) and b) in the low frequency region, here we note that both approximations are roughly equivalent for $\frac{\hbar\omega}{k_\mathrm{B}T} < 1$ (e.g at $T = 77\,\mathrm{K}$ for $\omega < 55\,\mathrm{cm}^{-1}$and at $T = 300\,\mathrm{K}$ for $\omega < 200\,\mathrm{cm}^{-1}$). Further, the spectral density, as defined in Eq. 4.13 can be obtained by dividing $J(\omega)$ by π.

4.6.4 Higher-order correlation function

From the theory of discrete processes, similarly to Eq. 4.49, we see that the (k, j)-th element of the three-time correlator is

$$C(k,j) = \frac{1}{(N-k-j)} \sum_{i=1}^{N-k-j} (\Delta X_i)(\Delta X_{i+k})(\Delta X_{i+k+j}) \tag{4.50}$$

with $\Delta X_i = X_i - \bar{X}$ where $\bar{X}$ is the mean and N is the number of time points (as defined in Sec. 4.6.1). We compare the two-time and the three-time correlators by dividing them by increasing powers of the standard deviation $s \equiv \sqrt{m^{(2)}}$, thus we use Eq. 4.49 for the two-time correlation function and divide it by s^2 and we divide Eq. 4.50 by s^3. The results for site 1 of the FMO complex at 77 and 300K are reported in Fig. 4.5. For the two-time correlator, Fig. 4.5 panels a) and b), we see correlations up to at least 1000 time steps, while for the three-time correlator, panels c), d), e) and f), we see a rather noisy profile with values about one/two orders of magnitude smaller than the largest value of the two-time correlations. This is observed for all sites and temperatures.

This means that since we find a small three-time correlator, the linear coupling to a harmonic bath assumption is probably good. In fact, as described in Sec. 4.5 this case corresponds to linear coupling to the bath and Gaussian correlated bath operators. Of course, the statistics of the three-time correlator is not great due to the finite length of the time trajectories, but we think that the general tendency is correct. One should also keep in mind that there may be fortuitous cases in which the three-time correlator is roughly zero and the bath is not harmonic. Further, this comparison is based on the order of magnitude of the correlations, the three-time correlator is only much smaller. It may be that for some modes of the system, certain frequencies, present in the three-time correlator's two dimensional Fourier transform give a more important contribution to the dynamics than other frequencies present in the spectral density. Nonetheless, the above result encourages the idea that the assumption of linear coupling and harmonic bath is valid. This, in turn, implies that one should use the Harmonic semiclassical correction in Sec. 4.2.3, which is also consistent with the prefactor found in 4.3.

On a final note, to confirm with certainty that the bath is Harmonic, one should evaluate higher order correlators, beyond the three-time correlator. However, to obtain a statistically relevant estimate, much longer time dependent energy gap trajectories, which are expensive in terms of the QM/MM propagation, would be required. Work in this direction is being carried out in our groups.

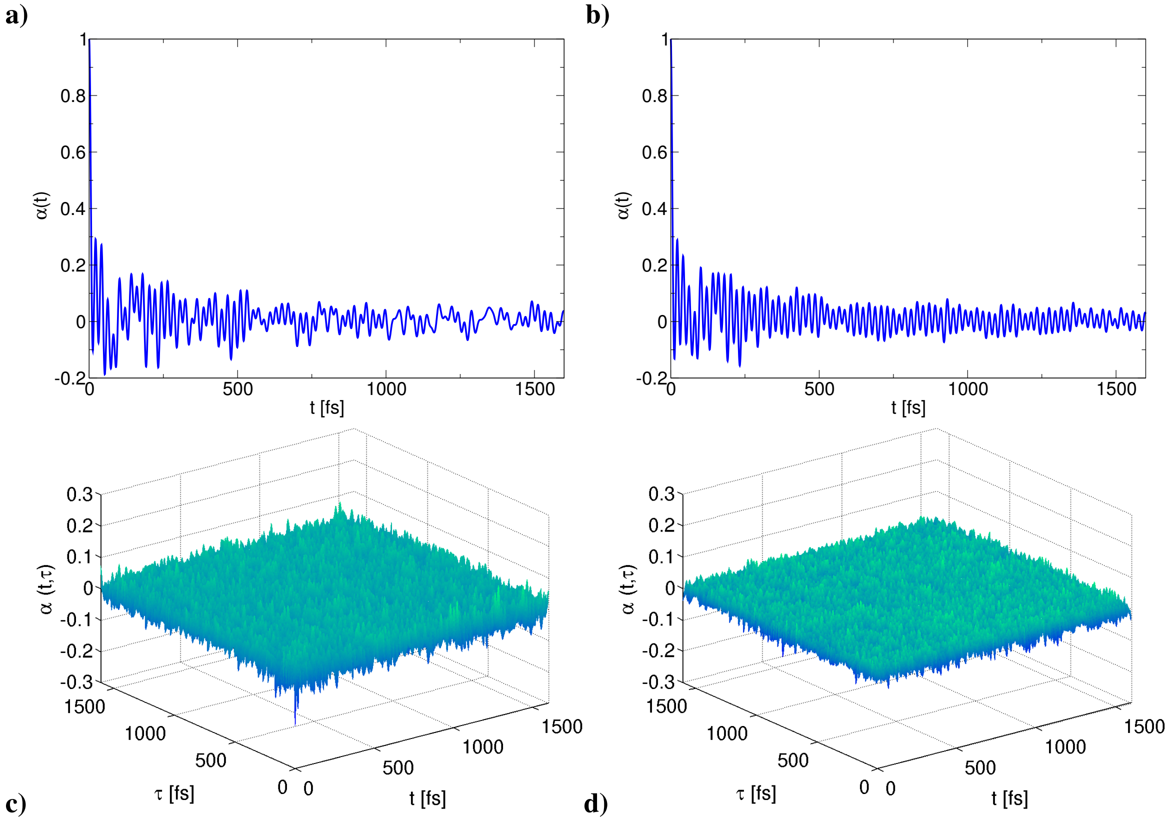

Figure 4.5: Panel **a**): Two-time correlation function of the energy gap fluctuations of site 1 of the FMO complex, normalized by s^2 (the variance) at 77 K after evaluating it as in Eq. 4.49. Panel **b**): Two-time correlation function for site 1 at 300 K. Panel **c**) Three-time correlation function of the energy gap fluctuations of site 1 of the FMO complex, as defined in Eq. 4.50 normalized by s^3 at 77 K. Panel **d**) Three-time correlation function for site 1 at 300 K.

4.7 Conclusions

In this work, we have investigated the connection between the gap correlation function extracted from ground state QM/MM and the bath spectral density used as input in many open quantum system approaches.

One important point is that the classical bath correlation function is real while the quantum mechanical one is generally complex. There exist several semiclassical *a posteriori* corrections which aim to fix this and we have employed them on our time traces to recover a part of the imaginary component.

The discussed prefactors originate from general expansions in orders of $\hbar$ and do not include information on the specific type of system-bath coupling, etc. We have investigated two simple models and found that the prefactors obtained correspond to two of the general semiclassical expressions. Thus, we have linked the semiclassical limits with a microscopic potential energy surface picture.

We have shown that the gap-correlation function extracted from ground state QM/MM only corresponds to the fully quantum excited state calculations in the case of shifted parabolas. This model for a few vibrational modes of the chromophores has been successfully used to describe the optical properties of molecular aggregates. Including only a finite number of internal vibrations is probably a good approximation for molecules in the gas phase or suprafluid Helium nanodroplets [146]. However, for molecules in solution or when a protein environment is present it is no longer a good approximation to include only only a few (undamped) modes. In particular, one has to take into account the interaction of the vibrations with the environment in addition to the direct interaction of the electronic excitation with the environment. For this general situation, it is no longer clear whether the model of shifted harmonic potential surfaces is indeed a good description of the system.

Therefore, we have investigated whether the approximation of harmonic bath and linear coupling is accurate for our QM/MM calculations for the FMO photosynthetic complex by computing the next higher order correlator beyond the two-time correlator. The three-point correlator seems to give a small contribution which, while not being conclusive, suggests to us that the Harmonic/linear coupling model is a good approximation. The evaluation of the four-time correlation function would be useful to bolster this claim.

The analysis of the temperature dependence of prefactors for the spectral density also suggests that the Harmonic approximation is preferred to use for the FMO complex, and perhaps other photosynthetic complexes, rather than the Standard one when employing it in Open Quantum system approaches.

Having made these choices, the theoretical results are in reasonably good agreement with the experimental spectral density. These result in a much better agreement than in our previous work, which underestimated the magnitude of the spectral density [25] and than other QM/MM calculations [33] which overestimate the coupling to the bath by one order of magnitude.

Finally, we have explained the link between bath correlation function and gap correlation function and found models under which the gap correlation function can actually be viewed as a general open quantum system bath correlation function.

Chapter 5

Atomistic study of energy funneling in the light-harvesting complex of green sulfur bacteria[i]

5.1 Introduction

Photosynthetic bacteria are among the simplest organisms on Earth which use sunlight as their main energy source [1]. To collect solar energy these bacteria exploit light-harvesting complexes (LHC), aggregates of pigment molecules, which absorb photons and transfer the associated energy at the submicron scale. The LHC in green sulfur bacteria contains large light absorbing antennae self-assembled in the so-called chlorosome [12]. These bacteria are obligate phototrophs – they are required to use sunlight to support metabolic reactions [150–152]. However, it has been observed that green sulfur bacteria can live in extremely low light conditions, even when receiving only a few hundred photons *per bacterium* per second [2, 153, 154]. These facts have inspired many conjectures and discussions on the functional properties, energy conversion efficiency and robustness of LHC in green sulfur bacteria [26, 38, 155–159].

In order to address this controversy we introduce a model which includes atomistic structural detail of the green bacteria LHC and allows for the simulation of excitation energy transfer (EET) at the systems level. As a specific example, we consider the LHC of *Chlorobium tepidum*. We observe fast relaxation of excitations within the subunits of LHC owing to the large overlap between exciton states and strong interaction with environmental fluctuations. The transfer between subunits involves collective excited states of the pigment molecules and supports the hypothesis of supertransfer [38,

---

[i] Joonsuk Huh, Semion K. Saikin, Jennifer C. Brookes, **Stéphanie Valleau**, Takatoshi Fujita, and Alán Aspuru-Guzik. Atomistic study of energy funneling in the light-harvesting complex of green sulfur bacteria. *Journal of the American Chemical Society*, 136, 2048 (2014)

157, 159]. The energy transport is robust to different initial excitation conditions, and changes in temperature. Finally, we show that the population of different parts of the LHC can be described using simple kinetic equations with time-dependent transfer rates characterizing intra-unit dynamics. This later model naturally explains the multiple timescales of EET reported in optical studies of green sulfur bacteria [160–164] and green non-sulfur bacteria [165–167].

Theoretical models have been applied mostly to single functional units of LHCs [25, 28, 76, 93, 114, 168–172] in order to understand the physical principles of energy transfer. Some of these studies also involved atomistic structures [25,103,104,171], which make the models computationally demanding. To the authors knowledge there are only a few atomistic studies of the complete light-harvesting systems of purple bacteria [173,174] but none for green sulfur bacteria. In addition to the large scale calculations the detailed analysis of excitation dynamics on the systems level [27, 167, 173–175] is complicated due to the lack of structural information. Thus, one usually needs to use macroscopic phenomenological models [176] or introduce additional constraints and approximations on the transport models [78, 115].

The LHC in green sulfur bacteria was described in Chapter 1 and is shown in Fig. 5.1. The distance between the pigments in LHCs is sufficiently large such that the overlap of electronic wave functions can be neglected. In this case the energy transfer is mediated by the near field interaction between molecular electronic transitions, the Förster interaction [53, 56, 177]. If the interaction between several molecules is sufficiently strong as compared to the energy difference between their electronic transitions, the exciton states are delocalized over the group of pigments [53, 177]. The preferential direction for energy transport is controlled by the frequencies of electronic transitions: the excitation goes to molecules or groups of molecules with lower excited state energy, while dissipating the energy difference to the environment.

5.1.1 Molecular aggregate model

A single LHC of *Chlorobium tepidum* contains 200–250 thousand BChl molecules [12, 162, 178]. Most of these molecules are found in the chlorosome. The model we have created is shown in Fig. 5.1, it is composed of 3988 pigments and represents all the functional units of LHC in green sulfur bacteria, excluding the reaction center.

In our model (Fig. 5.1 panel b) a double wall roll aggregate with diameter of about 16 nm and length of about 21 nm, represents the chlorosome. Several possible structural arrangements of BChls

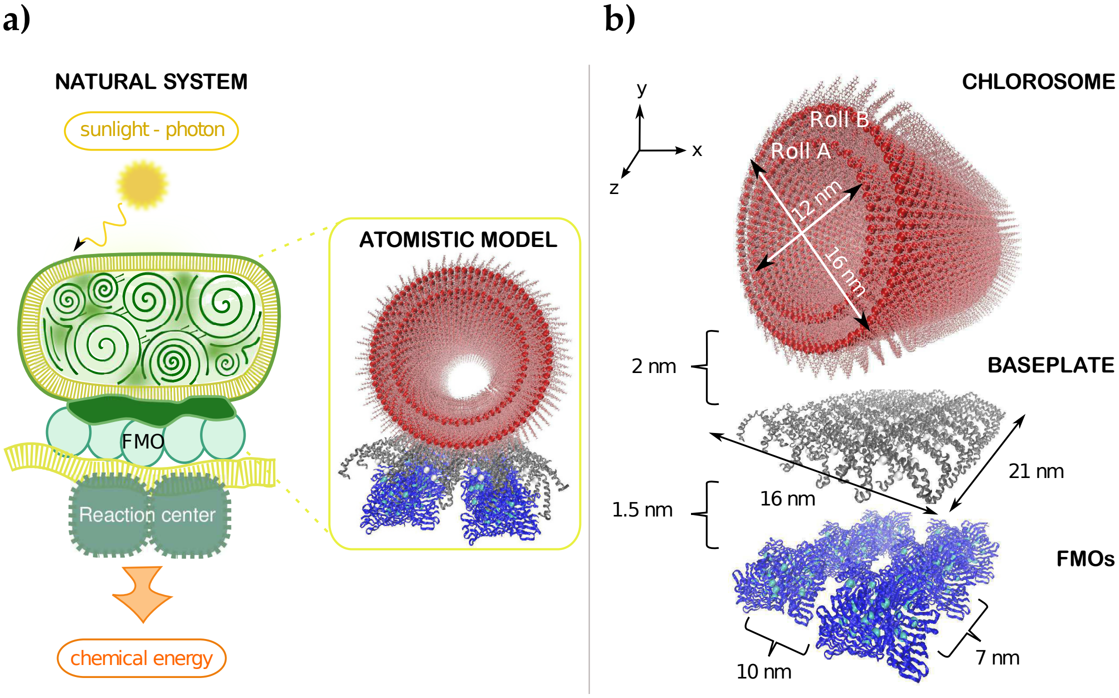
a)
NATURAL SYSTEM
sunlight - photon
FMO
Reaction center
chemical energy
ATOMISTIC MODEL
b)
CHLOROSOME
y
x
z
Roll B
Roll A
12 nm
16 nm
2 nm
BASEPLATE
21 nm
16 nm
1.5 nm
FMOs
10 nm
7 nm

Figure 5.1: Photosynthetic apparatus. Panel **a**) Cartoon of light-harvesting complex in green sulfur bacteria. The bacteria transform solar photons into chemical energy. Sunlight absorbed by the chlorosome is transferred in the form of an exciton through the baseplate and Fenna-Matthews-Olson (FMO) complexes subsequently to the reaction center. A snapshot of the model structure is also shown. Panel **b**) Atomistic model with corresponding length scales. The atomistic model is composed of a double wall roll for the chlorosome (roll A, 1620 (= 60 × 27) BChl c sites; and roll B, 2160 (= 80 × 27) BChl c sites), baseplate (64 BChl a sites), and 6 FMO trimer complexes (144 (= 24 × 6) BChl a sites).

in the chlorosome have been investigated theoretically and experimentally [179–185]. Here we use the structure of [185], obtained from a triple mutant bacteria and characterized with nuclear magnetic resonance and cryo-electron microscopy. This structure is also supported by 2-dimensional polarization fluorescence microscopy experiments [186].

The microscopic structure of the baseplate has not yet been experimentally verified [13]. We construct a baseplate lattice as following. The unit cell consists of dimers of CsmA proteins [187] containing 2 BChl *a* molecules sandwiched between the hydrophobic regions and bound near the histidine. To establish a stable structure of the baseplate, classical molecular dynamics simulations were done.[ii] The final structure complies with the periodicity and dimensions of the unit cell as seen in freeze frame fracture [190]. Finally, for the FMO protein complexes we employ the structure resolved by Tronrud *et al.* [87].

The ratio of BChl *c* in the chlorosome to BChl *a* in the baseplate (98.3:1.7) is comparable to the stoichiometry of the natural system (99:1, approximately) [12, 162]. The estimated density of FMO complexes is about 1 FMO/50 nm^2 [191]. Therefore, we distribute 6 FMO complexes under the baseplate which occupies about 300 nm^2 (see Fig. 5.1 panel b). This gives a pigment ratio of 2.3:1 (FMOs:baseplate), which is similar to the corresponding stoichiometry of *Chlorobium tepidum* 2:1 [178].

The distances between the chlorosome BChl *c* aggregates and the baseplate is determined by the length of BChl *c* esterifying alcohols. In the case of *Chlorobium tepidum* it is about 2 nanometers [13, 164, 167]. While the orientation of FMO relative to the baseplate has been verified experimentally [191], the relative distance between these units is unknown. In our model we set it to be 1.5 nm, which is larger than the inter-pigment distance within FMO but smaller than the baseplate-chlorosome distance. This choice is based on the argument that the FMO complex is strongly linked to the baseplate [89]. Minor variations of this distance do not affect the results.

The frequencies of exciton transitions in LHCs are controlled by multiple factors. In the model it is equivalent to use the relative shifts (energy gap) of these transitions, which are relevant to the EET. These shifts can be calculated from the pigment-pigment couplings and the electronic excitations of single BChls, site energies, modified by the local environment [22]. While the couplings can straightforwardly be computed using a screened dipole-dipole model [22], the calculation of site energies requires more complicated models or fitting to experimentally measured optical spectra.

[ii] The NAMD program package version 2.8 [188] was used. Force fields were parameterized with a combination of Amber ff99SB for the protein [189] and MMFF94 atomic charges for the BChl *a*.

Here, we set the frequency offset to be aligned with the lowest site energy of the FMO complex [89, 192].

The absorption domains of the baseplate and FMO composed of BChl *a* pigments are not clearly distinguishable. The absorption band of the baseplate covers the range 790–810 nm. This range also includes the absorption band of the FMO complexes [164, 192, 193]. In fact, the absorption band of the baseplate significantly overlaps with that of the chlorosome [164]. In order to reproduce these spectra using the constructed model we define the site energy of BChl *c* to be $2950\,\mathrm{cm}^{-1}$, which places the absorption maximum of the chlorosome of about $640\,\mathrm{cm}^{-1}$ above the absorption maximum of FMO complexes (see Fig. 5.2 panel a). Our choice is based on the fluorescence maximum of the chlorosome (786 nm) [164]. We shift the lowest exciton state obtained after taking 1000 ensemble average over the site energy fluctuation (standard deviation: $500\ \mathrm{cm}^{-1}$ [194]) at the fluorescence maximum. $12225\,\mathrm{cm}^{-1}$ (818 nm) is used as the offset energy value. We assign the site energy of the baseplate as $550\ \mathrm{cm}^{-1}$, which places the absorption maximum of the baseplate approximately in the middle of the absorption maxima of the FMO complexes and the chlorosome. The resulting absorption spectrum of the baseplate is shown in Fig. 5.2, panel a).

5.1.2 Exciton transfer model

The exciton transfer is modelled with a quantum master equation approach, which includes the coherent, dephasing and relaxation processes, for the open quantum dynamics [22, 31, 63, 73, 196]. We solve the quantum master equation to obtain the spacial distribution of the exciton.

In our model, the system-bath Hamiltonian of the light-harvesting apparatus is composed of three parts: the system consists of the local excitations of bacteriochlorophylls (BChls) and the point dipole interactions[iii] between them, described using a tight-binding Hamiltonian. Then, the system (BChls) is coupled linearly to the bath (proteins). The bath Hamiltonian consists of a sum of multidimensional quantum harmonic oscillators (see e.g. the reference [73]).

Within the secular approximation and in the Markov limit (i.e. secular Redfield), the equations

---

[iii] In general, the extended dipole or the transition charges from the electrostatic potentials (TrEsp) models for BChls may give more precise values for the electronic couplings. In Fujita *et al.* [197], we did a careful study of the TrEsp couplings and found out that TrEsp model can produce a 2–3 times longer decoherence times comparing to the point dipole model. However, the point dipole model can reproduce the proper experimental red shift for the chlorosome. Moreover, in the energy funneling process we expect the relative energy gaps are more important than the internal dynamics within an antenna unit because the time scale of the internal dynamics is faster than the energy transfer between different energy transfer units. In the TrEsp model [197], the electronic coupling strength between the pigments more than 2 nm apart is similar to the point dipole approximation. Therefore, we expect that the use of the more sophisticated model have a minor effect on the time scales between the antenna units, which is the main focus of this chapter.

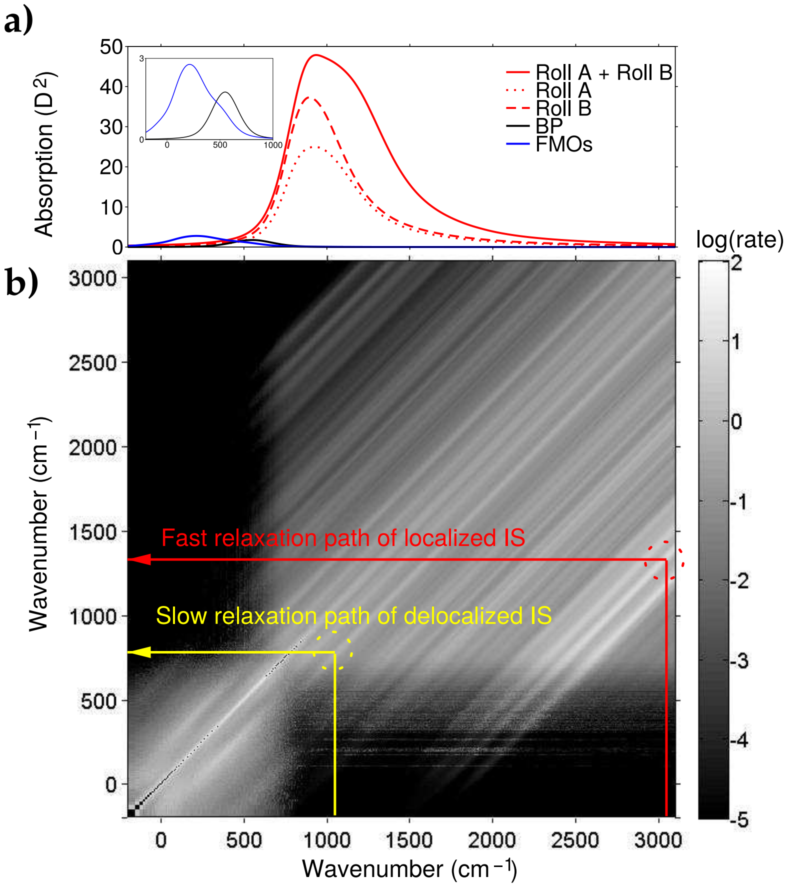

Figure 5.2: Calculated absorption spectra and exciton transfer rate matrix γ_{MN}. Panel **a**) Calculated absorption spectra [195] by direct diagonalization of the system Hamiltonians of the antenna units are shown. The absorption spectra are calculated and drawn for the double wall roll (roll A + roll B), the single rolls (roll A and roll B), the baseplate, and the 6 FMO complexes. The absorption spectrum of each antenna unit is obtained after taking 1000 ensemble average over the site energy fluctuations (static disorder). A Lorentzian line shape function with a full width at half-maximum of 100 cm^{-1} is convoluted, additionally, to take the homogeneous broadening into account. The inset is shown to magnify the spectra of the baseplate and FMO complexes in the original plot. Panel **b**) Transfer rate matrix γ_{MN} (cm^{-1}) at 300 K is presented in a logarithmic scale. γ_{MN} indicates population transfer rate between exciton states $|M\rangle$ and $|N\rangle$. We set here the frequency offset to be aligned with the lowest site energy of the FMO complex.

of motion of the reduced density operator $\hat{\rho}_{\mathrm{S}}(t)$ in the exciton basis, the population and coherence transfer are decoupled [29].

The resulting quantum master equation includes a term γ_{MN}, which is the exciton transition rate between the corresponding exciton states $|M\rangle$ and $|N\rangle$. γ_{MN} is calculated with the exciton eigenvectors and spectral density (exciton-phonon coupling strength) at the transition energy (see the references [73, 198] for the definition). It is shown in Fig. 5.2 panel b) as a matrix, for the EET dynamics at 300 K.

The validity of the Redfield method for the EET in natural light-harvesting structures had been discussed by many authors, see *e.g.* the references [29, 199–203] and the references cited therein.

When the energy gap between the exciton states is small, the Redfield model with a broad spectral density can be applicable [201]. Our molecular aggregate model in Fig. 5.1 and the corresponding spectral densities [25, 194] satisfy this condition: the absorption spectra of the antenna units overlap each other significantly, which implies the exciton states in this energy domain are delocalized over the two antenna units. The antenna units are coupled weakly (16–17 cm^{-1}).

Novoderezhkin and *et al.* [202] proposed to compensate the underestimation of the transfer rate between exciton states with large energy gaps by increasing the spectral density in the high frequency region. Therefore, we note here the exciton transition rate, which involves the exciton transfer with a large energy gap, could be underestimated because the Redfield model can only account for the single phonon process. Multiphonon processes could occur in the internal exciton dynamics of the antenna units due to its broad exciton bands (see Fig. 5.2 panel a). The internal exciton dynamics of the chlorosome is, however, much faster than the exciton transfer between the antenna units. Thus, the Redfield model should give a reasonable results (timescales) qualitatively for the exciton funneling process of the photosynthetic apparatus. For more accurate models, one would consider other methods such as the modified Redfield approach [199, 201, 203], hierarchical equations of motion [29, 70, 76, 117], iterative linearized density matrix dynamics [204], non-Markovian quantum state diffusion [93, 123], variational master equation [205], path integral Monte Carlo [206], and see the references cited in the review [207] of the methodologies in EET. However, most of these sophisticated methods, are not applicable to our large system because they are numerically too demanding.

The effects of slow fluctuations in the site energies (static disorder), which are responsible for the inhomogeneous broadening, are incorporated. We use $100\,\mathrm{cm}^{-1}$ for the Gaussian fluctuations in

FMO and the baseplate, and $500\,\mathrm{cm}^{-1}$ for the roll [192, 194]. All results are obtained from 1000 ensemble averages for the static disorder, unless otherwise mentioned.

The system Hamiltonian of FMO trimer complexes is taken from the work of Schmidt am Busch *et al.* [89]. The spectral density from our previous work [25] is used: where molecular dynamics and time-dependent density functional theory calculations were used for obtaining it. A harmonic prefactor was used for the spectral density [198]. The structure of the double wall roll is obtained based on the work of Ganapathy et al. [185] and the spectral density was obtained by time-dependent density functional theory calculations following the procedure described in Fujita et al. [194]

Instead of computing the spectral density of the baseplate, which is composed of BChl *a*, we use the spectral density of FMO [25]. This approximation is justified because we expect the vibrational structure to be similar to FMO's, which is surrounded by a protein environment (*cf.* chlorosome) and is also composed of BChl *a*.

To this end, we define the mean exciton energy to quantify the energy dissipation from the system to the bath during the energy funneling process,

$$\mathrm{MEE}(t) = \mathcal{E}\left(\mathrm{Tr_S}\left(\hat{H}_\mathrm{S}\hat{\rho}_\mathrm{S}(t)\right)\right), \tag{5.1}$$

where $\hat{H}_\mathrm{S}$ is the system Hamiltonian and $\mathrm{Tr_S}$ is the trace over the system degrees of freedom. $\mathcal{E}$ is the ensemble average over the static disorder.

Additionally, we introduce the exciton cooperativity, which is used to quantify the enhancement of transition dipole moment by coherence. $Cooperativity(t)$, the effective coherent excitation delocalization, is given as following

$$Cooperativity(t) = \frac{1}{|\mu|^2}\mathcal{E}\left(\sum_{\alpha=x,y,z}\left(\sum_{m,n\in\text{domain}}\mu_{n,\alpha}\mu_{m,\alpha}\left\langle n\middle|\hat{\rho}_S(t)\middle|m\right\rangle\right)\right) \tag{5.2}$$

where μ_n is the transition dipole moment vector of site n and a normalization factor $|\mu|^2 = 30\mathrm{D}^2$, which is the absolute square of the transition dipole moment of a single pigment, is used. The exciton cooperativity reveals the bright state dynamics (*i.e.* time-dependent emission strength). The complete decoherent mixed state gives the value 1, which implies the exciton "effectively" can be considered to be localized on a single pigment. On the other hand the coherent dark state gives the value 0, which is not visible in our cooperativity measurement. Accordingly, the cooperativity could give a lower bound to the coherent length. All pigments have the same magnitude of the transition dipole moment in our model (Fig. 5.1 panel b). The exciton cooperativity $|m\rangle$ and $|n\rangle$ are the site basis states. The summation is over the domain of interest.

5.2 Excitation energy funneling

To fully characterize the exciton transfer process of the photosynthetic apparatus model in Fig. 5.1, one needs to study the exciton dynamics for all possible initial (exciton) states within an ensemble at a finite temperature. For instance, the initial state prepared by a coherent light source (laser) could be considered as a single exciton state [208]. As an example, we perform exciton dynamics simulations for two cases of initial excitation at 300 K to see how the initial condition affects the EET dynamics. One is the brightest exciton state of the system Hamiltonian of Roll A, which is delocalized over Roll A (see the snapshot of Fig. 5.3, panel a) at 0 ps) and has energy $1018\,\mathrm{cm}^{-1}$. The other initial condition to be considered is a localized initial state (IS). In particular, a single site located on top and in the middle of Roll A is selected for the localized IS having energy $3022\,\mathrm{cm}^{-1}$ (see the snapshot of Fig. 5.3, panel b) at 0 ps).

Comparing the absorption spectra of Roll A and Roll B in Fig. 5.2 panel a), one can see the peak maximum of Roll B is red-shifted from the peak maximum of Roll A, thus there is an exciton energy gradient between the layers. As the radius of the roll increases (contrast A and B), the peak maximum shifts to the red [165, 181, 195]. This occurs because the roll curvature changes and this induces stronger dipole-dipole interactions between neighboring pigments. This energy gradient is favorable for the exciton energy funneling because EET from the outermost layer to the baseplate is important. Our choice of the initial states on the Roll A is based on this argument.

There are two important factors in determining the exciton transfer between the antenna units. These are the energy resonance condition and the electronic coupling between the energy levels of the antenna units [209]. The former is the necessary condition for the EET between the units and the later determines how fast EET should be. Figure 5.2 shows the delocalized IS is close to the energy levels of the baseplate and large multichromophoric excitonic coupling strengths to the baseplate exciton states. In contrast, the localized IS is far from the energy resonance level to the baseplate and the excitonic coupling strength is small.

Figure 5.3 summarizes the resulting exciton dynamics at 300 K. Figures 5.3, panel a) and 5.3, panel b) show the population dynamics using the delocalized IS and the localized IS respectively and up to 10 ps. Our choice of the time interval (10 ps) of the EET simulation is based on the timescales of the EET of *Chlorobium tepidum* [164]. Snapshots of the site populations at 0 ps, 0.1 ps and 10 ps are shown below the population plots. The exciton population distributions of individual antenna units at 10 ps are almost identical regardless of the initial conditions. For example, the total exciton population on FMOs is approximately 60 % for the two initial conditions.

In the rest of this section, we provide more detailed discussion of severe aspects of the exciton transfer. First, the exciton population dynamics of the two initial conditions are compared. Then, the multichromophoric effect is discussed for the exciton dynamics. The temperature dependence of the exciton dynamics comes afterwards. Lastly, the exciton dynamics is described in terms of the population kinetic model.

5.2.1 Exciton population dynamics

The EET dynamics of the delocalized IS and the localized IS become similar within 1 ps (Fig. 5.3). The short time dynamics (< 200 fs), however, are sufficiently different. Figure 5.3 panel a), shows a fast initial population decay for the roll comparing to that of the localized IS in Fig. 5.3, panel b). Characteristic time constants in Tab. 5.1 are extracted by the exponential fitting of the exciton populations of the roll such that amplitudes are summed to be 100 %. By comparing the time constants for the roll in Tab. 5.1, we see that Set I (delocalized IS) has a fast sub-100-fs component while Set III (localized IS) does not. However, τ_1 in Set I accounts for only 3 % of the 10 ps exciton dynamics. In the case of using the delocalized IS, the single exciton starts to migrate from the roll to the baseplate already at the very beginning (< 100 fs). This occurs because the frequency of the delocalized IS ($1018\,\mathrm{cm}^{-1}$) is close to the baseplate absorption region (see Fig. 5.2 panel a) and has a large collective transition dipole moment.[iv] In contrast, the localized IS ($3022\,\mathrm{cm}^{-1}$) is far from the energy resonant region and has a comparably weak transition dipole moment.

Equilibration in the roll is achieved within 100 fs for the localized IS dynamics and almost no exciton population is transferred to the baseplate in this short time. This can be seen in the inset figure of Fig. 5.4. The inset in Fig. 5.4 shows the diffusion process in the roll with the localized IS for the first 200 fs. Snapshots of the roll populations at 0, 10 and 20 fs are placed above the inset plot. In this plot, one can see how the single exciton diffuses within and between the layers. The black

---

[iv] Another delocalized IS, which is the brightest exciton state of Roll B, shows the similar short time dynamics (see Set II for the corresponding time constants and the exciton dynamics, respectively).

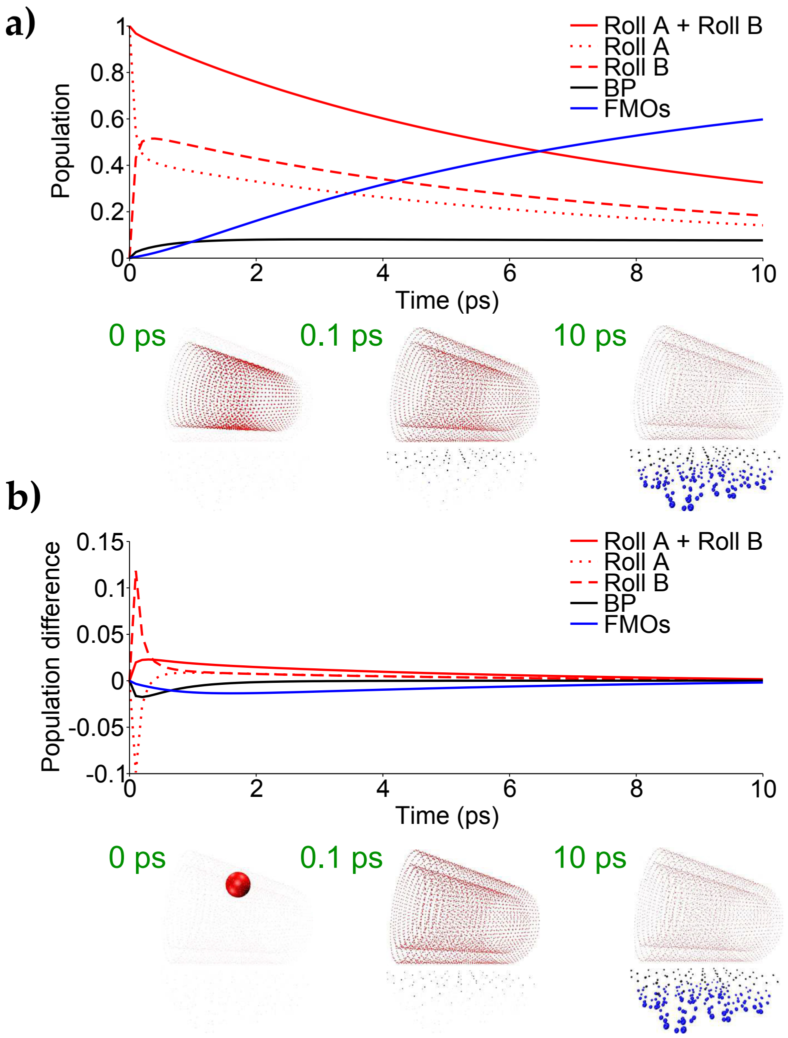

Figure 5.3: Exciton population dynamics with a delocalized and a localized initial state at 300 K. Panel **a**) The initial state (see the snapshot at 0 ps) is the brightest state of roll A. Panel **b**) The initial state (see the snapshot at 0 ps) is a localized state, that is, a site on the top and in the middle of roll A. The population difference with respect to the population in panel a) is plotted. The locations of magnesium (Mg) in the BChls represent the locations of exciton sites, and the sizes of the spheres are proportional to the populations of the corresponding sites. The populations of the rolls, the baseplate, and the FMOs are designated red, black, and blue, respectively.

Table 5.1: Time Constants of the Exciton Dynamics of the Chlorosome Roll. The values are obtained by the exponential fittings ($A_1\exp(-t/\tau_1)$ + $A_2\exp(-t/\tau_2)$ +$A_3\exp(-t/\tau_3)$) of the exciton population dynamics for each antenna unit. The amplitudes (A_1, A_2, and A_3) are summed to be 100%. (b) Corresponds to the exciton dynamics of the delocalized IS. (c) Brightest delocalized initial state of roll B is used. (d) Corresponds to the exciton dynamics of the localized IS. (e) Anisotropic decay of Chlorobium tepidum at 807 nm.

set	τ_1(ps) (A_1 (%))	τ_2 (ps) (A_2 (%))	τ_3 (ps) (A_3 (%))
I (b)	0.081 (3)	4.5 (36)	12.9 (61)
II (c)	0.060 (3)	4.7 (39)	13.1 (58)
III (d)		3.7 (25)	11.3 (75)
ref [164] (e)		1.1 (42)	12.1 (58)

solid line in the inset figure is the mean exciton energy (Eq. 5.1), which is normalized to the initial energy (3022 cm^{-1}). Interestingly, the curve is similar to the population dynamics of Roll A. From this we can conclude that the population transfer from Roll A to Roll B is the main energy relaxation channel and the slight difference of the two curves indicates the effect of population redistribution within the single layers. Thus the energy dissipation due to exciton-phonon coupling mainly causes exciton transfer between the layers in this initial short time period. The mean exciton energy of the total system (Roll+baseplate+FMOs) is given in Fig. 5.4 for two different initial excitations. The solid blue line and the solid red line correspond to the exciton dynamics of the two different initial conditions, respectively.

As mentioned above, the initial energy of the delocalized state is already close to the baseplate bright state energy domain (see Fig. 5.2), while that of the localized state is higher (3022 cm^{-1}). In the localized IS case, the excess energy (about 2000 cm^{-1}) should be released to the environment in order for resonant energy transfer to the baseplate to occur. In spite of the high initial energy of the localized IS, which is far from the energy resonance domain, the exciton population of each unit at 10 ps is similar to that of the delocalized IS case (see Fig. 5.3 panel a). This is possible because a rapid energy relaxation channel (Fig. 5.2 panel b) is available for the dynamics of Set III. The blue line in Fig. 5.4 shows a rapid energy drop within 100 fs. Then, within 1 ps, the total energy approaches the energy of the delocalized IS. The population snapshots at 100 fs indicate that population distributions are quite similar. Also, the population on the roll in the snapshots of Fig. 5.3 panel b) at that time indicates that, by 100 fs, the system population is mostly delocalized over the roll. The mean exciton energy obtained from the exciton dynamics with the delocalized IS and the localized IS become similar within 500 fs. The rapid relaxation within the roll results in robust energy transfer from the

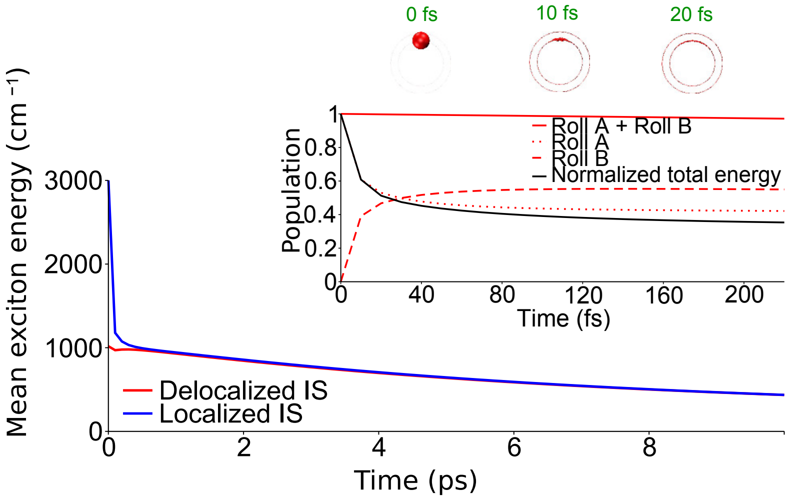

Figure 5.4: Mean exciton energy with a delocalized and a localized initial state at 300 K. Mean exciton energy (eq. 5.1) with the two different initial excitations, which correspond to those in Figure 5.3 panels a) and b). The short time dynamics for the first 200 fs of Figure 5.3, panel b) is given in the inset with the corresponding population snapshots. The populations in the snapshot are projected to the long axis of the rolls. The locations of magnesium (Mg) atoms in the BChls represent the locations of exciton sites, and the sizes of the spheres are proportional to the populations of the corresponding sites.

roll to the FMOs in the long time limit in our model study.

Microscopically, the energy dissipation dynamics is determined by thermal excitations and relaxation among exciton levels. The energy dissipation rate, in this model, depends on the spectral density, a quantity which indicates how strongly exciton states are coupled to the thermal bath, the probability distribution of the exciton states and temperature.

In Fig. 5.2 panel b), we show the exciton transfer matrix (γ_{MN}) at 300 K in logarithmic scale (log(cm^{-1})). We indicate the fast energy dissipation path for the localized IS with a red arrow. The strong white diagonal band corresponds to the strong exciton-phonon coupling at 1600–2000 cm^{-1} [125] , which leads to the rapid energy dissipation of the localized IS within the roll. We note here that this fast relaxation occurs only between the exciton states in the same antenna units not between the exciton states of different antenna units.

Damjanović *et al.* [103] suggested that a weakly bound polaron can be formed in BChl aggregates due to the interaction of excitons with intramolecular vibrational mode at about 1670 cm^{-1}. Their results were based on studies of LHC in purple bacteria. We do expect that the polaron couplings can renormalize energy levels and the mobility of the exciton energy is reduced [103]. This should be, however, weaker in the chlorosome where BChls are densely packed and the pigment-pigment

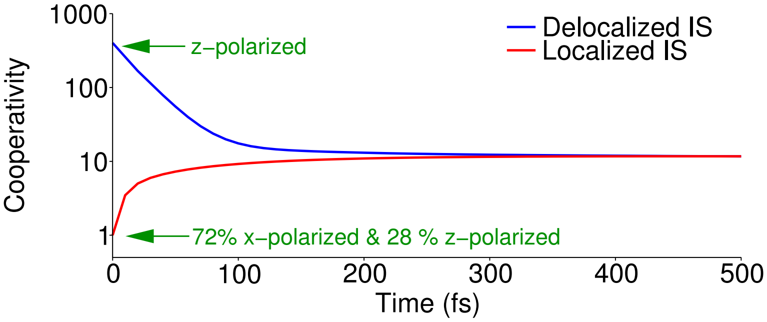

Figure 5.5: Time-dependent cooperativity of the chlorosome at 300 K. The cooperativity (eq. 5.2), dimensionless normalized collective transition dipole moment, is given in logarithmic scale. During the exciton dynamics in Figure 5.3 with the two initial states, the cooperativities are calculated for the chlorosome.

interaction is, accordingly, stronger than that of LHC in purple bacteria.

The exciton dynamics in the FMOs is conditioned mainly by the population of the baseplate because direct population transfer from the roll to FMOs is negligible.

5.2.2 Cooperativity of the excitonic states

In multichromophoric systems, coherent coupling between donor molecules can lead to a large collective transition dipole moment. This enhances the energy transfer from the donor to acceptor groups as compared to incoherent hopping between individual molecules [4, 38, 157, 159].

In Fig. 5.5, we show the cooperativity (Eq. 5.2) computed for first 500 fs. The cooperativity is calculated for the two different initial excitation conditions corresponding to the dynamics in 5.3.

The delocalized IS is z-polarized (along the length of the roll) and initially has a cooperativity of 402 (out of 1620 pigments in the Roll A). This strong collective oscillator strength can induce rapid supertransfer [38, 157, 159]. The localized IS, which is 72 % x- and 28 % z-polarized, has an initial cooperativity value of unity. This difference in cooperativity at varying initial condition is one of the reasons why a fast decay component is found for the delocalized IS case only.

Regardless of the initial conditions, within 500 fs, all cooperativity values converge to a similar value (∼12 out of 3780 pigments in the Roll A and B), which is still larger than 1, and the effective transition dipole moment becomes about 30 % x-, 30 % y- and 40 % z-polarized. This is a favorable situation, for our photosynthetic apparatus model, as y-polarization (normal direction to the baseplate) is useful to funnel energy towards the baseplate. These results may indicate a multichro-

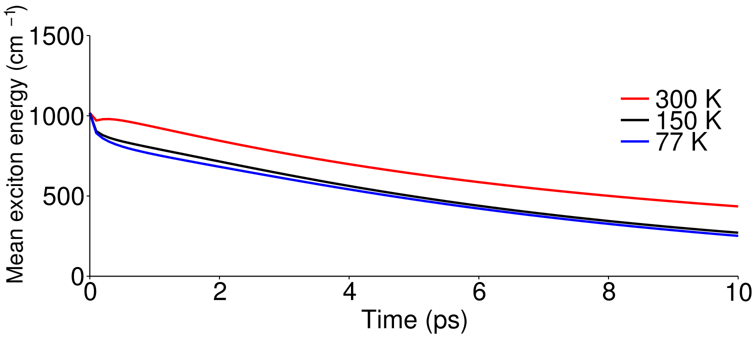

Figure 5.6: Temperature dependence of the mean exciton energy. The mean exciton energy of the system (eq. 5.1) is plotted at 300, 150, and 77 K. The delocalized exciton initial state in Figure 5.3 panel a) is used.

mophoric effect [209]; *i.e.* the effective dipole moment of the delocalized exciton state is enhanced by symmetry.

5.2.3 Temperature dependence of the energy funneling

In the previous subsections, we showed that the exciton energy funneling process is robust to variations in initial excitation conditions due to the fast internal exciton dynamics of the roll. We now investigate the temperature effect by simulating the exciton population dynamics with the delocalized IS initial condition, *i.e.* the brightest state of Roll A, at 150 K and 77 K in Fig. 5.6.

The mean exciton energy at room temperature (300 K) in Fig. 5.3 panel a) is only slightly different from the curves at 150 K and 77 K in Fig. 5.6. This indicates that exciton transfer is robust within this temperature range. The robust energy transfer within the temperature range is due to the fast internal exciton dynamics of the roll. The thermal excitation within the temperature range does not lift the exciton far from the energy resonance domain between the roll and the baseplate.

Thermal excitation in the temperature range (77 K, 150 K and 300 K) can provide various channels towards the neighboring exciton states for the relaxation process (see Fig. 5.2, panel b). Thermal excitation can also induce back transfer from the baseplate to the rolls [4] but it reduces the possibility of being trapped in dark states.

5.2.4 Population kinetics

So far, we have shown that regardless of initial conditions and temperature about 60–70 % of the exciton can be transferred to the FMOs within 10 ps. This robustness to the choice of initial conditions implies that internal dynamics within the roll is faster than energy transfer between the antenna units. We now proceed to examine the population dynamics by using a simple first order kinetic model (more sophisticated kinetic models in the EET of the LH complex networks can be found in *e.g.* the references [8, 78, 115, 210]):

$$\frac{\mathrm{d}}{\mathrm{d}t}\begin{pmatrix}[\mathrm{R}](t)\\ [\mathrm{BP}](t)\\ [\mathrm{FMO}](t)\end{pmatrix} = \begin{pmatrix}-k_{\mathrm{RBP}}(t) & 0 & 0\\ k_{\mathrm{RBP}}(t) & -k_{\mathrm{BPFMO}}(t) & 0\\ 0 & k_{\mathrm{BPFMO}}(t) & 0\end{pmatrix}\begin{pmatrix}[\mathrm{R}](t)\\ [\mathrm{BP}](t)\\ [\mathrm{FMO}](t)\end{pmatrix} \tag{5.3}$$

where $[\cdot](t)$ denotes the population of each antenna unit, and [R] and [BP] are the population of the full roll (Roll A + Roll B) and the baseplate respectively. $k_{\mathrm{RBP}}(t)$ is the exciton transfer rate from the roll to the baseplate and $k_{\mathrm{BPFMO}}(t)$ is the one from the baseplate to the FMOs. The population transfer between the antenna units is characterized by time-dependent rate constants $k(t)$. Note that the internal dynamics within the antenna units, such as relaxation and thermal excitation among the exciton states, is incorporated into the time dependence of $k(t)$. $k(t)$, physically, corresponds to the multichromophoric Förster resonance energy transfer rate [209], because it quantifies energy transfer between the donor group (exciton states) of the roll and the acceptor group of the baseplate. The enhancement of energy transfer due to coherence (Fig. 5.5) between donor molecules is also referred as to supertransfer [38, 157, 159].

The direct exciton transfer from the roll to the FMO complexes is virtually negligible within the time interval of the EET dynamics 10 ps. In this kinetic model, thus, we assume there is no population transfer from low to high energy units and no direct transfer from the roll to FMOs. The kinetic models are fitted to the exciton populations in Fig. 5.3 using least squares. The resulting time-dependent population transfer rates are shown in Fig. 5.7 for the exciton dynamics of Fig. 5.3, using both initial conditions (the delocalized IS and the localized IS). The initial and final values of the reciprocal rates of the (chlorosome) roll $1/k_{\mathrm{RBP}}(t)$ have similar values to τ_2 and τ_3 of Sets I and III in Tab. 5.1. Within 500 fs, $k_{\mathrm{RBP}}(t)$ for the delocalized IS drops rapidly to a slower rate, with a similar timescale to the equilibrium time of the cooperativity (Eq. 5.2), see solid blue line in Fig. 5.5. However we see that $k_{\mathrm{RBP}}(t)$ for the localized IS does not show this rapid drop. Regardless of the initial conditions, the rate constants become similar to each other within 500 fs. As could be

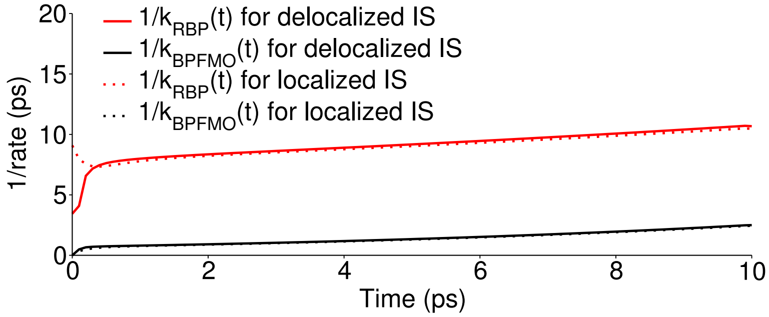

Figure 5.7: Time-dependent reciprocal rate. Time-dependent exciton transfer rates are given as the corresponding time constants, the reciprocal rate, for the exciton dynamics of the delocalized IS and the localized IS in Figure 5.3. $k_{\mathrm{RBP}}(t)$: Exciton transfer rate from the roll to the baseplate. $k_{\mathrm{BPFMO}}(t)$: Exciton transfer rate from the baseplate to the FMOs.

expected, $k_{\mathrm{BPFMO}}(t)$ has no dependence on the initial state in the roll.

5.3 Conclusion

The green sulfur bacteria are thought to be an incredibly efficient light processing machine (*cf.* purple bacterium [211]). We studied this system by investigating from an atomistic perspective and a top to bottom approach (*cf.* Linnanto *et al.* [212]). The excitation energy transfer route was taken from the chlorosome to the reaction center via the baseplate and FMO, under different initiating conditions. Analysis of the atomistic model indicates that resonant energy transfer is maximized given the multichromophoric excitonic coupling which is due to the molecular arrangements of these parts: the green sulfur bacteria are assembled to be most conducive towards efficient excitation energy transfer within the Förster energy transfer regime. It was further shown that whether the initial excitations are important in the energy funneling process. Though, the results differ qualitatively within a short time limit (500 fs). None of these scenario's, however, adversely affect the efficiency of energy transfer and the results converge within the overall timescale (10 ps) [164, 167]. Thus the mechanism is robust to initial conditions, including varying temperatures. This is due mainly to the fast internal exciton dynamics of the chlorosome, which is also observed by Fujita *et al.* [194,197]. Furthermore our measure of cooperativity quantifies this and indicates a preference (again regardless of initial conditions) to the polarization in the xy-plane (cross section of the chlorosome), which enhances the excitonic coupling strengths between the exciton states of the chlorosome and the baseplate. We suggest a multichromophoric effect may prevail over the absence of proximity by exploiting the symmetry in parts of the model. This calculation of cooperativity indicates a supertransfer effect inherent in: the green sulfur bacteria, which seems to be especially "tuned" towards thriving under low light conditions by making use of molecular aggregates, symmetry and self-assembly to capture light and funnel it to the reaction center aided, not hindered, by a fluctuating environment [73, 114].

Additionally we would like to comment here on the role of the baseplate in the energy funneling process based on our simulations. In our model study, the baseplate plays the role of a "bridge" allowing the exciton energy to funnel down to the FMOs from the chlorosome. The presence of the baseplate eases this process; without the baseplate energy transfer would be impeded. Whilst it could be the case that transfer is allowed without the baseplate- under the condition that the FMO's and chlorosomes be positioned close enough for Förster energy transfer- our results indicates that the baseplate offers a preferred route. However, the baseplate is considered to be a part of the chlorosome envelope and is likely to be the structure that is involved in its attachment it to the cell membrane [162]. Removal of the baseplate may result in an unstable structure or a different structure altogether. As an alternative working hypothesis for the role of the baseplate, one may consider replacing the BChl *a* molecules in the baseplate with BChl *c* without removing the baseplate structure from the model Hamiltonian. Then, one may expect no exciton transfer from the chlorosome to FMO complexes because the baseplate is not a J-aggregate and there is almost no spectral overlap between the baseplate and FMO complexes accordingly.

The baseplate receives the exciton quickly as shown in Fig. 5.3 and releases the exciton to the FMO complexes steadily. Since the chlorosome has a relatively large reorganization energy, which implies strong exciton-phonon couplings to the bath, compared to those of the baseplate and FMO complexes, the exciton could be lost to the environment if it is able to stay in the chlorosome for too long a time. Thus, we would like to introduce the idea of the baseplate as a biological (single) "exciton capacitor". It seems to be suitably designed for this purpose, making sure the route of the exciton is directed, by receiving the exciton from the chlorosome quickly, keeping the exciton from leaking to the surrounding environment, and supplying it to the FMO. It does so by providing appropriate excitonic sites, via chromophoric pigments, held in a unique and protein scaffold made of amphiphillic units that cross two very different dielectric boundaries (the interim gap between dry lipid chlorosomes and the more watery region at the FMOs) in a near perfect 2D lattice form in analogy to an actual capacitor (condenser) but made of soft materials.

Our model study depends on many undetermined parameters, such as the site energies of the baseplate, distance between the antenna units and the spectral density of the baseplate. Also, the structure of the chlorosome is still arguable [179–185]. Scanning of these parameters in all combinations is currently not tractable with current computer resources. However, fitting the parameters to experimental data would be useful to determine the structural information of the light-harvesting antenna complexes. Therefore we postpone this task for future work. Herein we comment on the two parameters, which would be important to determine the exciton transfer rate between the antenna units. One is the distance between the baseplate and the FMO complexes. We guess the distance would be 1–2 nm, at which range the local pigment to pigment (nearest neighboring pigments between the baseplate and the FMO) transfer rate would be scaled by 10–0.25 in the current model. However, our model study shows the multi-pigment to multi-pigment transfer is important and we expect the overall transfer rate would not be critically changed over this distance range. Exciton delocalization aids in making the transfer less sensitive to the distance change. The second is the site energy of the baseplate. We scanned the site energy of the baseplate with a simplified model system (smaller number of pigments) and we found ±50 cm^{-1} from the current value would result ±20 % exciton population difference at 10 ps. Regardless of the uncertainties in the model, our study shows characteristic time constants that fall within sub-100 fs-sub-100 ps and agree with experimental observations [164, 167] (or see Tab. 5.1).

Chapter 6

Machine learning exciton dynamics[i]

6.1 Introduction

The study of exciton dynamics in large photosynthetic complexes has been a topic of much theoretical and experimental interest in recent years [22,25,28,40,74,79,82,96,104,105,114,115,117,141]. The theoretical community has focused on employing and developing reduced models to understand and describe the dynamics of these complexes [28, 35, 40, 70, 73, 74, 79, 82, 93, 114–122, 124–126, 207, 213]. These models rely on the knowledge of a system Hamiltonian for the interacting chromophores and on spectral densities to describe the coupling of chromophores to their environments (protein, solvent) [198]. Computing a system Hamiltonian or spectral density is an arduous computational task due to the large number of degrees of freedom in these complexes. The most detailed approaches used to obtain these quantities have been mixed quantum mechanics/molecular mechanics (QM/MM) or semi-classical simulations [128, 214]. In particular, one QM/MM approach which has become popular in recent years [25, 33, 103, 104] consists in propagating the nuclei in the electronic ground state of the photosynthetic complex. We employed this approach in Chap. 3 and 5. This approximation ignores the change in electronic structure due to excitation of the chromophores. Subsequently, for a subset of time frames, excited state energies for the chromophores are computed using a quantum method such as time-dependent density functional theory (TDDFT) [25]. The energy trajectories are then employed to extract system-bath correlation functions and finally spectral densities to use in exciton dynamics.

The downside of this approach is the large computational cost. Long equilibration times of several tens of nanoseconds are required for the molecular dynamics (MD) [215, 216]. The typical computational scaling of MD codes with the system size N is $\mathcal{O}(N \cdot \log N)$ [217]. In contrast, TDDFT calculations scale as $\mathcal{O}(N^2)$ [218]. Very often calculations need to be repeated for identical chromophores in similar environments to account for the effect of small variations. For instance in the case of a single-point mutation typically one would need to rerun the entire set of simulations.

---

[i] Florian Häse, **Stéphanie Valleau**, Edward Pyzer-Knapp, and Alán Aspuru-Guzik. Machine Learning Exciton Dynamics. Chemical Science, in press, doi: 10.1039/C5SC04786B (2016)

In this work we propose an alternative route: using multi-layer perceptrons, a special class of neural networks, to predict the excited state along a MD trajectory. Such approaches typically scale as $\mathcal{O}(N)$ and were found to perform significantly faster than TDDFT approaches. As a test system we consider the Fenna-Matthews-Olson (FMO) complex of *P. Aestuarii.* We use multi-layer perceptrons as fully connected neural networks to predict the values of the first singlet excited state for the chromophores. We train the neural networks on the excited state energies obtained from QM/MM calculations. Several sampling methods are used to select the training data for the neural networks. In particular we tested a sampling method based on correlations of nuclear positions to improve the spectral density predictions. Once trained, the neural networks are employed to make excited state energy predictions. Then one can build a Hamiltonian from the predictions and compute the exciton dynamics.

With optimal neural network training and 12 trained neural networks per bacteriochlorophyll (BChl) we predicted excited state energies with errors contained to $0.01\,\text{eV}$ $(0.5\,\%)$ from the neural network ensemble average. Further, with neural networks trained on data based on correlation sampling we correctly determine the shape of the spectral density and observe an error which is squared with respect to the excited state prediction error. This demonstrates the power of machine learning in chemistry, as has also been found in recent work where neural networks were employed to extract other chemical properties [219–223] .

6.2 Methods and computational details

6.2.1 Ground state QM/MM simulations

A semi-classical description of the FMO complex was obtained by combining ground state MD simulations with TDDFT calculations of the first singlet excited state, known as the Q_y state [224], at given molecular conformations along the time-dependent trajectories. The MD runs were carried out using the NAMD software package [188] with the AMBER99 force field (ff99SB) [91]. The BChl-a parameters employed are reported in Ref. [92]. The X-ray crystal structure of the FMO trimer in *P.*

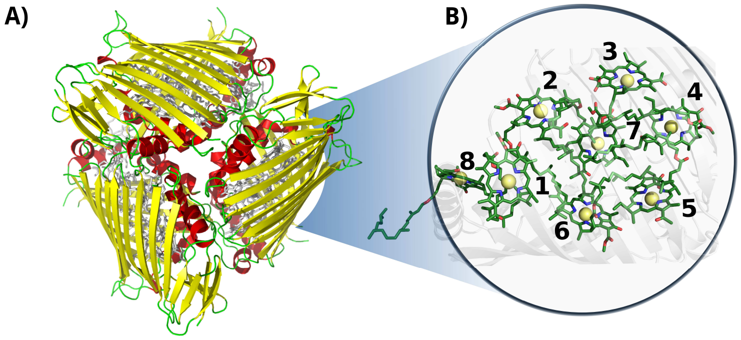

Figure 6.1: Crystal structure of the FMO complex in *P. Aestuarii* (PDB: 3EOJ [87]). Panel **A**) 3EOJ trimer crystal structure. Panel **B**) BChls' geometric arrangement in monomer A (residues 360 to 367, corresponding to sites 1 to 8). Hydrogens are not shown in this representation.

Aestuarii (PDB: 3EOJ [87], see Fig. 6.1) was chosen as initial configuration. The trimer was solvated using a TIP3P water box [225]. The minimum distance between the crystal structure and edges of the solvent box was taken to be $15\,\text{Å}$ [215,216]. The charge was neutralized by adding sodium ions. The total number of atoms in the system was 141624. The simulation was equilibrated for $4\,\text{ns}$ and the production run was $40\,\text{ps}$ long with a $2\,\text{fs}$ time-step. Electrostatic interactions were calculated with the Particle-Mesh Ewald method. Shake constraints were used for all bonds containing hydrogen. Simulations were carried out at $300\,\text{K}$ and 1 atm using a Langevin thermostat and a Langevin piston as implemented in NAMD.

The time-dependent Q_y excited ground state gaps of the BChl-a molecules were obtained using TDDFT with the PBE0 [226] functional within the Tamm-Dancoff approximation (TDA) [227] using Q-Chem [228]. We employed the 3-21G basis set due to the high computational cost of these simulations. The Q_y excited state was taken to be the one with the largest oscillator strength and the orientation of the transition dipole was verified using the same methodology as in Refs. [216] and [229]. Excited state energy trajectories can be downloaded from [230]. Excited state energies were computed at every $4\,\text{fs}$ of the production run. Some values were excluded based on the oscillator strength / angle criterion / failed convergence. The excluded values were at most $2.15\,\%$ of the full trajectory.

6.2.2 Machine Learning: neural networks training

Input data representation

Multi-layer perceptrons (neural networks) were used to predict quantum mechanical excited state energies of BChls in the FMO complex from the MD classical coordinate trajectory. Neural networks were trained in a supervised training scheme using the back propagation algorithm [231]. Excited state energies from the TDDFT calculations described previously were provided to the neural network as targets. BChl conformations were represented by Coulomb matrices as proposed in Ref. [219]. Both, input and target feature distributions, were rescaled to a zero mean and a unitary standard deviation prior to neural network training [232].

By using Coulomb matrices as input features, neural networks can be trained on a representation of BChls which is translation and rotation invariant. Coulomb matrices are particularly suitable to describe BChls in the FMO complex as these molecules do not undergo large conformational changes within time scales of several tens of picoseconds [215,216,221]. Coulomb matrices were adapted to account for external charges within and around the represented BChl. The electrostatic influence of particles in the environment N was described by adding additional Coulomb potential terms to the corresponding Coulomb matrix entries (see Eq. 6.1):

$$M_{ij} = \begin{cases} Z_i^{2.4}/2 + \sum\limits_{n\in N} \frac{Z_i Z_n}{|\vec{r}_i - \vec{r}_n|} & \text{for } i = j, \\ \frac{Z_i Z_j}{|\vec{r}_i - \vec{r}_j|} + \sum\limits_{n\in N} \frac{Z_i Z_n}{|\vec{r}_i - \vec{r}_n|} + \sum\limits_{n\in N} \frac{Z_j Z_n}{|\vec{r}_j - \vec{r}_n|} & \text{for } i \neq j. \end{cases} \tag{6.1}$$

Partial charges Z_i of atoms in the system were taken from the system topology (Amber 99SB force field [91] and Ref. [92]). Studies have shown that the tails of the BChls have little influence on the Q_y excited state energies [216,233]. Thus, instead of representing the entire BChl in a Coulomb matrix, the phytyl tail was neglected and only the 90 atoms closest to the magnesium in the BChls were represented in Coulomb matrices to reduce their dimensionality. We included all external partial charges present in the system to generate Coulomb matrices.

Neural network architecture, choice of BChl molecule and over-fitting

We chose to use multi-layer perceptrons (neural networks) with logistic activation functions and two hidden layers. This set-up has been shown to perform particularly well for supervised regression problems [234]. Optimal neural network hyperparameters were identified from a grid search. Both the learning rate and the number of neurons in the first and second hidden layer were varied to find the lowest deviations between predictions and target data.

Instead of performing the grid search on each BChl in the FMO complex individually, only the most representative BChl was used to determine optimal neural network hyperparameters to reduce the computational cost. We identified this BChl in terms of shared Coulomb matrix space. Coulomb matrices of all eight BChls were clustered and compared. We found that site 3 shares the most Coulomb matrix space with all other sites.

From the grid search, we found that a learning rate of 10^{-4} with 204 neurons in the first hidden layer and 192 neurons in the second hidden layer results in the smallest average absolute deviation of predicted and target excited state energies.

Target feature over-fitting was avoided by using *early stopping* [235]. For all training sessions a total of 4000 trajectory frames was assigned to the training set as a balance between information and computational cost. Neural networks were trained on Intel(R) Xeon(R) CPUs (X5650 @ $2.67\,\mathrm{GHz}$). Training one neural network on four cores took about $(23.9 \pm 5.0)\,\mathrm{h}$.

Reducing training set redundancies through clustering: taxicab, Frobenius and "correlation" clustering

We employed different methods to select Coulomb matrices and corresponding excited state energies for neural network training. In a first approach training set Coulomb matrices were drawn randomly from the entire trajectory as proposed in Ref. [235]. This led to excited state energy predictions with an average accuracy of $13\,\mathrm{meV}$.

However, as BChl conformations in the data set are not uniformly distributed a training set consisting of randomly drawn Coulomb matrices likely contains redundant information. MD simulations were carried out in the NPT ensemble with constant temperature and pressure. Thus, the BChl conformations are sampled from a Boltzmann distribution [236]. To avoid selecting many similar conformations and thus similar Coulomb matrices we performed a cluster analysis on all Coulomb matrices of the entire trajectory to determine the most distinct Coulomb matrices. We implemented a Coulomb matrix cluster algorithm following the principles of the gromos method [237].

Distances between Coulomb matrices were measured using p-norms. Two different metrics were applied: $p = 1$ (taxicab norm) and $p = 2$ (Frobenius norm). Both clustering approaches resulted in more accurate predictions of excited state energies with accuracies of $9\,\mathrm{meV}$ but the prediction of exciton dynamics remained quite inaccurate (see Sec. 6.3.2).

To improve the prediction of exciton dynamics, we developed a clustering method based on coordinate correlations in the classical MD trajectory. We will refer to this approach as the *"correlation"* clustering method. The Q_y state in BChls is mostly distributed along one of the diagonals which connects opposite nitrogen atoms [216]. Training set frames were thus selected based on high correlations in the nitrogen root-mean square deviation (RMSD). In particular, for the n-th BChl we sampled from

$$\left|C_n^{\mathrm{RMSD}}(t)\right|^2 = \left|\left\langle D_n^{\mathrm{Nitrogen}}(t)\;\; D_n^{\mathrm{Nitrogen}}(0)\right\rangle\right|^2 \tag{6.2}$$

until 4000 frames with the largest RMSD correlation were selected.
Here, $\mathrm{D}_n^{\mathrm{Nitrogen}}(t) = \sqrt{\frac{1}{4}\sum_{i=1}^{4}\left\|\vec{r}_{n,i}(t) - \vec{r}_{n,i}(0)\right\|^2}$ refers to the root-mean square difference in position of the four nitrogen atoms in the n-th BChl at time t with respect to their position in the energy minimized crystal structure at time $t = 0$. This sampling led to a more accurate prediction of the spectral density (see Sec. 6.3.2).

6.2.3 Exciton dynamics and spectral densities

To further compare the predicted excited state energy trajectories with the TDDFT trajectories we computed the exciton dynamics in the FMO complex using two different methods. The first is a stochastic integration of the Schrödinger equation as used in Ref. [25]. The second method is the Markov Redfield master equation [63]. Both of the methods are Markovian but the first relies only on the excited state energy trajectories while the latter also depends on the spectral density. Here we focus on the sensitivity of these methods to the changes related to using neural networks rather than to more subtle questions on dynamics such as those addressed by the comparison of Markovian with non Markovian methods.

Finally the spectral density $j(\omega)$, as used in the Redfield equations of motion, is obtained by normalizing the Fourier transform of the two-time correlation function as we discussed in Valleau et al. in Ref. [198]:

$$j(\omega) = \frac{J^{\mathrm{harm}}(\omega)}{\pi} \quad \text{with} \quad J^{\mathrm{harm}}(\omega) = \frac{\beta\hbar\omega}{2}\int_{-\infty}^{\infty} e^{i\omega t} C^{\mathrm{cl}}(t). \tag{6.3}$$

Table 6.1: Time required to compute excited state energies (10000 frames) for all eight bacteriochlorophylls (BChls) for TDDFT (PBE0/3-21G) and neural network (NN) predictions from correlation clustered Coulomb matrices. Reported times include neural network training (t_train) with input ($t_\text{Coul}^\text{input}$) and target feature ($t_\text{E}^\text{target}$) generation, excited state calculations/predictions (t_Calc) and the total time (t_tot). If trained neural networks are available, only Coulomb matrices need to be calculated for neural network predictions, reducing the required time to $48\,\text{h}$. Reported times correspond to training a total of 12 neural networks independently to obtain ensemble averaged excited state energies. All reported times refer to calculations on a single core of an Intel(R) Xeon(R) CPU (X5650 @ $2.67\,\text{GHz}$).

Method	Training time [h]			Calculation [h]	Total [h]
	$t_\text{Coul}^\text{input}$	t_E^target	t_train	t_Calc	t_tot
PBE0/3-21G	-	-	-	480000	480000
NN_Corr	48	192000	9178	< 0.1	201226

The superscript “harm” refers to the harmonic prefactor which is needed to connect the QM/MM results to the open quantum system approach. Here $C^\text{cl}(t)$ denotes the classical correlation function as defined in Ref. [198].

6.3 Results and discussion

6.3.1 Excited state energy prediction using neural networks

Acceleration of excited state energy computations with neural networks

Intel(R) Xeon(R) CPUs (X5650 @ $2.67\,\text{GHz}$) were used to train neural networks and predict excited state energies. A total of 12 neural networks was trained for each of the eight BChls in monomer A of the FMO complex. Predictions of each of the 12 neural networks per BChl were averaged in a neural network ensemble averaging approach to obtain a more accurate prediction for the excited state energy trajectory.

Training sets were generated with all four training set selection methods (see Sec. 6.2.2). Predicting Q_y excited state energies for the entire trajectory (10^4 frames) for one BChl with one neural network took on average $(3.9 \pm 0.8)\,\text{s}$ on one core. In contrast, the quantum chemistry calculations using the TDDFT (PBE0/3-21G) model chemistry required approximately $60000\,\text{h}$ for the entire trajectory on one core. Required calculation times to compute excited state energy trajectories for each of the eight BChls in the FMO complex are reported in Tab. 6.1.

If trained neural networks are available, excited state energies of given BChl conformations can be predicted directly from Coulomb matrices representing the BChl conformations. Thus, to obtain the excited state energies of an entire trajectory consisting of 10000 frames, Coulomb matrices need to be calculated first. With a calculation time of $2.19\,\mathrm{s}$ per Coulomb matrix on one Intel(R) Xeon(R) CPU (X5650 @ $2.67\,\mathrm{GHz}$) core, about $6\,\mathrm{h}$ are needed to compute all 10000 Coulomb matrices. With excited state energy predictions requiring less than a minute, excited state energy trajectories can be obtained from neural networks about four orders of magnitude faster compared to TDDFT calculations.

Accuracy of neural network predictions

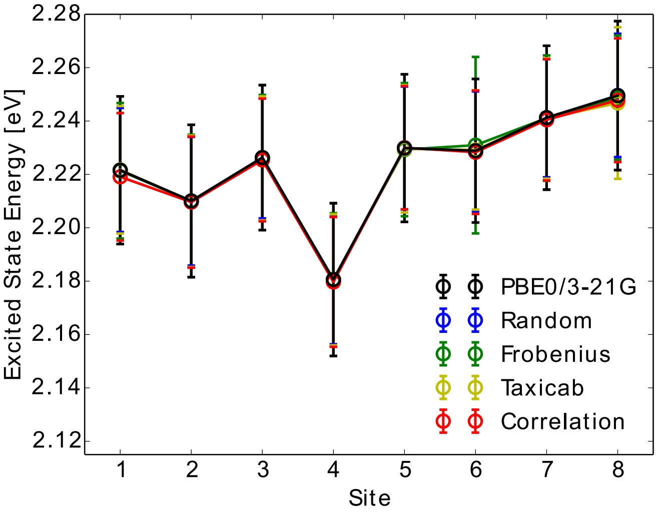

Figure 6.2: Mean and standard deviation of Q_y excited state energy distributions for all eight sites obtained from TDDFT calculations (PBE0/3-21G) and compared to neural network predictions. Neural networks were trained on Coulomb matrices selected from the classical MD trajectory by the indicated selection method. Error bars indicate the width of the excited state energy distribution.

As can be seen in Fig. 6.2 the ensemble average of 12 neural network predictions agrees well with the TDDFT data. Predictions from the average over 12 networks deviate from TDDFT values by $\sim 0.3\,\mathrm{meV}$ regardless of the site and the input selection method. When considering excited state energies predicted from a single network, we observed a deviation of $\sigma_{s,\text{random}}^{\text{single}} < 14\,\mathrm{meV}$ for all sites s when the neural network was trained on randomly drawn Coulomb matrices. This prediction error can be decreased to $\sigma_{\text{s,taxicab}}^{\text{single}} < 9\,\mathrm{meV}$ by selecting the training set based on the Coulomb matrix space clustering taxicab method (see Sec. 6.2.2). Frobenius clustering showed similar deviations. In contrast, predictions from neural networks trained on correlation clustered Coulomb matrices show a slightly higher deviation of $\sigma^{\text{single}}_{\text{s,correlation}} < 15\,\text{meV}$ on average.

Cross-predictions: predicting excited state energies for other bacteriochlorophylls

Since all BChl-a molecules in the FMO complex consist of the same atoms and show similar geometrical conformations, we also used neural networks trained on one BChl to predict excited state energies of other BChls in the same monomer. This enabled us to understand how well the trained network can adapt to changes in the environment from changes in the Coulomb matrices. We observed that for any clustering method, the prediction error is about two times larger when performing this type of cross-prediction, see Fig. 6.3. Nonetheless, as we see in panel a), the largest observed average absolute deviation is still below $1.14\,\%$ (corresponding to $25\,\text{meV}$).

Predicting excited state energies of bacteriochlorophylls in other monomers

All neural networks were trained on BChl-a molecules in monomer A. These neural networks were then used to predict excited state energies of BChls in the other two FMO monomers. Each neural network predicted the excited state energies of the BChl corresponding to the one on which it was trained (i.e. a neural network trained on site 1 in monomer A predicted site 1 in monomer B and C).

Due to the fact that the FMO complex is a homo-trimer, similar BChl conformations should be sampled during the MD simulation in each monomer. Thus, excited state energy averages are expected to be identical for corresponding BChls of different monomers, provided that the same phase space regions were covered in the simulation time. The results are presented in Fig. 6.4. In that figure, we show the time-averaged excited state energy predicted from 12 independently trained neural networks for each monomer as well as the time-averaged Q_y energies obtained from TDDFT for monomer A. The bars represent the spread of the distribution and not an error. The predicted distributions are narrower than the TDDFT distributions. This is probably due to the fact that frames corresponding to energies at the tails of the distribution are less sampled. Regarding the error on the other hand, the largest deviation encountered between mean values of excited state energy distributions is $3\,\text{meV}$.

We have found that trained neural networks can accurately predict TDDFT excited state energies. This allows for a large reduction of computational time. It is possible to train on a single BChl and predict excited state energies of other BChls in the same monomer or in different monomers.

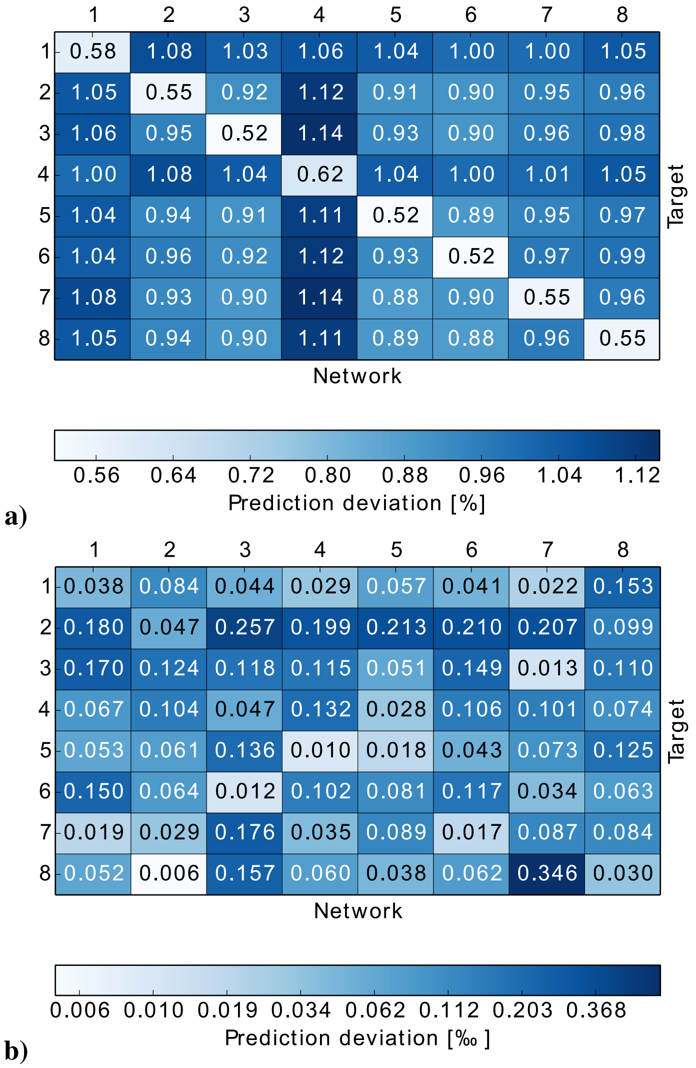

Target \ Network	1	2	3	4	5	6	7	8
1	0.58	1.08	1.03	1.06	1.04	1.00	1.00	1.05
2	1.05	0.55	0.92	1.12	0.91	0.90	0.95	0.96
3	1.06	0.95	0.52	1.14	0.93	0.90	0.96	0.98
4	1.00	1.08	1.04	0.62	1.04	1.00	1.01	1.05
5	1.04	0.94	0.91	1.11	0.52	0.89	0.95	0.97
6	1.04	0.96	0.92	1.12	0.93	0.52	0.97	0.99
7	1.08	0.93	0.90	1.14	0.88	0.90	0.55	0.96
8	1.05	0.94	0.90	1.11	0.89	0.88	0.96	0.55

Target \ Network	1	2	3	4	5	6	7	8
1	0.038	0.084	0.044	0.029	0.057	0.041	0.022	0.153
2	0.180	0.047	0.257	0.199	0.213	0.210	0.207	0.099
3	0.170	0.124	0.118	0.115	0.051	0.149	0.013	0.110
4	0.067	0.104	0.047	0.132	0.028	0.106	0.101	0.074
5	0.053	0.061	0.136	0.010	0.018	0.043	0.073	0.125
6	0.150	0.064	0.012	0.102	0.081	0.117	0.034	0.063
7	0.019	0.029	0.176	0.035	0.089	0.017	0.087	0.084
8	0.052	0.006	0.157	0.060	0.038	0.062	0.346	0.030

Figure 6.3: Relative absolute deviations of predicted excited state energies from TDDFT excited state energies. Neural networks trained on one particular site (indicated by "Network") were used to predict excited state energies of another site (indicated by "Target"). Panel **a)** shows the relative absolute deviation $\bar{\sigma}^{\mathrm{rel}}_{\mathrm{BChl}}$ of predicted excited state energies from TDDFT excited state energies for each BChl, $\bar{\sigma}^{\mathrm{rel}}_{\mathrm{BChl}} = \sum_i |\epsilon^{\mathrm{NN}}_{\mathrm{BChl}}(t_i) - \epsilon^{\mathrm{TDDFT}}_{\mathrm{BChl}}(t_i)| / (N_{\mathrm{frames}} \cdot \langle \epsilon^{\mathrm{TDDFT}}_{\mathrm{BChl}} \rangle)$, in percent. Panel **b)** shows the deviation $\sigma^{\mathrm{mean}}_{\mathrm{BChl}}$ of the mean of the predicted excited state energies from the mean of the TDDFT calculated excited state energies, $\sigma^{\mathrm{BChl}}_{\mathrm{mean}} = |\langle \epsilon^{\mathrm{NN}}_{\mathrm{BChl}} \rangle - \langle \epsilon^{\mathrm{TDDFT}}_{\mathrm{BChl}} \rangle| / \langle \epsilon^{\mathrm{TDDFT}}_{\mathrm{BChl}} \rangle$ in per-thousand.

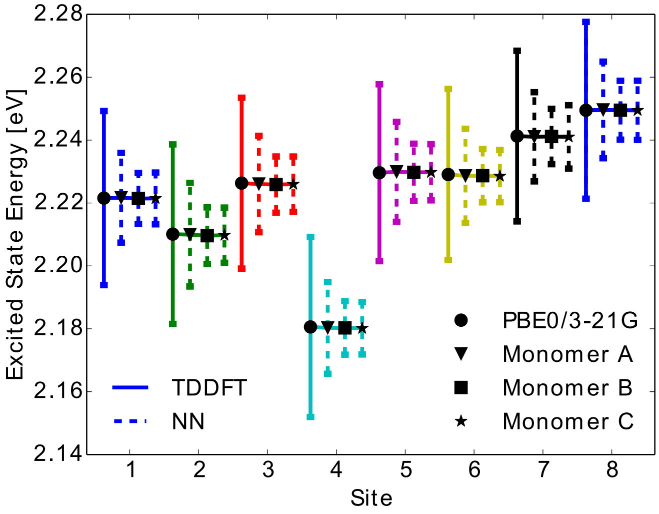

Figure 6.4: Mean and standard deviation of excited state energy distributions for all eight sites obtained using TDDFT PBE0/3-21G (solid line with circle), for monomer A, and using neural network prediction with training on 40% of all Coulomb matrices of monomer A for all three monomers (dashed lines and triangle, square and star symbol for monomers A, B, C). Error bars indicate the standard deviation of the obtained excited state energy distributions.

6.3.2 Spectral densities and exciton dynamics with neural networks

We then used the calculated excited state energy trajectories of all BChls to obtain information about interactions of the BChls with their environment by computing spectral densities. In addition, we built a Hamiltonian to extract the exciton dynamics in the system.

The spectral density $J^{\text{harm}}(\omega)$ (see Eq. 6.3) was computed for all eight sites in the FMO complex from the TDDFT excited state energies and neural network predicted excited state energies [198]. Spectral densities for each site were averaged over all BChls to obtain an averaged spectral density $J_{\text{ave}}(\omega)$. To minimize spurious effects in the Fourier transform, we multiplied the correlation function by a Gaussian of $\sigma^2 = 0.09 \cdot t_{max}^2$ with $t_{max} = 1600\,\text{fs}$ as done in Ref. [198]. The Gaussian is normalized to have unitary area in frequency domain so that in frequency domain this corresponds to a convolution with a Gaussian with a FWHM of $26\,\text{cm}^{-1}$.

In Fig. 6.5 we show the comparison to our neural network prediction with training and prediction on the same site and the various Coulomb matrix selection methods. We found that predicted spectral densities all have a shape which resembles the overall shape of the TDDFT spectral density. However, the height and accurate position of the peaks in the spectral density is most accurately predicted using correlation clustering.

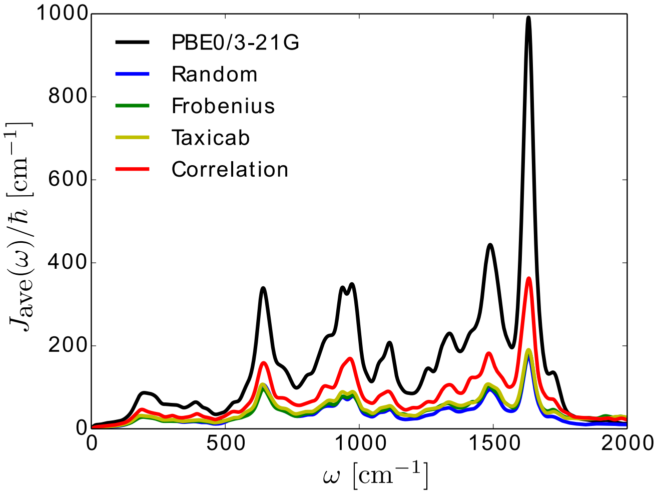

Figure 6.5: Spectral density averages $J_{\mathrm{ave}}(\omega) = \sum_{\mathrm{BChl}} J^{\mathrm{harm}}_{\mathrm{BChl}}(\omega)/N_{\mathrm{BChl}}$. The spectral densities were computed from excited state energy trajectories obtained from TDDFT calculations (PBE0/3-21G) and compared to spectral densities from neural network predicted excited state energy trajectories. Neural networks were trained on the bacteriochlorophyll they predicted with the indicated Coulomb matrix selection method. The correlation method (see Sec. 6.2.2) gives the best prediction.

Table 6.2: We report the percentage deviation of neural network predicted reorganization energies λ_{NN} from TDDFT (PBE0/3-21G) calculated reorganization energies λ_{TDDFT} as $\sigma_\lambda = |\lambda_{\mathrm{TDDFT}} - \lambda_{\mathrm{NN}}|/\lambda_{\mathrm{TDDFT}}$, for each type of initial Coulomb matrix selection. Results are given in percent $\%$.

Method	Random	Frobenius	Taxicab	Correlation
σ_λ [%]	70.0	54.9	53.4	46.6

Average spectral densities were used to calculate the reorganization energy $\lambda = \int_0^\infty J_{\mathrm{ave}}(\omega)/\omega \; d\omega$. Comparisons of reorganization energies are reported in Tab. 6.2. We observe that the smallest deviation between neural network predicted results and TDDFT results occurs for neural networks trained on correlation clustered Coulomb matrices.

We also computed the population dynamics in the FMO complex monomer with a stochastic integration method [25]. We averaged 4000 stochastic trajectories to obtain converged population dynamics. The initial excited site was chosen to be site 1 and the dynamics was propagated for all eight coupled sites at $300\,\mathrm{K}$. The couplings of the Hamiltonian were taken from Ref. [229, 238]. Results are shown in Fig. 6.6. We see that neural network predictions from neural networks trained on randomly drawn and correlation clustered Coulomb matrices predict the exciton dynamics in agreement with TDDFT calculations.

We also employed the Markovian Redfield method to compute the exciton dynamics in the FMO

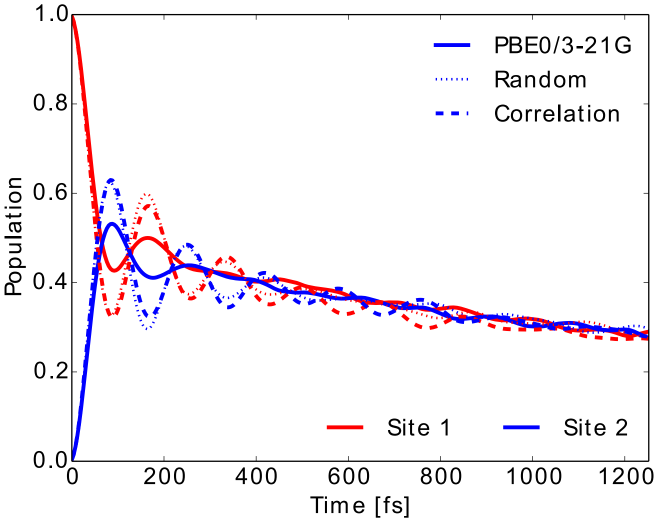

Figure 6.6: Population dynamics of the FMO complex calculated at 300 K with initial state in site 1. Here only two site populations are shown but dynamics was carried out for the 8 BChls. Excited state energy trajectories were obtained from TDDFT calculations (PBE0/3-21G) as well as neural networks trained on randomly drawn and correlation clustered Coulomb matrices.

complex (see Sec. 6.2.3) [63]. In this case there is an explicit dependence of the exciton dynamics on the spectral density. The energies in the Hamiltonian were taken to be the averages from the TDDFT or neural network predicted excited state energy trajectories. The same couplings as for the stochastic integration method were used.

To investigate the importance of excited state energies and spectral densities on the Redfield exciton dynamics we calculated the exciton dynamics in two different ways. First, we computed the exciton dynamics with neural network predicted excited state energies and the average spectral density obtained from TDDFT calculations and then we used the neural network predicted energies as well as the neural network predicted spectral densities. Results are presented in Fig. 6.7 panel a), for predicted excited state energies and TDDFT spectral densities and panel b), for excited state energies and spectral densities predicted by neural networks. We initialized the dynamics with the excitation in BChl 1 and propagated the dynamics for all eight coupled sites at 300 K.

In panel a) we see that given a constant spectral density the error on energies is small and does not strongly influence the exciton dynamics. The main role is played by the spectral density as can be seen in panel b). Here we see much larger differences depending on the neural network sampling method and we notice that the prediction of neural networks trained on correlation clustered Coulomb matrices agrees better with the TDDFT exciton dynamics. Further methods should be

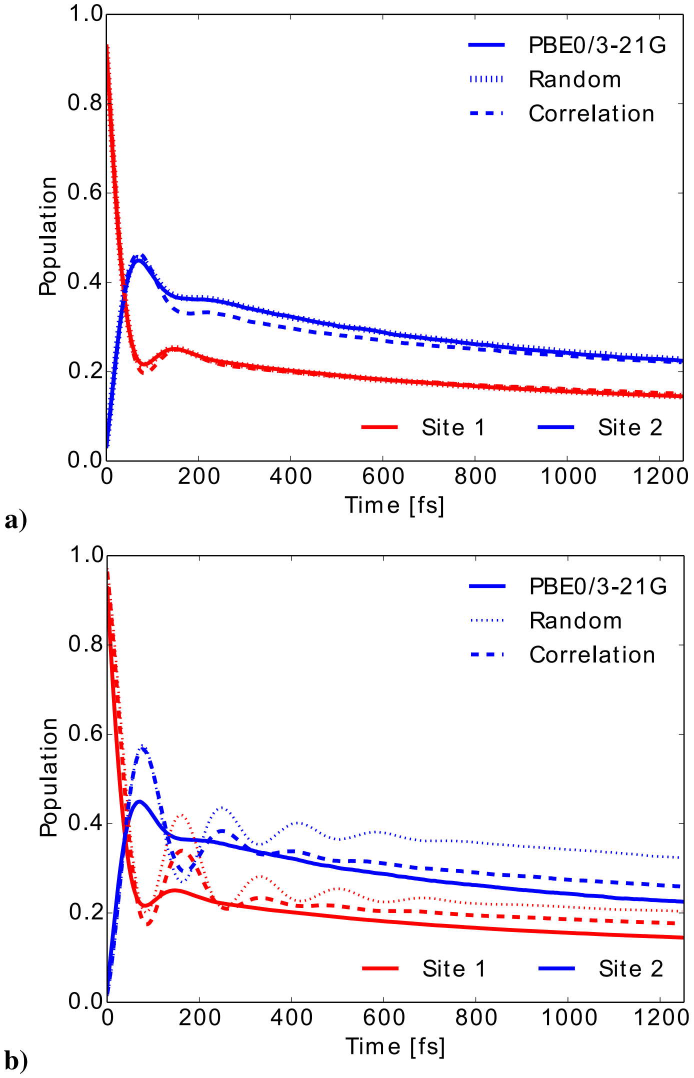

Figure 6.7: Time evolution of the exciton population for BChl 1 (red) and BChl 2 (blue) in the FMO complex calculated from excited state energy trajectories and average spectral densities using the Redfield method. The initial state is site 1 excited. Panel **a**) shows the exciton dynamics for neural network predicted excited state energies using the same TDDFT calculated average spectral density in all cases. Panel **b**) shows the exciton dynamics with both, excited state energy trajectories and harmonic average spectral densities predicted by neural networks trained with the indicated selection method.

investigated to improve the prediction of the spectral density, the error on the energy should be reduced further by an order of magnitude to predict spectral densities with the optimal reorganization energy.

6.4 Conclusion

The computational study presented in this article showed that multi-layer perceptrons (neural networks) can be used to successfully predict excited state energies of BChls in the FMO complex. Using different methods to select a training data set for neural network training we were able to generate neural networks which can predict TDDFT excited state energies with high accuracy (0.01 eV). Furthermore, the neural networks can predict properties such as QM/MM derived spectral densities or exciton population dynamics. The prediction of excited state energies using the neural networks is about seven orders of magnitude faster than TDDFT. If we include training feature generations we still observe a speed-up of about four orders of magnitude. Even if neural networks need to be trained first, excited state energies are obtained in less than half the time needed for TDDFT.

Based on the observations we made on the FMO complex we recommend the following procedure to apply machine learning to predict excited state properties of other systems:

1. Represent all molecules of interest and their chemical environment with Coulomb matrices.
2. Obtain optimal neural network architectures from hyperparameter grid searches. In particular, it is important identify the most representative molecule in terms of the space which contains the features used for neural network predictions.
3. Determine an optimal training set. Training sets for neural networks with optimal network architecture can be generated by selecting Coulomb matrices based on properties which are related to the desired quantum mechanical properties. We observed that selecting Coulomb matrices which represent Coulomb matrix space clusters improves excited state energy predictions. However, these do not necessarily work well for dynamics.
4. Make predictions. To predict spectral densities and exciton dynamics with high accuracy, Coulomb matrices should be selected for the training set if they reveal high excited state energy

> correlations. We found that nitrogen RMSD correlations in the BChls are a good indicator for excited state energy correlations. Thus, we selected Coulomb matrices based on high nitrogen RMSD correlations. Of course this might be complicated for some molecules with very delocalized excited states.

In conclusion, this approach provides a gigantic speedup to ground state QM/MM. From a neural network trained on a single BChl molecule, we can predict the excited states of 23 other molecules in the system at a very low additional computational cost. This enables the simulation of larger and more complex light-harvesting systems. Further, it will be helpful to study, for instance, the role of small changes in the environment, such as a single point mutation, on the exciton dynamics. Questions we would like to address in the future include the possibility of extending the prediction to other temperatures using for example multi-target machine learning.

Part II

Synthetic and model molecular aggregate systems for exciton transport

Page intentionally left blank.

Chapter 7

Exciton transport in thin-film cyanine dye J-aggregates[i]

7.1 Introduction

In organic materials, excitons, quasiparticles of bound electron-hole pairs, act as the intermediates between light (photons) and charge (electrons and hole). Understanding which physical properties make certain molecular aggregates optimal for exciton transfer is one of the main current technological goals in organic materials research. In this chapter, we develop a computational model and employ it to explore excitonic energy transport in a particular class of organic materials: cyanine dye J-aggregates.

Discovered over 50 years ago [41, 42], J-aggregates are typically formed by organic fluorescent dye molecules and can be identified spectroscopically by the narrowing and batochromic shift (J-band) of the lowest electronic excitation relative to the monomer band [43, 44]. These structures are characterized by the unique properties associated with their J-band: a large absorption cross-section, short radiative lifetimes, a small Stokes shift of the fluorescence line and efficient energy transfer within the aggregate [44].

The applications of J-aggregates range from their use as "reporter molecules" in mitochondrial membrane potentials in living cells [45] to photosensitizing silver halides in photography [46]. Moreover, J-aggregates are employed in dye-sensitized organic solar cells which provide several advantages over inorganic solar cells [47, 48]. Recently, cyanine dye J-aggregates have been combined with optical cavities [49–51] or coupled to quantum dots [52] to form hybrid systems. However, the current understanding of exciton transport properties, even for the most ordered J-aggregates, is rather limited. This limitation arises from the challenges encountered in the experimental characterization of their structure [44] and from the lack of information on the dissipation processes involved. In an effort to overcome these difficulties, the aim of our study is to provide a theoretical model, with a minimal number of phenomenological parameters, which is useful for the determination of the J-aggregate structure and able to describe the exciton dynamics in hybrid excitonic-photonic and excitonic-electronic devices.

---

[i] **Stéphanie Valleau**, Semion K. Saikin, Man-Hong Yung and Alán Aspuru Guzik. Exciton transport in thin-film cyanine dye J-aggregates. *Journal of Chemical Physics*, 137, 034109 (2012)

J-aggregates can be found in various structural arrangements including one-dimensional, planar and cylindrical [44] aggregates each exhibiting different optical and exciton energy transfer properties [239–241]. The structure of liquid-crystal cyanine dyes was initially studied using absorption and fluorescence spectroscopy by Scheibe and Kandler [242], and more recently using X-Ray diffraction and NMR by Harrison et al. [243]. Nonetheless, the packing structure of J-aggregates remains unknown [44]. Different theoretical packing models for two-dimensional arrays of these pseudocyanine dye (PIC) aggregates have been proposed by Nakahara and Kuhn [244]. In this study we focus on modeling the exciton transport properties of two-dimensional (2D) thin-films using cyanine dye J-aggregates such as those realized experimentally in Ref. [245]. These highly efficient light absorbing thin-films are employed in various opto-electronic systems for applications such as lasers and optical switches [246, 247]. Exciton dynamics in these films, in general, possesses both ballistic (quantum) and diffusive (classical) regimes and can be analyzed at different levels of approximation.

Experimentally, transport properties, such as exciton diffusion coefficients in organic materials, have been obtained using indirect methods only. These include exciton-exciton annihilation [51, 248, 249], photoluminescence quenching [250, 251], transient grating [252] and photocurrent response [253, 254]. In a recent study by Akselrod et. al. [51] the singlet exciton diffusion length in a 2D cyanine dye film was estimated to be of the order of 50 nm at room temperature which is more than twice larger than the diffusion length measured in standard organic semiconductor films [251] and is comparable to the spatial resolution of the recently developed coherent nanoscopy technique [255].

Theoretically, exciton transport has been studied using a classical hopping model [256]. However, this approach is applicable only in the weak Förster coupling regime [57], where the exciton mobility is low. Beyond this regime, the tight-binding Hamiltonian with classical noise model, proposed in the 70's by Haken, Strobl, and Reineker [68, 69] allows for a unified description of ballistic and diffusive exciton dynamics. For perfect structures with translational symmetry this model can provide analytic solutions for the moments of the exciton wave function [257] that characterize exciton transport.

Variations of this type of analysis have been provided by others [258–260].

In this chapter we introduce a multi-scale computational model to study exciton transport properties in J-aggregates. Within the model the diffusion coefficients are extracted from the finite-time stochastic propagation of the exciton wave function. The molecular properties are computed using density functional theory (DFT), and the coupling to the environment is simulated by adding stochastic noise in the molecular electronic transition frequencies. To illustrate its applicability, we present a detailed study of exciton diffusion in three types of cyanine-dye J-aggregates, namely TC (5,5'-dichloro-3,3'-disulfopropyl thiacyanine), TDBC (5,6-dichloro-2[3-[5,6-dichloro-1-ethyl-3-(3-sulfopropyl)-2(3H)-benzimidazolidene]-1-propenyl]-1-ethyl-3-(3-sulfopropyl) benzimidazolium hydroxide), and U3 (3-[(2Z)-5-chloro-2-[((3E)-3-[5-chloro-3-(3-triethylammonium-sulfonatopropyl)-1,3-benzothiazol-3-ium-2 -yl] methylene-2,5,5-trimethylcyclohex-1-en-1-yl)) methylene]-1,3-benzothiazol-3(2H)-yl] propane-1-sulfonate). While the model doesn't explicitly include the molecular vibronic structure, and fluctuations in the molecule-molecule interaction were not presently accounted for, the computed diffusion coefficient for a TDBC J-aggregate agrees qualitatively with the value measured from exciton-exciton annihilation experiments [51]. The model is flexible and different sources of noise as well as different aggregate geometries or even coupling to optical cavities [49–51] can be incorporated. Our findings indicate anisotropy in the exciton diffusion, the presence of coherent dynamics at times shorter than tens of femtoseconds and finally a dependence of transport on the specific molecular excitation parameters.

The chapter is organized as follows. In Section 7.2, we describe the theoretical model for the exciton dynamics. In particular, we introduce the Hamiltonian of the system and the associated Langevin equation. The static and dynamic noises, which represent different types of disorder present in J-aggregate films, are discussed. The description of the model is completed with a derivation of the diffusion equation. Section 7.3 includes details of the calculation of the Hamiltonian's parameters and also gives an overview of the Monte-Carlo Wave Function method (MCWF) employed in the study of exciton propagation. In Section 7.4 we analyze exciton transport in thin-film J-aggregates of three different cyanine dyes: TC, TDBC, and U3 (structures are shown in Fig. 7.1). We conclude the study by summarizing our results in Section 7.5.

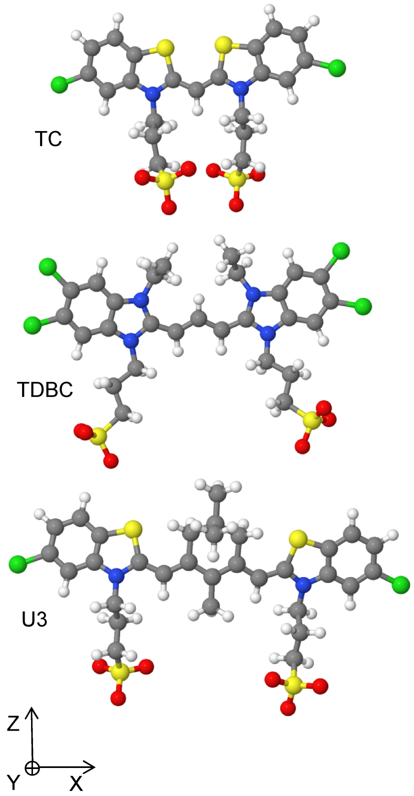

Figure 7.1: Structure of the monomer dye molecules TC, TDBC, and U3 which form the aggregates. The full IUPAC names of the molecules are given in the text.

7.2 The model

7.2.1 Hamiltonian and single exciton dynamics

We apply the general exciton theory developed previously for molecular crystals and molecular aggregates [261] to the specific system - a 2D monolayer J-aggregate of fluorescent dye molecules. The Hamiltonian for a single exciton in a molecular aggregate can be written as

$$\hat{H} = \hat{H}^{\text{el}} + \hat{V}^{\text{el-bath}} + \hat{H}^{\text{bath}}, \tag{7.1}$$

where $\hat{H}^{\text{el}}$ is the system Hamiltonian which includes the electronic degrees of freedom, $\hat{V}^{\text{el-bath}}$ is the system-bath interaction Hamiltonian, and $\hat{H}^{\text{bath}}$ is the bath Hamiltonian which models environmental degrees of freedom. In the site basis the electronic Hamiltonian of an aggregate consisting of

N monomers can be expressed as

$$\hat{H}^{\mathrm{el}} = \sum_{n=1}^{N} \epsilon_n \left|n\right\rangle\!\left\langle n\right| + \frac{1}{2} \sum_{n,m=1}^{N} J_{nm} \left|n\right\rangle\!\left\langle m\right|, \tag{7.2}$$

where ϵ_n are the energies of the electronic excitations at each site n and J_{nm} are the couplings between electronic transitions of monomers at sites n and m. In Eq. 7.2, $|n\rangle = |0...1_n...0\rangle$ corresponds to the state where an exciton is localized at the n-th molecule and all other molecules are in their ground electronic state. In the aggregate, each monomer is modeled as a two level system and the environment is assumed to be a harmonic bath formed by the intra and intermolecular vibrations

$$\hat{H}^{\mathrm{bath}} = \sum_{n} \sum_{q} \omega_q \hat{b}_{qn}^{\dagger} \hat{b}_{qn}, \tag{7.3}$$

where q runs over all vibrational modes and ω_q is the vibrational frequency of mode q, while $\hat{b}_{nq}^{\dagger}$ and $\hat{b}_{nq}$ are the (bosonic) creation and annihilation operators for the bath modes at site n. The system-bath interaction term in the linear coupling limit is

$$\hat{V}^{\mathrm{el-bath}} = \sum_{n} \left|n\right\rangle\!\left\langle n\right| \sum_{q} \kappa_q \left(\hat{b}_{qn}^{\dagger} + \hat{b}_{qn}\right), \tag{7.4}$$

where κ_q is the coupling constant between the $q-th$ vibrational mode and the electronic system, assumed to be equal for all sites.

For singlet exciton transport the major contribution to the J_{nm} coupling terms in Eq. 7.2 is due to the Förster interaction [57]. In practice, numerical calculations of the Förster term can be computationally heavy, especially for large structures. For J-aggregates, where the distance between stacked molecules is comparable to the spatial extent of each molecule, it is possible to use the extended dipole model [262]. Within this model, the Förster interaction between two particular electronic transitions is parametrized by a transition charge, q, and a transition dipole length l. The interaction term can therefore be simplified and written as a sum of Coulomb interactions between the transition charges located on different molecules

$$J_{nm}^{\mathrm{F}} = \frac{q^2}{4\pi\varepsilon_0\varepsilon} \left(\frac{1}{r_{nm}^{++}} + \frac{1}{r_{nm}^{--}} - \frac{1}{r_{nm}^{+-}} - \frac{1}{r_{nm}^{-+}} \right), \tag{7.5}$$

where r_{nm}^{+-} is the distance between the charge $+q$ located on the n-th molecule and the charge $-q$

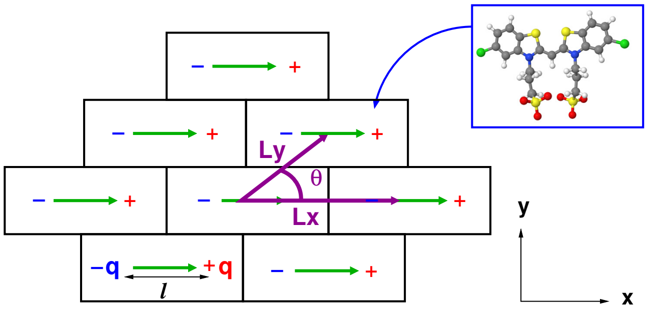

Figure 7.2: Brickstone lattice of a 2D J-aggregate. Each brick represents a molecule. Green arrows indicate extended molecular transition dipoles and l their length. The three lattice parameters are θ, L_x and L_y which can be identified by the lattice vectors $\mathbf{L}_x$ and $\mathbf{L}_y$.

located on the m-th molecule.

Fluorescent dyes may self-aggregate in a number of different structures. When dealing with two dimensional films of cyanine dye aggregates, the brickstone model is one of most commonly employed models which can account for the experimentally observed optical properties of these aggregates. Therefore, in our work, the molecular arrangement within the 2D layer is modeled as a brickstone lattice [263], as shown schematically in Fig. 7.2. In this model, the dye molecules are stacked parallel to each other and subsequent rows are displaced by an angle θ. The lattice is characterized by two lattice vectors $\mathbf{L}_x$ and $\mathbf{L}_y$.

Given the Hamiltonian of the system, we proceed to derive an equation for the quantum evolution of the system's wave function on this lattice. We define a quantum stochastic equation following the Langevin procedure, as described in Ref. [67] as

$$\frac{\partial \left|\psi(t)\right\rangle}{\partial t} = \left(-\frac{i}{\hbar}\hat{H}^{\text{eff}} + \sum_{m,\mu} \eta_m^{\mu}(t)\hat{C}_m^{\mu}\right)\left|\psi(t)\right\rangle, \tag{7.6}$$

where the effective Hamiltonian $\hat{H}^{\text{eff}} = \hat{H}^{\text{el}} - \frac{i\hbar}{2}\sum_{m,\mu}\left(\hat{C}_m^{\mu}\right)^{\dagger}\hat{C}_m^{\mu}$ includes a decay term and a stochastic fluctuation term $\eta_m^{\mu}(t)$ for site m and channel μ which represents a dynamic noise force and is introduced to conserve the norm of the wave function. The $\hat{C}_m^{\mu}$ are Lindblad operators for two channels $\mu \in \{\wr, \phi\}$ (relaxation or dephasing) for each site m. These channels allow the initially excited exciton state to eventually decay back to the ground state due to interaction with the environment. These terms can be expressed as

$$\begin{aligned}\hat{C}_m^{\wr} &= \sqrt{\Gamma_m^{\wr}}\, |0\rangle\langle m| \\ \hat{C}_m^{\phi} &= \sqrt{\Gamma_m^{\phi}} \left(\sum_{k \neq m} |k\rangle\langle k| - |m\rangle\langle m| \right),\end{aligned} \tag{7.7}$$

where $\hat{C}_m^{\wr}$ describes single exciton relaxation and $\hat{C}_m^{\phi}$ is introduced for dephasing processes, which are associated with the relaxation $\Gamma_m^{\wr}$ and dephasing Γ_m^{ϕ} rates. The states $|m\rangle$ span over the single exciton manifold, and the state $|0\rangle$ denotes the ground state, where no exciton is present. The relaxation and dephasing rates are taken to be equal for all sites $\Gamma^{\wr} = \Gamma_m^{\wr}$ and $\Gamma^{\phi} = \Gamma_m^{\phi}$, because the aggregate is constructed of identical molecules which are assumed to be in identical local environments. It is easy to see that with the noise operators written in the site basis this model is equivalent to the Haken, Strobl and Reineker model [68].

7.2.2 Static and dynamic noise

The environmental noise can be introduced into this J-aggregate model as fluctuations of site energies and of the site-to-site couplings as well as a term which induces exciton relaxation. When studying transport properties within the single exciton manifold, one is mostly interested in the dynamics occurring on a timescale sufficiently shorter than the exciton relaxation time, this corresponds to saying that over the time scale of the dynamics, in Eq. 10, $\hat{C}_m^{\wr} \sim 0$. Moreover, in the provided examples we do not consider fluctuations of intermolecular interactions. These fluctuations can give a noticeable contribution to the transport properties [258] and can easily be included in the model. However we have chosen to neglect them since no experimental data is currently available to estimate relative contributions of site energy fluctuations and fluctuations in the couplings.

We introduce the standard distinction between static and dynamic noise based on the correlation time characterizing the fluctuations as compared to the exciton propagation time. Static noise is associated with fluctuations in site energies which are correlated for long time respect to the lifetime of the exciton, while dynamic noise is associated to instantaneous fluctuations in the site energies respect to the lifetime.

Static noise can be accounted for in the Hamiltonian, Eq. 7.2, by introducing random shifts in the site energies. In our model, we extract the random shifts from a Gaussian distribution

$$f\left(\epsilon_n-\epsilon_0\right)=\frac{1}{\sqrt{2\pi\sigma^2}}e^{-(\epsilon_n-\epsilon_0)^2/2\sigma^2} \tag{7.8}$$

where σ is the variance, and ϵ_0 is the transition energy of each isolated molecule. The static noise distribution is assumed to be identical for all monomers. Other choices of static disorder models are possible. For instance, a more general Levy distribution can be used, which results in different state distributions and optical properties [264].

Dynamic noise directly enters the Schrödinger-Langevin equation, Eq. 7.6, described in the previous section. The stochastic force $\eta(t)$, which is a result of multiple uncorrelated microscopic movements of the molecules constituting the aggregate lattice, does not have memory, i.e., $\langle\eta(t)\eta(t')\rangle \propto \Gamma^{\phi}\delta(t-t')$. This corresponds to the Markov approximation, in the sense that the system-bath interaction is assumed to be quasi instantaneous and successive interaction events are not correlated. In general, the Markov approximation holds, as long as the bath correlation time is much smaller than the time over which one extracts properties of the system. Therefore it is only necessary that the bath correlator be sharply peaked [67]. Within this argumentation, the dynamic noise can be characterized by a single parameter Γ^{ϕ}, which describes both the bath dynamics and the system-bath coupling. While avoiding a detailed description of the specific environment of a J-aggregate we can make a rather qualitative assumption that Γ^{ϕ} is of the order of k_BT. Such assumption is not strictly justified but can be intuitively explained as following.

If we assume that the bath modes can be modeled as a set of harmonic oscillators, we can define, within linear response theory, a system bath interaction term linear in the displacement of the bath modes. It follows that the bath correlator can be expressed as [63]

$$\begin{aligned}\langle\eta(\tau)\eta(0)\rangle &= \sum_q |\kappa_q|^2\left\langle\left(\hat{b}_q^{\dagger}(\tau)+\hat{b}_q(\tau)\right)\left(\hat{b}_q^{\dagger}(0)+\hat{b}_q(0)\right)\right\rangle \\ &= \int d\omega J\left(\omega\right)\left[\coth\left(\frac{\hbar\omega\beta}{2}\right)\cos\left(\omega\tau\right)-i\sin\left(\omega\tau\right)\right]\end{aligned} \tag{7.9}$$

where the bath operators are given in the interaction picture and we have assumed that the noise correlator is the same for all sites and that each bath is uncorrelated from that of other sites. The second line corresponds to the approximation of a continuous bath spectrum with a spectral density $J(\omega)$. Such approximation provides a qualitative correspondence between the temperature and the dynamic noise in the system. In general, a more quantitative analysis should include explicitly the bath vibrational modes. By using the continuous limit of the spectral density we intentionally simplified the model making it independent of the specific molecular vibrational modes. Several forms of bath spectral densities are used for modeling dissipative quantum dynamics in molecular aggregates [90, 265]. We choose to employ the Ohmic exponentially cutoff spectral density $J(\omega) = \frac{\lambda}{\hbar\omega_c}\omega e^{-\frac{\omega}{\omega_c}}$ where λ is the reorganization energy and ω_c is the cutoff frequency. In our model, the correlator in Eq. 7.9 can only be used in the limit where the time dependent characteristics of exciton dynamics remain steady on timescales sufficiently longer than the bath correlation time. In this case, the temperature-dependent dephasing rate can be defined as [22]

$$\Gamma^{\phi} = 2\pi\frac{k_B T}{\hbar}\frac{\lambda}{\hbar\omega_c}, \tag{7.10}$$

where physical properties of the bath and the system-bath coupling are introduced through the slope of the spectral density at zero frequency $\frac{dJ(\omega)}{d\omega}|_{\omega=0} = \frac{\lambda}{\hbar\omega_c}$ (Ref. [90]). Eq. 7.10 is strictly valid for $T \gg \frac{\hbar\omega_c}{k_B}$ (Ref. [34]). If we use values of $\omega_c = 150\,\mathrm{cm}^{-1}$ and $\lambda = 35\,\mathrm{cm}^{-1}$, typical for the analysis of quantum dynamics in photosynthetic systems [73, 74], the dephasing rate $\Gamma^{\phi} \approx 1.4 k_B T$. The reorganization energy of J-aggregates is comparable to this value, for instance, $\lambda_{\mathrm{TDBC}} = 29\,\mathrm{cm}^{-1}$ (Ref. [266]). By setting $\Gamma^{\phi} = k_B T$ we choose a lower bound for the exciton dephasing rates. For room temperature we thus have $\Gamma^{\phi} \approx 26\,\mathrm{meV}$. In reality, there may be more sources of dissipation, and different estimates for the bath spectral density [90, 107] can give values of the dephasing rate, Γ^{ϕ} which are several times larger than the value we use.

7.2.3 Diffusion model

In this section, we consider methods for calculating the diffusion constant D from the transport properties of the excitonic system. For classical Brownian motion, it is well-known that the diffusion constant is related to the long-time limit of the second moment $\left\langle (\mathbf{r}(t) - \mathbf{r}_0)^2 \right\rangle$ evaluated for the initial condition where the particle is localized at a single point $\mathbf{r}_0$ in space. Explicitly, it is given by

$$D = \lim_{t\to\infty} \frac{1}{2\,d\,t} \left\langle (\mathbf{r}(t) - \mathbf{r}_0)^2 \right\rangle, \tag{7.11}$$

where d is the dimension of the space. For excitonic systems, in the first place, we will not assume that exciton motion can be described as the motion of classical Brownian particles. Here our goal is to show that the above relationship (Eq. 7.11) holds even for excitonic systems where a fully quantum mechanical treatment is assumed.

To get started, we consider a dilute system of excitons where their reciprocal interaction can be ignored. We will trace the motion of a "tagged" exciton. The probability $P(\mathbf{r}, t)$ of finding that exciton at location $\mathbf{r}$ and time t is given by $P(\mathbf{r}, t) = \mathrm{Tr}[|\mathbf{r}\rangle\langle\mathbf{r}|\hat{\rho}(t)]$, where $\hat{\rho}(t)$ is the density matrix of the total system (i.e. exciton plus the bath) at time t. Using the following identity

$$|\mathbf{r}\rangle\langle\mathbf{r}| = \frac{1}{(2\pi)^d}\int_{-\infty}^{\infty} d\mathbf{k} e^{-i\mathbf{k}\cdot(\hat{\mathbf{r}}-\mathbf{r})}, \tag{7.12}$$

where d is the dimension, and $\hat{\mathbf{r}} \equiv \sum_{\mathbf{r}'} \mathbf{r}'|\mathbf{r}'\rangle\langle\mathbf{r}'|$ is the position operator for the exciton, we write the probability of finding the exciton as

$$P(\mathbf{r}, t) = \frac{1}{(2\pi)^d}\int_{-\infty}^{\infty} d\mathbf{k}\mathrm{e}^{\mathrm{i}\mathbf{k}\cdot\mathbf{r}}\widetilde{P}_k(t), \tag{7.13}$$

where $\widetilde{P}_k(t) \equiv \mathrm{Tr}[e^{-i\mathbf{k}\cdot\hat{\mathbf{r}}(t)}\hat{\rho}(0)]$, $\hat{\mathbf{r}}(t) \equiv \hat{U}^{\dagger}(t)\hat{\mathbf{r}}\hat{U}(t)$, where $\hat{U}(t) = e^{-i\hat{H}t}$ and $\hat{H}$ is defined in Eq. 7.1.

Since we are considering the fluctuations of the exciton in some steady-state (long-time $t \to \infty$) limit, measurable physical quantities, including the diffusion constant, should not depend on the initial condition. We can therefore choose the following initial state $\hat{\rho}(0) = \hat{\mathbb{I}}_S \otimes \hat{\rho}_B / \mathrm{Tr}\left(\hat{\mathbb{I}}_S\right)$, where $\hat{\mathbb{I}}_S$ is the identity matrix for the system, i.e. the exciton, and $\hat{\rho}_B = e^{-\beta\hat{H}^{\mathrm{bath}}}/\mathrm{Tr}\left(e^{-\beta\hat{H}^{\mathrm{bath}}}\right)$ is the density matrix of the bath, which is assumed to be in thermal equilibrium. Now, inserting the resolution of the identity, $\hat{\mathbb{I}}_S = \sum_{\mathbf{r}_0}|\mathbf{r}_0\rangle\langle\mathbf{r}_0|$, we can write $\widetilde{P}_k(t) = \left(1/\mathrm{tr}\left(\hat{\mathbb{I}}_S\right)\right)\sum_{\mathbf{r_0}} e^{-i\mathbf{k}\cdot\mathbf{r_0}}\mathrm{Tr}[e^{-i\mathbf{k}\cdot\Delta\hat{\mathbf{r}}(t)}|\mathbf{r}_0\rangle\langle\mathbf{r}_0| \otimes \hat{\rho}_B]$, where $\Delta\hat{\mathbf{r}}(t) \equiv \hat{\mathbf{r}}(t) - \mathbf{r}_0$. Performing the cumulant expansion [67] and keeping terms up to the second-order, we obtain

$$\widetilde{P}_k(t) \approx \frac{1}{\mathrm{tr}(\hat{\mathbb{I}}_S)}\sum_{\mathbf{r_0}} e^{-i\mathbf{k}\cdot\mathbf{r_0}} e^{-(1/2)\langle[\mathbf{k}\cdot\Delta\hat{\mathbf{r}}(t)]^2\rangle_0} \tag{7.14}$$

where $\langle[\mathbf{k}\cdot\Delta\hat{\mathbf{r}}(t)]^2\rangle_0 \equiv \mathrm{Tr}\{[\mathbf{k}\cdot\Delta\hat{\mathbf{r}}(t)]^2|\mathbf{r}_0\rangle\langle\mathbf{r}_0|\otimes\rho_B\}$. Then, we arrive at the diffusion equation

$$\frac{\partial}{\partial t}P(\mathbf{r},t) \approx \sum_{i,j\epsilon\{x,y,z\}} D_{ij}(t)\frac{\partial^2}{\partial r_i \partial r_j}P(\mathbf{r},t)\,, \tag{7.15}$$

where

$$D_{ij}(t) \equiv \frac{1}{2}\frac{d}{dt}\langle\Delta\hat{r}_i(t)\Delta\hat{r}_j(t)\rangle \equiv \frac{1}{2}\frac{d}{dt}M^{(2)}_{ij}(t) \tag{7.16}$$

is the time-dependent tensor of the diffusion coefficients. Here we have defined the second moments $M^{(2)}_{ij}(t) \equiv \langle\Delta\hat{r}_i(t)\Delta\hat{r}_j(t)\rangle$. In order for the diffusion coefficients $D_{ij}(t)$ to converge in the long time limit ($t \to \infty$), the right-hand side of Eq. 7.16 should scale at most linearly in t. This result coincides with that in Eq. 7.11, which is a special case of isotropic diffusion.

7.3 Computational details

7.3.1 Monomer properties

Density-functional calculations of the molecular structure and electronic excitation spectra were performed with the quantum-chemistry package Turbomole, version 5.10. (Ref. [267]). Triple-ζ valence-polarization basis sets (def2-TZVP [268]) were used together with the hybrid functional of Perdew, Burke, and Ernzerhof (PBE0) [226]. Dielectric properties of the medium where accounted for by using COSMO [269] as implemented in Turbomole.

To calculate the extended dipole parameters of the fluorescent dyes, the HOMO and LUMO orbitals of the molecules were computed on a homogeneous spatial grid. The grid steps are $dx = 0.5\,\text{Å}$, $dz = 0.5\,\text{Å}$ in the plane of the molecular backbone, and $dy = 0.25\,\text{Å}$ in the direction orthogonal to the backbone. The Förster [57], and the Dexter [270] interactions between pairs of molecules were calculated for center-to-center displacements scanned over $x = [-60, 60]\,\text{Å}$ and $y = [-10, 10]\,\text{Å}$ with step size $\Delta x = \Delta y = 0.5\,\text{Å}$.

7.3.2 Monte Carlo wave function propagation

Eq. 7.6 is a Markovian stochastic open quantum system equation, which is equivalent to a Lindblad master equation for the density matrix [67]. As such one can evolve single stochastic eigenfunction

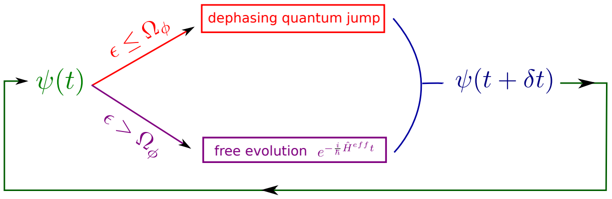
dephasing quantum jump
$\epsilon \leq \Omega_\phi$
$\psi(t)$
$\epsilon > \Omega_\phi$
free evolution $e^{-\frac{i}{\hbar}\hat{H}^{eff}t}$
$\psi(t+\delta t)$

Figure 7.3: Monte Carlo Wavefunction stochastic dephasing jump evolution. Each stochastic trajectory $\psi(t)$ will evolve either by making a dephasing quantum jump or according to a non-Hermitian effective Hamiltonian $\hat{H}^{\text{eff}}$. The choice of making a dephasing jump is determined by a Monte-Carlo type algorithm, where one extracts a random number ϵ and compares it to the dephasing jump probability Ω_ϕ. The procedure is repeated up to the final propagation time. One then repeats the procedure to obtain an ensemble of trajectories and average over this ensemble to obtain the desired observables.

trajectories instead of the full density matrix, using the Markov Monte-Carlo wave function method [271].

The initial wavefunction $|\psi(0)\rangle = |00...1....0\rangle$ is defined as an exciton localized at the center of the lattice (i.e., in the position $\left[\frac{n_x}{2};\frac{n_y}{2}\right]$). At time $t+\delta t$, $|\psi(t+\delta t)\rangle$ can be obtained from $|\psi(t)\rangle$ according to the stochastic scheme depicted in Fig. 7.3. In particular, at each time step, if the stochastic variable extracted, $\mathcal{E}$, is larger than the quantum dephasing jump probability Ω_ϕ, the wavefunction will propagate freely under the non-Hermitian effective Hamiltonian $\hat{H}^{\text{eff}}$ introduced in Eq. 7.6

$$|\psi(t+\delta t)\rangle = \frac{1}{\sqrt{\mathcal{N}}}\left(1 - \frac{i\hat{H}^{\text{eff}}\delta t}{\hbar}\right)|\psi(t)\rangle\,, \tag{7.17}$$

where $\mathcal{N} = \sqrt{\langle\psi(t+\delta t)|\psi(t+\delta t)\rangle}$ is the normalization constant. However, if ϵ is smaller than Ω_ϕ, a quantum dephasing jump will occur. The quantum dephasing jump, a specific type of quantum jump, is described as a flip of the sign of wavefunction's coefficient corresponding to a site m and corresponds to applying the dephasing jump operator $\hat{C}^{\phi}_{m}$, Eq. 7.7, to the wavefunction [271]. The phase jump occurs in position $N = \text{round}(\frac{\epsilon}{\Omega_\phi} n_x n_y)$ where Ω_ϕ is defined as $\Omega_\phi = \frac{\delta t}{2}\Gamma^{\phi} n_x n_y$, and where Γ^{ϕ} was given in Eq. 7.10, while δt is the time step which is assumed to be small enough so that $\Omega_\phi \ll 1$. For the trajectories controlled by exciton dephasing only, the effective Hamiltonian $\hat{H}^{\text{eff}}$ is the same as $\hat{H}_0$, thus the norm of the wavefunction in Eq. 7.17 is conserved.

To analyze the exciton transport properties of TC, TDBC and U3 aggregates the exciton wavefunction was propagated on a lattice of 2601 monomers ($n_x = n_y = 51$) for a total time of $t = 100\,\text{fs}$. The quantum trajectories were averaged over 1000 different realizations of static disorder (convergence on the populations was reached with 1000 realizations within an error $\leq 4\%$). The averaging over static disorder and realizations of quantum jumps were combined in such a way that for each quantum trajectory we introduced a unique realization of the static disorder and a unique sequence of quantum jumps. This procedure is applicable as long as both disorders are not correlated and could be consider in analogy with the Monte-Carlo integration of a multi-dimensional function. It should be noticed that the obtained results characterize an inhomogeneous ensemble of quantum systems averaged over multiple disorder realizations. The time step in the propagation was set to $\delta t = 0.6\,\mathrm{as}$ thus the probability of the quantum jump within the step is sufficiently smaller than 1, and the wave function was collected at each femtosecond. The long range interaction between the molecules was accounted for within the cutoff distance $l_{\mathrm{cutoff}} = 6 \cdot L_x$, more details about this cutoff can be found in Section 7.4.1. At the initial time the exciton was localized on the central site (26,26) of the lattice. The energy of this site can be varied to study the dependence of the exciton dynamics on the initial conditions. The results were obtained in general over the range $\Gamma^{\phi} = 20 - 110\,\mathrm{meV}$ and $\sigma = 0 - 110\,\mathrm{meV}$. Exciton diffusion coefficients where estimated from a linear fit of the second moments of the exciton distribution functions $M_{ii}^{(2)}$, as per Eq. 7.16. A flow-chart, summarizing this procedure is given in Fig.7.4

7.4 Results and discussion

7.4.1 Model parameters

Monomer calculations and absorption spectra

The structures of the TC, TDBC, and U3 cyanine dye molecules have been optimized using DFT. In the computation, we considered single-charged anions and assumed that the Na^{+} ions were dissociated. For each molecule, although the conjugated part of the structures remain almost planar, there are many conformations which differ slightly by the orientations of the sulphonated group side chains and are all closely spaced in energy. Examples of such conformations for the *cis*-isomers are shown in Fig. 7.1. It should be noted that the computed spectra reflect pure electronic transitions and do not include vibronic components. The difference between the ground-state energies of *cis* and *trans*-isomers of the molecules is of the order of hundreds of meV. We have chosen cis-isomers as our reference structure because it is most likely that in this conformation, with the sulphonate groups pointing towards the surface and binding chemically or physically to it, that one would obtain the

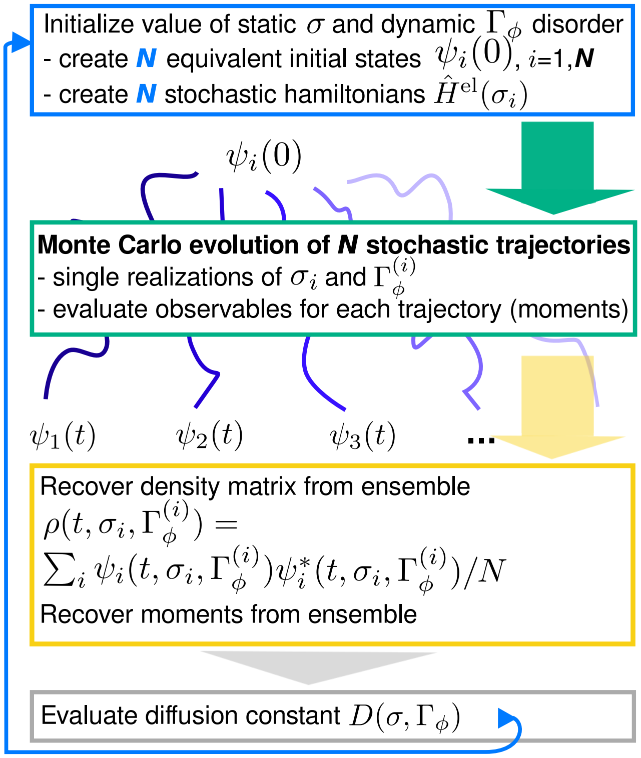
Initialize value of static σ and dynamic Γ_ϕ disorder
- create **N** equivalent initial states $\psi_i(0)$, i=1,**N**
- create **N** stochastic hamiltonians $\hat{H}^{\mathrm{el}}(\sigma_i)$
$\psi_i(0)$
Monte Carlo evolution of N stochastic trajectories
- single realizations of σ_i and $\Gamma_\phi^{(i)}$
- evaluate observables for each trajectory (moments)
$\psi_1(t)$
$\psi_2(t)$
$\psi_3(t)$
...
Recover density matrix from ensemble
$\rho(t,\sigma_i,\Gamma_\phi^{(i)}) =$
$\sum_i \psi_i(t,\sigma_i,\Gamma_\phi^{(i)})\psi_i^*(t,\sigma_i,\Gamma_\phi^{(i)})/N$
Recover moments from ensemble
Evaluate diffusion constant $D(\sigma,\Gamma_\phi)$

Figure 7.4: Flow chart summarizing the procedure employed to obtain the system density matrix and the diffusion constant. One first generates N copies of the initial state and N stochastic realizations of the Hamiltonian with diagonal energies σ_i taken from the Gaussian distribution centered around σ. The Monte Carlo evolution of the trajectories follows as in Fig. 7.3. Then one averages over both disorders to obtain the wavefunction.

observed 2D monolayers [245]. For each optimized molecular structure, we have computed the 100 lowest electronic excitations which fall in the energy range 2-7 eV. The computed spectra of the molecules shown in Fig. 7.1 are provided in Fig. 7.5. The strong lowest excitation can be accounted for by the HOMO to LUMO transition for more than 98%. Such transition is generally assigned to the lowest absorption peak observed in the monomer spectra of fluorescent dyes. The second electronic transition is separated from the lowest one by about 0.7 eV, 1.0 eV, and 1.4 eV for TC, TDBC and U3 respectively. Moreover, the oscillator strengths of these subsequent transitions are about two orders of magnitude smaller than that of the lowest one. These results support the two-level model provided that the static energy disorder is of the order of 100 meV. The computed frequencies of the lowest electronic transitions are systematically blue-shifted by about several hundreds of meV as compared to the experimental values. This shift typically occurs in DFT calculations with the PBE0 functional [218]. Similarly to what was found for the ground state energies, the lowest electron transition frequencies for *trans* and *cis*-isomers differ by hundreds of meV's. The high frequency part of the computed spectrum shows multiple electronic states with about double the exciton energy. These states may be involved in the exciton-exciton annihilation process [51].

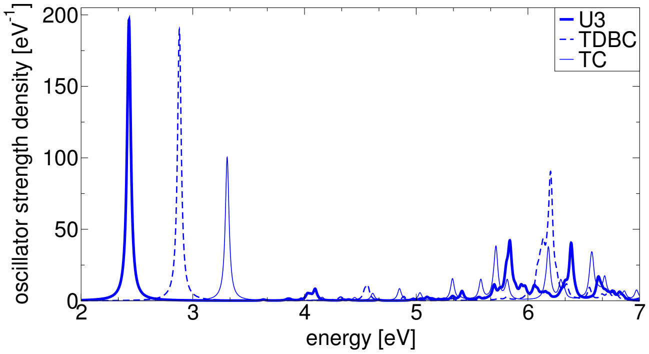

Figure 7.5: Computed spectra of electronic excitations in TC, TDBC, and U3 *cis*-isomers. The lines are broadened with Lorentzians of 20 meV linewidth.

Couplings

The extended dipole parameters for the lowest electronic excitation are calculated within the Frontier Orbital Approximation (FAO) [272], in which one assumes that only the HOMO-LUMO transition gives a significant contribution. To obtain the l and q parameters in the extended dipole coupling formula Eq. 7.5, we assume that the only type of interaction involved is Förster interaction [57]

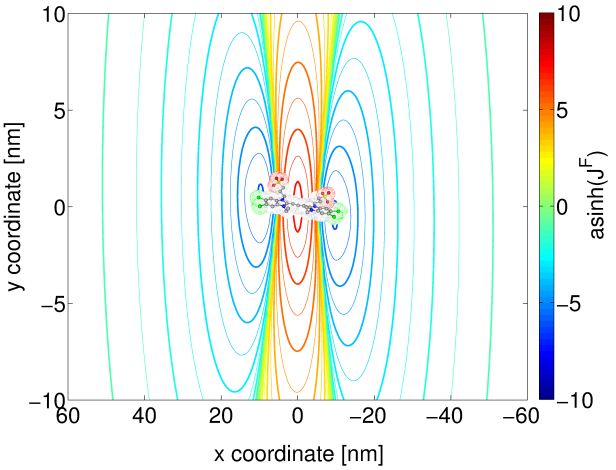

Figure 7.6: 2D map of the Förster interaction between two TDBC molecules. The axes show center-to-center displacement of the molecules. The inset figure shows the orientation of the molecules in the plane. The color map represents asinh(J^{F}) to emphasize the long-range behaviour of the interaction. The blue-green colors define the negative frequency shift of the lowest electronic excitation, while the yellow-red colors indicate the positive shift.

Table 7.1: Computed excitation properties of fluorescent dye molecules. Ω is the frequency of the electronic excitation, μ is the transition dipole associated with the transition computed using TDDFT, μ_{HL} is the transition dipole computed using HOMO-LUMO orbitals only, l is the length of the extended dipole, and q is the charge associated with the extended dipole.

Dye	Ω[eV]	μ[D]	μ_{HL} [D]	l [Å]	q [e]
TC	3.3	8.9	8.3	9.1	0.20
TDBC	2.9	13.1	11.0	10.5	0.22
U3	2.4	14.6	12.5	11.1	0.24

and fit the interaction between two molecules on the $x - y$ plane to the Förster results. An example of the calculated interaction contour plot for a pair of TDBC molecules is shown in Fig. 7.6. For intermolecular distances larger than 2 Å, the profile reproduces the interaction of two dipoles and can easily be fitted with the extended dipole formula. The largest positive shift of the electron transition is obtained when the molecules are displaced along the y-axis (direction orthogonal to the backbone of the molecules). The largest negative shift of the electron transition corresponds to the case when molecules are displaced along the x-axis approximately by half of their length. These results are consistent with the extended dipole model. The computed properties of TC, TDBC, and U3 monomers are summarized in Table 7.1. We also computed Dexter couplings and these were much smaller than the corresponding Förster terms for distances of the order of the physical spacing between molecules and were therefore neglected.

Lattice parameters and absorption spectra

The brickstone lattice parameters where determined as following. The horizontal distance between monomers $L_x = |\mathbf{L}_x|$ was chosen to be the optimized length of the molecule in the *cis*-geometry l_0^{cis} plus twice the Van der Waals radius of the chlorine atom. In particular we chose the longitudinal Van der Waals radius determined for a C-Cl type bond $r_{\mathrm{Cl}} = 1.58\,\text{Å}$, as reported in Table 11 of Ref. [273]. The angle between monomers was set to $\theta = \tan^{-1}\left(\frac{2L_y}{L_x}\right)$. Having fixed θ and L_x we then determined the vertical distance between layers of monomers $L_y{\cdot}\sin\theta$ by fitting the theoretical position of the J-band in the absorption spectra to the experimental result. All of these parameters are reported in Table 7.2

Table 7.2: Lattice parameters for the three molecules. l_0^{cis} is obtained from the DFT optimization of the molecular structure, L_y parameters were obtained from fitting the theoretical spectrum to the experimental J-band shift.

Dye	$l_0^{cis}\left[\text{Å}\right]$	$L_x\left[\text{Å}\right]$	$L_y{\cdot}\sin\theta\left[\text{Å}\right]$	$\theta\,[\mathrm{rad}]$
TC	15.01	18.17	3.815	0.421
TDBC	17.36	20.52	4.600	0.404
U3	19.72	22.88	5.120	0.427

The measured energies of the lowest electronic transitions for TC, TDBC and U3 dyes in solution and also in the aggregated form are collected in Table 7.3.

Table 7.3: Experimental data for electronic excitations in monomer and J-aggregated dyes as well as the energy shift Δ between monomer and J-band.

Dye	Monomer transition [eV]	J-band [eV]	Δ [eV]	Ref.
TC	2.900	2.613	0.287	[274]
TDBC	2.396	2.115	0.281	[275]
U3	1.864	1.571	0.293	[276]

To estimate the shifts of the J-band due to the molecular aggregation the excitonic spectra of the aggregates have been computed by diagonalizing the Hamiltonian, Eq. 7.2, for all three dyes. The oscillator strength of a particular transition is proportional to the square of the corresponding transition dipole. To account for the static disorder the transition frequencies of the monomers were taken from a Gaussian distribution of width $70\,\mathrm{meV}$. In Fig. 7.7 the calculated spectra of J-aggregates are shown as compared to the energies of single molecule excitations. The peak positions where fitted to the experimental results. To obtain the correct shift within 5% of error, we determined that the cut-off distance for the molecule-molecule interaction is $l_{\text{cutoff}} = 6 \cdot L_x$. We observe the typical band narrowing of the J-band whereas the exact vibrational structure of the monomer and the J-band cannot be captured with this simple analysis and is beyond the scope of the present chapter. Moreover, the present analysis doesn't account for the line shift due to non-resonant (van der Waals) interactions.

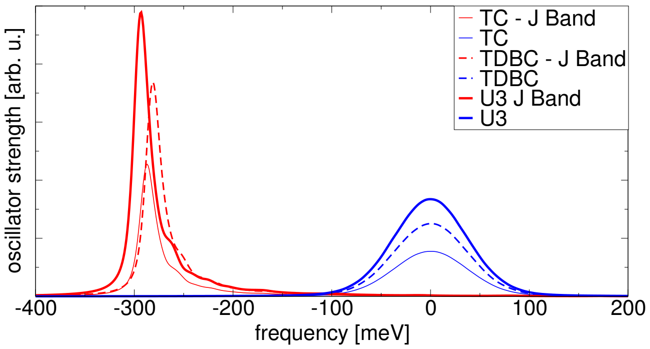

Figure 7.7: Calculated electronic excitation spectra of the three molecular aggregates, TC, TDBC and U3, as compared to the electronic transitions of monomers that form the aggregates. Zero frequency correspond to the energy of a monomer excitation. The transition frequencies of the monomers were taken from a Gaussian distribution of width $70\,\mathrm{meV}$ to account for the static disorder.

7.4.2 Quantum exciton dynamics

The developed model accounts for both coherent and incoherent properties of exciton dynamics. In view of the recent interest in the presence of coherences over long times in photosynthetic aggregates [26] this type of analysis is useful to identify the time over which one should truncate the dynamics and extract with sufficient accuracy the diffusion constant. In the long time limit, the contribution to the dynamics is mostly incoherent and this is when one enters the diffusive regime. These properties can be monitored by following the spatial distribution of the exciton population

$$P_{ij}(t) = \overline{\langle ij|\psi(t)\rangle \, \langle\psi(t)|ij\rangle}, \tag{7.18}$$

where (i, j) is the pair of cartesian indices for a particular molecule on the 2D lattice and the bar above the expression corresponds to the ensemble average over quantum trajectories. In addition, to characterize specifically the role of coherences in the exciton transport we analyze the two-point one-time correlations between the central site (the point of the exciton injection) and the current site

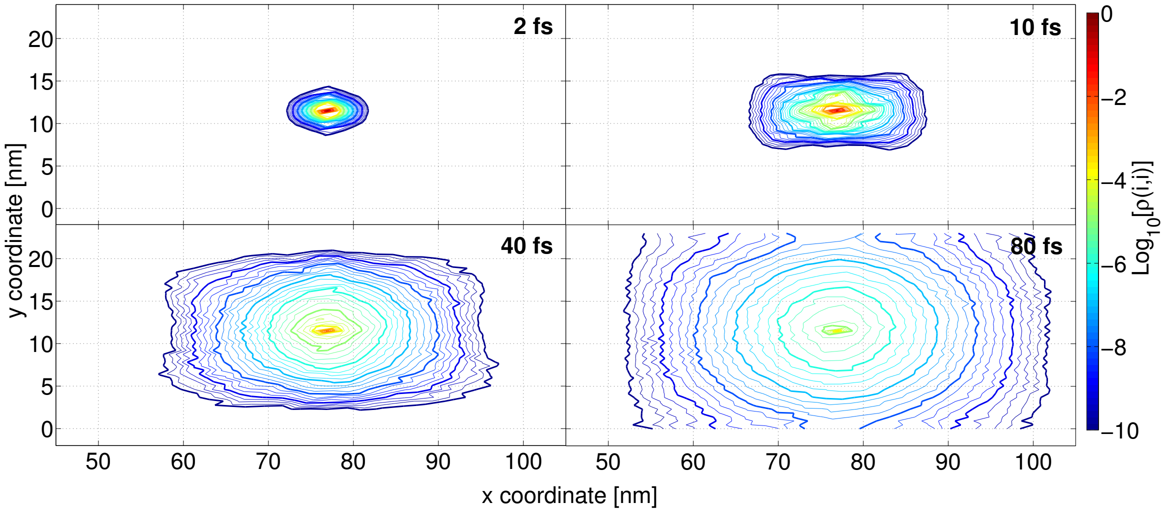

Figure 7.8: Contour plots of logarithm of exciton population in TDBC J-aggregate projected onto coordinate space at 2, 10, 40 and 80 fs. Here, the static disorder is $\sigma = 70\,\mathrm{meV}$ and the dynamic disorder is $\Gamma^{\phi} = 30\,\mathrm{meV}$. Population spreads more rapidly in the x direction than in the y direction. This behavior is observed for all studied values of dynamic and static disorder and can be explained by the couplings between monomers as described in the text.

(i, j)

$$C_{ij}(t) = \overline{|\langle ij|\psi(t)\rangle\,\langle\psi(t)|0\rangle|}. \tag{7.19}$$

A similar quantity has been used previously in Refs. [277,278] to estimate the exciton delocalization length in natural molecular aggregates. If the exciton transport is completely incoherent and represented by the hopping of exciton population between sites, the correlation function, Eq. 7.19, should remain zero for all times provided that no initial site-site correlations were created. This is consistent with the conventional Bloch equations, where the coherence dynamics and the population dynamics are separated.

In Figs. 7.8 and 7.9 we show an example of the population and coherence dynamics in TDBC J-aggregate when the dynamic disorder is $\Gamma^{\phi} = 30\,\mathrm{meV}$ and static disorder is $\sigma = 70\,\mathrm{meV}$. Based on the discussion in Section 7.2.2, this value of dynamic disorder represents a lower bound to the exciton dephasing rate (upper bound to the exciton diffusion length) at room temperature. One can see that exciton transport is anisotropic and the population spreads in time following approximately an elliptic shape with major axis x and minor axis y (such directions are indicated in Fig. 7.2). The population spreads about 2 to 3 times faster in the x direction than it does in the y direction. This can be explained by analyzing the direction of maximum coupling between nearest neighbors. In fact,

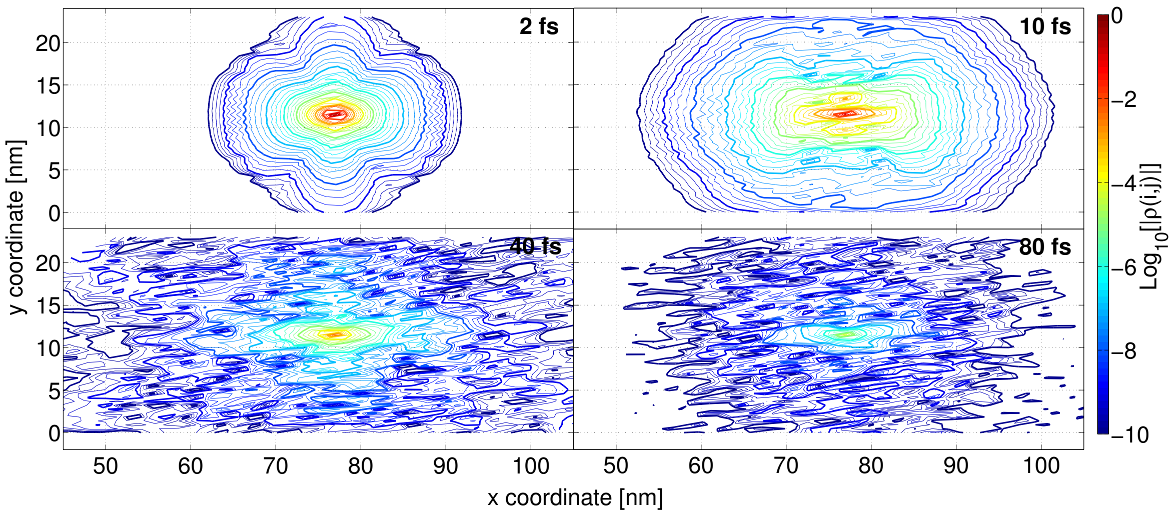

Figure 7.9: Contour plots of logarithm of exciton coherences in TDBC J-aggregate projected onto coordinate space at 2, 10, 40 and 80 fs. Here, the static disorder is $\sigma = 70\,\mathrm{meV}$ and the dynamic disorder is $\Gamma^{\phi} = 30\,\mathrm{meV}$. Coherences spread more rapidly in the x direction than in the y direction. This behavior is observed for all studied values of dynamic and static disorder and can be explained by the couplings between monomers as described in the text. Further, coherences spread and decay much more rapidly than populations, as can be seen by comparing to Fig. 7.8.

looking at the lattice in Fig. 7.2 and considering the molecule placed at the origin of the purple lattice vectors, we see that it has four first nearest neighbors, one of which is indicated by the $\mathbf{L}_y$ vector. The sum of the nearest neighbors coupling vectors taken in pairs along the x axis is greater than that along the y axis. The fact that the exciton is transported in the direction of maximum coupling is also seen in Fig. 7.10 where the population is more rapidly transferred to site (26,27) along the principle x direction respect to site (24,27) which is along the y axis.

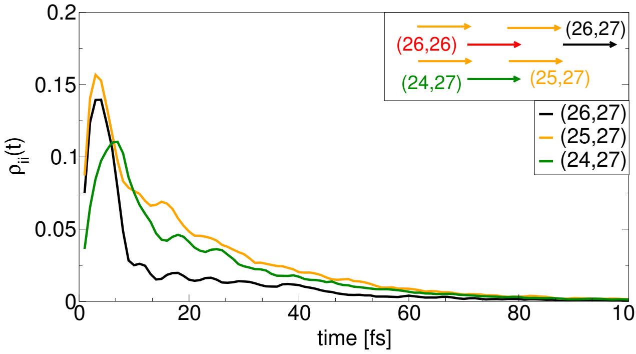

Figure 7.10: Populations of sites neighboring source (26,26) as a function of time for TDBC with $\sigma = 70\,\mathrm{meV}$ and $\Gamma^{\phi} = 30\,\mathrm{meV}$. Population is transferred most rapidly from the central site (26,26) to site (25,27), the first nearest neighbor and then to site (26,27) which is in the direction of maximum transport.

By comparing Fig. 7.8 to Fig. 7.9, we notice that coherences spread and are suppressed much more rapidly than populations. However, the principal transport axis remains the same, i.e it is the major axis of the ellipse. This is true for all examined values of static and dynamic disorder. At times shorter than about $30\,\mathrm{fs}$ the dynamics is coherent and interesting shapes such as a four leaved clover at $2\,\mathrm{fs}$ appear in the coherence plot. At longer timescales incoherent diffusion prevails and these features mostly disappear. The peaks of these correspond to beats in coherences between second to fourth nearest neighbors but such beats die off rapidly over a couple of tens of femtoseconds. At $40\,\mathrm{fs}$ only a small fraction of sites populated by the exciton are correlated with the injection site. This timescale also corresponds to the decay of coherent beatings in the population of sites near the injection point, Fig. 7.10. Thus, within the approximations of our model the exciton diffusion properties can be extracted from $100\,\mathrm{fs}$ dynamics. While quantitative differences are observed between the molecules, the general trend is qualitatively similar to the one shown in the example. As a possible extension of this initial study of coherent dynamics it would be interesting to explore the phase directed exciton transport in these two-dimensional aggregates as has been done for the one dimensional case [279].

While the initial condition (a localized exciton) determines a rather large population of the central site even at relatively long times, this does not globally affect the exciton diffusion properties of the aggregate. Furthermore, the localized excitation can be viewed as exciton injection from a donor.

7.4.3 Diffusion coefficient and diffusion length

The computed wave function provides the most complete source of information about the exciton dynamics. Its second moment can capture the main diffusive and ballistic features of the transport. For a homogeneous system with stochastic dephasing noise and translational invariance, the moments of the wave function in Eq. 7.6 can be written analytically [257]. If the exciton is initially localized on a particular molecule one should expect a ballistic exciton propagation (the second moment scales quadratically in time, $M^{(2)} \propto t^2$) followed by the diffusive motion (the second moment is linear in time, $M^{(2)} \propto t$). For systems with static disorder similar transport regimes should be observed provided that the dynamic noise is strong enough to overcome exciton localization. To verify this the second moments of the wave functions each trajectory were computed over an interval of $100\,\mathrm{fs}$ with a time step of $1\,\mathrm{fs}$ and averaged over a thousand trajectories. In Fig. 7.11 an example of $M^{(2)}(t)$

for the TDBC J-aggregate with static disorder $\sigma = 70\,\mathrm{meV}$ and dynamic disorder $\Gamma^{\phi} = 30\,\mathrm{meV}$ is shown. On timescales shorter than about 30 fs the scaling of $M^{(2)}$ is approximately quadratic, while

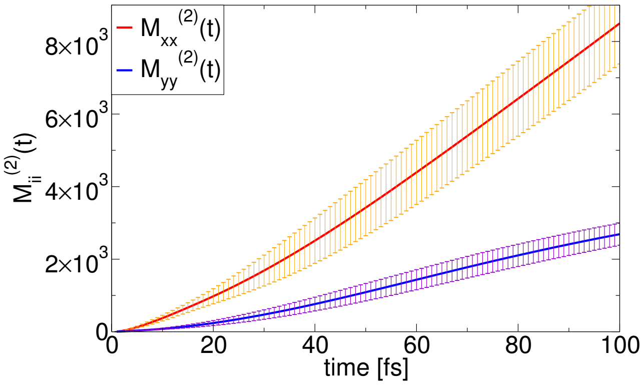

Figure 7.11: Second moment of the exciton wavefunction in time for TDBC aggregate with static disorder $\sigma = 70\,\mathrm{meV}$ and dynamic disorder $\Gamma^{\phi} = 30\,\mathrm{meV}$. Both xx and yy components are included with their respective error bars. A transition from a ballistic regime to a diffusive regime is observed at about $30\,\mathrm{fs}$. For all studied values of static and dynamic disorder these two regimes are observed and the transition is always at about $20 - 30\,\mathrm{fs}$.

the longer time dynamics reflects the diffusive transport. A similar tendency is observed for other molecules within the whole studied spectrum of σ and Γ^{ϕ} with the free exciton propagation time shrinking down to below 20 fs for large values of Γ^{ϕ} .

The exciton transport properties depend on the energy of the central lattice site where the exciton is localized at time zero - the initial injection energy E_{in} - relative to the J-band. This reflects which eigenstates are populated at the initial time. If the injection energy is close to the monomer transition, almost all eigenstates are populated. In contrast, if this energy is far below the J-band the exciton remains localized. Results showing the second moment as a function of E_{in} together with the exciton density of states (DOS) are reported in Fig. 7.12. We see that there is a maximum in the moments somewhere between the J-band ($E_{\mathrm{in}} = -281\,\mathrm{meV}$) and the monomer band ($E_{\mathrm{in}} = 0\,\mathrm{meV}$). This is true at all times and the position of the maximum is different for the xx component than it is for the yy component. This can be correlated to the large density of states in that energy interval (Fig. 7.12 top panel). The high density of states is not sufficient to explain the exact position of the maximum, in fact, while the density of states has a maximum at about $-72\,\mathrm{meV}$, the second moment is peaked at about $-170\,\mathrm{meV}$ for the xx component. The same trend in the second moments is observed for TC, and the only apparent difference is that the values of the second moment are smaller. One aspect to keep into consideration is that although there is a large density of states around $60 - 80\,\mathrm{meV}$,

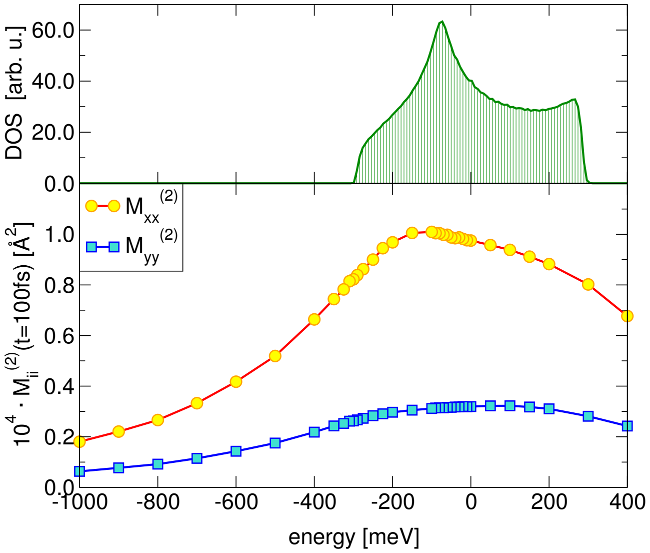

Figure 7.12: Top panel: Density of exciton states as a function of energy of states computed for an aggregate of 51x51 TDBC molecules and averaged over 1000 realizations of static disorder $\sigma = 70\,\mathrm{meV}$. The zero of energy corresponds to the electronic transition of a single molecule. The energy of the central site (injection point) in the lattice is assumed to be zero. Bottom panel: Plot of second moments of the wave function at time $t = 100\,\mathrm{fs}$ as a function of the initial injection energy for TDBC with static disorder $\sigma = 70\,\mathrm{meV}$ and $\Gamma^{\phi} = 30\,\mathrm{meV}$.

these states mostly have small oscillator strengths (See Fig. 7.7). To investigate further the origin of the differences in these maxima one should look into the structure and spatial overlap of the exciton states.

To estimate the exciton diffusion coefficients the linear fit was taken over the time interval $\Delta t_1 = 30 - 100\,\mathrm{fs}$ to exclude the initial ballistic propagation of the exciton. The injection energy was set equal to the J-band frequency. For most values of static and dynamic disorder, the boundary effects associated with the finite size of the simulated lattice are negligible on the timescale of $100\,\mathrm{fs}$. However, for weak dynamic noise the exciton wavefunction reaches the boundary of the simulated lattice along the y-axis at about $70\,\mathrm{fs}$. In such cases the yy component of the diffusion coefficient D was fitted on the time range $30 - 70\,\mathrm{fs}$. With the initial condition of injection into the J-band, the diffusion coefficients components were calculated using

$$M_{ii}^{(2)}(t) = 2D_{ii}t \tag{7.20}$$

for each type of aggregate. The results are shown in Fig. 7.13. Two distinct characteristics emerge from this plot. First of all, we notice that diffusion is greater for U3 than it is for TDBC which in turn is greater than that of the TC aggregate. This can be explained by looking at the physical characteristics of the molecules (Tab. 7.1). U3 has the largest transition dipole, this leads to stronger coupling between the monomers and thus to more rapid exciton density transfer. The diffusion coefficients normalized with respect to the square of the corresponding transition dipole (not shown in the figures) are similar for two molecules, TDBC and U3, while the normalized diffusion for TC is still higher. We attribute this difference to the closer packing of TC molecules. This trend is robust to both static and dynamic disorder, so long as both are finite and not so large as to lead to localization. This implies that independently of temperature, within the studied interval, the transport efficiency is dictated by the specific physical properties of the molecules. Of course, the geometric arrangement is a criteria which can alter this trend since it will explicitly modify the couplings. Then secondly, as noticed from the wavefunction propagation, diffusion is faster along the x axis than it is along the y axis. This difference is largest for small values of disorder (about a 3-fold difference) where the propagation is fastest, in the quasi-ballistic regime. Going to larger disorder, the wavefunction spreads much slower and propagation is reduced in both directions.

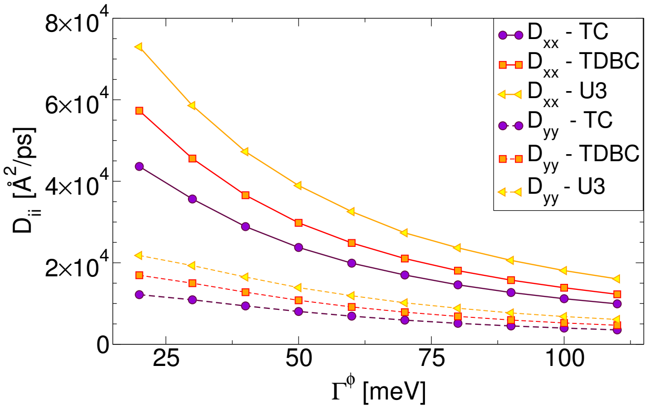

Figure 7.13: Comparison of diffusion constants as a function of dynamic disorder Γ^{ϕ} for TC, TDBC and U3 with static disorder $\sigma = 70\,\mathrm{meV}$. As dynamic disorder is increased, the diffusion constants decrease. Further, xx diffusion constants components are larger than yy components for all values of dynamic disorder. Finally, diffusion is larger for U3 than it is for TDBC and TC. This can be explained by the molecular coupling parameters as described in the text.

Finally, we investigated the transport as a function of static disorder as well. The three dimensional surface plots for TC and TDBC are shown in Fig. 7.14. We notice that diffusion is strongly dependent on Γ^{ϕ} and much less dependent on σ. For each fixed value of Γ^{ϕ}, the largest variation of D_{ii} over the σ interval is of about 30% of the largest values. On the other hand, the largest variation of D_{ii} at fixed σ and varying Γ^{ϕ} is of the order of 80% of the largest value. Due to the presence of static disorder the dependence of the diffusion coefficient on the dephasing rate Γ^{ϕ} deviates from the conventional $D \propto 1/\Gamma^{\phi}$ derived within the Haken-Strobl-Reineker model for homogeneous systems [257].

Recently, Akselrod et. al. [51], have estimated the exciton diffusion length in thin-film J-aggregates of TDBC molecules based on an exciton-exciton annihilation experiment at room temperature. In that study, the exciton lifetime obtained from time-dependent photoluminescence was determined to be $\tau_{\text{exp}} = 45\,\text{ps}$, and an expression for three-dimensional exciton diffusion was used to determine the annihilation rate. However, the sulphonated group side chains are about 6 Å long and in addition, in the growth process a layer of polymer molecules is introduced between the J-aggregate layers. As a result the spacing between the monolayers of fluorescent dyes is several times larger than the distance between nearest neighbor molecules in a layer. Therefore we can assume that diffusion in these aggregates is two dimensional rather than three dimensional. Using a 2D model, we find that the experimental exciton diffusion length is about $\ell_{\text{exp}} \approx 60$ nm. We can estimate the exciton diffusion length along the i-th direction using the measured lifetime and a computed diffusion coefficient as

$$\ell_i = \sqrt{2D_{ii}\tau_{\text{exp}}}. \tag{7.21}$$

For the value of the dynamic disorder $\Gamma^{\phi} = 30\,\text{meV}$, which should approximately correspond to room temperature, as discussed in Section 7.2.2, and the static disorder $\sigma = 70\,\text{meV}$ we find $\ell_x \approx 200\,\text{nm}$ and $\ell_y \approx 100\,\text{nm}$. These values are in a good qualitative agreement with the measured one. However, the quantitative discrepancy can be due to a number of factors such as different lattice constants of the aggregate, additional exciton dephasing and relaxation channels, and also domain boundaries in the experimental structures. All of these aspects can be incorporated into the model provided that one can extract the actual parameters from experiments.

7.5 Conclusions

In this chapter, a mixed model combining an open quantum systems approach to *ab-initio* calculations has been employed to gain insight on the exciton dynamics of thin-film J-aggregates. This model can capture both coherent and incoherent transport and allows for a detailed study of transport parameters such as diffusion coefficients and diffusion length. The role of the initial state of the

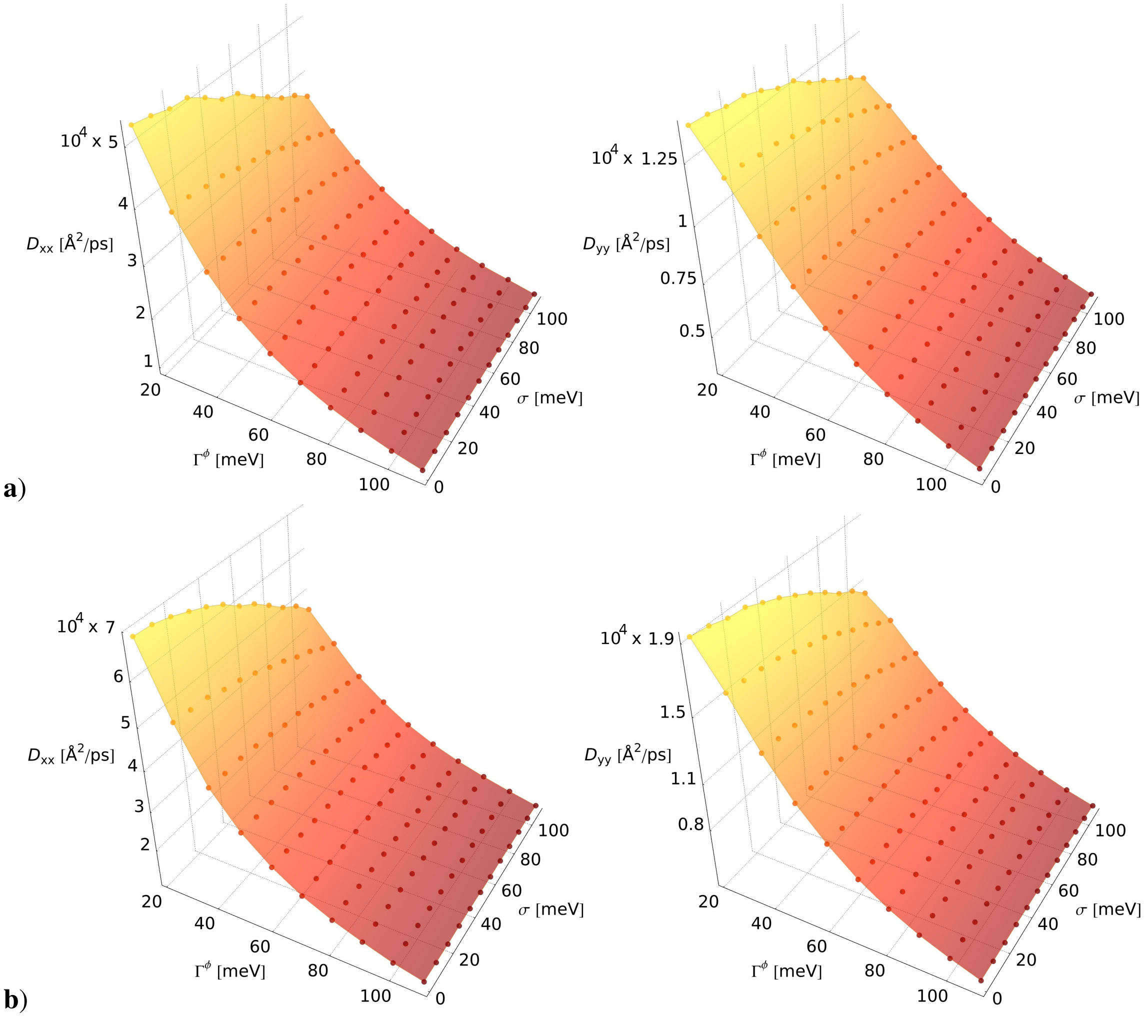

Figure 7.14: Diffusion coefficients of singlet excitons in 2D J-aggregates of TC (panel **a**) and TDBC (panel **b**) as functions of static σ and dynamic disorders Γ^{ϕ}. The initial condition for propagation was injection at $E_{in} = -281\,\mathrm{meV}$ for TDBC and $E_{in} = -287\,\mathrm{meV}$ for TC. The red color corresponds to smaller diffusion while the yellow indicates larger diffusion coefficients.

system on transport can also be captured. Further one can investigate all these aspects as a function of the structure of the aggregates through the lattice parameters.

As an example the model was applied to three different cyanine dye aggregates. Within this model we conclude that transport depends explicitly on the molecular properties of the monomers which compose the aggregate. In particular, for molecules packed in a brickstone arrangement, transport increases with the monomers' transition dipoles and hence with the coupling between monomers. Furthermore, the coupling induces a preferential direction for transport which leads to an anisotropic spread of populations and coherences. Such directionality is robust to both static and dynamic disorder within the investigated ranges and does not change for different molecules. This model has permitted the identification of timescales for the different transport regimes. A ballistic regime is present for all values of disorder at times smaller than $20\,\mathrm{fs}$ while afterwards a diffusive regime is observed. The transport is also determined by the choice of the initial condition, at a specific value of injection energy a maximum in diffusion is observed. Investigation on the origin of the exact position of this maximum are planned but qualitatively it can be explained by the large DOS located between the J-band and the monomer transition.

The obtained diffusion length is in good agreement with experimental results, however a more accurate comparison to experiment would only be possible after including relaxation in the excited state manifold and fluctuations in the off-diagonal elements of the Hamiltonian. The model also does not account for exciton domains which would reduce diffusion, and further it cannot be applied straightforwardly in the low temperature regime. Work in these directions is currently in progress in our research group.

The efficient exciton transport observed in these thin-film aggregates and the possibility of tuning this transport by the choice of monomers or by selecting the initial condition makes these aggregates good candidates for devices where large exciton diffusion lengths are sought. In particular coupling them to optical micro-cavities [213] opens the road to a range of control possibilities which we plan to study in future work. Finally, coupling these large-exciton diffusion length materials to high-hole mobility materials [280] might also provide some advantages for technological applications such as all-organic photon detectors.

Chapter 8

Electromagnetic study of the chlorosome antenna complex of Chlorobium tepidum[i]

8.1 Introduction

The life cycle of plants, photosynthetic bacteria and algae is based on the harvesting of solar energy. In all of these organisms solar light is absorbed and processed by a photosynthetic system. This unit typically consists of an aggregate of light absorbing molecules, *e.g.* bacteriochlorophylls (BChls) (See Fig. 8.1, panel II). Photosynthetic systems vary in composition and size, for instance, their dimensions can range from tens to hundreds of nanometers with up to $\sim 2 \cdot 10^5$ pigment molecules. Solar energy is transferred in these systems through molecular excitations known as excitons. Success in nature's competition for resources is crucial for the survival of phototrophic organisms. Therefore, optimal efficiency of light absorption and energy transfer within the photosynthetic systems are essential characteristics.

Recently, much scientific effort has been devoted to understanding the microscopic principles which govern the efficiency of photosynthetic systems [1]. Amongst these systems, green sulfur bacteria is one of the most widely studied. The photosynthetic system of green sulfur bacteria consists of three main elements (See Fig. 8.1, panel I). The first is the chlorosome: a large nanostructure array of BChl's which functions as a light absorbing antennae. The second elements are intermediates (these include the baseplate and the Fenna-Matthews-Olson protein complex) which play the role of exciton bridges connecting the chlorosome to the third and last element, the reaction center,

---

[i] **Stéphanie Valleau**, Semion K. Saikin, Davood Ansari-Oghol-Beig, Masoud Rostami, Hossein Mosallaei, and Alán Aspuru-Guzik. Electromagnetic study of the chlorosome antenna complex of Chlorobium-tepidum. *ACS Nano*, 8, 3884 (2014)

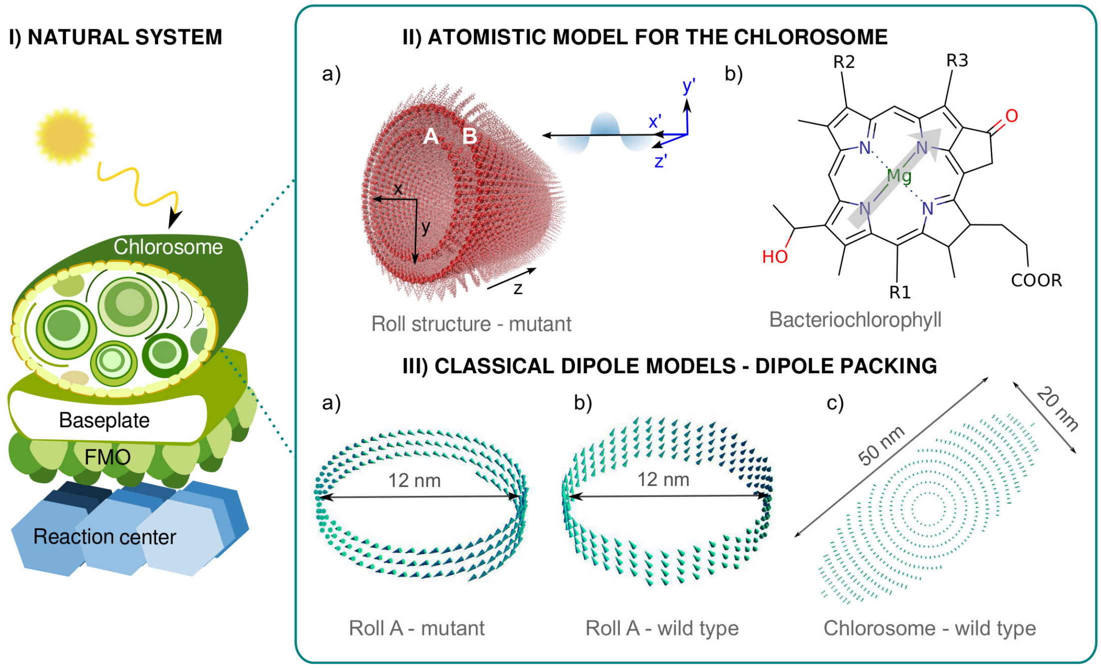
I) NATURAL SYSTEM
Chlorosome
Baseplate
FMO
Reaction center
II) ATOMISTIC MODEL FOR THE CHLOROSOME
a)
A
B
x
y
z
y'
x'
z'
Roll structure - mutant
b)
R2
R3
O
N
Mg
N
N
N
HO
R1
COOR
Bacteriochlorophyll
III) CLASSICAL DIPOLE MODELS - DIPOLE PACKING
a)
12 nm
Roll A - mutant
b)
12 nm
Roll A - wild type
c)
50 nm
20 nm
Chlorosome - wild type

Figure 8.1: Panel **I**) - model of the photosynthetic units in the natural system of green sulfur bacteria - the main elements are the chlorosome, the baseplate and the FMO complexes which transfer excitons to the reaction center. Panel **II**): Atomistic model for the chlorosome (Ref. [185]); in a) the chlorosome nanostructure consisting of two concentric rolls, roll A and B, is shown. Further, the reference system for the incoming field propagating along the x' direction is indicated. In b) the molecular structure of a bacteriochlorophyll (BChl), the main building block of chlorosomes, is indicated. Here, the R, R1, R2 and R3 symbols represent molecular chains (not drawn for simplicity) which vary depending on the type of BChl. The grey arrow indicates the direction of the transition dipole for the first molecular optical transition. Panel **III**): three classical dipole models for the chlorosome nanostructure. In a) we see a slice of a single cylinder (full length ~30nm) and the molecular packing of BChl-d as obtained by Ganapathy, *et al.* (Ref. [185]). In b) another type of packing using BChl-c molecules is shown (full length ~30nm). Finally in c) we show a slice of the model for the entire chlorosome nanostructure. This last structure is built using the packing motif of panel b). Due to the type of pigment molecules, structures b) and c) are denoted as "wild-type" structures. See Methods for more details.

where the exciton energy is employed in the synthesis of metabolic compounds.

Similarly, in the nanostructure community, much research has focused on the study of nano-antennas [281–284]. Various types of antennas have been devised and studied [285, 286] in order to understand which materials and shapes are optimal to enhance and direct radiation. Models for nonradiative energy transfer between nanostructures have also been developed [287] in an effort to answer these questions.

It is interesting that nature has evolved to generate antennas in biological organisms as well. The chlorosome nanostructure has dimensions of the order of hundreds of nanometers and works exactly like an antenna: it absorbs photons and transmits them to the next subunits very efficiently. A question naturally arises: can energy transfer principles be deduced from the study of these natural systems and applied to the field of nano-antennas? To begin to answer this question, in this chapter, we investigate the electromagnetic properties of the chlorosome antenna complex.

Previously, we investigated reduced models of this photosynthetic unit using open-quantum system approaches coupled to *ab-initio* simulations. Energy transfer was found to be a non-Markovian process [194] which can be characterized by multiple timescales [197]. Recently, some of us investigated a reduced model of the entire photosynthetic system atomistically, Ref. [288]. We found energy transfer to be robust to initial conditions and temperature. Other theoretical studies on energy transfer dynamics as well as the spectroscopy of the antenna complex have been carried out for small models of the chlorosome structure [195] using open-quantum system theories. Spectra were also obtained for helical aggregates using the CES approximation and including the vibrational structure [239]. In this paper, we present a new perspective: an electrodynamic study of the full chlorosome antenna.

The chlorosome antenna complex is composed of up to tens of thousands of BChls (see Fig. 8.1) which makes it the largest of the photosynthetic antenna units known. This nanostructure is thought to be the main element responsible for capturing photons at the extremely low photon densities of the bacteria's environment [2,153]. Quantum mechanical models, as employed in some of the recent theoretical work on photosynthetic systems [25,28,93,194,197,198,207], cannot be used here due to the large size of the full chlorosome antenna complex. Electrodynamic modeling thus provides a viable alternative. This approach can capture, within certain approximations, both coherent and incoherent excitation dynamics and has already been described and employed in the simple case of a molecular dimer [289]. Further, we have recently [290] devised an algorithm to solve the electrodynamic equations very efficiently even in the presence of thousands of molecules.

The chlorosome antenna complexes are composed of different types of BChls, namely BChl-c, BChl-d or BChl-e, with varying chemical composition according to the species in question. Because of the large amount of disorder present in the natural system, the definitive structure for the complex is unknown. However, several models have been proposed [182,185,291–293]. Recently, Ganapathy *et al.* [185] determined the structure of a synthetic triple mutant chlorosome antennae, generated to mimic natural chlorosomes. This mutant structure replicated various structural signatures of the natural chlorosome while, however, being less efficient in terms of growth rates at different light intensities respect to the wild type chlorosome. Other experimental efforts have been made in this direction using a combination of NMR and X-Ray diffraction [181, 294, 295]. The structure by Ganapathy *et al.* will be the first of three nanostructures which we will consider in this work and their experimental findings inspire the remaining two structures. The first structure comprises a series of concentric cylinders of aggregated BChl-d molecules (Fig. 8.1 II-a and III-a). We will consider both the case of a single cylinder and of two concentric cylinders in this work. The second system is a similar cylindrical array, built of BChl-c molecules rather than BChl-d (See Fig. 8.1 III-b). This structure is obtained following the findings of Ganapathy *et al.* [185]. Finally we will consider a model for the entire chlorosome (panel III-c)) consisting of over 70000 BChl-c. More detail on these three structures can be found in the Methods section.

Using our recent algorithm to solve the electromagnetic equations [290], we efficiently compute the induced polarization and fields of the three chlorosome structures. The role of different initial excitations, *i.e* frequency and polarization of the incoming field, are investigated. We also study the field enhancement and field depolarization as a function of structural disorder and dynamical noise. Finally, we determine fluxes of energy transferred in time to acceptors located around the antenna nanostructures.

8.2 Results and discussion

8.2.1 Antenna spectra and resonances

The chlorosome antennae absorbs incoming light in the visible range. The resulting spectrum shows resonances determined by the presence of molecular transitions at about 750 nm. The chlorosome aggregate resonances are shifted respect to the pigment transitions due to the couplings between monomers. In order to understand which regions are of interest for energy transfer, we calculated the absorption and circular dichroism spectra of the structures. Due to the three-dimensional arrangement of the dipoles in a cylindrical structure, we expect there to be two components in the absorption spectra, a z polarization component, parallel to the main axis of the cylinder, and an in-plane xy component, orthogonal to the main axis. Panel a) of Fig. 8.2 shows the computed absorption spectra for the roll structure III-a) of Fig. 8.1. The spectra were obtained using a semiclassical approach (see Methods) and using the Fermi-Golden rule quantum approach. The spectra were broadened by adding disorder through the rate $\Gamma = 1\,\mathrm{meV}$ (See Eq. 8.1). As remarked previously in the literature (see *e.g.* Ref.296) the quantum and classical spectra are simply shifted (see Methods for more details). More importantly, in both approaches we see the expected z and xy, components at about $\Delta\omega_z = -280\,\mathrm{meV}$ and $\Delta\omega_{xy} = [-260;-230]\,\mathrm{meV}$ for the classical spectrum. A higher oscillator strength is observed for the z component. The range over which transitions are observed is consistent with experiments [164] though a direct comparison of the components is not possible due to the large amount of noise present in the natural system. The CD spectra in panel b) also follows the same trend[ii] as the experimentally observed CD, Ref. 164,184. The alternating negative and positive peaks in the CD spectra are related to the orientation of the incoming field respect to the helicity of the structure. These spectra were also calculated for structure III-b) of Fig. 8.1 and these follow a similar pattern.

The inter- and intra-molecular vibrations, interaction with the solvent, and other environmental fluctuations, generate a source of noise which needs to be taken into account when modeling the system. Generally speaking, we can distinguish between static/structural disorder and dynamic noise based on the time scales of the associated fluctuations. Fluctuations related to structural disorder oscillate on a much longer timescale compared to the dynamics of the system whereas dynamical noise fluctuations are more rapid. The noise source is the same for both types of disorder.

In this model, one can include noise by introducing a molecular response function [297]

$$\chi_{i,s}(\omega) = \frac{2}{\hbar}\frac{\left|\vec{\mu}_{i,s}\right|^2 \omega_{i,s}}{(\omega_{i,s} + i\frac{\Gamma}{2})^2 - \omega^2}. \tag{8.1}$$

Here, $\vec{\mu}_{i,s}$ is the transition dipole of the $s-th$ transition for the $i-th$ molecule and $\omega_{i,s}$ the corresponding transition frequency. The dynamical noise is accounted for by the rate constant, Γ, and structural disorder can be included by introducing noise in the transition frequencies, $\omega_{i,s}$. Usually, $\omega_{i,s}$, is taken from a Gaussian distribution, and structural disorder is characterized by the width of the Gaussian, σ.

There is no straightforward way to quantify structural and dynamical noise in the localized molecular basis experimentally. The sum of structural disorder, σ, and dynamic disorder, Γ, in the exciton, delocalized energy basis[iii] corresponds to the linewidth of the absorption spectrum. The overall disorder in the localized site basis should be of the same order of magnitude. In this case the linewidth is $\approx 70\,\mathrm{meV}$ both for the BChl-c monomeric spectrum and for the Chlorosome spectrum [166].

[ii] Note that the structure of Ref.[185] was chosen with opposite helicity in agreement with experimental findings.

[iii] The exciton basis corresponds to the basis of delocalized energy states which is obtained by diagonalizing the Hamiltonian in the localized molecular basis.

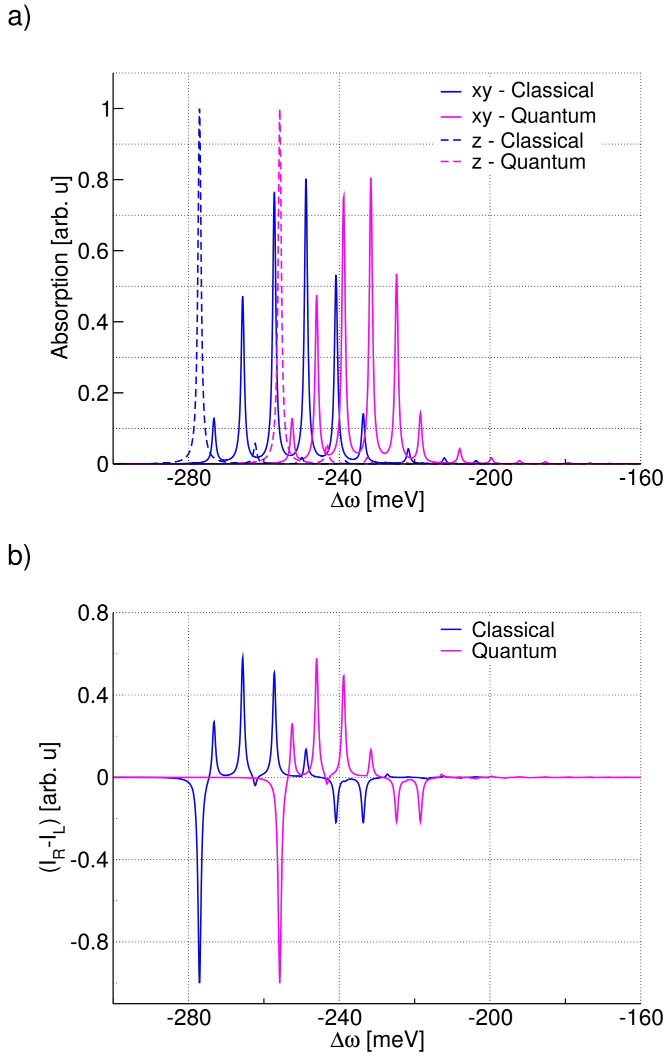

Figure 8.2: Panel **a**) Absorption spectrum and its components obtained using a classical electrodynamic approach and the quantum Fermi-Golden rule approach. Panel **b**) Circular dichroism spectrum (CD) obtained using the classical and quantum approaches. The spectra were broadened with disorder $\Gamma = 1\,\mathrm{meV}$, and the frequency axis corresponds to the shift in energy respect to the monomer transition frequency. All spectra were computed for structure III-a) in Fig. 8.1.

8.2.2 Induced fields

Within the electromagnetic framework, we can obtain information on the exciton transfer properties from the induced polarizations. Indeed, once the nanostructure interacts with an incoming plane wave, the induced polarizations generate fields and thus transport can be quantified in terms of field enhancement. The directionality of transport can also be determined by computing the field depolarization.

Field concentration and depolarization

Plane wave incoming fields propagating along the x direction (see Fig. 8.1 panel II-a), were used to study the electric field enhancement and depolarization from the dipole arrays of the chlorosome. Two different polarizations of the incoming field are considered, along the y' direction and along the z' direction, as shown in Fig. 8.1, panel II-a.

The roll-A structure (Fig. 8.1; III-a), was employed to obtain the field enhancement $\kappa = \frac{|\vec{E}|}{|\vec{E}_0|}$ plots shown in Fig. 8.3. In these plots, we see the values of the scattered field calculated on a grid orthogonal to the structure (panels a and b) and on a grid parallel to the structure (panels c and d). By comparison of panels a) and b) we notice a larger field enhancement when the incoming field is polarized along the z' direction. This is expected due to the more favorable overlap with the dipole orientations in the structure. The field enhancement overall is not very big in this case due to the large value of the noise $\Gamma = 50\,\mathrm{meV}$. We notice that the field is enhanced homogeneously in the radial direction (panels b,d), for y'-polarized incoming field. This trend supports the idea of exciton transfer in the radial direction. This feature is observed even when including structural disorder. For the z'-polarized incoming field (panels a,c), we see enhancement radially but also at the edges of the structure (panel c) this suggests that excitons may be transferred between layers and at the edges amongst neighboring substructures. In the next section, we look at how κ varies with noise and structural disorder.

In Fig. 8.4, we show contour plots of the depolarization $\eta = \left(|\vec{E}|_{\parallel} - |\vec{E}|_{\perp}\right) \Big/ |\vec{E}|$ of the electric field on a horizontal grid across the structures. Panel a) and b) indicate η computed for the roll A structure (Fig. 8.1; III-a) while panels c) and d) correspond to calculations for the chlorosome model structure with $7 \cdot 10^4$ molecules (Fig. 8.1; III-c).

In panels a) and c) the depolarization is calculated for a z'-polarized incoming field and in panels

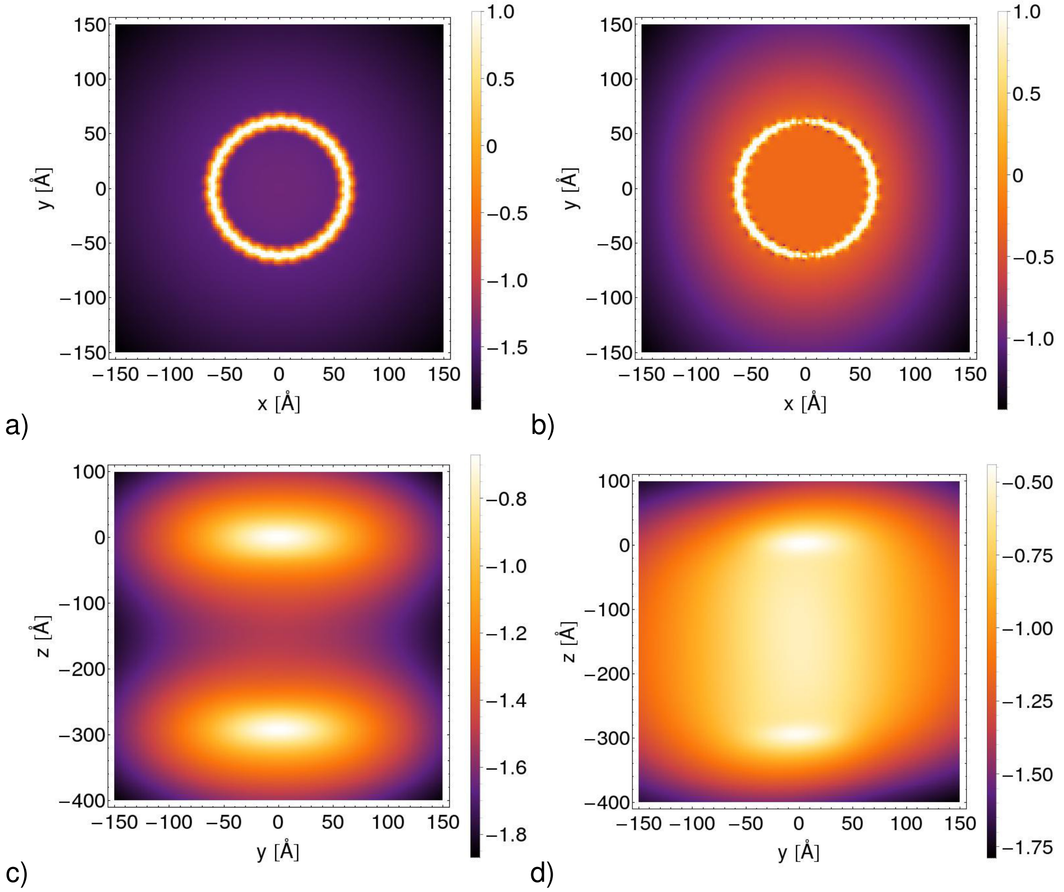

Figure 8.3: Panel **a**) Base ten logarithm of the electric field enhancement, $\log_{10}\kappa$, calculated on a grid orthogonal to the roll structure in Fig. 8.1, III-a). The dynamical noise rate is $\Gamma = 50\,\mathrm{meV}$, the initial field excitation frequency is shifted by $\Delta\omega = 0.23\,\mathrm{eV}$ (see Fig. 8.2). The polarization of the initial field is along the z' direction. Panel **b**), same as panel a) but for external field polarized along the y' direction. Panel **c**) same as panel a) but here field is calculated on a grid parallel to the longest axis of the roll and at a distance of $r = 80\,\mathring{A}$ from the origin. Panel **d**) same as panel c) but for y'-polarization.

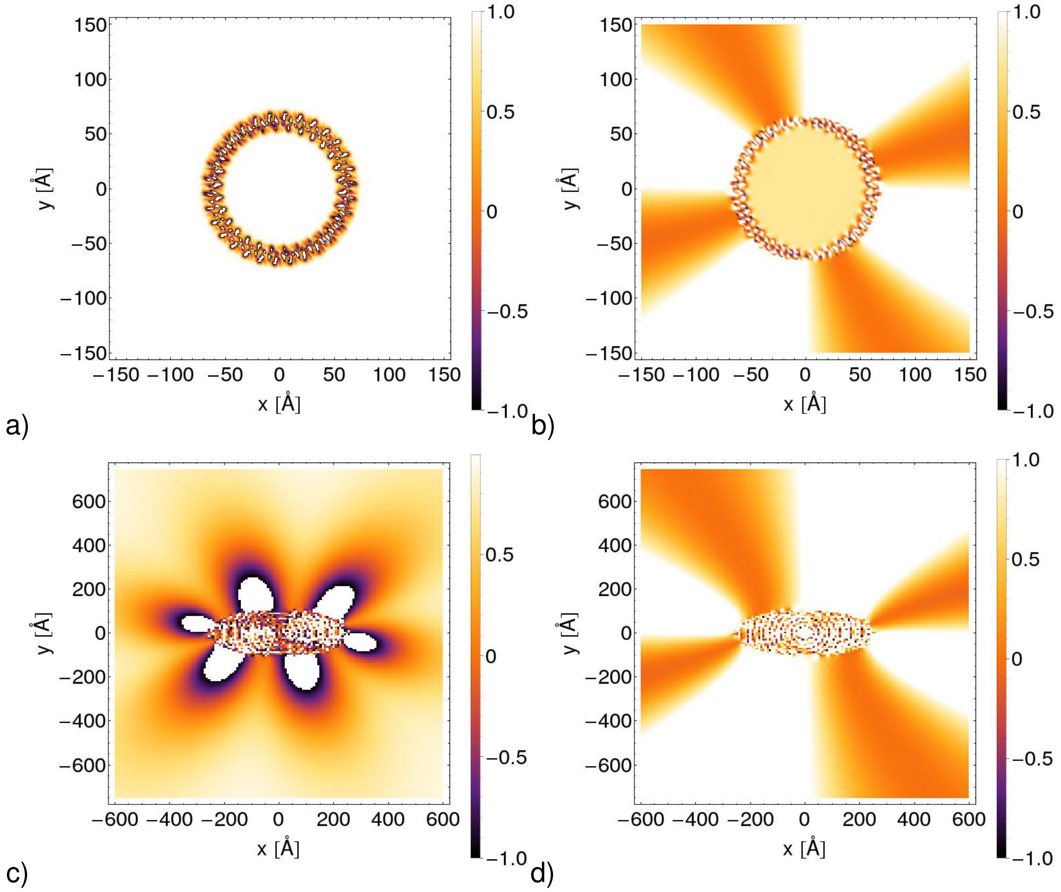

Figure 8.4: Panel **a**) Depolarization of electric field $\eta = \left(|\vec{E}|_{||} - |\vec{E}|_{\perp}\right) \Big/ |\vec{E}|$ calculated on a grid orthogonal to the roll structure in Fig. 8.1, III-a). The dynamical noise rate is $\Gamma = 50\,\mathrm{meV}$, the initial field excitation frequency is shifted by $\Delta\omega = \omega_0 - \omega_{\mathrm{ext}} = 0.23\,\mathrm{eV}$ (See Fig. 8.2). The polarization of the initial field is along the z' direction. Panel **b**), same as panel a) but for y'-polarization of the external field. Panels **c**) and **d**), same as a) and b) but for the wild type chlorosome model structure III-c) with $\Delta\omega = \omega_0 - \omega_{\mathrm{ext}} = 0.22\,\mathrm{eV}$.

b) and d) for a y'-polarized incoming field. The depolarization, η, was also computed for the wild type roll-A structure (Fig. 8.1; III-b) and the pattern is analogous to that shown here in panels a) and b) for structure III-a. For these two cylindrical structures, the z'-polarized incoming field is not significantly depolarized, this is probably due to the fact that the dipoles' z-component is largest.

For the third model chlorosome structure, we see in panel c) that the field gets depolarized in an interesting pattern which most likely originates from the dipole packing at the edges. For the y'-polarized incoming field, the depolarization pattern is similar for all three structures (panels b, d) and the field remains polarized for specific directions, perhaps those corresponding to where other substructures might be found. The observed depolarization patterns ensure that a photon of arbitrary polarization will be transferred to the next layer following the radial direction.

The observed robustness to structural variations of the field polarization is in agreement with recent experimental findings by Tian *et al.,* Ref. 186. In this work the authors used 2D fluorescence polarization microscopy on a series of wild type chlorosomes of C-tepidum grown in homogeneous conditions. They found that all spectral properties were homogeneous independent of the selected chlorosome and their results suggested that BChl molecules must possess a distinct organization within the chlorosomes. A similar organization is present in our model structures and it appears that even when adding structural disorder, the overall transition dipole moment components are not significantly modified and the largest component remains along the z axis thus leading to the field polarization patterns we have obtained. It would be interesting to obtain a theoretical estimate of the modulation depth for each of the three structures so as to compare to these experimental findings.

Scaling of field enhancement with disorder

In Fig. 8.5 we show the scaling of the field enhancement κ as a function of distance from the center of the structure (panel III-a of Fig. 8.1) for different values of structural disorder and dynamical noise. In panel a) the field intensity as a function of distance is shown for different values of dynamical noise. We notice that as dynamical noise increases, the field scaling tends to go as $\sim \frac{1}{r}$, but there are different slopes of the scaling on shorter distances. In panel b), the scaling as a function of structural disorder σ is investigated at fixed small Γ. In this case the trend of the field is $\sim \frac{1}{r^3}$. It is not immediately clear to us why a different scaling with respect to r is observed in the case of dynamical *versus* structural disorder, however it is interesting that perhaps nature may tune one or

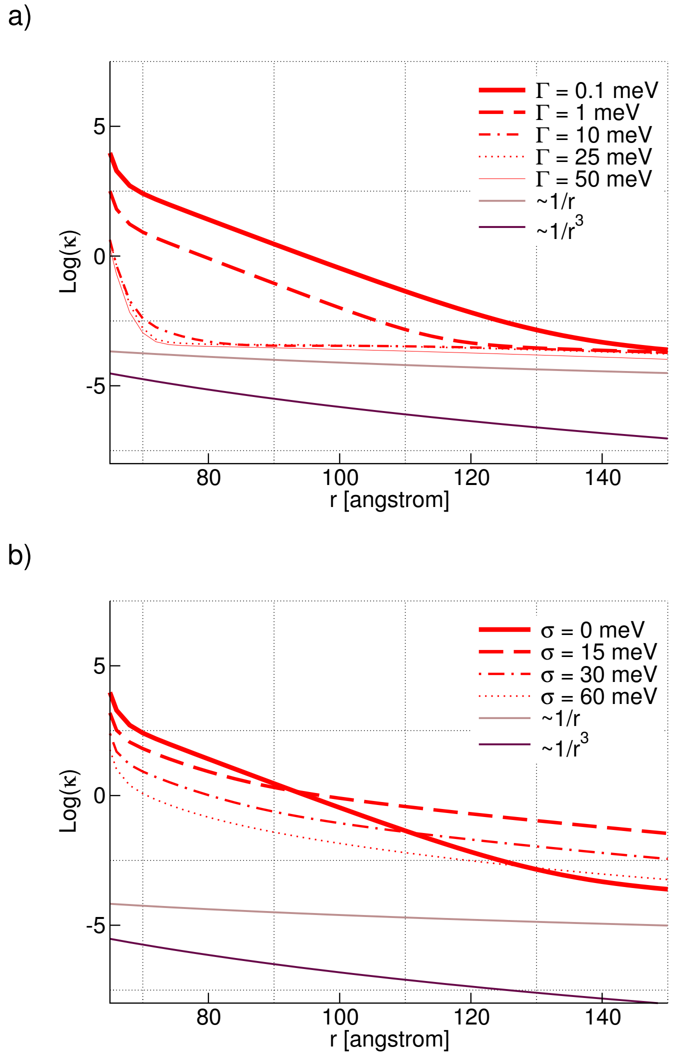

Figure 8.5: Scaling of field enhancement κ with dynamical noise, (panel **a**)) and structural disorder (panel **b**)) for the roll-A structure (Fig. 8.1; III-a) as a function of distance r from the center of the structure ($r_{\text{center}} = 0\,\mathring{A}$). The incoming field is polarized along the z' direction.

the other type of disorder to modify the intensity of energy transferred through structural variations. The distance amongst substructures has experimentally [185] been determined to be $r_{\text{phys}} \sim 2\,\text{nm}$. The slope of the fields around this distance is not homogeneous as a function of Γ. In the case of structural disorder, at about r_{phys}, we notice (Fig. 8.5, panel b) that a similar slope is observed with a smaller variation in intensity respect to panel a).

In Fig. 8.6, we plot the field enhancement κ at the biological distance r_{phys} for the two cylindrical structures (panels III-a and III-b of Fig. 8.1) as a function of dynamical noise (panel a) and structural disorder (panel b). It appears that dynamical noise has the strongest effect. In such large structures it is more likely that the main source of disorder is actually structural disorder however. This means that overall the excitation energy transfer is quite robust to disorder. Further, for all values of Γ and σ, the enhancement is larger for the wild type structure. This suggest that the dipole arrangement of the wild type structure leads to higher efficiency in terms of field enhancement. This is also observed at the physiological distance, r_{phys}, relevant for transport.

8.2.3 Energy flux

The main role of the chlorosome is that of transmitting the collected solar energy: it is therefore important to investigate how fast energy is transferred amongst these nanostructures. In our electrodynamic model, the energy flow can be obtained from the induced fields and polarizations. In particular, one defines some acceptor molecules which are not initially excited by the incoming field and some donor molecules which are excited by the incoming field and later interact with the acceptors.

The rates of energy flow absorbed by the acceptors, $R(t)$, can be obtained from the divergence of the pointing vector as $R(t) = \sum_{\text{acc}} \vec{E}_{\text{acc}}(t) \cdot \frac{d}{dt}\vec{p}_{\text{acc}}(t)$, where $\vec{E}_{\text{acc}}$ is the electric field at the acceptor at time t and $\vec{p}_{\text{acc}}$ is the induced polarization of the acceptor at time t. This approach has been discussed in Ref. 289.

In Fig. 8.7, panel a), we show these fluxes of energy as a function of time, $R(t)$, for transfer from a roll of donors (structure III-a of Fig. 8.1) to a dipole acceptor positioned at different distances from the center of the cylinder. The dipole acceptor is oriented vertically along the main axis of the cylinder and has transition frequency $\omega_{\text{acc}} = 1.51\,\text{eV}$, in the region where the roll absorbs (see Fig. 8.2). The external field which interacts with donors is polarized along the z' direction. The energy flux is normalized by the number of donor molecules squared, N^2_{donor}. In these calculations,

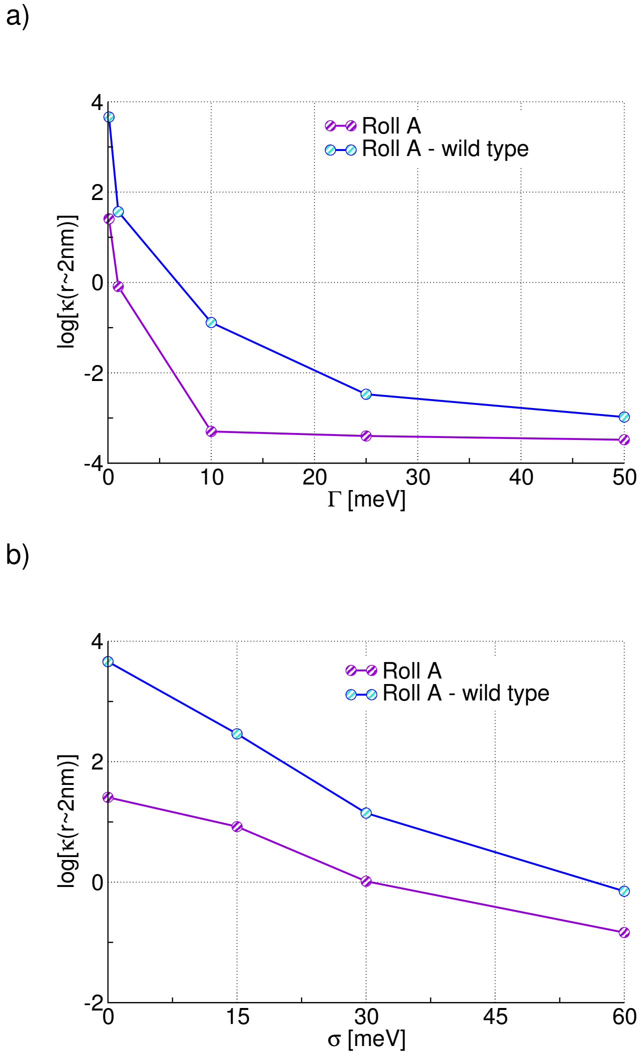

Figure 8.6: Panel **a**) scaling of field enhancement κ with dynamical noise rate Γ for each structure, at a distance of $r_{\text{phys}} = 2\,\text{nm}$. Panel **b**) scaling of field with structural disorder σ for each structure, at a distance of $r_{\text{phys}} = 2\,\text{nm}$. The incoming field is polarized along the z' direction. Roll-A and Roll-A wild type, correspond to the structures in panels III-a) and b) of Fig. 8.1.

the dynamic disorder rate $\Gamma = 50\,\mathrm{meV}$. We notice that the energy flux $R(t)$ does not decrease monotonically with distance, in fact there are some distances more favorable for transfer. This can be explained by the fact that the components of the field at each distance are not the same but may rotate. This effect can be thought of as some type of coherence between acceptor and donor.

We also computed the flux of energy transferred between two concentric cylindrical structures (Structure of Fig. 8.1, panel II-a) for an external field polarized along the z' direction. The resulting fluxes are shown in Fig. 8.7, panel b) for two different values of the dynamic rate constant Γ. Here, R_A indicates the flux when roll-A (the roll with the smaller diameter) is the acceptor and roll-B the donor and R_A indicates the opposite case. When $\Gamma = 50\,\mathrm{meV}$, *i.e.* the incoherent limit, the fluxes from roll-A and B are equivalent, as expected and decay within $300\,\mathrm{fs}$. When the disorder is decreased, the flux is much larger and decays fully only after about $800\,\mathrm{fs}$. Further, in this case the fluxes are different in each direction (from roll-A to B and from B to A). This model however does not account for relaxation, therefore the estimated fluxes should be considered upper bounds of the actual rates.

8.3 Conclusions

We have analyzed the chlorosome antenna complex in the green sulfur bacteria Chlorobium-tepidum using an electrodynamic model. Three structures were considered as models for the natural chlorosome complex. Each antenna structure shows robustness to structural variations. This effect was seen in the values of the field enhancement which is much more sensitive to noise than to structural disorder.

At the physiological distance, the minimum distance observed for packing amongst nanostructures, the field enhancement trend follows different slopes as a function of disorder. Therefore no clear trend regarding variations of induced fields and polarization as a function of disorder can be deduced. However, at this same distance, the wild type nanostructure antenna shows larger field enhancement. This suggests that the molecular packing can be tuned to maximize transport properties. A preferential direction for transfer is observed consistently for all structures for specific polarizations. This suggests that this type of structure acts as a concentrator by enhancing transport for specific photon polarizations. This is also confirmed by the patterns of field depolarization which

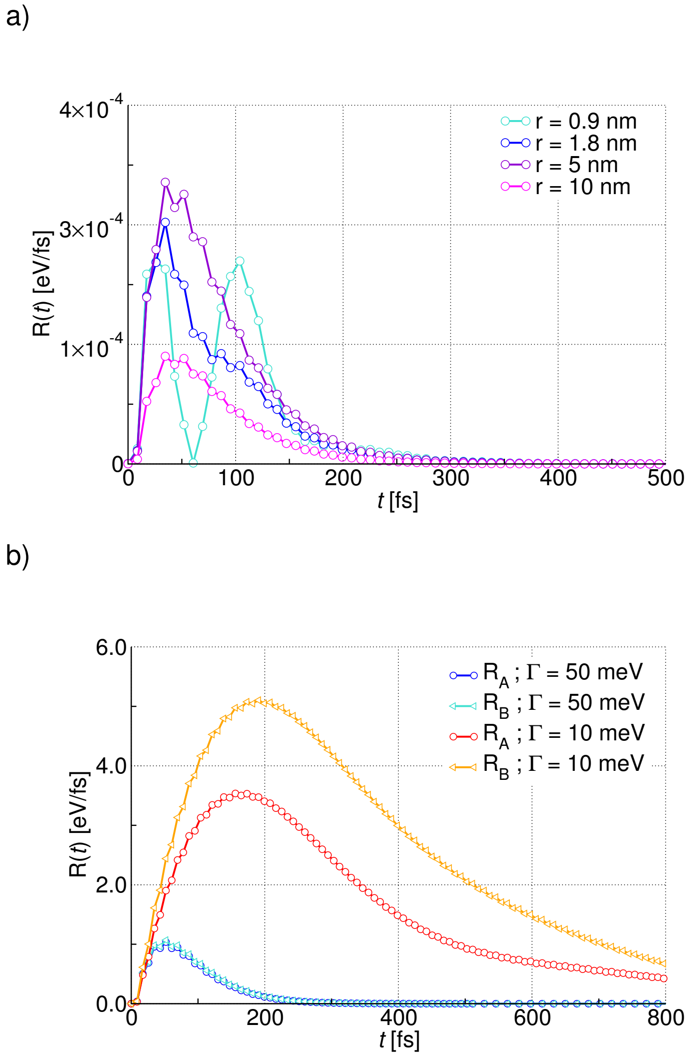

Figure 8.7: Panel **a**) Flux of energy transferred from roll-A (Fig. 8.1, III-a) to a single dipole acceptor, oriented along the z direction and located at various distances r from the outside of the roll along the radial direction, here $\Gamma = 50\,\mathrm{meV}$. Panel **b**) Flux of energy transferred from roll-A to roll-B, $R_B(t)$ and from roll-B to roll-A, $R_A(t)$ for different values of the dynamic noise constant Γ. The incoming field is polarized along the z' direction.

strongly depend on initial field polarization but not on structural variations. In particular we observe that the field is concentrated in the radial direction and at the edges of the cylinders (depending of the incoming field polarization), which would enable exciton transport to neighboring structures and to other layers. The field depolarization also supports transport to neighboring layers. Finally, transport has been quantified by calculating the flux of electromagnetic energy transferred between the cylindrical structure and a dipole acceptor. In this case there is a specific distance which maximizes transport. One can think of it in terms of coherence amongst the donor field polarization and the acceptor molecule dipole orientation. The timescale for the flux of energy transfer is roughly 300 fs which is an upper bound to the true timescale, in fact the model does not account for relaxation. We also computed these fluxes of energy for transfer amongst cylindrical structures and found that depending on dynamic noise, it is enhanced in the radial direction. This study opens the road to the possibility of creating antennae that mimic this type of natural system. For instance, we could consider the idea of the chlorosome outside of its natural environment: if one could devise a nanoantenna based on the structural arrangement of dipoles in the chlorosome, how efficient would it be?

8.4 Methods

8.4.1 Physical model of the chlorosome structure

In this section, we describe the structures employed as models of the chlorosome in more detail. In both of the molecular packing motifs employed to construct the chlorosome structures, BChl molecules are stacked in columns such that the oxygen from the hydroxyl, OH, group of one molecule, see Fig. 8.1 panel II-b), binds to the Mg atom of the next molecule [179]. The columns of BChl molecules couple to each other through $\mathrm{OH} \cdots \mathrm{O}$ hydrogen bonds thus forming two dimensional layers (this is shown in Fig. 8.8). These layers are then folded to form cylinders or curved lamellar structures [184]. Two distinct types of layer folding have been proposed previously. In Ref. [185] the authors suggested that BChl layers are folded such that BChl columns form concentric rings. This structure was obtained by fitting the 2D nuclear magnetic resonance (NMR) spectra of mutant Chlorobium tepidum bacteria which produce chlorosomes with BChl-d molecules. This packing motif was also supported by cryo-electron microscopy images [295]. The first structure we consider (III-a in Fig. 8.1) comes from these studies. In contrast, in Ref. 183 the same group of authors used a different folding pattern, where BChl columns are parallel to the cylinder's symmetry

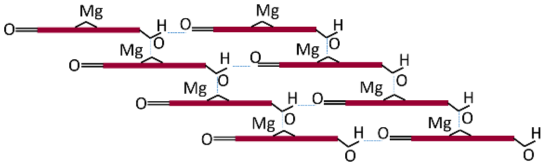

Figure 8.8: Two columns of BChl molecules linked together through a network of hydrogen bonds.

axis. The latter structure was also supported by 2D NMR studies of a different mutant bacteria, which is more similar to wild-type species (the chlorosome was packed with BChl-c). The choice of these cylindrical structures is also bolstered by recent 2D fluorescence polarization microscopy experiments [186].

We used this second type of folding to obtain the second structure, *i.e* III-b in Fig. 8.1. Finally, the layer structures are packed inside of an ellipsoidal shaped body: the chlorosome. While the chlorosome may contain multiple rolls packed in parallel [163], here we use a different model (structure III-c in in Fig. 8.1) which is composed of concentric rolls [184]. This concentric assembly is in-line with the cryo-EM images [295].

In the electromagnetic model, each molecule is represented by a transition dipole, in particular we use the Q_y transition dipole. The frequency of the transition [298] is taken to be $\omega_0 = 1.904\text{eV}$ for BChl-d and $\omega_0 = 1.881\text{eV}$ for BChl-c as obtained experimentally. The dipole intensity is taken to be $\mu = 5.48\,\text{D}$, following the values given in literature, *e.g.* Ref. 299,22,163.

8.4.2 Polarizability model

The system considered is an array of aggregated BChl monomers (as shown in Fig. 8.1). In quantum models, a Hamiltonian in the molecule localized basis $|n\rangle$ is often used to describe this type of system

$$\hat{H}_0 = \sum_n \epsilon_n |n\rangle\langle n| + \sum_{n<m} J_{nm} \left(|n\rangle\langle m| + |m\rangle\langle n|\right). \tag{8.2}$$

The energy ϵ_n of the $n - th$ monomer is typically taken to be the first excited state energy, and all higher excited states are ignored. Such approximation is valid so long as the higher energy states of the monomers are well separated from the first. This energy corresponds to the Q_y transition for BChl's. J_{mn} indicates the coupling between monomers and $|n\rangle$ is the localized basis in which the $n - th$ molecule is excited. When the molecules interact with radiation, an extra interaction term with the field must be added to this expression V_{field}, so that the overall Hamiltonian can be divided into a time independent Hamiltonian $\hat{H}_0$ and a time dependent interaction term V_{field}. $\hat{H}(t) = \hat{H}_0 + V_{\text{field}}(t)$. One can then write an equation of motion for the system density matrix as a function of the Hamiltonian and solve it perturbatively in orders of interaction with the field. From the density matrix equation optical properties can be obtained (Sec. Optical properties).

A similar approach can be followed using molecular polarizabilities. Each molecular transition s is approximately described by an electronic transition dipole $\vec{\mu}_{n,s}$ (for the $n-th$ molecule) [297, 300], and the frequency of the transition is taken to be $\omega_{n,s} = \epsilon_{n,s}/\hbar$. The expression for the overall electric field at the $n-th$ molecule located at $\vec{x}_n$ is the sum of the internal field $\vec{E}_{\text{int}}$ which comes from the interactions with all other dipoles and the external field $\vec{E}_{\text{ext}}$,

$$\vec{E}(t,\vec{x}_n) = \vec{E}_{\text{int}}(t,\vec{x}_n) + \vec{E}_{\text{ext}}(t,\vec{x}_n). \tag{8.3}$$

In particular, in the case of classical dipoles this equation can be written as [297]

$$\vec{E}(t,\vec{x}_n) = 4\pi k^2 \sum_{m\neq n} \mathbf{G}\left(\vec{x}_m,\vec{x}_n\right)\cdot\vec{p}_n + \vec{E}_{\text{ext}}(t,\vec{x}_n). \tag{8.4}$$

Here, $\vec{p}_n$ is the induced electric dipole moment at molecule n due to the electric field and the constant k is the magnitude of the wavevector of the incident light. The free-space Green's function tensor $\mathbf{G}$ includes all interactions amongst dipoles and is directly proportional to the field at point $\vec{x}$ due to a dipole oscillating at position $\vec{x}_n$. It is expressed as

$$\mathbf{G}(\vec{x}_m,\vec{x}_n) = g(r)\left[(\mathbf{1}-\vec{e}\vec{e}) - \left(\frac{1-ikr}{k^2r^2}\right)(\mathbf{1}-3\vec{e}\vec{e})\right] - \frac{\mathbf{1}}{3\epsilon_0 k^2}\delta^3\left(\vec{r}\right), \tag{8.5}$$

with $g(r) = \exp(ikr)/(4\pi\epsilon_0 r)$. In Eq. 8.5 the last term compensates for self-interaction. The unit vector $\vec{e}$ is defined as $\vec{e} = \frac{\vec{r}}{r}$ with $\vec{r} = \vec{x}_m - \vec{x}_n$ and $r = |\vec{r}|$. The field at each molecule and the polarization can be obtained by solving the linear system of equations (Eq. 8.4) with $n = 1, ..., N$ where N is the number of molecules in the aggregate. Details of how these equations can be solved efficiently for large systems can be found in Ref. [290]. The field enhancements and depolarizations as presented in the “Results” section, are obtained by solving for the induced dipole moments of all the molecules (Eq. 8.4).

8.4.3 Optical properties

Linear absorption

Using the formalism introduced in "Polarizability model " section, an equation for the induced electric dipole $\vec{p}$ on each molecule can be obtained as a function of the index of refraction [297, 300]. In the limit of the dipole approximation, the expression for the molar extinction coefficient is then

$$\epsilon_{\mathrm{abs}} = -\frac{4\pi\omega}{3000 \cdot \ln(10)c}\mathcal{N}_{\mathrm{av}} \sum_{ij} \mathrm{Im}\mathbf{A}_{ij}\vec{u}_i \cdot \vec{u}_j, \tag{8.6}$$

with $\vec{u}_i = \frac{\vec{\mu}_i}{|\vec{\mu}_i|}$. Here the matrix $\mathbf{A}$ is defined as

$$\mathbf{A}_{ij} = \left[\frac{\delta_{ij}}{\chi_i} + \mathbf{D}_{ij}\right]^{-1}, \tag{8.7}$$

with $\mathbf{D}_{ij} = \vec{u}_i \cdot \mathbf{G}_{ij} \cdot \vec{u}_j$, the term which includes dipole-dipole interactions and χ_i the molecular response function as defined in Eq. 8.1. In the limit of static dipole interactions, the tensor $\mathbf{G}$ takes the simple form $\mathbf{G}_{ij} \equiv \mathbf{G}\left(\vec{x}_i, \vec{x}_j\right) = \frac{3\vec{e}\vec{e}-1}{r^3}$.

To better understand where resonances occur, we can look at the eigenvalues of $\mathbf{A}$. For zero dynamical noise rate Γ and for identical molecules ($\vec{\mu}_k \equiv \vec{\mu}$, $\omega_k = \omega_{\mathrm{mol}}$) we see that resonances are the roots of

$$\Omega^2_{\mathrm{agg},k} \equiv \omega^2_{\mathrm{mol}} + 2\frac{|\vec{\mu}|^2}{\hbar}\gamma_k\omega_{\mathrm{mol}}. \tag{8.8}$$

Here, γ_k is the $k-th$ eigenvalue of $\mathbf{G}$. We can define $\frac{|\vec{\mu}|^2}{\hbar}\gamma_k = \tilde{\gamma}_k$ to get proper units of energy for the coupling. Thus $\Omega^2_{\mathrm{agg},k} \equiv \omega^2_{\mathrm{mol}} + 2\tilde{\gamma}_k\omega_{\mathrm{mol}}$. In this expression it is clear that the aggregate resonances will be shifted respect to the molecular transition frequency ω_{mol} and this shift will depend on the coupling between monomers, here captured by γ_k. Eq. 8.6 was employed to compute the linear absorption spectrum shown in Fig. 8.2. A similar approach, the CES method, has also been used for excitonic systems [239] and leads essentially to the same equations that are used in the present work.

Now, in the quantum case, the simplest approach to obtain the absorption spectrum consists in applying Fermi's Golden rule

$$\epsilon^{(\mathrm{qtm})}_{\mathrm{abs}}\left(\omega\right) = \frac{4\pi\omega}{3c}\sum_k |\vec{\mu}|^2 \pi\delta\left(E_k - \hbar\omega\right), \tag{8.9}$$

here, E_k is the $k-th$ eigenvalue of the Hamiltonian given in Eq. 8.2 and $\vec{\mu}$ is it's transition dipole. In this case resonances in the aggregate spectrum will be obtained as the roots of $\Omega^2_{\text{agg,k}} = E_k^2/\hbar^2 = (\omega_{\text{mol}} + \tilde{\gamma}_k)^2$. The expression given in Eq. 8.9 is the one used to compute the quantum absorption spectrum shown in Fig. 8.2. We see that respect to the classical case (Eq. 8.8), the frequencies squared are shifted by $\tilde{\gamma}_k^2$: this comes from the absence of counter rotating terms in the classical response function [296]. In fact, in classical electromagnetics only one type of time ordering of interactions between photons and molecules is allowed. For optical frequencies the counter-rotating term only gives a small shift, however it becomes important for long wavelengths, for instance, in microwave cavities. It should be noted that the counter-rotating term is still partly included in our model through the susceptibility functions of the single molecules. However, its contribution to the intermolecular interaction is not accounted for. Another way to see how the shift arises is by comparison of the eigenstates of a quantum Hamiltonian with the normal modes for a set of driven coupled classical oscillators. The comparison can be made after applying the Dirac mapping and realistic coupling (RCA) approximation. This approach has been discussed in Ref. [301]. The two approaches become equivalent in the limit where the couplings are small compared to the monomer transition frequency $\gamma_k \lll \omega_{\text{mol}}$.

Circular dichroism

Circular dichroism is another important optical quantity which can help identify the correct structure of a system. It can also be obtained both classically and quantum mechanically. Following the classical approach [297] of the previous sections, one can arrive at the following expression for the molar ellipticity

$$\theta = -\sum_{ij} \mathbf{C}_{ij} \mathrm{Im} \mathbf{A}_{ij}. \tag{8.10}$$

Here we have used the standard definition of CD, as the difference between left polarized and right polarized intensity. The matrix $\mathbf{C}$ is defined as

$$\mathbf{C}_{ij} = \frac{6\omega^2 \mathcal{N}_{\text{av}}}{c^2} \left(\vec{u}_i \times \vec{u}_j\right) \cdot \left(\vec{x}_i - \vec{x}_j\right) \tag{8.11}$$

in the absence of any magnetic dipoles or polarizations. Here, $\vec{x}_i$ corresponds to the position of the i-th molecule respect to the origin.

Similarly, in the quantum case one finds (see *e.g.* Ref. [302]) that in the exciton basis, *i.e.* the basis in which the Hamiltonian of Eq. 8.2 is diagonal, the rotation strength associated with the exciton level J is

$$R_J = -\frac{6\omega^2\mathcal{N}_{\mathrm{av}}}{c^2}\sum_{ik}\sigma_{Ji}\sigma_{Jk}\left(\vec{u}_i\times\vec{u}_j\right)\cdot\left(\vec{x}_i-\vec{x}_j\right). \tag{8.12}$$

The coefficients σ are the coefficients of the matrix $\mathbf{S}$ which diagonalizes the Hamiltonian of the system. Eq. 8.10 and eq. 8.12 are used in this work to compute the circular dichroism spectra shown in Fig. 8.2.

Conclusions and future work

Page intentionally left blank.

In the first part of this dissertation we discussed the use of atomistic models combined with open-quantum systems methods to study the exciton dynamics of the Fenna-Matthews-Olson complex. These theoretical tools proved powerful and able to provide insight in the physical factors which guide the exciton dynamics in this system. We also discussed the connection between the ground state QM/MM approach and the open-quantum system formalism and how one needs to proceed in order to maintain consistency. This is often a problem in theoretical chemistry when different communities merge to gain knowledge and methods from one another. In those cases, the exact connection between the theories may remain unexplored. Finally, for the first time, we studied the exciton dynamics of the entire light-harvesting complex of Chlorobaculum tepidum using an atomistic model.

Nonetheless, one question remains open. Although one observes some quantum effects in the exciton dynamics, it is as of yet unclear whether this happened serendipitously or whether this was something that nature selected for, as many have claimed. There have only been a few efforts to understand whether and how protein evolution might have influenced it. For instance, in ref. [23], the authors computed the BChl transition energies and looked at the effect of including the point charges coming from the protein or not. They also looked at how changes in polar groups of the amino acids, such as the amino or hydroxyl group, influence the BChl transition energies. They found that while the alpha helices seem to influence the energies strongly, modifications to side groups, such as those which would occur from a point mutation, played less of a role[iv]. From this, they concluded that the protein is robust to point mutations. In this work however, structures where not optimized after mutations and thus, the results might be inconclusive. Experimentally, the Blankenship group [87] looked at comparing the optical properties of FMO coming from three different species to understand the effect of the protein scaffold. The observed spectral differences were assigned to the way the BChl molecules bind to the protein scaffold in each specie. This suggests that mutations may play an important role in the exciton dynamics, especially those occurring in the vicinity of binding sites.

For the above reasons, I am currently investigating the protein complex from an evolutionary perspective. I have reconstructed the ancestral protein structure of the FMO complex as well as that of intermediates which connect the ancient protein to current day structures. My future work now consists in comparing the exciton transport efficiency for these structure and looking at the stability of all structures in terms of free energy upon folding. From this study it will be possible to establish whether the protein has evolved to optimize exciton transport or whether other factors such as biological fitness were more important. This work will also provide the possibility of designing biological exciton transport materials theoretically through selected mutations.

[iv] In particular they found that excluding the α-helix charge distribution lead to a shift in energies of $-300\,\mathrm{cm}^{-1}$ while changes in amino acid side chain distributions lead to shifts of $180\,\mathrm{cm}^{-1}$ at most. Within $2\,\mathrm{ps}$, the native system transfers 50% of the initial excitation to the lowest energy sites. For the "mutant" 40% of the excitation is transferred within that time and if one takes energies which come from excluding the charge distribution of the α-helix, only 20% of the excitation gets transferred.

Given the huge computational cost of ground state QM/MM simulations I have developed a trained neural network algorithm to predict the first excited state energy based on the Coulomb matrix obtained from MD. This approach was also described in the first part of the thesis. Here the main cost is in training the network but once trained, energy trajectories can be obtained within seconds. This will be very helpful for the study of mutations. It would also be useful to determine which mutations have the strongest effect on exciton dynamics and whether one can tune future evolution towards increased exciton transport or coherence.

This idea is connected to the second part of the dissertation were model exciton transport materials are investigated to establish the physical parameters which lead to enhanced transport. Here we looked at a series of cyanine dye thin-film J-aggregates and found that with the model employed, molecular properties such as molecular couplings and transition dipoles were the determining factors for exciton transport. This same conclusion was true for the cylindrical aggregate models which were studied using classical electrodynamics in Chapter 8.

Bibliography

[1] R. E. Blankenship. *Molecular Mechanisms of Photosynthesis*. World Scientific, London, 2002.

[2] J. T. Beatty, M. T. Lince, A. K. Manske, A S Lang, R. E. Blankenship, C. L. Van Dover, T. A. Martinson, and F. G. Plumley. An obligately photosynthetic bacterial anaerobe from a deep-sea hydrothermal vent. *Proc. Natl. Acad. Sci.*, 102:9306–9310, 2005.

[3] M. F. Hohmann-Marriott and R. E. Blankenship. Evolution of photosynthesis. *Annu. Rev. Plant Biol.*, 62:515–48, 2011.

[4] T. P. Causgrove, D. C. Brune, and R. E. Blankenship. Förster energy transfer in chlorosomes of green photosynthetic bacteria. *J. Photochem. Photobiol. B: Biol.*, 15:171–9, 1992.

[5] G. S. Engel. Quantum coherence in photosynthesis. *Procedia Chem.*, 3:222–231, 2011.

[6] P. Benoit, D. Abramavicius, and S. Mukamel. Lindblad equations for strongly coupled populations and coherences in photosynthetic complexes. *J. Chem. Phys.*, 130:204512, 2009.

[7] Y. Xin, S. Lin, G. A. Montaño, and R. E. Blankenship. Purification and characterization of the B808-866 light-harvesting complex from green filamentous bacterium Chloroflexus aurantiacus. *Photosynth. Res.*, 86:155–63, 2005.

[8] L. Valkunas, J. Chmeliov, G. Trinkunas, C. D. P. Duffy, R. van Grondelle, and A. V. Ruban. Excitation migration, quenching, and regulation of photosynthetic light harvesting in photosystem II. *J. Phys. Chem. B*, 115:9252–60, 2011.

[9] R. E. Fenna, B. W. Matthews, J. M. Olson, and E. K. Shaw. Structure of a bacteriochlorophyll-protein from the green photosynthetic bacterium Chlorobium limicola: Crystallographic evidence for a trimer. *J. Mol. Biol.*, 84:231–240, 1974.

[10] R. E. Fenna and B. W. Matthews. Chlorophyll arrangement in a bacteriochlorophyll protein from Chlorobium limicola. *Nature*, 258:573–577, 1975.

[11] J. Wen, Y. Tsukatani, W. Cui, H. Zhang, M. L. Gross, D. A. Bryant, and R. E. Blankenship. Structural model and spectroscopic characteristics of the FMO antenna protein from the aerobic chlorophototroph, Candidatus Chloracidobacterium thermophilum. *BBA-Bioenergetics*, 1807:157–164, 2011.

[12] G. T. Oostergetel, H. van Amerongen, and E. J. Boekema. The chlorosome: a prototype for efficient light harvesting in photosynthesis. *Photosynth. Res.*, 104:245–255, 2010.

[13] M. Ø. Pedersen, J. Linnanto, N.-U. Frigaard, and N. C. Nielsen, N. C. Nielsen. A model of the protein-pigment baseplate complex in chlorosomes of photosynthetic green bacteria. *Photosynth. Res.*, 104:233–43, 2010.

[14] J. M. Olson. The fmo protein. *Photosynth. Res.*, 80:181–187, 2004.

[15] J. Deisenhofer, O. Epp, K. Miki, R. Huber, and H. Michel. X-ray structure analysis of a membrane protein complex: Electron density map at 3Å resolution and a model of the chromophores of the photosynthetic reaction center from Rhodopseudomonas viridis. *J. Mol. Biol.*, 180:385–398, 1984.

[16] W. Kühlbrandt, D. N. Wang, and Y. Fujiyoshi. Atomic model of plant light-harvesting complex by electron crystallography. *Nature*, 367:614, 1994.

[17] G. McDermott, S. M. Prince, A. A. Freer, A. M. Hawthornthwaite-Lawless, M. Z. Papiz, R. J. Cogdell, and N. Isaacs. Crystal structure of an integral membrane light-harvesting complex from photosynthetic bacteria. *Nature*, 374:517, 1995.

[18] N. Krauss, W.-D. Schubert, O. Klukas, P. Fromme, H. T. Witt, and W. Saenger. Photosystem I at 4 Ångstrom resolution represents the first structural model of a joint photosynthetic reaction centre and core antenna system. *Nature Struct. Biol.*, 3:965, 1996.

[19] D. Gülen. Interpretation of the excited-state structure of the Fenna-Matthews-Olson pigment protein complex of Prosthecochloris aestuarii based on the simultaneous simulation of the 4 K absorption, linear dichroism, and singlet-triplet absorption difference spectra: A possible excitonic explanation? *J. Phys. Chem.*, 100:17683–17689, 1996.

[20] S. Savikhin, D. R. Buck, and W. S. Struve. Pump-probe anisotropies of Fenna-Matthews-Olson protein trimers from Chlorobium tepidum: a diagnostic for exciton localization? *Biophys. J.*, 73:2090–6, 1997.

[21] M Wendling, T Pullerits, M. A. Przyjalgowski, S. I. E. Vulto, T. J. Aartsma, R. van Grondelle, and H. van Amerongen. Electron-vibrational coupling in the Fenna-Matthews-Olson complex of Prosthecochloris aestuarii determined by temperature-dependent absorption and fluorescence line-narrowing measurements. *J. Phys. Chem. B*, 104:5825–5831, 2000.

[22] J. Adolphs and T. Renger. How proteins trigger excitation energy transfer in the FMO complex of green sulfur bacteria. *Biophys. J.*, 91:2778–2797, 2006.

[23] F. Müh, M. E-A. Madjet, J. Adolphs, A. Abdurahman, B. Rabenstein, H. Ishikita, E-W. Knapp, and T. Renger. Alpha-helices direct excitation energy flow in the Fenna-Matthews-Olson protein. *Proc. Natl. Acad. Sci.*, 104:16862–7, 2007.

[24] E. L. Read, G. S. Schlau-Cohen, G. S. Engel, J. Wen, R. E. Blankenship, and G. R. Fleming. Visualization of excitonic structure in the Fenna-Matthews-Olson photosynthetic complex by polarization-dependent two-dimensional electronic spectroscopy. *Biophys. J.*, 95:847–856, 2008.

[25] S. Shim, P. Rebentrost, S. Valleau, and A. Aspuru-Guzik. Atomistic study of the long-lived quantum coherences in the Fenna-Matthews-Olson complex. *Biophys. J.*, 102:649 – 660, 2012.

[26] G. S. Engel, T. R. Calhoun, E. L. Read, T. K. Ahn, T. Mancal, Y. C. Cheng, R. E. Blankenship, and G. R. Fleming. Evidence for wavelike energy transfer through quantum coherence in photosynthetic systems. *Nature*, 446:782–786, 2007.

[27] A. Olaya-Castro, C. Lee, F. Olsen, and N. Johnson. Efficiency of energy transfer in a light-harvesting system under quantum coherence. *Phys. Rev. B*, 78:085115, 2008.

[28] A. Ishizaki and G. R. Fleming. Theoretical examination of quantum coherence in a photosynthetic system at physiological temperature. *Proc. Natl. Acad. Sci.*, 106:17255–17260, 2009.

[29] A. Ishizaki and G. R. Fleming. Unified treatment of quantum coherent and incoherent hopping dynamics in electronic energy transfer: reduced hierarchy equation approach. *J. Chem. Phys.*, 130:234111, 2009.

[30] A. Ishizaki and G. R. Fleming. On the adequacy of the Redfield equation and related approaches to the study of quantum dynamics in electronic energy transfer. *J. Chem. Phys.*, 130:234110, 2009.

[31] P. Rebentrost, M. Mohseni, and A. Aspuru-Guzik. Role of quantum coherence and environmental fluctuations in chromophoric energy transport. *J. Phys. Chem. B.*, 113:9942–9947, 2009.

[32] F. Fassioli and A. Olaya-Castro. Distribution of entanglement in light-harvesting complexes and their quantum efficiency. *New J. Phys.*, 12:085006, 2010.

[33] C. Olbrich, T. L. C. Jansen, J. Liebers, M. Aghtar, J. Strümpfer, K. Schulten, J. Knoester, and U. Kleinekathöfer. From atomistic modeling to excitation transfer and two-dimensional spectra of the FMO light-harvesting complex. *J. Phys. Chem. B*, 115:8609–21, 2011.

[34] L. A. Pachón and P. Brumer. Physical basis for long-lived electronic coherence in photosynthetic light-harvesting systems. *J. Phys. Chem. Lett.*, 2:2728–2732, 2011.

[35] A. Ishizaki and G. R. Fleming. On the interpretation of quantum coherent beats observed in two-dimensional electronic spectra of photosynthetic light harvesting complexes. *J. Phys. Chem. B*, 115:6227–6233, 2011.

[36] J. Yuen-Zhou, J. J. Krich, M. Mohseni, and A. Aspuru-Guzik. Quantum state and process tomography of energy transfer systems via ultrafast spectroscopy. *Proc. Natl. Acad. Sci.*, 108:17615–20, 2011.

[37] P. Rebentrost, S. Shim, J. Yuen-Zhou, and A. Aspuru-Guzik. Characterization and quantification of the role of coherence in ultrafast quantum biological experiments using quantum master equations, atomistic simulations, and quantum process tomography. *Procedia Chemistry*, 3:332–346, 2011.

[38] I. Kassal, J. Yuen-Zhou, and S. Rahimi-Keshari. Does coherence enhance transport in photosynthesis? *J. Phys. Chem. Lett.*, 4:362–367, 2013.

[39] P. Rebentrost, R. Chakraborty, and A. Aspuru-Guzik. Non-markovian quantum jumps in excitonic energy transfer. *J. Chem. Phys.*, 131:184102, 2009.

[40] J. Moix, J. Wu, P. Huo, D. Coker, and J. Cao. Efficient energy transfer in light-harvesting systems, III: The influence of the eighth bacteriochlorophyll on the dynamics and efficiency in FMO. *J. Phys. Chem. Lett.*, 2:3045–3052, 2011.

[41] E. E. Jelley. Spectral absorption and fluorescence of dyes in the molecular state. *Nature*, 138:1009–1010, 1936.

[42] G. Scheibe. *Angew. Chem.*, 49:563, 1936.

[43] D. A. Higgins, P. J. Reid, and P. F. Barbara. Structure and exciton dynamics in J-aggregates studied by polarization-dependent near-field scanning optical microscopy. *J. Phys. Chem.*, 100:1174–1180, 1996.

[44] F. Würthner, T. E. Kaiser, and C. R. Saha-Möller. J-aggregates: From serendipitous discovery to supramolecular engineering of functional dye materials. *Angew. Chem. Int. Ed.*, 50:3376–3410, 2011.

[45] S. T. Smiley, M. Reers, C. Mottola-Hartshorn, M. Lin, A. Chen, and T. W. Smith. Intracellular heterogeneity in mitochondrial membrane potentials revealed by a J-aggregate forming lipophilic cation JC-1. *Proc. Natl. Acad. Sci.*, 88:3671–3675, 1991.

[46] T. H. James. *The Theory of the Photographic Process*. Macmillian, New York, 1977.

[47] K. Saito. Quenching of excited J-aggregates on metals by surface plasmon excitations. *J. Phys. Chem. B*, 103:6579–6583, 1999.

[48] K. Sayama, S. Tsukagoshi, K. Hara, Y. Ohga, A. Shinpou, Y. Abe, S. Suga, and H. Arakawa. Photoelectrochemical properties of J-aggregates of benzothiazole merocyanine dyes on a nanostructured TiO_2 film. *J. Phys. Chem. B*, 106:1363–1371, 2002.

[49] D. Lidzey, D. Bradley, T. Virgili, A. Armitage, M. Skolnick, and S. Walker. Room temperature polariton emission from strongly coupled organic semiconductor microcavities. *Phys. Rev. Lett.*, 82:3316–3319, 1999.

[50] J. Bellessa, C. Bonnand, J. C. Plenet, and J. Mugnier. Strong coupling between surface plasmons and excitons in an organic semiconductor. *Phys. Rev. Lett.*, 93:036404, 2004.

[51] G. M. Akselrod, Y. Tischler, E. R. Young, D. G. Nocera, and V. Bulovic. Exciton-exciton annihilation in organic polariton microcavities. *Phys. Rev. B*, 82:113106, 2010.

[52] B. J. Walker, V. Bulović, and M. G. Bawendi. Quantum dot/j-aggregate blended films for light harvesting and energy transfer. *Nano Lett.*, 10:3995–3999, 2010.

[53] Volkhard May and Oliver Kühn. *Charge and Energy Transfer Dynamics in Molecular Systems*. Wiley-VCH Verlag, Weinheim, 2004.

[54] V. V. Egorov. Theory of the J-band: from the frenkel exciton to charge transfer. *Physics procedia*, 2:223–326, 2009.

[55] V. Bulovic, M. A. Baldo, and S. R. Forrest. *Organic electronic materials: Conjugated polymers and low molecular weight organic Solids*, chapter Excitons and Energy transfer in doped luminescent molecular organic materials, pages 391–439. Springer series in materials science, 2001.

[56] T. Föster. Zwischenmolekulare energiewanderung und fluoreszenz. *Ann. Phys.*, 437:55–75, 1948.

[57] T. Förster. *Modern Quantum Chemistry*, chapter Delocalized excitation and excitation transfer, pages 93–137. New York and London: Academic Press, 1965.

[58] S. Saikin, A. Eisfeld, S. Valleau, and A. Aspuru-Guzik. Photonics meets excitonic: natural and artificial molecular aggregates. *Nanophotonics*, 2:21–38, 2012.

[59] A. A. Deniz, M. Dahan, J. R. Grunwell, T. Ha, A. E. Faulhaber, D. S. Chemla, S. Weiss, and P. G. Schultz. Single-pair fluorescence resonance energy transfer on freely diffusing molecules: Observation of Förster distance dependence and subpopulations. *Proc. Natl. Acad. Sci.*, 96:3670–3675, 1999.

[60] P. Andrew and W. L. Barnes. Förster energy transfer in an optical microcavity. *Science*, 290:785–788, 2000.

[61] D. M. Willard, L. L. Carillo, J. Jung, and A. Van Orden. CdSe-ZnS quantum dots as resonance energy transfer donors in a model protein-protein binding assay. *Nano*, 1:469–474, 2001.

[62] J. Hofkens, M. Cotlet, T. Vosch, P. Tinnefeld, K. D. Weston, C. Ego, A. Grimsdale, K. Müllen, D. Beljonne, J.-L. Brédas, S. Jordens, G. Schweitzer, M. Sauer, and F. De Schryver. Revealing competitive Förster-type resonance energy-transfer pathways in single bichromophoric molecules. *Proc. Natl. Acad. Sci.*, 100:13146–13151, 2003.

[63] H.-P. Breuer and F. Petruccione. *The Theory of Open Quantum Systems*. Oxford University Press, New York, 2002.

[64] V. M. Agranovich and G. F. Bassani. *Electronic Excitations in Organic Based Nanostructures. Thin Films and Nanostructures, vol. 31*. Elsevier Academic Press, 2003.

[65] H. J. Carmicheal. *Statistical Methods in Quantum Optics 1: Master equations and Fokker-Planck equations*. Springer, 1999.

[66] A. G. Redfield. On the theory of relaxation processes. *IBM J. Res. Dev.*, 1:19–31, 1957.

[67] N. G. Van Kampen. *Stochastic processes in physics and chemistry*. North-Holland personal library. Elsevier, 2007.

[68] H. Haken and P. Reineker. The coupled coherent and incoherent motion of excitons and its influence on the line shape of optical absorption. *Z. Phys.*, 249:253–268, 1972.

[69] H. Haken and G. Strobl. An exactly solvable model for coherent and incoherent exciton motion. *Z. Phys.*, 262:135–148, 1973.

[70] J. Zhu, S. Kais, P. Rebentrost, and A. Aspuru-Guzik. Modified scaled hierarchical equation of motion approach for the study of quantum coherence in photosynthetic complexes. *J. Phys. Chem. B.*, 115:1531–1537, 2011.

[71] H. Lee, Y.-C. Cheng, and G. R. Fleming. Coherence dynamics in photosynthesis: Protein protection of excitonic coherence. *Science.*, 316:1462–1465, 2007.

[72] G. Panitchayangkoon, D. Hayes, K. A. Fransted, J. R. Caram, E. Harel, J. Wen, R. E. Blankenship, and G. S. Engel. Long-lived quantum coherence in photosynthetic complexes at physiological temperature. *Proc. Natl. Acad. Sci.*, 107:12766–12770, 2010.

[73] P. Rebentrost, M. Mohseni, I. Kassal, S. Lloyd, and A. Aspuru-Guzik. Environment-assisted quantum transport. *New J. Phys.*, 11:033003, 2009.

[74] M. B. Plenio and S. F. Huelga. Dephasing-assisted transport: quantum networks and biomolecules. *New J. Phys.*, 10:113019, 2008.

[75] S. Jang, Y.-C. Cheng, D. R. Reichman, and J. D. Eaves. Theory of coherent resonance energy transfer. *J. Chem. Phys.*, 129:101104, 2008.

[76] J. Strumpfer and K. Schulten. Light harvesting complex II B850 excitation dynamics. *J. Chem. Phys.*, 131:225101, 2009.

[77] A. M. Virshup, C. Punwong, T. V. Pogorelov, B. A. Lindquist, C. Ko, and T. J. Martínez. Photodynamics in complex environments: Ab initio multiple spawning quantum mechanical/molecular mechanical dynamics. *J. Phys. Chem. B.*, 113:3280–3291, 2009.

[78] F. Caruso, A. W. Chin, A. Datta, S. F. Huelga, and M. B. Plenio. Highly efficient energy excitation transfer in light-harvesting complexes: The fundamental role of noise-assisted transport. *J. Chem. Phys.*, 131:105106, 2009.

[79] J. Wu, F. Liu, Y. Shen, J. Cao, and R. Silbey. Efficient energy transfer in light-harvesting systems, I: optimal temperature, reorganization energy and spatial-temporal correlations. *New J. Phys.*, 12:105012, 2010.

[80] A. G. Dijkstra and Y. Tanimura. Correlated fluctuations in the exciton dynamics and spectroscopy of DNA. *New J. Phys.*, 12:055005, 2010.

[81] F. Caruso, A. W. Chin, A. Datta, S. F. Huelga, and M. B. Plenio. Entanglement and entangling power of the dynamics in light-harvesting complexes. *Phys. Rev. A.*, 81:062346, 2010.

[82] M. Sarovar, G. R. Fleming, and K. B. Wahley. Quantum entanglement in photosynthetic light-harvesting complexes. *Nat. Phys.*, 6:462–467, 2010.

[83] M. Tamoi, T. Tabuchi, M. Demuratani, K. Otori, N. Tanabe, T. Maruta, and S. Shigeoka. Point mutation of a plastidic invertase inhibits development of the photosynthetic apparatus and enhances nitrate assimilation in sugar-treated arabidopsis seedlings. *J. Biol. Chem.*, 285:15399–15407, 2010.

[84] P. Jahns, M. Graf, Y. Munekage, and T. Shikanai. *Single point mutation in the Rieske iron-sulfur subunit of cytochrome b6/f leads to an altered pH dependence of plastoquinol oxidation in Arabidopsis*, volume 519, pages 99–102. Elsevier Science B.V., 2002.

[85] P. Pesaresi, D. Sandon, E. Giuffra, and R. Bassi. A single point mutation (e166q) prevents dicyclohexylcarbodiimide binding to the photosystem II subunit CP29. *FEBS Lett.*, 402:151–156, 1997.

[86] A. Freiberg, S. Lin, K. Timpmann, and R. E. Blankenship. Exciton dynamics in FMO bacteriochlorophyll protein at low temperatures. *J. Phys. Chem. B.*, 101:7211–7220, 1997.

[87] D. E. Tronrud, J. Wen, L. Gay, and R. E. Blankenship. The structural basis for the difference in absorbance spectra for the FMO antenna protein from various green sulfur bacteria. *Photosynth. Res.*, 100:79–87, 2009.

[88] S. I. E. Vulto, S. Neerken, R. J. W. Louwe, M. A. de Baat, J. Amesz, and T. J. Aartsma. Excited-state structure and dynamics in FMO antenna complexes from photosynthetic green sulfur bacteria. *J. Phys. Chem. B.*, 102:10630–10635, 1998.

[89] M. Schmidt am Busch, F. Müh, M. El-Amine Madjet, and T. Renger. The eighth bacteriochlorophyll completes the excitation energy funnel in the FMO protein. *J. Phys. Chem. Lett.*, 2:93–98, 2011.

[90] J. Gilmore and R. H. McKenzie. Quantum dynamics of electronic excitations in biomolecular chromophores: Role of the protein environment and solvent. *J. Phys. Chem. A.*, 112:2162–2176, 2008.

[91] W. D. Cornell, P. Cieplak, C. I. Bayly, I. R. Gould, K. M. Merz, D. M. Ferguson, D. C. Spellmeyer, T. Fox, J. W. Caldwell, and P. A. Kollman. A second generation force field for the simulation of proteins, nucleic acids, and organic molecules. *J. Am. Chem. Soc.*, 117:5179–5197, 1995.

[92] M. Ceccarelli, P. Procacci, and M. Marchi. An ab initio force field for the cofactors of bacterial photosynthesis. *J. Comp. Chem.*, 24:129–142, 2003.

[93] G. Ritschel, J. Roden, W. T. Strunz, A. Aspuru-Guzik, and A. Eisfeld. Absence of quantum oscillations and dependence on site energies in electronic excitation transfer in the Fenna–Matthews–Olson trimer. *J. Phys. Chem. Lett.*, 2:2912–2917, 2011.

[94] Y. Shao, L. F. Molnar, Y. Jung, J. Kussmann, C. Ochsenfeld, S. T. Brown, A. T.B. Gilbert, L. V. Slipchenko, S. V. Levchenko, D. P. O'Neill, R. A. DiStasio Jr, R. C. Lochan, T. Wang, G. J.O. Beran, N. A. Besley, J. M. Herbert, C. Yeh Lin, T. Van Voorhis, S. Hung Chien, A. Sodt, R. P. Steele, V. A. Rassolov, P. E. Maslen, P. P. Korambath, R. D. Adamson, B. Austin, J. Baker, E. F. C. Byrd, H. Dachsel, R. J. Doerksen, A. Dreuw, B. D. Dunietz, A. D. Dutoi, T. R. Furlani, S. R. Gwaltney, A. Heyden, S. Hirata, C.-P. Hsu, G. Kedziora, R. Z. Khalliulin, P. Klunzinger, A. M. Lee, M. S. Lee, W. Z. Liang, I. Lotan, N. Nair, B. Peters, E. I. Proynov, P. A. Pieniazek, Y. Min Rhee, J. Ritchie, E. Rosta, D. Sherrill, A. C. Simmonett, J. E. Subotnik, H. Lee Woodcock III, W. Zhang, A. T. Bell, A. K. Chakraborty, D. M. Chipman, F. J. Keil, A. Warshel, W. J. Hehre, H. F. Schaefer III, J. Kong, A. I. Krylov, P. M. W. Gill, and M. Head-Gordon. Advances in methods and algorithms in a modern quantum chemistry program package. *Phys. Chem. Chem. Phys.*, 8:3172–3191, 2006.

[95] C.-P. Hsu, Z.-Q. You, and H.-C. Chen. Characterization of the short-range couplings in excitation energy transfer. *J. Phys. Chem. C.*, 112:1204–1212, 2008.

[96] B. P. Krueger, G. D. Scholes, and G. R. Fleming. Calculation of couplings and energy-transfer pathways between the pigments of LH2 by the ab initio transition density cube method. *J. Phys. Chem. B*, 102:5378–5386, 1998.

[97] J. Dalibard, Y. Castin, and K. Mølmer. Wave-function approach to dissipative processes in quantum optics. *Phys. Rev. Lett.*, 68:580–583, 1992.

[98] J. Piilo, S. Maniscalco, K. Härkönen, and K.-A. Suominen. Non-markovian quantum jumps. *Phys. Rev. Lett.*, 100:180402, 2008.

[99] M. Wendling, M. Przyjalgowski, D. Gülen, S. Vulto, T. Aartsma, R. van Grondelle, and H. van Amerongen. The quantitative relationship between structure and polarized spectroscopy in the FMO complex of Prosthecochloris aestuarii: refining experiments and simulations. *Photosynth. Res.*, 71:99–123, 2002.

[100] Z. Vokácová and J. V. Burda. Computational study on spectral properties of the selected pigments from various photosystems: Structure transition energy relationship. *J. Phys. Chem. A.*, 111:5864–5878, 2007.

[101] A. J. Leggett, S. Chakravarty, A. T. Dorsey, Matthew P. A. Fisher, Anupam Garg, and W. Zwerger. Dynamics of the dissipative two-state system. *Rev. Mod. Phys.*, 59:1–85, 1987.

[102] R. M. Peralstein. *Theoretical Interpretation of Antenna Spectra*. CRC Press, New York, 1991.

[103] A. Damjanović, I. Kosztin, U. Kleinekathöfer, and K. Schulten. Excitons in a photosynthetic light-harvesting system: A combined molecular dynamics, quantum chemistry, and polaron model study. *Phys. Rev. E*, 65, 2002.

[104] C. Olbrich and U. Kleinekathöfer. Time-dependent atomistic view on the electronic relaxation in light-harvesting system II. *J. Phys. Chem. B*, 114:12427–37, 2010.

[105] P. Huo and D. F. Coker. Iterative linearized density matrix propagation for modeling coherent excitation energy transfer in photosynthetic light harvesting. *J. Chem. Phys.*, 133:184108, 2010.

[106] D. B. Percival and A. T. Walden. *Spectral Analysis for Physical Application*. Cambridge University Press, 1993.

[107] M. Cho, H. M. Vaswani, T. Brixner, J. Stenger, and G. R. Fleming. Exciton analysis in 2D electronic spectroscopy. *J. Phys. Chem. B*, 109:10542–10556, 2005.

[108] S. A. Egorov, K. F. Everitt, and J. L. Skinner. Quantum dynamics and vibrational relaxation. *J. Phys. Chem. A*, 103:9494–9499, 1999.

[109] G. Stock. Classical simulation of quantum energy flow in biomolecules. *Phys. Rev. Lett.*, 102:118301, 2009.

[110] J. L. Skinner and K. Park. Calculating vibrational energy relaxation rates from classical molecular dynamics simulations: Quantum correction factors for processes involving vibration-vibration energy transfer. *J. Phys. Chem. B*, 105:6716–6721, 2001.

[111] A. Nazir. Correlation-dependent coherent to incoherent transitions in resonant energy transfer dynamics. *Phys. Rev. Lett.*, 103:146404, 2009.

[112] D. Abramavicius and S. Mukamel. Exciton dynamics in chromophore aggregates with correlated environment fluctuations. *J. Chem. Phys.*, 134:174504, 2011.

[113] C. Olbrich, J. Liebers, and U. Kleinekathöfer. Modeling of light-harvesting in purple bacteria using a time-dependent Hamiltonian approach. *Phys. Status Solidi (B)*, 248:393–398, 2011.

[114] M. Mohseni, P. Rebentrost, S. Lloyd, and A. Aspuru-Guzik. Environment-assisted quantum walks in photosynthetic energy transfer. *J. Chem. Phys.*, 129:174106, 2008.

[115] Jianshu Cao and Robert J Silbey. Optimization of exciton trapping in energy transfer processes. *J. Phys. Chem. A*, 113:13825–38, 2009.

[116] D. Abramavicius and S. Mukamel. Quantum oscillatory exciton migration in photosynthetic reaction centers. *J. Chem. Phys.*, 133:064510, 2010.

[117] C. Kreisbeck, T. Kramer, M. Rodríguez, and B. Hein. High-performance solution of hierarchical equations of motion for studying energy transfer in light-harvesting complexes. *J. Chem. Theory Comput.*, 7:2166–2174, 2011.

[118] N. Skochdopole and D. A. Mazziotti. Functional subsystems and quantum redundancy in photosynthetic light harvesting. *J. Phys. Chem. Lett.*, 2:2989–2993, 2011.

[119] N. Singh and P. Brumer. Electronic energy transfer in model photosynthetic systems: Markovian vs. non-markovian dynamics. *Faraday Discuss.*, 153:41–50, 2011.

[120] N. Singh and P. Brumer. Non-markovian second-order quantum master equation and its markovian limit: Electronic energy transfer in model photosynthetic systems. *arXiv:1106.5911v1*, 2011.

[121] S. Vlaming and R. J. Silbey. Correlated interaction fluctuations in photosynthetic complexes. *arXiv:1111:3627v1*, 2011.

[122] M. Mohseni, A. Shabani, S. Lloyd, and H. Rabitz. Optimal and robust energy transport in light-harvesting complexes:(II) a quantum interplay of multichromophoric geometries and environmental interactions. *arXiv:1104.4812v1*, 2011.

[123] G. Ritschel, J. Roden, W. T. Strunz, and A. Eisfeld. An efficient method to calculate excitation energy transfer in light-harvesting systems: application to the Fenna-Matthews-Olson complex. *New J. Phys.*, 13:113034, 2011.

[124] Seogjoo Jang, Marshall D. Newton, and Robert J. Silbey. Multichromophoric Förster resonance energy transfer from B800 to B850 in the light harvesting complex 2: Evidence for subtle energetic optimization by purple bacteria. *J. Phys. Chem. B*, 111:6807–6814, 2007.

[125] J. Roden, A. Eisfeld, W. Wolff, and W. Strunz. Influence of complex exciton-phonon coupling on optical absorption and energy transfer of quantum aggregates. *Phys. Rev. Lett.*, 103:058301, 2009.

[126] I. de Vega. Non-markovian stochastic schrödinger description of transport in quantum networks. *J. Phys. B: At., Mol. Opt. Phys.*, 44:245501, 2011.

[127] C. Olbrich, J. Strümpfer, K. Schulten, and U. Kleinekathöfer. Theory and simulation of the environmental effects on FMO electronic transitions. *J. Phys. Chem. Lett.*, 2:1771–1776, 2011.

[128] I. P. Mercer, I. R. Gould, and D. R. Klug. A quantum mechanical / molecular mechanical approach to relaxation dynamics: Calculation of the optical properties of solvated bacteriochlorophyll-a. *J. Phys. Chem. B*, 103:7720–7727, 1999.

[129] S. A. Egorov and B. J. Berne. Vibrational energy relaxation in the condensed phases: Quantum vs classical bath for multiphonon processes. *J. Chem. Phys.*, 107:6050, 1997.

[130] S. A. Egorov, E. Rabani, and B. J. Berne. On the adequacy of mixed quantum-classical dynamics in condensed phase systems. *J. Phys. Chem. B*, 103:10978–10991, 1999.

[131] H. Kim and P. J. Rossky. Evaluation of quantum correlation functions from classical data. *J. Phys. Chem. B*, 106:8240–8247, 2002.

[132] R. Ramírez, T. López-Ciudad, P. Kumar P, and D. Marx. Quantum corrections to classical time-correlation functions: hydrogen bonding and anharmonic floppy modes. *J. Chem. Phys.*, 121:3973–83, 2004.

[133] L. Frommhold. *L. Collision-induced absorption in gases*, volume 2. Cambridge University Press, 1st ed. edition, 1993.

[134] P. H. Berens, G.M. White, and K. R. Wilson. Molecular dynamics and spectra. II. diatomic raman. *J. Chem. Phys.*, 75:515, 1981.

[135] B. J. Berne and G. D. Harp. *On the Calculation of Time Correlation Functions*, pages 63–227. John Wiley and Sons, Inc., 1970.

[136] A. Sung-Chung, C. J. Montrose, and T. A. Litovitz. Low-frequency structure in the depolarized spectrum of argon. *J. Chem. Phys.*, 64:3717–3719, 1976.

[137] D. W. Oxtoby. *Vibrational Population Relaxation in Liquids*, pages 487–519. John Wiley and Sons, Inc., 2007.

[138] Y. Yan and R. Xu. Quantum mechanics of dissipative systems. *Ann. Rev. Phys. Chem.*, 56:187–219, 2005.

[139] P. Schofield. Space-time correlation function formalism for slow neutron scattering. *Phys. Rev. Lett.*, 4:239–240, 1960.

[140] P. A. Egelstaff. Neutron scattering studies of liquid diffusion. *Adv. Phys.*, 11:203–232, 1962.

[141] G. D. Scholes, C. Curutchet, B. Mennucci, R. Cammi, and J. Tomasi. How solvent controls electronic energy transfer and light harvesting. *J. Phys. Chem. B*, 111:6978–6982, 2007.

[142] J. Neugebauer, C. Curutchet, A. Muñoz Losa, and B. Mennucci. A subsystem TDDFT approach for solvent screening effects on excitation energy transfer couplings. *J. Chem. Theory Comput.*, 6:1843–1851, 2010.

[143] F. C. Spano. Analysis of the UV/Vis and CD spectral line shapes of carotenoid assemblies: Spectral signatures of chiral H-aggregates. *J. Am. Chem. Soc.*, 131:4267–4278, 2009.

[144] P. O. J. Scherer and S. F. Fischer. On the theory of vibronic structure of linear aggregates. application to pseudoisocyanin (PIC). *Chem. Phys.*, 86:269–283, 1984.

[145] J. Guthmuller, F. Zutterman, and B. Champagne. Multimode simulation of dimer absorption spectra from first principles calculations: Application to the 3,4,9,10-perylenetetracarboxylic diimide dimer. *J. Chem. Phys.*, 131:154302, 2009.

[146] J. Roden, A. Eisfeld, M. Dvořák, O. Bünermann, and F. Stienkemeier. Vibronic line shapes of PTCDA oligomers in helium nanodroplets. *J. Chem. Phys.*, 134:054907, 2011.

[147] E. S. Medvedev and V. I. Osherov. *Radiationless Transitions in Polyatomic Molecules*, volume 57 of *Springer Series in Chemical Physics*. Springer-Verlag, 1995.

[148] D. V. LeBard, D N. .and Matyushov. Dynamical transition, hydrophobic interface, and the temperature dependence of electrostatic fluctuations in proteins. *Phys. Rev. E*, 78:061901, 2008.

[149] A. Warshel and W. W. Parson. Dynamics of biochemical and biophysical reactions: insight from computer simulations. *Q. Rev. Biophys.*, 34:563–679, 2001.

[150] D.E. Canfield, B. Thamdrup, and E. Kristensen. *Aquatic geomicrobiology*. Elsevier, London, 2005.

[151] J. Overmann. *The Prokaryotes. Volume 7: Proteobacteria: Delta, Epsilon Subclass*, chapter The Family Chlorobiaceae, pages 359–378. Springer, 2006.

[152] X. Feng, K.-H. Tang, R. E. Blankenship, and Y. J. Tang. Metabolic flux analysis of the mixotrophic metabolisms in the green sulfur bacterium Chlorobaculum tepidum. *J. Bio. Chem.*, 285:39544–50, 2010.

[153] J. Overmann, H. Cypionka, and N. Pfennig. An extremely low-light-adapted phototrophic sulfur bacterium from the black sea. *Limnol. Oceanog.*, 37:150–155, 1992.

[154] A. K. Manske, J. Glaeser, M. M. M. Kuypers, and J. Overmann. Physiology and phylogeny of green sulfur bacteria forming a monospecific phototrophic assemblage at a depth of 100 meters in the black sea physiology and phylogeny of green sulfur bacteria forming a monospecific phototrophic assemblage at a depth of 100 m. *Appl. Environ. Microbiol.*, 71:8049, 2005.

[155] G. D. Scholes, G. R. Fleming, A. Olaya-Castro, and R. van Grondelle. Lessons from nature about solar light harvesting. *Nat. Chem.*, 3:763–74, 2011.

[156] A.Y. Borisov. On the structure and function of chlorosomes of green bacteria. *Biophysics*, 57:562–564, 2012.

[157] S. Lloyd and M. Mohseni. Symmetry-enhanced supertransfer of delocalized quantum states. *New J. Phys.*, 12:075020, 2010.

[158] S. Hoyer, M. Sarovar, and K. B. Whaley. Limits of quantum speedup in photosynthetic light harvesting. *New J. Phys.*, 12:065041, 2010.

[159] D. F. Abasto, M. Mohseni, S. Lloyd, and P. Zanardi. Exciton diffusion length in complex quantum systems: the effects of disorder and environmental fluctuations on symmetry-enhanced supertransfer. *Phil. Trans. R. Soc. A*, 370:3750–70, 2013.

[160] S. Savikhin, P. I. van Noort, Y. Zhu, S. Lin, R. E. Blankenship, and W. S. Struve. Ultrafast energy transfer in light-harvesting chlorosomes from the green sulfur bacterium Chlorobium tepidum. *Chem. Phys.*, 194:245–258, 1995.

[161] J. Psencík, T. Polívka, J. Dian, J. Kudrna, and P. Malý. Fast energy transfer and exciton dynamics in chlorosomes of the green sulfur bacterium Chlorobium tepidum. *J. Phys. Chem. A*, 102:4392–4398, 1998.

[162] J. Psencík, Y-Z. Ma, J. B. Arellano, J. Hála, and T. Gillbro. Excitation energy transfer dynamics and excited-state structure in chlorosomes of Chlorobium phaeobacteroides. *Biophys. J.*, 84:1161–79, 2003.

[163] V. I. Prokhorenko, D. B. Steensgaard, and A. R. Holzwarth. Exciton dynamics in the chlorosomal antennae of the green bacteria Chloroflexus aurantiacus and Chlorobium tepidum. *Biophys. J.*, 79:2105–2120, 2000.

[164] J. Martiskainen, J. M. Linnanto, V. Aumanen, P. Myllyperkiö, and J. Korppi-Tommola. Excitation energy transfer in isolated chlorosomes from Chlorobaculum tepidum and Prosthecochloris aestuarii. *Photochem. Photobiol.*, 88:675–683, 2012.

[165] Z. Fetisova, A. Freiberg, K. Mauring, V. Novoderezhkin, A. Taisova, and K. Timpmann. Excitation energy transfer in chlorosomes of green bacteria: theoretical and experimental studies. *Biophys. J.*, 71:995–1010, 1996.

[166] Y. Shibata, Y. Saga, H. Tamiaki, and S. Itoh. Polarized fluorescence of aggregated bacteriochlorophyll c and baseplate bacteriochlorophyll a in single chlorosomes isolated from Chloroflexus aurantiacus. *Biochemistry (Mosc.)*, 46:7062–7068, 2007.

[167] J. Martiskainen, J. Linnanto, R. Kananavičius, V. Lehtovuori, and J. E. I. Korppi-Tommola. Excitation energy transfer in isolated chlorosomes from Chloroflexus aurantiacus. *Chem. Phys. Lett.*, 477:216–220, 2009.

[168] K. Mukai, S. Abe, and H. Sumi. Theory of rapid excitation-energy transfer from b800 to optically-forbidden exciton states of B850 in the antenna system LH2 of photosynthetic purple bacteria. *J. Phys. Chem. B*, 103:6096–6102, 1999.

[169] S. Jang. Generalization of the Förster resonance energy transfer theory for quantum mechanical modulation of the donor-acceptor coupling. *J. Chem. Phys.*, 127:174710, 2007.

[170] C. Kreisbeck. Quantum transport through complex networks? From light-harvesting proteins to semiconductor devices, dissertation. 2012.

[171] H. W. Kim, A. Kelly, J. W. Park, and Y. M. Rhee. All-atom semiclassical dynamics study of quantum coherence in photosynthetic Fenna-Matthews-Olson complex. *J. Am. Chem. Soc.*, 134:11640–51, 2012.

[172] G. L. Celardo, F. Borgonovi, M. Merkli, V. I. Tsifrinovich, and G. P. Berman. Superradiance transition in photosynthetic light-harvesting complexes. *J. Phys. Chem. C*, 116:22105–22111, 2012.

[173] X. Hu, T. Ritz, A. Damjanovic, and K. Schulten. Pigment organization and transfer of electronic excitation in the photosynthetic unit of purple bacteria. *J. Phys. Chem. B*, 101:3854–3871, 1997.

[174] M. K. Sener, J. D. Olsen, C. N. Hunter, and K. Schulten. Atomic-level structural and functional model of a bacterial photosynthetic membrane vesicle. *Proc. Natl. Acad. Sci.*, 104:15723–8, 2007.

[175] A. K. Ringsmuth, G. J. Milburn, and T. M. Stace. Multiscale photosynthetic and biomimetic excitation energy transfer. *Nat. Phys.*, 8:562–567, 2012.

[176] J. Dostál, T. Mančal, R. Augulis, F. Vácha, J. Pšenčík, and D. Zigmantas. Two-dimensional electronic spectroscopy reveals ultrafast energy diffusion in chlorosomes. *J. Am. Chem. Soc.*, 134:11611–7, 2012.

[177] E. N. Zimanyi and R. J. Silbey. Theoretical description of quantum effects in multichromophoric aggregates. *Phil. Trans. R. Soc. A*, 370:3620–37, 2012.

[178] N.-U. Frigaard, A. Gomez Maqueo Chew, H. Li, J. A. Maresca, and D. A. Bryant. Chlorobium tepidum: insights into the structure, physiology, and metabolism of a green sulfur bacterium derived from the complete genome sequence. *Photosynth. Res.*, 78:93–117, 2003.

[179] A. R. Holzwarth and K. Schaffner. On the structure of bacteriochlorophyll molecular aggregates in the chlorosomes of green bacteria. A molecular modelling study. *Photosynth. Res.*, 41:225–233, 1994.

[180] R. Frese, U. Oberheide, I. van Stokkum, R. van Grondelle, M. Foidl, and H. van Amerongen. The organization of bacteriochlorophyll c in chlorosomes from Chloroflexus aurantiacus and the structural role of carotenoids and protein: an absorption, linear dichroism, circular dichroism and stark spectroscopy study. *Photosynth. Res.*, 54:115–126, 1997.

[181] J. M. Linnanto and J. E. I. Korppi-Tommola. Investigation on chlorosomal antenna geometries: tube, lamella and spiral-type self-aggregates. *Photosynth. Res.*, 96:227–45, 2008.

[182] J. Psencík, T. P. Ikonen, P. Laurinmäki, M. C. Merckel, S. J. Butcher, R. E. Serimaa, and R. Tuma. Lamellar organization of pigments in chlorosomes, the light harvesting complexes of green photosynthetic bacteria. *Biophys. J.*, 87:1165–1172, 2004.

[183] S. Ganapathy, G. T. Oostergetel, M. Reus, Y. Tsukatani, A. Gomez Maqueo Chew, F. Buda, D. A. Bryant, A. R. Holzwarth, and H. J. M. de Groot. Structural variability in wild-type and BChl-q BChl-r mutant chlorosomes of the green sulfur bacterium Chlorobaculum tepidum. *Biochemistry*, 51:4488–4498, 2012.

[184] J. K. H. Tang, S. K. Saikin, S. V. Pingali, M. M. Enriquez, J. Huh, H. A. Frank, V. S. Urban, and A. Aspuru-Guzik. Temperature and carbon assimilation regulate the chlorosome biogenesis in green sulfur bacteria. *Biophys. J.*, 105:1346–1356, 2013.

[185] S. Ganapathy, G. T. Oostergetel, P. K. Wawrzyniak, M. Reus, A. Gomez Maqueo Chew, F. Buda, E. J. Boekema, D. A. Bryant, A. R. Holzwarth, and H. J. M. de Groot. Alternating syn-anti bacteriochlorophylls form concentric helical nanotubes in chlorosomes. *Proc. Natl. Acad. Sci.*, 106:8525–8530, 2009.

[186] Y. Tian, R. Camacho, D. Thomsson, M. Reus, A. R. Holzwarth, and I. G. Scheblykin. Organization of bacteriochlorophylls in individual chlorosomes from Chlorobaculum tepidum studied by 2-dimensional polarization fluorescence microscopy. *J. Am. Chem. Soc.*, 133:17192–17199, 2011.

[187] M. Ø. Pedersen, L. Pham, D. B. Steensgaard, and M. Miller. A reconstituted light-harvesting complex from the green sulfur bacterium Chlorobium tepidum containing csma and bacteriochlorophyll a. *Biochemistry (Mosc.)*, 47:1435–41, 2008.

[188] J. C. Phillips, R. Braun, W. Wang, J. Gumbart, E. Tajkhorshid, E. Villa, C. Chipot, R. D. Skeel, L. Kale, and K. Schulten. Scalable molecular dynamics with NAMD. *J. Comput. Chem.*, 26:1781–1802, 2005.

[189] V. Hornak, R. Abel, A. Okur, B. Strockbine, A. Roitberg, and C. Simmerling. Comparison of multiple Amber force fields and development of improved protein backbone parameters. *Proteins*, 65:712–25, 2006.

[190] R. E. Blankenship, M. T. Madigan, and C. E. Bauer. *Anoxygenic photosynthetic bacteria*. Kluwer Academic Publishers, New York, 1995.

[191] J. Wen, H. Zhang, M. L. Gross, and R. E. Blankenship. Membrane orientation of the FMO antenna protein from Chlorobaculum tepidum as determined by mass spectrometry-based footprinting. *Proc. Natl. Acad. Sci.*, 106:6134–9, 2009.

[192] M. T. W. Milder, B. Brüggemann, R. van Grondelle, and J. L. Herek. Revisiting the optical properties of the FMO protein. *Photosynth. Res.*, 104:257–74, 2010.

[193] C. Francke and J. Amesz. Isolation and pigment composition of the antenna system of four species of green sulfur bacteria. *Photosynth. Res.*, pages 137–146, 1997.

[194] T. Fujita, J. C. Brookes, S. K. Saikin, and A. Aspuru-Guzik. Memory-assisted exciton diffusion in the chlorosome light-harvesting antenna of green sulfur bacteria. *J Phys. Chem. Lett.*, 3:2357–2361, 2012.

[195] V. I. Prokhorenko, D. B. Steensgaard, and A. R. Holzwarth. Exciton theory for supramolecular chlorosomal aggregates: 1. Aggregate size dependence of the linear spectra. *Biophys. J.*, 85:3173–3186, 2003.

[196] W. H. Louisell. *Quantum Statistical Properties of Radiation*. John Wiley and Sons, 1990.

[197] T. Fujita, J. Huh, S. K. Saikin, J. C. Brookes, and A. Aspuru-Guzik. Theoretical characterization of excitation energy transfer in chlorosome light-harvesting antennae from green sulfur bacteria. *Photosynth. Res., in press*, 2014.

[198] S. Valleau, A. Eisfeld, and A. Aspuru-Guzik. On the alternatives for bath correlators and spectral densities from mixed quantum-classical simulations. *J. Chem. Phys.*, 137:224103(1)–224103(13), 2012.

[199] W. M. Zhang, T. Meier, V. Chernyak, and S. Mukamel. Exciton-migration and three-pulse femtosecond optical spectroscopies of photosynthetic antenna complexes of photosynthetic antenna complexes. *J. Chem. Phys.*, 108:7763, 1998.

[200] T. Pullerits. Exciton states and relaxation in molecular aggregates: Numerical study of photosynthetic light harvesting. *J. Chin. Chem. Soc.*, 47:773–784, 2000.

[201] M. Yang and G. R. Fleming. Influence of phonons on exciton transfer dynamics: comparison of the Redfield, Förster and modified Redfield equations. *Chem. Phys.*, 275:355–372, 2002.

[202] V. I. Novoderezhkin, J. M. Salverda, and H. van Amerongen. Exciton modeling of energy-transfer dynamics in the LHCII complex of higher plants: A Redfield theory approach. *J. Phys. Chem. B*, pages 1893–1912, 2003.

[203] V. I. Novoderezhkin, M. A. Palacios, and H. van Amerongen. Energy-transfer dynamics in the LHCII complex of higher plants: Modified Redfield. *J. Phys. Chem. B*, pages 10363–10375, 2004.

[204] P. Huo and D. F. Coker. Theoretical study of coherent excitation energy transfer in cryptophyte phycocyanin 645 at physiological temperature. *J. Phys. Chem. Lett.*, 2:825–833, 2011.

[205] D. P. S. Mccutcheon and A. Nazir. Consistent treatment of coherent and incoherent energy transfer dynamics using a variational master equation. *J. Chem. Phys.*, 135:114501, 2011.

[206] L. Mühlbacher and U. Kleinekathöfer. Preparational effects on the excitation energy transfer in the FMO complex. *J. Phys. Chem. B*, 116:3900–6, 2012.

[207] L. A. Pachón and P. Brumer. Computational methodologies and physical insights into electronic energy transfer in photosynthetic light-harvesting complexes. *Phys. Chem. Chem. Phys.*, 14:10094–108, 2012.

[208] P. Brumer and M. Shapiro. Molecular response in one-photon absorption via natural thermal light vs. pulsed laser excitation. *Proc. Natl. Acad. Sci.*, 109:19575–8, 2012.

[209] S. Jang, M. Newton, and R. J. Silbey. Multichromophoric Förster resonance energy transfer. *Phys. Rev. Lett.*, 92:218301–4, 2004.

[210] M. Yang and G. R. Fleming. Construction of kinetic domains in energy trapping processes and application to a photosynthetic light harvesting complex. *J. Chem. Phys.*, 119:5614, 2003.

[211] R. Hildner, D. Brinks, J. B. Nieder, R. J. Cogdell, and N. F. van Hulst. Quantum coherent energy transfer over varying pathways in single light-harvesting complexes. *Science*, 340:1448–1451, 2013.

[212] J. M. Linnanto and J. E. I. Korppi-Tommola. Exciton description of chlorosome to baseplate excitation energy transfer in filamentous anoxygenic phototrophs and green sulfur bacteria. *J. Phys. Chem. B*, 117:11144–11161, 2013.

[213] F. Caruso, S. K. Saikin, E. Solano, S. Huelga, A. Aspuru-Guzik, and M. B. Plenio. Probing biological light-harvesting phenomena by optical cavities. *Phys. Rev. B*, 85:125424, 2012.

[214] G. Tao and W. H. Miller. Semiclassical description of electronic excitation population transfer in a model photosynthetic system. *J. Phys. Chem. Lett.*, 1:891–894, 2010.

[215] C. Olbrich, J. Strümpfer, and U. Schulten, K.and Kleinekathöfer. Quest for spatially correlated fluctuations in the FMO light-harvesting complex. *J. Phys. Chem. B.*, 115:758–764, 2011.

[216] S. Jurinovich, C. Curutchet, and B. Mennucci. The Fenna-Matthews-Olson protein revisited: A fully polarizable (TD)DFT/MM description. *ChemPhysChem*, 15:3194–3204, 2014.

[217] Y. Shan, J. L. Klepeis, M. P. Eastwood, R. O. Dror, and D. E. Shaw. Gaussian split Ewald: A fast Ewald mesh method for molecular simulation. *J. Chem. Phys.*, 122:054101, 2005.

[218] D. Rappoport and J. Hutter. *Fundamentals of Time-Dependent Density Functional Theory (Lecture Notes in Physics 837)*, chapter Excited-State Properties and Dynamics, pages 317–336. Springer Berlin / Heidelberg, 2012.

[219] M. Rupp, A. Tkatchenko, K-R. Müller, and O. A. von Lilienfeld. Fast and accurate modeling of molecular atomization energies with machine learning. *Phys. Rev. Lett.*, 108:058301, 2012.

[220] R. Ramakrishnan, M. Hartmann, E. Tapavicza, and O. A. von Lilienfeld. Electronic spectra from TDDFT and machine learning in chemical space. *J. Chem. Phys.*, 143, 2015.

[221] O. Anatole von Lilienfeld, Raghunathan Ramakrishnan, Matthias Rupp, and Aaron Knoll. Fourier series of atomic radial distribution functions: A molecular fingerprint for machine learning models of quantum chemical properties. *Int. J. Quantum Chem.*, 115:1084–1093, 2015.

[222] K. Hansen, F. Biegler, R. Ramakrishnan, W. Pronobis, O. A. von Lilienfeld, K. R. Müller, and A. Tkatchenko. Machine learning predictions of molecular properties: Accurate many-body potentials and nonlocality in chemical space. *J. Phys. Chem. Lett.*, 6:2326–2331, 2015.

[223] E. O. Pyzer-Knapp, K. Li, and A. Aspuru-Guzik. Learning from the harvard clean energy project: The use of neural networks to accelerate materials discovery. *Adv. Funct. Mater.*, 25:6495–6502, 2015.

[224] M. Olivucci. *Computational Photochemistry*, chapter Density Functional Methods for Excited States: Equilibrium Structure and Electronic Spectra, pages 93–128. Elsevier, 2005.

[225] W. L. Jorgensen and J. D. Madura. Solvation and conformation of methanol in water. *J. Am. Chem. Soc.*, pages 1407–1413, 1983.

[226] J. P. Perdew, M. Ernzerhof, and K. Burke. Rationale for mixing exact exchange with density functional approximations. *J. Chem. Phys.*, 105:9982, 1996.

[227] J. C. Taylor. Tamm-Dancoff method. *Phys. Rev.*, 95:1313–1317, 1954.

[228] Y. Shao, Z. Gan, E. Epifanovsky, A. T. B. Gilbert, M. Wormit, J. Kussmann, A. W. Lange, A. Behn, J. Deng, X. Feng, D. Ghosh, M. Goldey, P. R. Horn, L. D. Jacobson, I. Kaliman, R. Z. Khaliullin, T. Kús, A. Landau, J. Liu, E. I. Proynov, Y. M. Rhee, R. M. Richard, M. A. Rohrdanz, R. P. Steele, E. J. Sundstrom, H. L. Woodcock III, P. M. Zimmerman, D. Zuev, B. Albrecht, E. Alguire, B. Austin, G. J. O. Beran, Y. A. Bernard, E. Berquist, K. Brandhorst, K. B. Bravaya, S. T. Brown, D. Casanova, C.-M. Chang, Y. Chen, S. H. Chien, K. D. Closser, D. L. Crittenden, M. Diedenhofen, R. A. DiStasio Jr., H. Dop, A. D. Dutoi, R. G. Edgar, S. Fatehi, L. Fusti-Molnar, A. Ghysels, A. Golubeva-Zadorozhnaya, J. Gomes, M. W. D. Hanson-Heine, P. H. P. Harbach, A. W. Hauser, E. G. Hohenstein, Z. C. Holden, T.-C. Jagau, H. Ji, B. Kaduk, K. Khistyaev, J. Kim, J. Kim, R. A. King, P. Klunzinger, D. Kosenkov, T. Kowalczyk, C. M. Krauter, K. U. Lao, A. Laurent, K. V. Lawler, S. V. Levchenko, C. Y. Lin, F. Liu, E. Livshits, R. C. Lochan, A. Luenser, P. Manohar, S. F. Manzer, S.-P. Mao, N. Mardirossian, A. V. Marenich, S. A. Maurer, N. J. Mayhall, C. M. Oana, R. Olivares-Amaya, D. P. O'Neill, J. A. Parkhill, T. M. Perrine, R. Peverati, P. A. Pieniazek, A. Prociuk, D. R. Rehn, E. Rosta, N. J. Russ, N. Sergueev, S. M. Sharada, S. Sharmaa, D. W. Small, A. Sodt, T. Stein, D. Stück, Y.-C. Su, A. J. W. Thom, T. Tsuchimochi, L. Vogt, O. Vydrov, T. Wang, M. A. Watson, J. Wenzel, A. White, C. F. Williams, V. Vanovschi, S. Yeganeh, S. R. Yost, Z.-Q. You, I. Y. Zhang, X. Zhang, Y. Zhou, B. R. Brooks, G. K. L. Chan, D. M. Chipman, C. J. Cramer, W. A. Goddard III, M. S. Gordon, W. J. Hehre, A. Klamt, H. F. Schaefer III, M. W. Schmidt, C. D. Sherrill, D. G. Truhlar, A. Warshel, X. Xua, A. Aspuru-Guzik, R. Baer, A. T. Bell, N. A. Besley, J.-D. Chai, A. Dreuw, B. D. Dunietz, T. R. Furlani, S. R. Gwaltney, C.-P. Hsu, Y. Jung, J. Kong, D. S. Lambrecht, W. Liang, C. Ochsenfeld, V. A. Rassolov, L. V. Slipchenko, J. E. Subotnik, T. Van Voorhis, J. M. Herbert, A. I. Krylov, P. M. W. Gill, and M. Head-Gordon. Advances in molecular quantum chemistry contained in the Q-Chem 4 program package. *Mol. Phys.*, 113:184–215, 2015.

[229] S. Chandrasekaran, M. Aghtar, S. Valleau, A. Aspuru-Guzik, and U. Kleinekathöfer. Influence of force fields and quantum chemistry approach on spectral densities of BChl a in solution and in FMO proteins. *J. Phys. Chem. B*, 119:9995–10004, 2015. PMID: 26156758.

[230] F. Häse, S. Valleau, E. Pyzer-Knapp, and A. Aspuru-Guzik. Machine learning for exciton dynamics: Qy trajectories. *figshare*, 2015.

[231] D. E. Rumelhart, G. E. Hinton, and R. J. Williams. Parallel distributed processing: Explorations in the microstructure of cognition, vol. 1. chapter Learning Internal Representations by Error Propagation, pages 318–362. MIT Press, Cambridge, MA, USA, 1986.

[232] J. Heaton. Encog: Library of interchangeable machine learning models for Java and C#. *J. Mach. Learn. Res.*, 16:1243–1247, 2015.

[233] N. H. List, C. Curutchet, S. Knecht, B. Mennucci, and J. Kongsted. Toward reliable prediction of the energy ladder in multichromophoric systems: A benchmark study on the FMO light-harvesting complex. *J. Chem. Theory Comput.*, 9:4928–4938, 2013.

[234] M. Riedmiller. Advanced supervised learning in multi-layer perceptrons - from backpropagation to adaptive learning algorithms. *Comp. Stand. Inter.*, 16:265–278, 1994.

[235] L. Prechelt. Automatic early stopping using cross validation: quantifying the criteria. *Neural Netw.*, 11:761 – 767, 1998.

[236] D. Frenkel and B. Smit. *Understanding Molecular Simulation*, chapter Free Energies and Phase Equilibria, pages 165–199. Academic Press, 2002.

[237] X. Daura, K. Gademann, B. Jaun, D. Seebach, W. F. van Gunsteren, and A. E. Mark. Peptidfaltung: Wenn die simulation das experiment erreicht. *Angew. Chem.*, 111:249–253, 1999.

[238] M. Aghtar, J. Strümpfer, C. Olbrich, K. Schulten, and U. Kleinekathöfer. The FMO complex in a glycerol-water mixture. *J. Phys. Chem. B*, 117:7157–7163, 2013. PMID: 23697741.

[239] A. Eisfeld, R. Kniprath, and J. S. Briggs. Theory of the absorption and circular dichroism spectra of helical molecular aggregates. *J. Chem. Phys.*, 126:104904(1)–104904(13), 2007.

[240] L. D. Bakalis and J. Knoester. Optical properties of one-dimensional exciton systems: Beyond the Heitler-London approximation. *J. Chem. Phys.*, 106:6964, 1997.

[241] A. Pugzlys, R. Augulis, P. H. M. Van Loosdrecht, C. Didraga, V. A. Malyshev, and J. Knoester. Temperature-dependent relaxation of excitons in tubular molecular aggregates: Fluorescence decay and stokes shift. *J. Phys. Chem. B*, 110:20268–20276, 2006.

[242] G. Scheibe and L. Kandler. Anisotropie organischer farbstoffmoleküle. nebenvalenz-bindung als energieüberträger. *Naturwissenschaften*, 26:412–413, 1938.

[243] W. J. Harrison, D. L. Mateer, and G. J. T. Tiddy. J-aggregates and liquid crystal structures of cyanine dyes. *Faraday Discuss.*, 104:139, 1996.

[244] H. Nakahara, K. Fukuda, D. Moebius, and H. Kuhn. Two-dimensional arrangement of chromophores in J-aggregates of long-chain merocyanines and its effect on energy transfer in monolayer systems. *J. Phys. Chem.*, 90:6144–6148, 1986.

[245] M Bradley, J Tischler, and V Bulovic. Layer-by-layer J-aggregate thin films with a peak absorption constant of 106 wavenumbers. *Adv. Mater.*, 17:1881–1886, 2005.

[246] E. Maltsev, D. Lypenko, B. Shapiro, G. Milburn, J. Wright, M. Brusentseva, V. Berendyaev, B. Kotov, and A. V. Vannikov. Electroluminescence of polyimide-based composites containing nanocrystalline J-aggregates. *Polym. Sci. Ser. A.*, 42:299–305, 2000.

[247] J. McKeever, A. Boca, A. D. Boozer, J. R. Buck, and H. J. Kimble. Experimental realization of a one-atom laser in the regime of strong coupling. *Nature*, 425:268–271, 2003.

[248] P. E. Shaw, A. Ruseckas, J. Peet, G. C. Bazan, and I. D. W. Samuel. Exciton-exciton annihilation in mixed-phase polyfluorene films. *Adv. Funct. Mater.*, 20:155–161, 2010.

[249] H. Marciniak, X.-Q. Li, F. Würthner, and S. Lochbrunner. One-dimensional exciton diffusion in perylene bisimide aggregates. *J. Phys. Chem. A*, 115:648–654, 2011.

[250] B. Lyons and A. Monkman. The role of exciton diffusion in energy transfer between polyfluorene and tetraphenyl porphyrin. *Phys. Rev. B*, 71:1–5, 2005.

[251] R. R. Lunt, N. C. Giebink, A. A. Belak, J. B. Benziger, and S. R. Forrest. Exciton diffusion lengths of organic semiconductor thin films measured by spectrally resolved photoluminescence quenching. *J. Appl. Phys.*, 105:053711, 2009.

[252] J. Salcedo, A. Siegman, D. Dlott, and M. Fayer. Dynamics of energy transport in molecular crystals: The picosecond transient-grating method. *Phys. Rev. Lett.*, 41:131–134, 1978.

[253] A. K. Ghosh and T. Feng. Merocynanine organic solar cells. *J. Appl. Phys.*, 49:5982, 1978.

[254] V. Bulovic and S. Forrest. Excitons in crystalline thin films of 3,4,9,10-perylenetetracarboxylic dianhydride studied by photocurrent response. *Chem. Phys. Lett.*, 238:88–92, 1995.

[255] M. Aeschlimann, T. Brixner, A. Fischer, C. Kramer, P. Melchior, W. Pfeiffer, C. Schneider, C. Strüber, P. Tuchscherer, and D. V. Voronine. Coherent two-dimensional nanoscopy. *Science*, 333:1723–1726, 2011.

[256] C. Madigan and V. Bulović. Modeling of exciton diffusion in amorphous organic thin films. *Phys. Rev. Lett.*, 96:046404, 2006.

[257] P. Reineker. Equations of motion for the moments of the coupled coherent and incoherent motion of triplet and singlet excitons. *Z. Phys.*, 261:187–190, 1973.

[258] V. Ern, A. Suna, Y. Tomkiewicz, P. Avakian, and R. Groff. Temperature dependence of triplet-exciton dynamics in anthracene crystals. *Phys. Rev. B*, 5:3222–3234, 1972.

[259] P. Reineker. Drift mobility of photo-electrons in organic molecular crystals: Quantitative comparison between theory and experiment. *Phys. Lett. A*, 84:294–296, 1981.

[260] V. M. Kenkre, R. Kuhne, and P. Reineker. Connection of the velocity autocorrelation function to the mean-square-displacement and to the memory function of generalized master equations. *Z. Phys. B. Cond. Matt.*, 41:177–180, 1981.

[261] A. S. Davydov. *Theory of Molecular Excitons*. McGraw-Hill, New York, 1962.

[262] V. Czikklely, H. D. Forsterling, and H. Kuhn. Extended dipole model for aggregates of dye molecules. *Chem. Phys. Lett.*, 6:207–210, 1970.

[263] D. Möbius and H. Kuhn. Energy transfer in monolayers with cyanine dye Scheibe aggregates. *J. Appl. Phys.*, 64:5138, 1988.

[264] A. Eisfeld, S. M. Vlaming, V. A. Malyshev, and J. Knoester. Excitons in molecular aggregates with levy-type disorder: Anomalous localization and exchange broadening of optical spectra. *Phys. Rev. Lett.*, 105:137402–137406, 2010.

[265] T. Renger and R. A. Marcus. On the relation of protein dynamics and exciton relaxation in pigment protein complexes: An estimation of the spectral density and a theory for the calculation of optical spectra. *J. Chem. Phys.*, 116:9997, 2002.

[266] D. M. Coles, A. J. H. M. Meijer, W. C. Tsoi, M. D. B. Charlton, J.-S. Kim, and D. G. Lidzey. A characterization of the raman modes in a J-aggregate forming dye: a comparison between theory and experiment. *J. Phys. Chem. A*, 114:11920–7, 2010.

[267] R. Ahlrichs, M. Bär, M. Häser, H. Horn, and C. Kölmel. Electronic structure calculations on workstation computers: The program system turbomole. *Chem. Phys. Lett.*, 162:165, 1989.

[268] F. Weigend and R. Ahlrichs. Balanced basis sets of split valence, triple zeta valence and quadruple zeta valence quality for H to Rn: Design and assessment of accuracy. *Phys. Chem. Chem. Phys.*, 7:3297, 2005.

[269] K. Klamt and G. Schüürmann. COSMO: A new approach to dielectric screening in solvents with explicit expressions for the screening energy and its gradient. *J. Chem. Soc. Perkin Trans.*, 2:799–805, 1993.

[270] D. L. Dexter. A theory of sensitized luminescence in solids. *J. Chem. Phys.*, 21:836–850, 1953.

[271] K. Mølmer, Y. Castin, and J. Dalibard. Monte carlo wave-function method in quantum optics. *J. Opt. Soc. Am. B*, 10:524, 1993.

[272] K. Fukui, T. Yonezawa, and H.H. Shingu. A molecular orbital theory of reactivity in aromatic hydrocarbons. *J. Chem. Phys.*, 20:722–725, 1952.

[273] S. S. Batsanov. Van der waals radii of elements. *Inorg. Mater.*, 37:871–885, 2001.

[274] N. Kometani, M. Tsubonishi, T. Fujita, K. Asami, and Y. Yonewaza. Preparation and optical absorption spectra of dye-coated Au, Ag, and Au/Ag colloidal nanoparticles in acqueous solutions and in alternate assemblies. *Langmiur*, 17:578–580, 2001.

[275] W. Xu and D. Akins. Absorption and exciton emission by an aggregated cyanine dye occluded within mesoporous sba-15. *J. Phys. Chem. B*, 106:1991–1994, 2002.

[276] J. Wenus, S. Ceccarelli, D. Lidzey, A. I. Tolmachev, J. L. Slominskii, and J. L. Bricks. Optical strong coupling in microcavities containing J-aggregates absorbing in near-infrared spectral range. *Org. Electron.*, 8:120–126, 2007.

[277] M. Chachisvilis, O. Kühn, T Pullerits, and V. Sundström. Excitons in photosynthetic purple bacteria: Wavelike motion or incoherent hopping? *J. Phys. Chem. B*, 101:7275–7283, 1997.

[278] V. Sundström, T. Pullerits, and R. van Grondelle. Photosynthetic light-harvesting: Reconciling dynamics and structure of purple bacterial LH2 reveals function of photosynthetic unit. *J. Phys. Chem. B*, 103:2327–2346, 1999.

[279] A. Eisfeld. Phase directed excitonic transport and its limitations due to environmental influence. *Chem. Phys.*, 33:1–7, 2011.

[280] A. N. Sokolov, S. Atahan-Evrenk, R. Mondal, H. B. Akkerman, R. S. Sanchez-Carrera, S. Granados-Focil, J. Schrier, S. C. B. Mannsfeld, A. P. Zoombelt, Z. Bao, and A. Aspuru-Guzik. From computational discovery to experimental characterization of a high hole mobility organic crystal. *Nat. Commun.*, 2:437, 2011.

[281] A. Devilez, B. Stout, and N. Bonod. Compact metallo-dielectric optical antenna for ultra directional and enhanced radiative emission. *ACS nano*, 4:3390–3396, 2010.

[282] L. Novotny and N. van Hulst. Antennas for light. *Nat. Photonics*, 5:83–90, 2011.

[283] N. S. King, M. W. Knight, N. Large, A. M. Goodman, P. Nordlander, and N. J. Halas. Orienting nanoantennas in three dimensions to control light scattering across a dielectric interface. *Nano Lett.*, 13:5997–6001, 2013.

[284] M. W. Knight, H. Sobhani, P. Nordlander, and N. J. Halas. Photodetection with active optical antennas. *Science*, 332:702–704, 2011.

[285] J.A. Schuller, S. E. Barnard, W. Cai, Y. C. Jun, J. S. White, and M. L. Brongersma. Plasmonics for extreme light concentration and manipulation. *Nat. Mater.*, 9:193–204, 2010.

[286] M. W. Knight, L. Liu, Y. Wang, L. Brown, S. Mukherjee, N. S. King, H. O. Everitt, P. Nordlander, and N. J. Halas. Aluminum plasmonic nanoantennas. *Nano Lett.*, 12:6000–6004, 2012.

[287] P. L. Hernández-Martínez, A. O. Govorov, and H. V. Demir. Generalized theory of Förster-type nonradiative energy transfer in nanostructures with mixed dimensionality. *J. Phys. Chem. C*, 117:10203–10212, 2013.

[288] J. Huh, S. K. Saikin, J. Brookes, S. Valleau, T. Fujita, and A. Aspuru-Guzik. Atomistic study of energy funneling in the light-harvesting complex of green sulfur bacteria. *J. Am. Chem. Soc.*, 136:2048–2057, 2014.

[289] E. N. Zimanyi and R. J. Silbey. Unified treatment of coherent and incoherent electronic energy transfer dynamics using classical electrodynamics. *J. Chem. Phys.*, 133:144107(1)–144107(10), 2010.

[290] D. Ansari-Oghol-Beig, M. Rostami, E. Chernobrovkina, S. Saikin, S. Valleau, H. Mosallaei, and A. Aspuru-Guzik. Parametric hierarchical matrix approach for the wideband optical response of large-scale molecular aggregates. *J. App. Phys.*, 114:164315(1)–164315(10), 2013.

[291] B.-J. van Rossum, D. B. Steensgaard, F. M. Mulder, G. J. Boender, K. Schaffner, A. R. Holzwarth, and H. J. M. de Groot. Refined model of the chlorosomal antennae of the green bacterium Chlorobium tepidum from proton chemical shift constraints obtained with high-field 2D and 2-D MAS NMR dipolar correlation spectroscopy. *Biochem.*, 40:1587–1595, 2001.

[292] M. F. Hohmann-Marriott, R. E. Blankenship, and R. W. Roberson. The ultra structure of Chlorobium tepidum chlorosomes revealed by electron microscopy. *Photosynth. Res.*, 86:145–154, 2005.

[293] I. de Boer, J. Matysik, K. Erkelens, S. Sasaki, T. Miyatake, S. Yagai, H. Tamiaki, A. R. Holzwarth, and H. J. M. de Groot. MAS NMR structures of aggregated cadmium chlorins reveal molecular control of self-assembly of chlorosomal bacteriochlorophylls. *J. Phys. Chem. B*, 108:16556–16566, 2004.

[294] A. Egawa, T. Fujiwara, T. Mizoguchi, Y. Kakitani, Y. Koyama, and H. Akutsu. Structure of the light-harvesting bacteriochlorophyll c assembly in chlorosomes from Chlorobium limicola determined by solid-state nmr. *Proc. Natl. Acad. Sci.*, 104:790–805, 2007.

[295] G. T. Oostergetel, M. Reus, A. Gomez Maqueo Chew, D. A. Bryant, E. J. Boekema, and A. R. Holzwarth. Long-range organization of bacteriochlorophyll in chlorosomes of Chlorobium tepidum investigated by cryo-electron microscopy. *FEBS Lett.*, 581:5435–9, 2007.

[296] G. D. Mahan. Davydov splittings in anthracene. *J. Chem. Phys.*, 41:2930–2933, 1964.

[297] H. DeVoe. Optical properties of molecular aggregates. II Classical theory of the refraction, absorption, and optical activity of solutions and crystals. *J. Chem. Phys.*, 43:3199–3208, 1965.

[298] J. M. Linnanto and J. E. I. Korppi-Tommola. Spectroscopic properties of mg-chlorin , mg-bacteriochlorin , and bacteriochlorophylls a , b , c , d , e , f , g , and h studied by semiempirical and ab initio MO / CI methods. *J. Phys. Chem.*, pages 3855–3866, 2001.

[299] R. S. Knox and B. Q. Spring. Dipole strengths in the chlorophylls. *Photochem. Photobiol.*, 77:497–501, 2003.

[300] D. Keller and C. Bustamante. Theory of the interaction of light with large inhomogeneous molecular aggregates. II. Psitype circular dichroism. *J. Chem. Phys.*, 84:2972–2980, 1986.

[301] J. S. Briggs and A. Eisfeld. Coherent quantum states from classical oscillator amplitudes. *Phys. Rev. A*, 85:052111(1)–052111(10), 2012.

[302] O. J. G. Somsen, R. van Grondelle, and H. van Amerongen. Spectral broadening of interacting pigments: Polarized absorption by photosynthetic proteins. *Biophys. J.*, 71:1934–1951, 1996.